UNIVERSITY OF CALIFORNIA,
RIVERSIDE

Synthesis and Applications of High Spin Paramagnetic Metal-Organic Cages

A Dissertation submitted in partial satisfaction
of the requirements for the degree of

Doctor of Philosophy

in

Chemistry

by

Tabitha Francine Miller

September 2020

Dissertation Committee:
Dr. Richard J. Hooley, Chairperson
Dr. Catherine Larsen
Dr. Christopher Switzer

The Dissertation of Tabitha Francine Miller is approved:

_____

_____

_____

Committee Chairperson

University of California, Riverside

ACKNOWLEDGMENTS

First, I would like to thank my advisor, Professor Richard Hooley, as without guidance and push I mostly likely would have left the program at one point and not completed this prestigious degree. While many of his ideas were not as akin to "falling off a log" as he thought they would be his push continued to force me to grow to become a better scientist and more fully understand the physical world around me.

I feel very lucky that the university and this degree has allowed me to stay close to friends and family and working the 5 years in the space with the same people has allowed me to make several new friendships as well. During my time in the Hooley lab, it was able to develop into a safe space and refuge. My co-workers have increased my scientific understanding but have also become friends by sharing in each other's happiness during good times and creating a safe space to breathe a bit easier during hard times. I would like to thank Dana Chambers, Bryce Da Camara, Adam Gill, Briana Hickey, Courtney Ngai and Conner Woods for letting me ask arguable too many dumb questions and help blow off steam from the pressure of graduate school. Thanks also to my lab mentor/mom Lauren Holloway for defining what it means to be a hard worker but also encouraging me to get outside and explore the world around me.

Additionally, I would like to thank my undergraduate lab mentor Chris Sanborn and his wife Amy for their continued love and support in both my professional and personal life, and the many wine and cheese nights that brought us close. To my closest and dearest friends Emily Young, Maddie Jahn, and Saswata Roy my immense thanks for helping me

have perspective on myself, this degree, pretty much everything and helping me keep it together. Your friendship cannot be overstated. I love you each dearly.

I also want to thank my husband, William North White, for his unwavering confidence in me. He had been my sun and my moon and my stars guiding me when I cannot lead myself. His view of me makes me want to be the best version of myself I can be. Thanks also to my husband's incredibly warm and loving family for including me immediately. Each of you intimately know what getting this degree is like and your encouragement has meant the world to me. To my brother Chris and his wife Megan thank you for your love and support and allowing me to be a role model to Ashley, who will undoubtedly have many accomplishments of her own. Candace, thank you for making me want to be someone you can look up to. Then on your own you also became a chemist and now I have someone else I can talk to about what I do, and you truly understand. I am so proud of you. Finally, Mom thank you for saying "your education is the one thing people can't take away from you" enough that I took it to heart, went as far as I could, and finished this goal. I love you.

The text of this dissertation, in part or in full, is a reprint of the material as they appear in the following publications:

Chapter 2: Miller, T. F.; Holloway, L. R.; Nye, P. P.; Lyon, Y.; Beran, G. J. O.; Harman, W. H.; Julian, R. R.; Hooley, R. J. Small Structural Variations have Large Effects on the

Assembly Properties and Spin State of Room Temperature High Spin Fe(II) Iminopyridine Cages. *Inorg. Chem.* **2018**, *57*, 13386-13396.

The co-author Richard J. Hooley listed in these publications directed and supervised the research which forms the basis for this dissertation. All other co-authors listed in these publications contributed technical expertise.

DEDICATION

To

my mom, Ellen, and my husband, Will,

through their overwhelming love and support, I am able to finish this degree.

And to my sister, Candace, I can't wait to see you finish yours.

ABSTRACT OF THE DISSERTATION

Synthesis and Applications of High Spin Paramagnetic Metal-Organic Cages

by

Tabitha Francine Miller

Doctor of Philosophy, Graduate Program in Chemistry
University of California, Riverside, September 2020
Dr. Richard J. Hooley, Chairperson

Supramolecular self-assembled metal-ligand cages have been used as reaction containers, molecular switches, and sensors. While many diamagnetic cage complexes are known, studies into spin-state switching cage complexes have only recently begun to emerge. These magnetically active complexes have applications in information storage, electronic switches, and display devices. To create stable, robust high spin complexes, new ligand structures must be explored focusing on the chelating portion of the ligand to affect the spin state of the metal centers.

This work analyzes the characteristics needed in ligands to form favorable paramagnetic cage complexes, using reversible multicomponent metal-ligand self-assembly methods. Using novel termini to interact as metal coordinators allows the formation of high spin Fe(II) metal centers. High spin Fe(II) can be obtained *via* two types of ligand interactions, either distortion of the octahedral coordination environment due to excess bulk at the metal center, or using a weak coordinator. The addition of steric bulk near the metal center requires a certain amount of flexibility in the ligand backbone to allow

favorable coordination. The spin states of these paramagnetic systems were examined to determine their magnetic moments and define the relationship between the metal centers. Alternatively, spin state switching complexes can be formed by using novel heterocyclic chelators. Using new termini allowed creation of novel paramagnetic cages and subsequently the functional properties of these cages were investigated. Slight differences made it possible to tease out the relative favorability between the two seemingly energetically equivalent coordination positions of imidazole termini. Synthesis of novel ligands with amine termini was pursued to bestow a wider range of functionality on cage systems. New amine capped complexes were characterized and found to bind biological molecules of interest. Additionally, the amine-capped complexes were found to be much more sensitive to the counterion employed, distinctly limiting the number of isomers formed.

TABLE OF CONTENTS

LIST OF FIGURES

Page

LIST OF TABLES

Chapter 1 Introduction to Self-Assembled Cage Complexes, their Properties and Functions

1.1 Rational Design and Organization

Self-assembled metal-ligand cages have a variety of physical properties that are dependent on the individual components, including solubility[1–8] paramagnetism,[9] and host-guest binding.[4,10–13] As well as their popular functions as enzyme mimics, supramolecular complexes have been used as novel sensors, switches, and responsive materials.[14–18] A common approach for creating cage complexes is to consider the subunits of the ligand and the metals as building blocks, which can be interchanged to form new complexes. These building blocks allow for fine-tuning of properties by iteratively switching out subunits until the desired product is achieved. By intelligently designing ligands to include hydrogen bonding or π-stacking, favorable environments can be created for specific reactions or for the binding and sensing of small molecules. Each component greatly affects the structure and properties of the cage, with components synergistically working together to make the most favorable complex.

Many cage ligands have two chelating groups bound to metal atoms, which include imidazoles,[19] pyridyl pyrazoles,[20] or pyridines,[21–23] with each group displaying different coordination angles between the metal and ligand. Organic ligands are able to form cage complexes with transition metal salts including Fe^{2+},[22] Co^{2+},[2] Cu^{2+},[24] Cd^{2+},[25] Pd^{2+},[16] and Pt^{2+},[26] many metals favor octahedral coordination (6 binding sites), but Pt and Pd favor square planar (4 binding sites). Metal-organic cages using ditopic ligands (i.e. ligands that attach to two metals), can take many shapes ranging from relatively simple 2D polygons

to intricate 3D polyhedra. Cage complexes that exploit octahedral metals and ditopic ligands generally display a metal to ligand stoichiometry of 2M:3L, which matches the ratio of vertices to edges of many prismatic polyhedra such as tetrahedra (M_4L_6), cubes(M_8L_{12}), and so forth continuing to form more elaborate complexes (Figure 1.1).

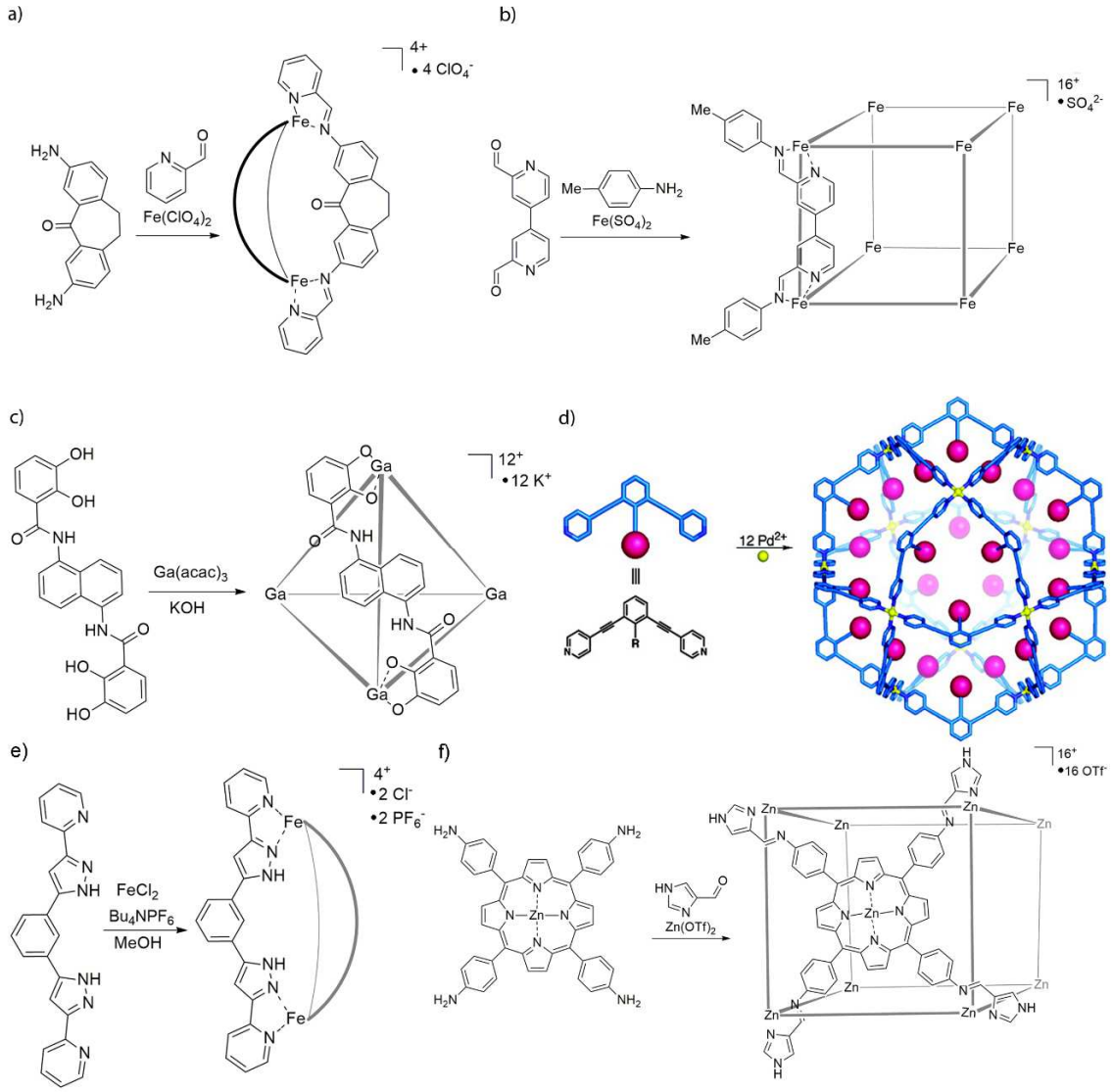

Figure 1.1: Synthesis of metal organic cage complexes: a) an M_2L_3 helicate using iminopyridine ligands and Fe(II), b) an M_8L_{12} cube from "reverse" iminopyridine chelators and Fe(II),[27] c) an M_4L_6 tetrahedron from a deprotonated catechol chelator and Ga(III),[28] d) $M_{12}L_{24}$ nanoball,[29] e) M_2L_3 helicate using pyridyl pyrazole coordinators and Fe(II),[30] and f) M_8L_6 cube from iminoimidazole coordinators and Zn(II).[20]

The formation of discrete cage products (as opposed to aggregates or coordination polymers) is dependent on the favorability of metal-ligand interactions, which determine coordination angles based on flexibility and steric constraints of the ligand. A common scaffold for self-assembled cage ligands is the iminopyridine ligand, which forms when an amine, aldehyde, and metal salt are combined in a reaction flask. The metal facilitates the reaction, coordinating to the amine and the aldehyde separately, bringing them in close proximity to each other to react. The metal enables a faster and cleaner reaction than attempting to make the bis-iminopyridine ligand, followed by addition of metal. Typically, the amine will be in the central part of the ligand and the aldehyde will function as the termini. Complexation also relies on the reversibility of imine condensation, which allows formation of the most thermodynamically stable product. Initial products from imine condensation are most likely disordered aggregates,[31] polymers, or fragments,[32,33] but the reversible nature of the reaction allows for dissociation and reformation of the cage complex. Through an equilibrium process, the most energetically favorable product is formed, favoring unstrained assemblies with fully coordinated metal vertices.

The shape and flexibility of the ligand is the main factor that defines the geometry of the cage complex. To form a discrete complex the ligand and metal must interact such that the ligand's flexibility is in an optimal range. The flexibility of the ligand should not undermine structural integrity, but the ligand must also not be so rigid that it prevents complexation and coordination with the metal. Having relatively rigid ligands is preferred as they tend to form highly symmetrical complexes and are able to communicate chiral information across the complex.[34] Using substituted phenyl rings to create rigid ligands has

been exploited by the community to gain benefits of high symmetry complexes and π-stacking (Figure 1.2).[12,22,28,29,35–39] Ligands can also have endohedrally oriented functional groups to aid in the formation of specific stoichiometric or geometric structures.[1,22]

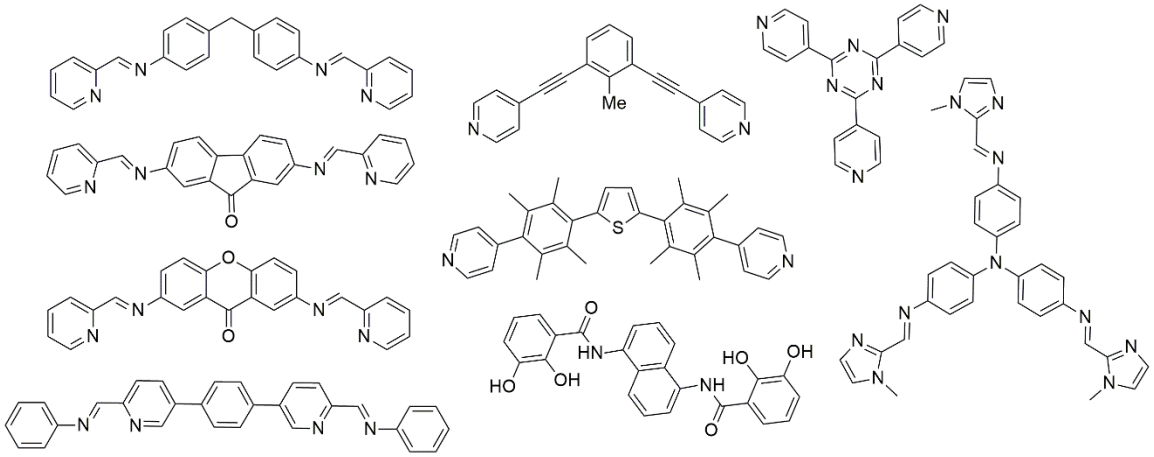

Figure 1.2: A selection of *bis*-and *tris*-coordinating ligands with substituted phenyl rings and varying coordination angles.

The building block approach allows iterative changes to find a ligand that will result in discrete complexation, then analysis of metal coordination can begin. Octahedral metals have two coordination orientations with bidentate ligands, and so multi-metal cage complexes can form multiple isomers. Chelating ligands can orient themselves as either facial, *fac*, where all ligands occupy the same face, or meridional, *mer*, where three ligands and the metal ion are in a plane. The *fac* coordination type has two enantiomers, respective of the directional rotation of the ligand around the metal center (Figure 1.3). The number of isomers is obviously related to the number of metal vertices included in the complex. Being able to control assembly of the complex by limiting the number of isomers aids in simple structural analysis via spectroscopic methods such as NMR.

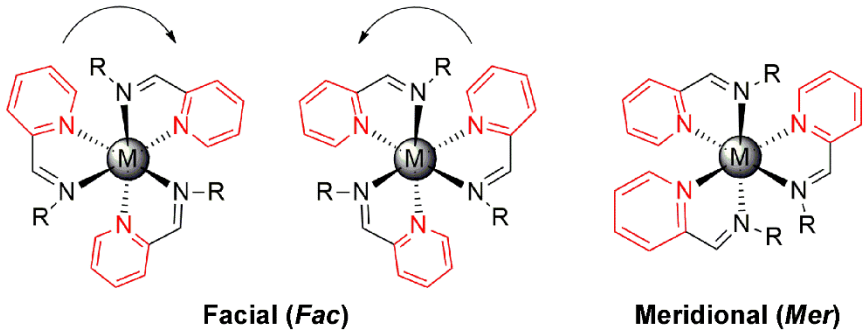

Figure 1.3: The two types of octahedral coordinators for bidentate ligands. The *mer* isomer displaying two intersecting planes, and the two enantiomers of the *fac* isomer with Λ (left) and Δ (right) rotation.

Analyzing the smallest cages is a good way to understand how quickly the number of isomers increases. The *fac* isomer has two possibilities designated *fac*-Λ and *fac*-Δ, representing clockwise and counterclockwise rotation, respectively. The smallest cage possible is an M_2L_3, a structure which forces *fac* configurations, eliminating all *mer* possibilities due to the geometric constraints necessary for formation. With only *fac* configurations for the metal centers of an M_2L_3 cage the options are ΔΔ or ΛΛ for a helicate or ΛΔ for the *meso*-helicate conformation.[40] However, applications for small helicate cages remains rather limited. Cages with larger cavities and more complex geometries are desirable for more exciting applications. The M_4L_6 cage can access a wider variety of symmetry groups, which results in more intricate combinations of the cage. The more linear ligands in M_4L_6 complexes tend to have a wider angle between imines, and in all-*fac* tetrahedra being more frequently observed than those with *mer* centers. For T-symmetry, the metal vertices are either *fac*-ΔΔΔΔ or *fac*-ΛΛΛΛ, achiral S_4 metal centers are observed as *fac*-ΔΔΛΛ, and for C_3 symmetry either *fac*-ΔΔΔΛ, *fac*-ΛΛΛΔ,[41] with each isomer by increasing the number of signals by 8. There is an additional isomer *fac*$_3$*mer* which can add

more signals. These slight changes in the arrangement of components increase the difficulty for each isomer present when performing spectroscopic analysis, thereby creating more hardship when performing experiments that rely on examining small details. Rigid ligand structures aid in forming cage stoichiometries that have a larger internal cavity size compared to helicates. One way to create rigid ligands is to incorporate phenyl rings, but planar rings limit addition of functional groups and reduce the number of applications for the cage complexes. Novel complexes therefore must determine how to create rigid ligands while maintaining opportunities for functionalization.

1.2 Host-Guest Binding

Guest (or substrate) binding is desirable for many applications such as separations, drug transport, and catalysis. When attempting to bind small molecules in a synthetic host, there are two main properties to consider: cavity size and functional groups participating in the binding event. When determining potential guests, Rebek's law, which states that guests should fill 55±9% of the cavity or binding pocket, remains the most accurate and significant variation in either direction results in a decrease in binding strength.[42–44] Endohedral (internally faced) functional groups can largely affect what will bind in the cavity. Functionality can be effective in a wide range of cage sizes and include species as small as lone pairs to larger H-bonding pendant groups.

Guest recognition in smaller cages will be more easily affected by minimalist groups such as simple lone pairs (e.g. from pyridine-containing ligands) due to the small cavity. Anionic guests have been shown to interact with electron poor C-H bonds which can aid

in pre-organizing cage components before imine condensation forming a singular favorable isomer of the complex.[1,19] The ClO_4^- anion is known to affect cage formation in this manner. Cage **1.1** has an alkyl ligand with no groups capable of traditional hydrogen bonding, but the interactions between the internally facing imidazole C-H bonds and the ClO_4^- anion were able to direct the flexible ligands to form only the single *T* isomer.[19,45]

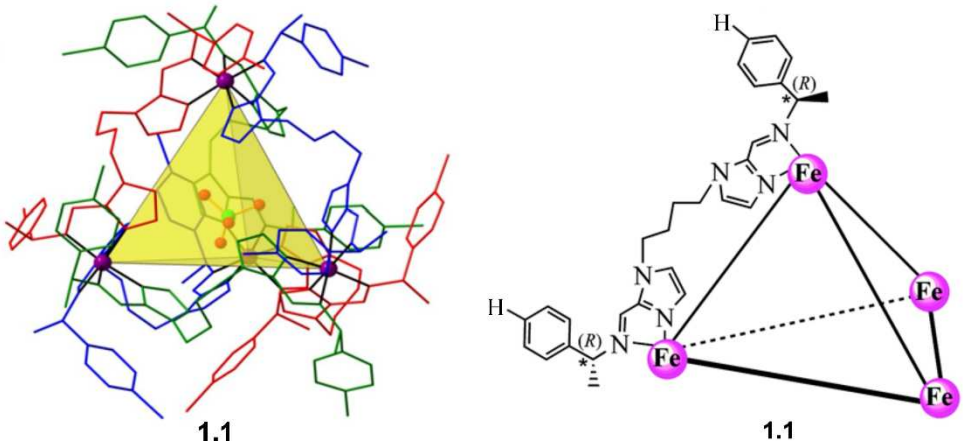

Figure 1.4: Crystal structure of enantiopure cage **1.1** with singularly bound ClO_4^- anion in cavity (left) and cage with ligand structure (right).[19,45]

"Reverse" iminopyridine cages that use an oligo-aldehyde core with amine caps exist as well, however their synthesis tends to be more challenging. Reverse iminopyridine M_4L_6 cages **1.2** and **1.3** selectively bind anionic guests of a specific size.[46] The addition of a competitive anion (hexafluorophosphate) to a solution of both cages and their respective guests result in displacement of perchlorate from the smaller cage **1.2**, which then enters the larger cage **1.3**. The incoming perchlorate guest causes the triflimide anion previously bound with **1.3** to be ejected from the complex.

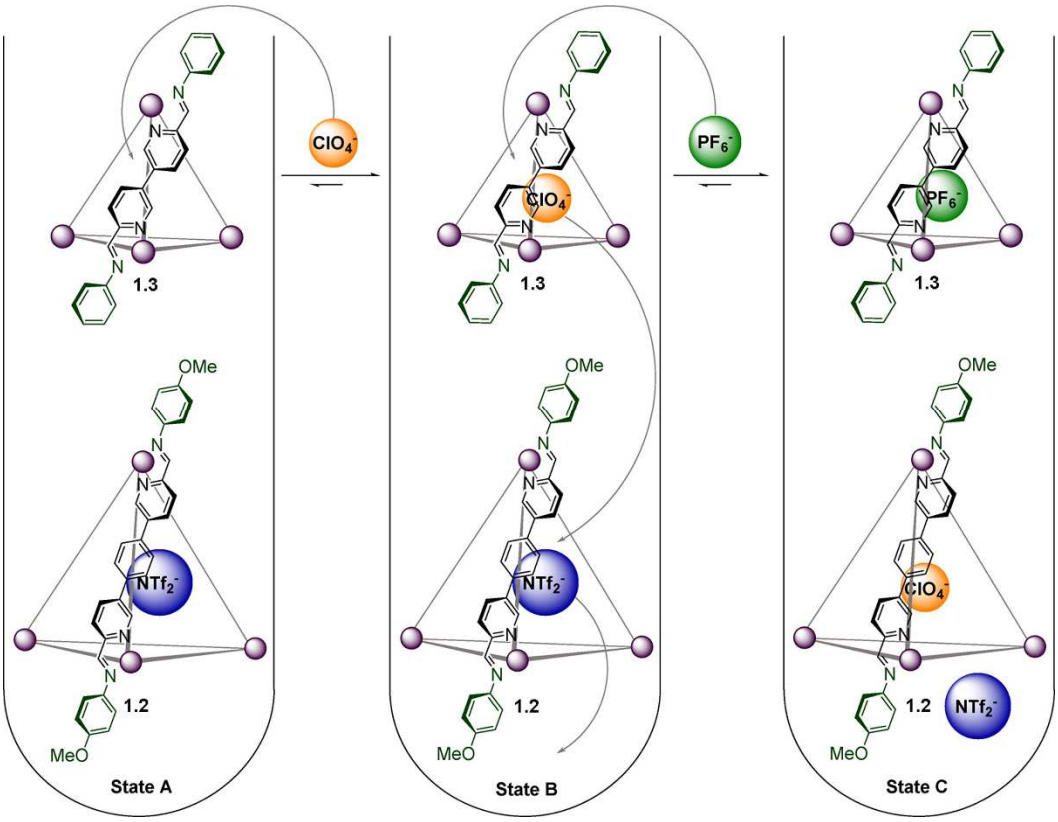

Figure 1.5: Anion exchange sequence: binding of ClO_4^- within cage **1.3**, followed by its displacement by PF_6^-, and subsequent displacement of NTf_2^- from cage **1.2** by the released ClO_4^-.[46]

Binding small neutral molecules often requires a larger binding pocket and favorable interaction between the cage host and small molecule guest. Typically, neutral molecules are bound through exploiting intermolecular forces hydrogen bonding or creating a nonpolar organic environment in a polar solution. Cage **1.4** is soluble in water when SO_4^{2-} is present in solution, and nitromethane with the $^-NTf_2$ anion present in solution.[11] In organic solvent, nitromethane, cage **1.4** is able to selectively bind coronene from other polycyclic aromatic hydrocarbons (PAHs), most likely due increased solvation and size. The binding was noticeable via titrations monitored by ^1H NMR or UV-vis spectral changes. In the case of ^1H NMR shifts, when comparing spectra for unbound coronene and

cage against host-guest complex **coronene⊂1.4** the coronene peak has shifted upfield indicating the guest is bound in the cage cavity.[11] UV-vis absorbance spectroscopy is another technique that can ascertain if a binding event occurred, by performing a titration of guest into a solution of the host and determining if an isosbestic point is present.

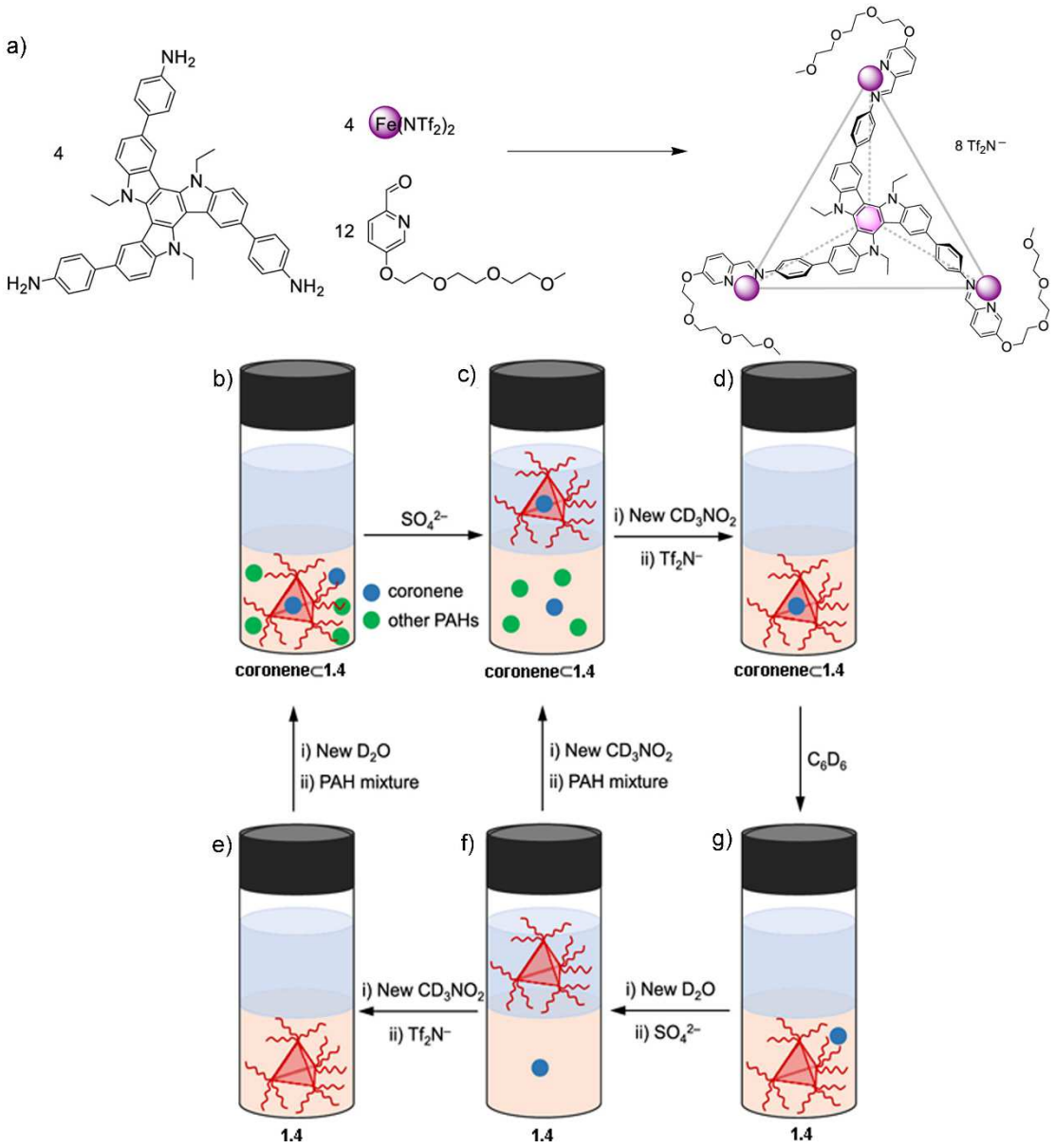

Figure 1.6: a) Synthesis of iminopyridine cage **1.4**. Selective separation and recovery of coronene from a mixture of other PAHs. All upper layers in these schematic vials are D_2O, and the lower layers are CD_3NO_2. b) Cage **1.4** took up coronene selectively in CD_3NO_2 and c) transferred to the aqueous layer together with its coronene cargo after the addition of SO_4^{2-}; d) addition of new CD_3NO_2 layer and addition of NTf_2^- drove the complex into CD_3NO_2. e) Cage **1.4** discharged the coronene cargo upon addition of C_6D_6, and the released coronene f) was separated by transferring empty **1.4** to D_2O upon addition of SO_4^{2-}. g) Cage **1.4** was recovered in fresh CD_3NO_2. following the addition of NTf_2^-. Free **1.4** paired with SO_4^{2-} in D_2O could also directly extract coronene from a new mixture of PAHs in CD_3NO_2. (f→c).[11]

1.3 Iron(II) Iminopyridine Cage Properties

A careful examination of iminopyridine complexes shows how synergistic effects allow complex formation. The Fe(II) iminopyridine cages are formed in a one-pot reaction from three components: aldehyde, amine, and metal salt. These components most frequently take on the structures of 2-formylpyridine derivatives, a ligand core with two or more amine groups, and an Fe(II) salt. Iminopyridine is an excellent scaffold for favorable Fe(II) chelation cage complex formation. The condensation reaction used to form the imine ligand is reversible, so building blocks can be exchanged easily to create novel complexes.[38,47–49] "Reverse" iminopyridine cage examples are more rare, being formed from a dialdehyde core, amine terminus, and Fe(II) salt. There are fewer examples in the literature of this coordination scaffold, mainly because pyridine dialdehydes are slightly more difficult to access. There are small differences in properties when using the "reverse" coordination. Coordination around metal centers is very sensitive, showing some obvious physical differences, like color, when using similar ligand coordinators. Despite the difficulty involved in dialdehyde formation, reverse iminopyridine cages remain desirable due to the wide scope of amines available to be incorporated in cage synthesis as "termini". Many of these amines represent doors to novel functionality and new avenues of research including amino acids, chirality,[34] and water solubility.[11] While there are many paths to amine capped cages, iminopyridine complexes are a preferred method for cage creation because of how much is known about their properties in formation, tunability, and reactivity.

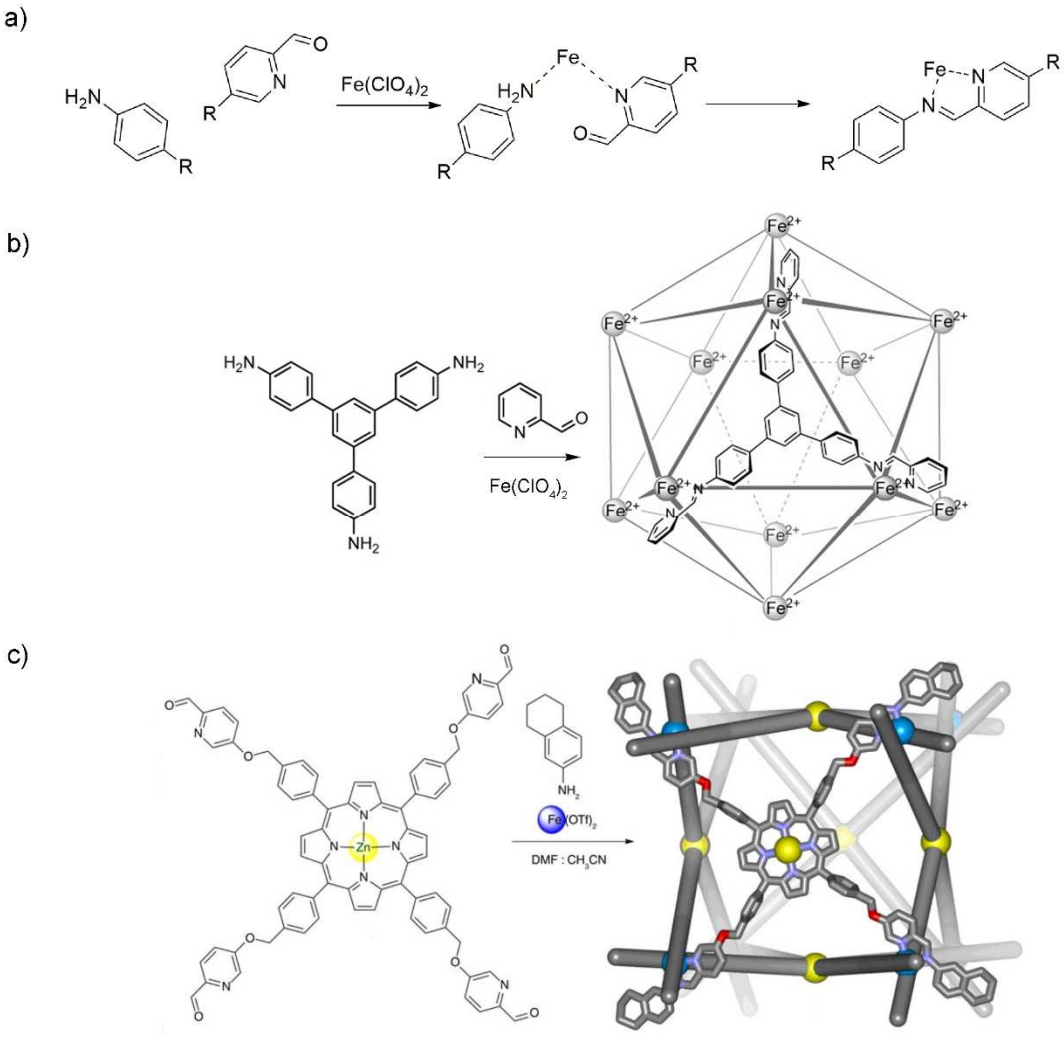

Figure 1.7: a) The metal catalyzed imine condensation used in the synthesis of Fe(II) iminopyridine cages. Synthesis of iminopyridine b) $M_{12}L_{12}$ icosahedron,[50] and "reverse" iminopyridine c) M_8L_6 cubic cage complexes.[51]

The properties of the cage and cavity can be altered in multiple ways, mainly ligand modification but also by solvent, reaction conditions, counterions, and metal ions used. Solvent affects host-guest properties, determining favorable uptake as cage cavities can have a different environment than the bulk solution.[4,27] Changes to reaction conditions can affect the number of stoichiometries produced, for example forming both tetrahedral M_4L_6 and prismatic $M_{10}L_{15}$ from the same starting materials.[6] Switching the guest anion or metal

cation is one way to dramatically alter the size of the cavity and the stoichiometry of the complex.[10,52,53]

1.3.1 Component Exchange in Iminopyridine Cage Structures

The final structure of iminopyridine cages is determined by finding the most stable outcome, given the components in the system. The reversibility of imine condensation means that regardless of the first product made through equilibration, the most stable, low energy product will dominate. Therefore, if a new component, be it amine, aldehyde, metal, or anion, is introduced to the system, there is a possibility for component exchange, but only if the new complex is more energetically favorable. If a new component is added that could make a new cage complex, but one that is less energetically favorable than the original cage, no exchange occurs. When multiple possibilities for the same ligand component type are combined there are three different sorting possibilities. The first is narcissistic self-sorting where only one of the component possibilities (e.g. one metal or amine) is incorporated into assembly, resulting in the formation of homocomplex. The second option is called social[54] or integrative[55] sorting where many of the same component type are combined in assembly to form a specific favored heterocomplex.[56] The last option is when a statistical mixture or dynamic library is formed. In this case there is no control over sorting.[57]

The preference between type of sorting observed is not always clear. In the case of narcissistic sorting, favorability is frequently dependent on small variances between structures. For example, cage **1.5** was assumed to be favorable than cage **1.6** due to hydrogen bonding interactions between interactions between ligands, but hydrogen

bonding interactions with the solvent destabilized the cage. Cages **1.5** and **1.6** were able to narcissistically self-sort to form homoleptic complexes with no heteroleptic (mixed ligand) complexes present despite having very similar structures and properties.[22]

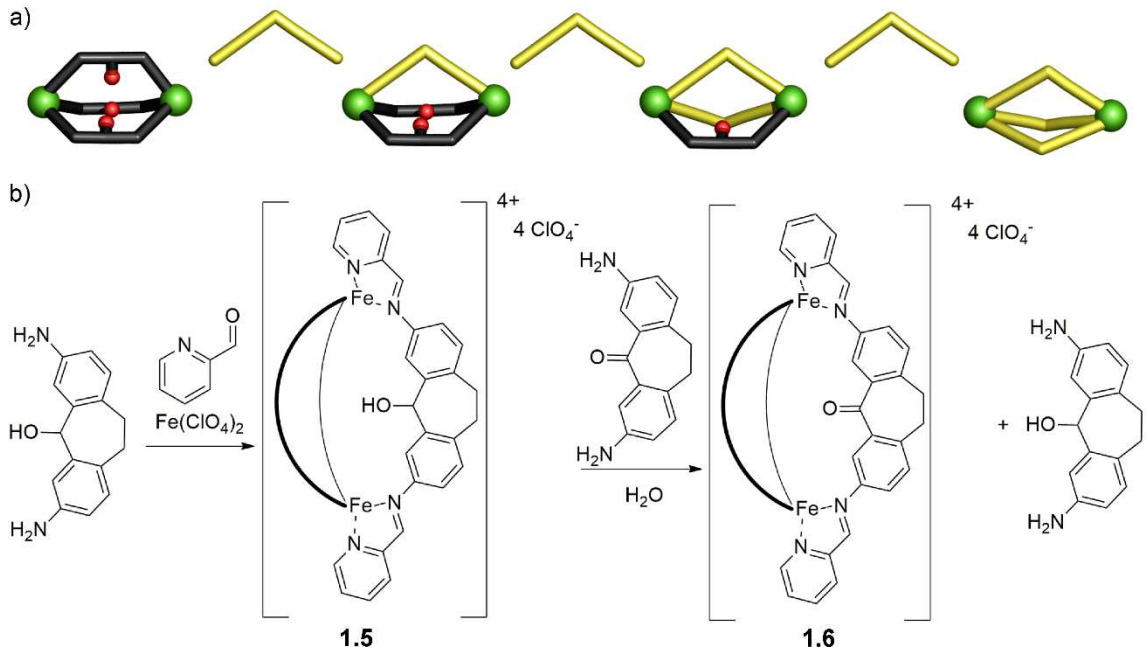

Figure 1.8: a) Cartoon demonstrating narcissistic self-sorting with component exchange, and b) formation of suberol cage followed by displacement of suberol with diaminosuberone.

1.3.2 The Electronic Effects of the Ligand on Complex Assembly

While there are many ways to affect the structure of iminopyridine cages, structural modification of ligands is doubtless the most effective way to identify trends in complexation and create new complexes. Altering the electron donating effects of the ligand is one way to analyze how small changes in the ligand affect complexation. By simply using a fluorinated ligand core, the electron donating effects can greatly change the outcome between two structurally similar cores (Figure 1.9).[41] More structurally complex assemblies are available with *mer* orientations at the structural vertices, and self-assemblies

are formed with prism-like geometries.[41] While *fac* coordination is more common, it remains structurally limiting compared to the variety of geometries available when *mer* coordination can be incorporated. The *mer* coordination is favored by designing ligands with more sterically bulky and electron withdrawing components, which have increased π-stacking effects with electron rich anilines.

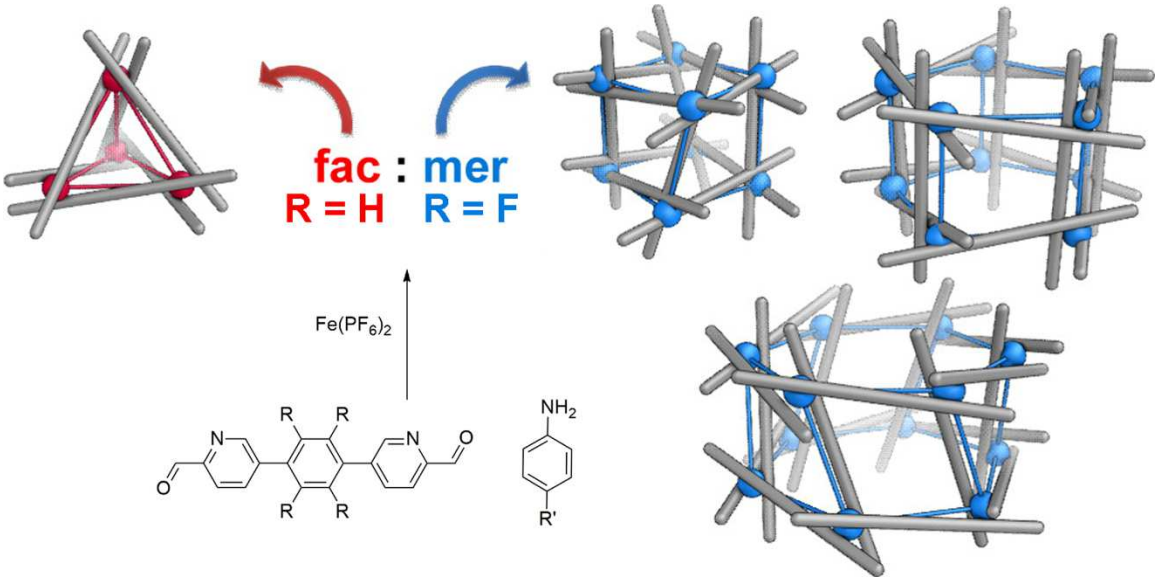

Figure 1.9: Synthesis of M_4L_6 tetrahedron with *fac* vertices and the more atypical *mer* coordination to form M_8L_{12}, $M_{10}L_{15}$, and $M_{12}L_{18}$ due to addition of electron withdrawing groups.[41]

Changes in electron donating effects in the formyl pyridine can also affect multicomponent assembly. Adding groups with small electron donating or electron withdrawing effects at the 5-position of the formyl pyridine caps is able to affect favorability of the complex formed and the rate of formation (Figure 1.10).[58] Using 5-methyl-2-formylpyridine showed electron donating "caps" could replace simple 2-formylpyridines in self-assembled helicates. In addition, 5-methyl-2-formylpyridine can create homocomplexes (eg. **1.7•Me$_6$**) with different diamine ligands more quickly than did

2-formylpyridine. Conversely, 5-bromo-2-formylpyridine was less likely to be incorporated in heterocomplexes **1.7•Br$_x$H$_y$**, with ligands demonstrating clear preference for 5-methyl-2-formylpyridine or 2-formylpyridine complexes. Formation of homocomplexes using 5-bromo-2-formylpyridine (eg. **1.7•Br$_6$**) showed slower rates of formation than complexes with 2-formylpyridine, when tested across multiple different ligand cores. Very small differences in electron donating properties were able to have a clear response on complexation.

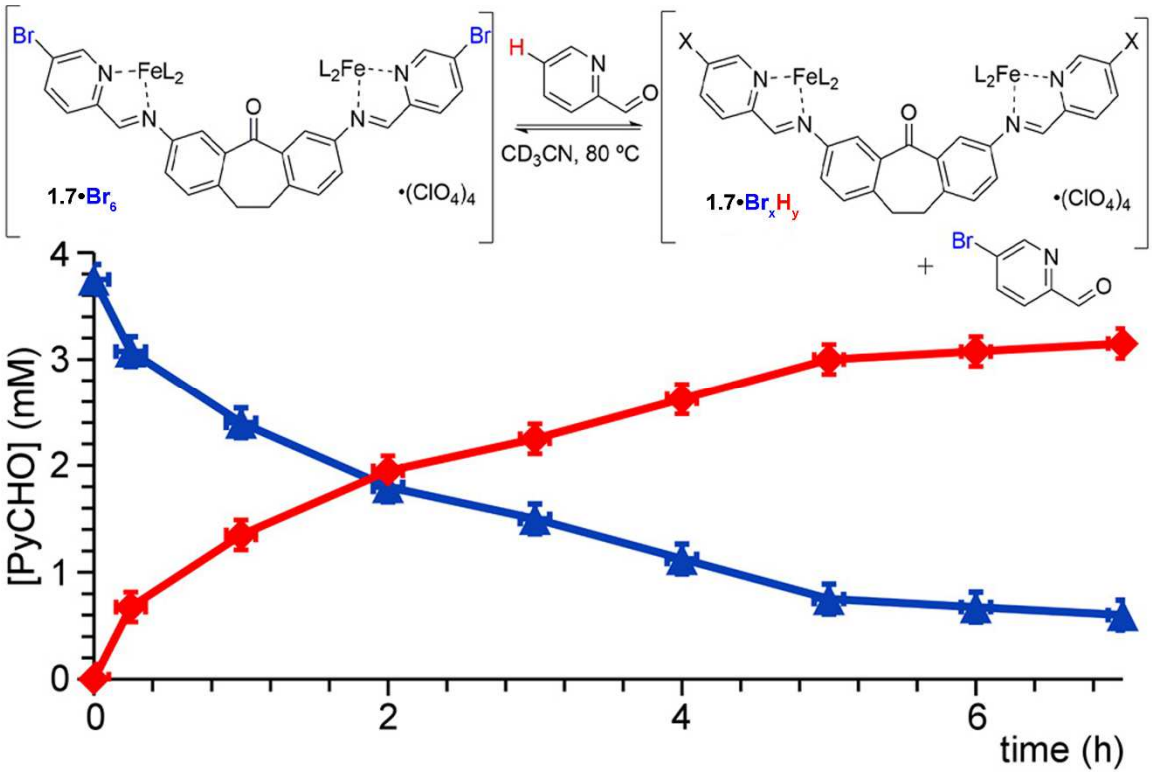

Figure 1.10: Aldehyde displacement experiment complex with 5-bromo-2-formylpyridine was heated with 5-methyl-2-formylpyridine, resulting in the incorporation of 5-methyl-2-formylpyridine into the cage complex.[58]

1.3.3 Counterion Interactions Affect Assembly and Solubility

Choosing the correct counterion can make the difference between forming a discrete assembly instead of a disordered aggregate (Figure 1.11a). Anions, such as ClO_4^-, can act as templates helping to pre-organize components before assembly by directing hydrogen bonding groups or π-π stacking.[1,19] Anion choice can be vital for cage formation, as seen with cage **1.8**, as directing and preorganization ensures discrete cage formation instead of disordered aggregate or the formation of too many isomers, which would prevent structural information from being collected. The reversibility of the iminopyridine scaffold allows for transition from disordered aggregate **1.8•**OTf to distinct assembly **1.8•**ClO_4. The responsive nature of the complex can be used to change the complex's properties if more favorable components are introduced to the system. Anion templation can be hierarchical, requiring primary and secondary templating anions to achieve the desired complex structure (Figure 1.11f).[52,53] Varying ions allows for multiple distinct assemblies, with each complex having unique properties despite similar components. As the geometry and stoichiometry of the complex change, so do the applications. The cavity's properties change to be more adept at creating a separate environment from the bulk solution to capture anions.

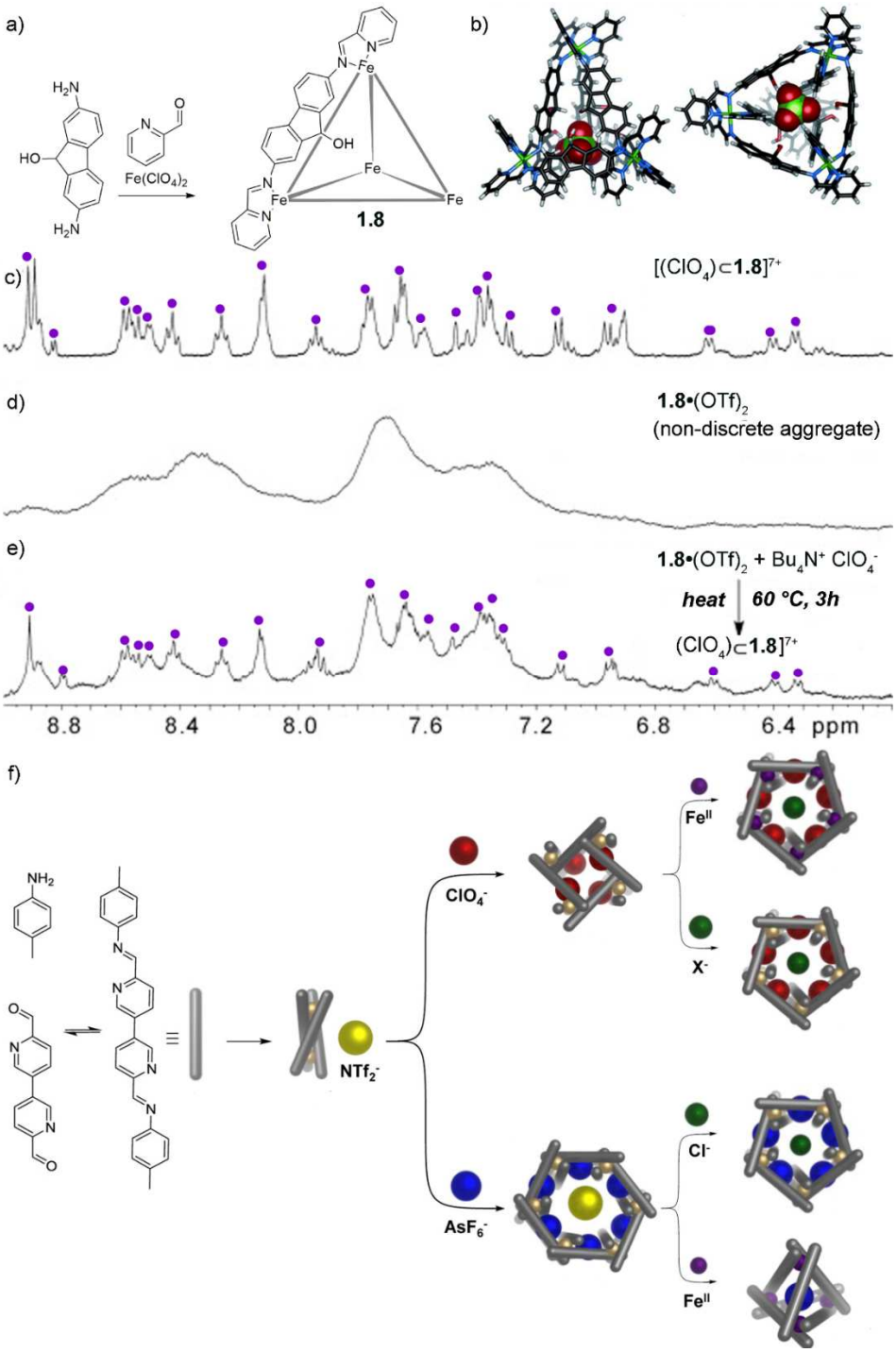

Figure 1.11: The a) synthesis and b) crystal structure of M_4L_6 cage **1.4**. ^{1}H NMR anion templation studies of c) $[ClO_4\subset\mathbf{1.4}](ClO_4)_7$, d) non-discrete aggregate when synthesis preformed with $Fe(OTf)_2$, and e) formation of $[ClO_4\subset\mathbf{1.4}](OTf)_7$.[1] f) Structural interconversion between cages using hierarchical ion templation.[52]

Cages that are soluble in organic solvents such as acetonitrile and insoluble in aqueous solvents can undergo anion exchange using SO_2^- or SO_4^{2-} to become water soluble (Figure 1.13).[3,4,7,59,60] Several cycles of phase transfer between organic and aqueous layers occur with high recovery (90-95%) of the cage complex.[3,59,60] Using anions to achieve water solubility is not possible for every cage, however, cages with large cavities that were able to perform phase transfer were also able to move organic cargo in the cavity across phases. Cage **1.9-10**•SO_4 is exchanged across the solvent barrier into ethyl acetate (EtOAc) as the $B(C_6F_5)_4^-$ anion is added. Cages **1.9-11** can be returned to the aqueous phase when SO_4^{2-} is added to **1.9-11**• $B(C_6F_5)_4$. Guest release is possible when new components or solvent is added, triggering disassembly and reassembly of the cage and allowing guests either to leave or be captured in the system.[3,59–61]

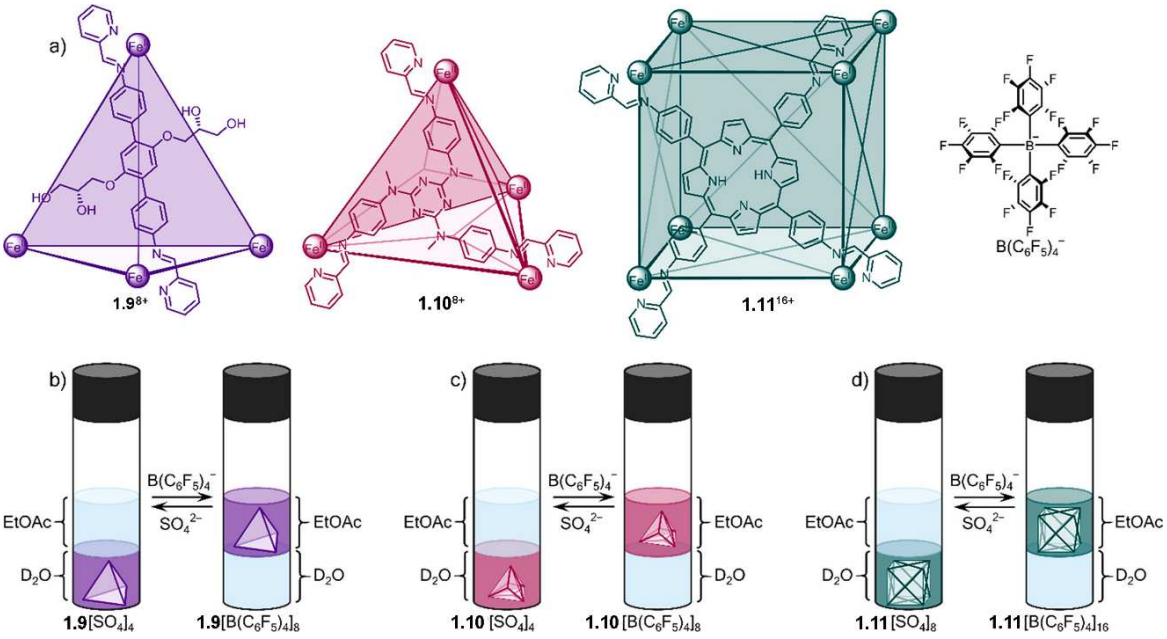

Figure 1.12: a) The structural representations of M_4L_6 tetrahedral cage **1.9**$^{8+}$, M_4L_4 tetrahedral cage **1.10**$^{8+}$, and M_8L_6 cubic cage **1.11**$^{16+}$ and anion $B(C_6F_5)_4$. Reversible phase transfer of cages b) **1.9**, c) **1.10**, and d) **1.11** into water and EtOAc via addition of hydrophilic SO_4^{2-} or hydrophobic $B(C_6F_5)_4^-$.[59]

1.4 Iron (III) Cage Complexes

Both oxidation states Fe(II) and Fe(III), have been of particular interest in the supramolecular cage community. Using Fe(III) produces paramagnetic cages which are challenging to analyze via NMR spectroscopy. Most commonly, elemental analysis, UV-vis, MS, and Mossbauer spectroscopy along with XRD are used to obtain structural information instead. Some early examples of Fe(III) cage complexes were formed with $FeCl_2$ using deprotonated oxygen-containing chelating ligands, such as acetoactate, to make tetrahedral (**1.12**) and trigonal antiprism (**1.13**) cages.[14,62] Fe(III) forms stronger bonds with oxygen chelators, as opposed to Fe(II), which favors neutral nitrogen ligands. The tritopic ligands, in complexes **1.12** and **1.13**, lie on the face of the structure rather than

on the edges, as was seen previously with ditopic ligands. Each Fe(III) vertex attaches to three ligands, maintaining an octahedral coordination. However, it was initially unclear as to why either the M_4L_4 or M_6L_6 stoichiometry was favored. Molecular modeling became key in understanding favorability. When models were made of all four complexes (two ligands with either M_4L_4 or M_6L_6 stoichiometry), the differences were most notably in the angle strain energies, with **1.12** having an M_4L_4 stoichiometry being more favorable due to lessened steric crowding and **1.13** having an M_6L_6 stoichiometry being favored because of π-stacking.[14]

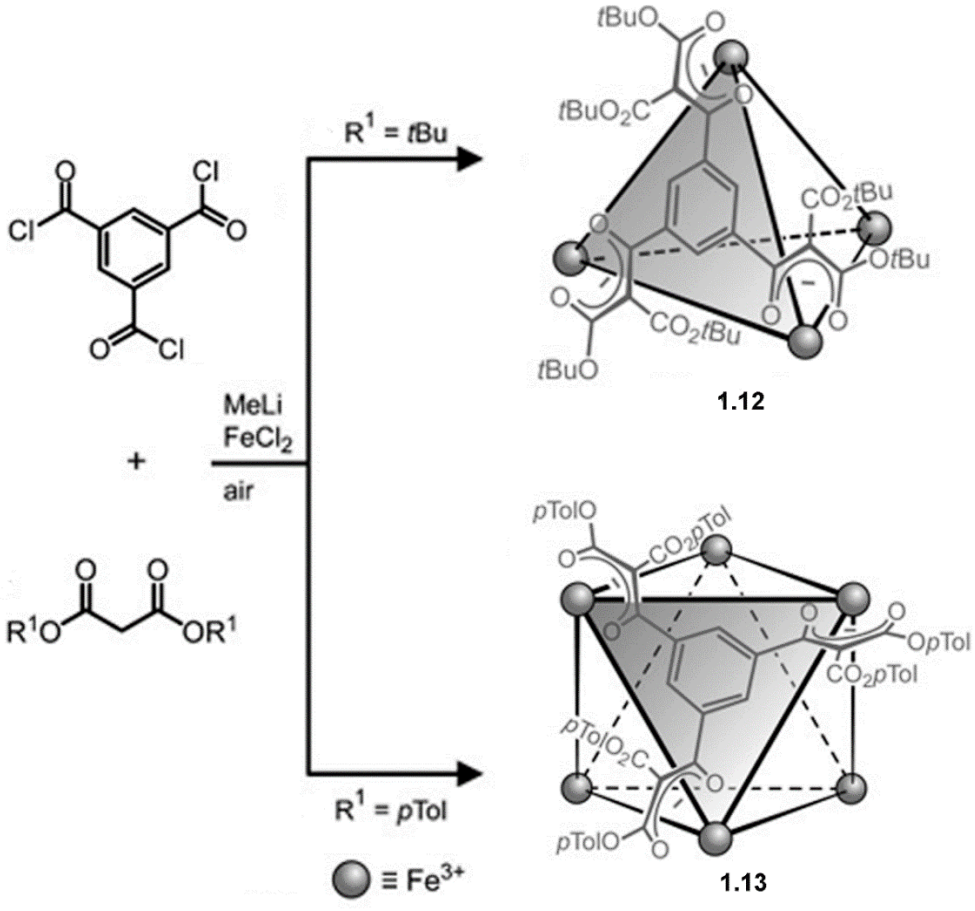

Figure 1.13: Synthesis of paramagnetic Fe(III) cages using acetoacetate coordinators.[14]

1.5 Spin-Crossover Complexes

While Pd and Pt-containing cages are obviously diamagnetic and Fe(III) cages are paramagnetic, some cage complexes can exploit transition metal coordination to alter their magnetic properties. Octahedral metals with 4-7 electrons most frequently exist either in high spin (HS) or low spin (LS) configurations, and in certain circumstances intermediate spin. A LS configuration has the greatest number of paired electrons, whereas HS is the electron configuration with the highest number of unpaired electrons. Intermediate spin occurs when the spin state falls somewhere between the highest energy state and the lowest energy state and usually correlates with spin state transition.[63] A HS configuration occurs when ligand field strength (Δ_O) is small, resulting in the e_g* and t_{2g} levels being closer together, overcoming the electron pairing energy (Figure 1.14).[9] Modulating magnetic properties can be achieved by altering the ligand by changing functional groups and internal cavity size. Paramagnetic complexes are desirable because magnetic properties can be tuned for device applications, host-guest sensing, and can be affected by interactions with external stimuli to create responsive small molecule magnets. There are many paramagnetic helicates and cages[64–71] that use Fe(III), Co, or Ni salts as metal vertices. There are many fewer examples of paramagnetic HS Fe(II) cage complexes, as most are diamagnetic. Furthermore, while temperature-dependent spin-crossover is a phenomenon that has been well documented, there are only a few examples of external chemical stimuli affecting magnetism other than harsh conditions and redox reactions.

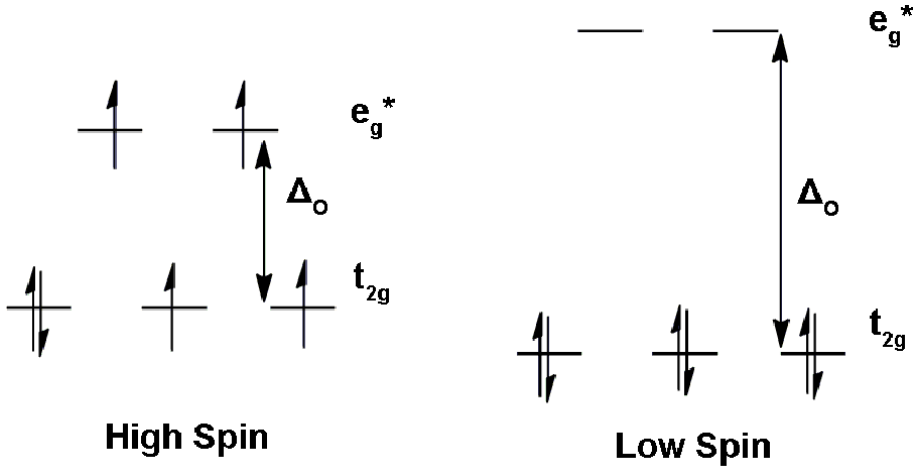

Figure 1.14: Low spin and high spin configurations of octahedral d^6 Fe(II). Spin crossover occurs as a response to ligand field strength (Δ_O) approaching electron pairing energy.

Paramagnetic HS behavior notably affects NMR properties, rendering spectra difficult to interpret.[72] Intermediate spin complexes suffer from line broadening and low signal to noise ratios, but HS complexes show even greater effects. While the typical ^{1}H NMR signals lie between 0-10 ppm, ^{1}H NMR signals for HS complexes can have a range up to 300 ppm.[73,74] The reason for the distinct change in shift of the signals is due the change in the metal's electronic structure. The metal superimposes its magnetic field on nearby protons, so that they are affected by the magnetic fields of both the NMR and the metal. The protons closest to the metal vertices are the most shifted signals. Having a wider range in paramagnetic NMR spectra is helpful as it reduces signal overlap. However, accurate shift analysis is difficult, and integration and most coupling data is lost.[74] The most common way to assign protons and signals to each other is to use NMR techniques such as measuring and correlating T_1 relaxation times, and COSY NMR.[13,72,74,75] It is important to note that the paramagnetism affects not only the complex, but also guests inside the cage

cavity and other compounds in solution. Encapsulated guests show NMR signals shifted to -10 to -20 ppm.

Spin-crossover (SCO) complexes are temperature-dependent, showing reversible changes in magnetic properties, usually from LS to HS as temperature increases, and can form intricate geometries.[76] In solution phase, Evans method NMR experiments can determine the magnetic moment by measuring the shift of a standard added to solution with the SCO complex. Multiple studies have been performed on mononuclear SCO complexes, but these studies are not always applicable to complex self-assembled cage structures. The main difference is that the metal centers in multi-metal cages can communicate information through ligands, unlike mononuclear complexes. Multi-metal cages can also be more stable, reducing the propensity for spin crossover. Aromi and co-workers noted the simplest cases for spin crossover in self-assembled cages are two metal helicates, having only three options: metals have the same spin state, high spin-high spin (HS-HS) or low spin- low spin (LS-LS), or metals are inequivalent, high spin-low spin (HS-LS).[77,78] If the change in an SCO complex from low spin to high spin happens abruptly this means that there is a high level of cooperativity in the complex. Ligands that are rigid can effectively communicate between metal centers to change the properties of the complex. Poor cooperativity between ligands results in stepwise transition, forming HS-LS complexes. For this to be the case there must be a clear distinction at the first temperature where SCO occurs and the temperature where the second SCO occurs.[77,78]

Small structural variations have large effects on the assembly properties and spin state of SCO cages. The rational design of SCO supramolecular cages has difficulties that are

not typically found with "regular" supramolecular cages. For instance, including π-π stacking or hydrogen bonding into assemblies can often aid in the self-assembly process, forming fewer possible isomers and aiding in preorganization of the complex. However, in SCO complexes all these qualities can also affect SCO behavior due to interactions with solvent and counter anions. For example, cage **1.14** showed different magnetic behavior based on which counterion (PF_6^-, BF_4^- or ClO_4^-) was used (Figure 1.15b), due to interactions with the external N-H bonds from the imidazole groups.[77] When either PF_6^- or BF_4^- was used, distinct hydrogen bonding between N-H and F was seen in the crystal structure and only incomplete switching was observed (HS-LS). When ClO_4^- was used, there was a clear preference for oxygen donating solvents which also displaying hydrogen bonding in the crystal structure, and cage **1.9**•ClO_4 was observed to undergo two-step SCO and achieve HS-HS behavior.[77]

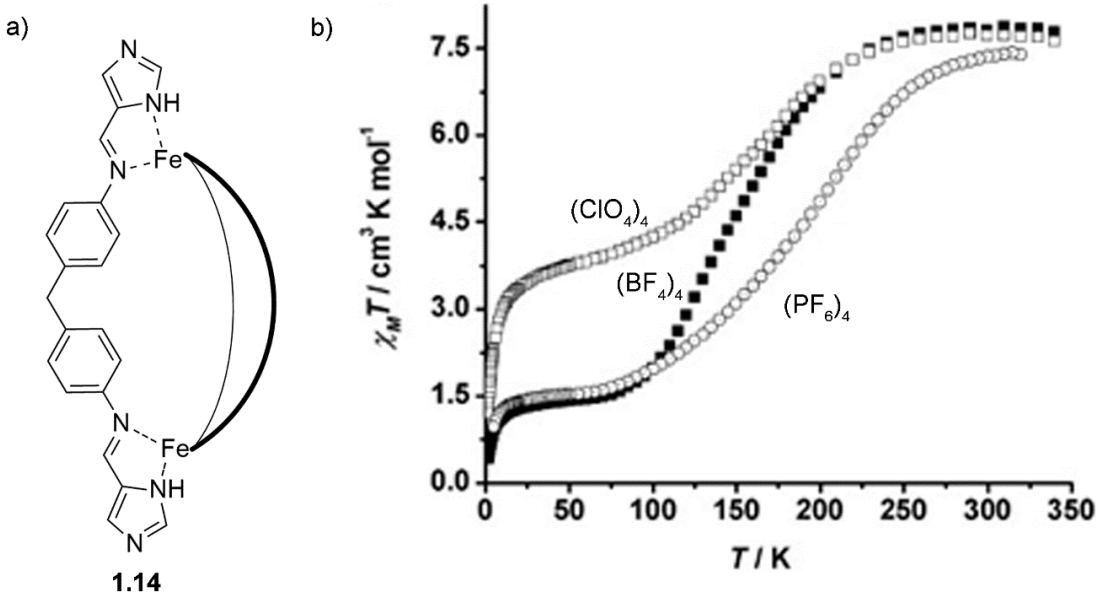

1.14

Figure 1.15: a) The structure of cage **1.14** and it's b) magnetic susceptibility $\chi_M T$ vs. T plot with anions PF_6^-, BF_4^-, or ClO_4^-.[77]

The cavity of helicate cage **1.15** is just large enough to accommodate Cl^- or Br^- and show stepwise SCO. The SCO of cage **1.15** is affected by not only anion, but solvent as well. The crystal structures of the HS-LS and LS-LS complexes showed changes in anion and solvent interactions with Fe centers (Figure 1.15b).[79] In the HS-LS configuration, the interior Cl^- is inequivalently shared, with the high spin imidazole N-H bonds more strongly hydrogen bonding to the Cl^-. The HS Fe is stabilized by an exterior chloride ion hydrogen bonding with imidazole, where the imidazole N-H bonds near the LS Fe were hydrogen bonding to the O in methanol solvent molecules. Conversely, in the LS-LS configuration, the chloride is strongly participating in hydrogen bonding with all the imidazoles and water has replaced the methanol molecules.

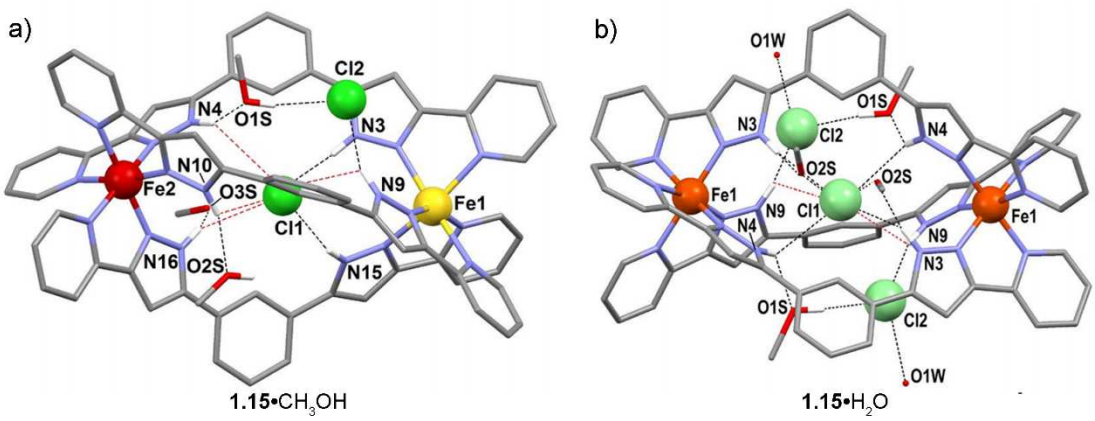

Figure 1.16: Single crystal to single crystal transformation upon prolonged exposure to air of (a) HS(Fe1)-LS (Fe2) complex [$Cl^- \subset$ **1.15**]$Cl(PF_6)_2$•5.7 CH_3OH to (b) LS-LS complex [$Cl^- \subset$ **1.15**]$Cl(PF_6)_2$·3 CH_3OH·H_2O containing crystallographically equivalent but magnetically different Fe(II) centers due to disorder of external components over two equivalent positions (shown). Strong (black) and weaker (red) hydrogen bonding between the helicate and anions or solvent molecules are represented by dashed lines. Reproduced with permission from reference.[79]

Creating SCO supramolecular complexes is a still relatively new field and careful ligand design is necessary for appropriate coordination around the metal center to facilitate spin-state switching. Depending on how effective communication between metal centers is, SCO behavior can be exhibited as stepwise or abrupt.[34,77] Despite the many additional considerations involved in SCO complex formation, methods used to find new diamagnetic complexes can still be applied to SCO complexes. Spin-state has been correlated to steric bulk of the coordinating groups, and has been used to exert control over the spin state of the cage complex.[65] The key theory in the building blocks principle is the reversibility of reactions such as imine condensation, which is still present and used to create SCO complexes, therefore component exchange is still a viable method for cage synthesis. For example, component exchange of SCO cages was performed as a synthetic method to alter spin state. Tetrahedral paramagnetic cage **1.16** was transformed to cage **1.17** via aldehyde exchange by adding 2-formylpyridine and 5% D_2O in acetonitrile (Figure 1.17).[74] The transition to a low spin complex was visibly noticeable as the solution changed from orange to deep purple, indicative of a diamagnetic iminopyridine complex. Having pyridine caps with increased steric bulk allowed the cage to exhibit paramagnetic behavior, by favoring the longer N-Fe bond lengths upon self-assembly. Properties investigated with SCO Fe(II) complexes tend to include ligand flexibility, coordination, steric bulk, and donor ability on the assembly to determine any trends in complex stability and component exchange.

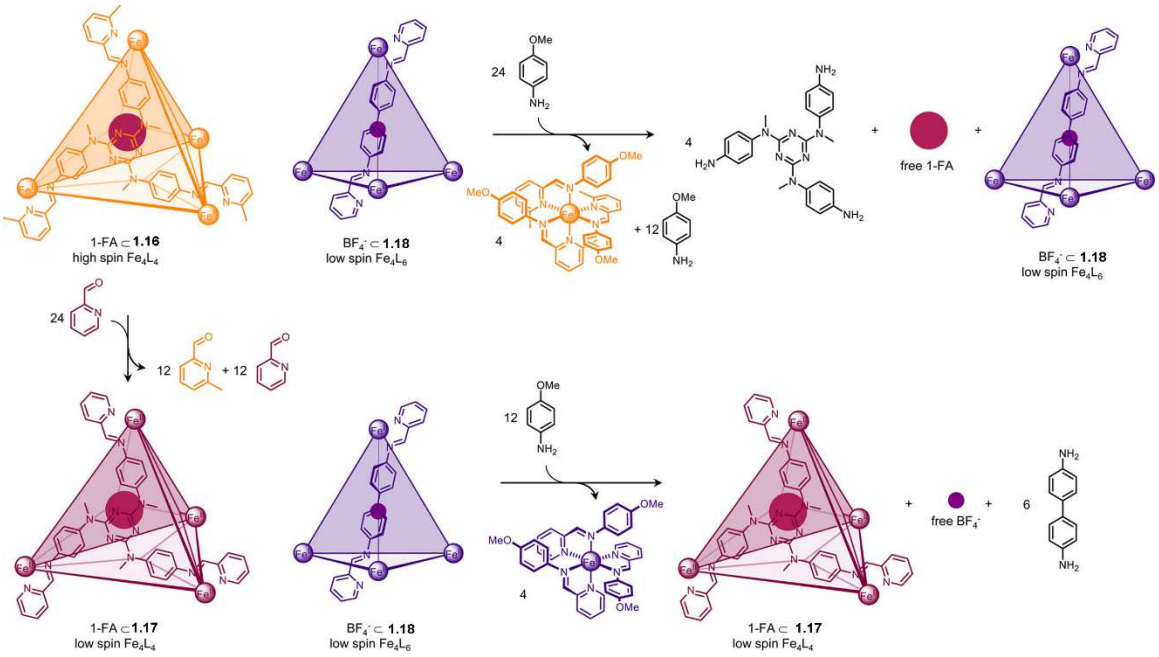

Figure 1.17: Transformation of HS cage **1.16** to LS cage **1.17** upon addition 2-formylpyridine. When cage **1.16** is combined with p-anisidine in the presence of LS cage **1.18** results in the destruction of cage **1.16** triggering release of the guest 1-fluoroadamantane (1-FA). Combing LS cage **1.17** with p-anisidine in the presence of LS cage **1.18** results in the destruction of cage **1.18** triggering release of the guest BF_4^-.[74]

1.6 Co Cages

Only specific metals and chelating ligands can be used to analyze paramagnetic effects in cage complexes, and the scope is further limited if NMR spectroscopy is desired. Varying the metals in self-assembled cages is important as Fe(II) is not "one size fits all" and many ligands are unable to coordinate with Fe(II), but are suitable for cage synthesis with other metals. Co(II) complexes are strongly paramagnetic and are generally amenable to analysis by NMR spectroscopy.[9] Co(II) cage complexes show proton resonances in NMR spectra, but the signals are altered in the same way as other SCO complexes (line broadening, incorrect integration, and peak shift).

While Fe(II) dominates iminopyridine coordinating cages, Co(II) is used mainly with pyridylpyrazole coordinators. Pyridylpyrazole ligands typically have an aromatic spacer in the middle, which provides a scaffold for multiple shapes and coordination sites for the pyridylpyrazole arms to branch off. Additionally, Co(II) has octahedral coordination, so vertices can access both *fac* and *mer* configurations. These ligand systems have been able to generate a cage geometries of varying complexity with from Co_2L_3 helicate to tetrahedron to tetra-capped truncated tetrahedron.[2] These cages purposely include methylene spacers giving ligands an opportunity to maintain flexibility instead of making them rigid. Ligand flexibility limits structural predictability but allows for the most favorable structure to be formed by metal-ligand coordination and interligand stacking interactions. However, ligand flexibility is also limiting as assemblies can transform into alternate stoichiometries over time rendering it difficult to perform studies on applications, such as necessitating host guest interactions. (Figure 1.18).

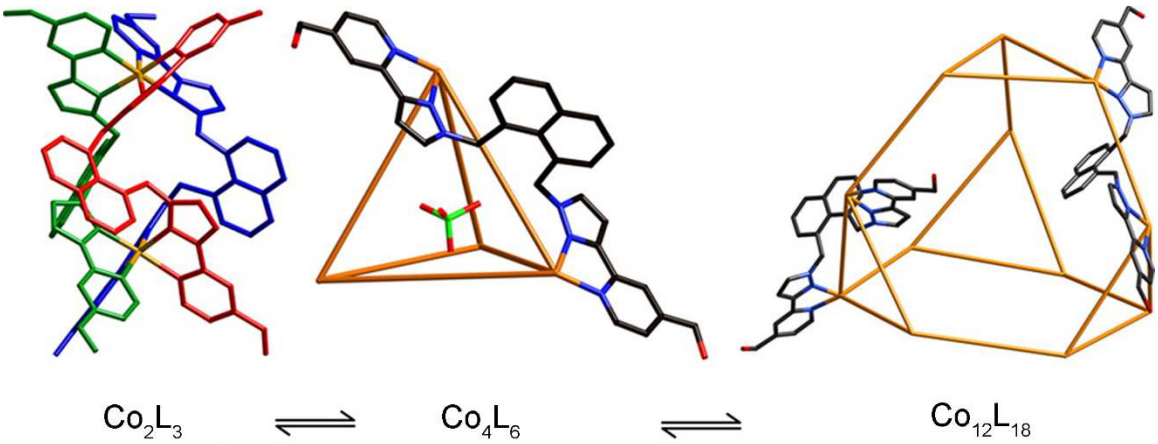

Figure 1.18: Equilibrium transformation in water between Co_2L_3, Co_4L_6, and $Co_{12}L_{18}$.[2]

Only stable non-transforming complexes can be analyzed for host-guest behavior as they have consistent structure and cavity size. Guest are chosen to comply with Rebek's law to predict likelihood of a binding event.[80] Water solubility can drive guest binding by creating a hydrophobic pocket in the cage cavity for guests to bind with.[5] The best guests for cages similar to **1.19** are electron-rich aromatic compounds with an easily ionizable group (typically those containing O or N). Electron rich groups on the guests can participate in hydrogen bonding with C-H hydrogen bond donor groups on the cavity wall.[19,80] Cage **1.19** is water soluble and was observed to see an increase in binding constants of guests in water, with hydrophobic guests binding most strongly.[20]

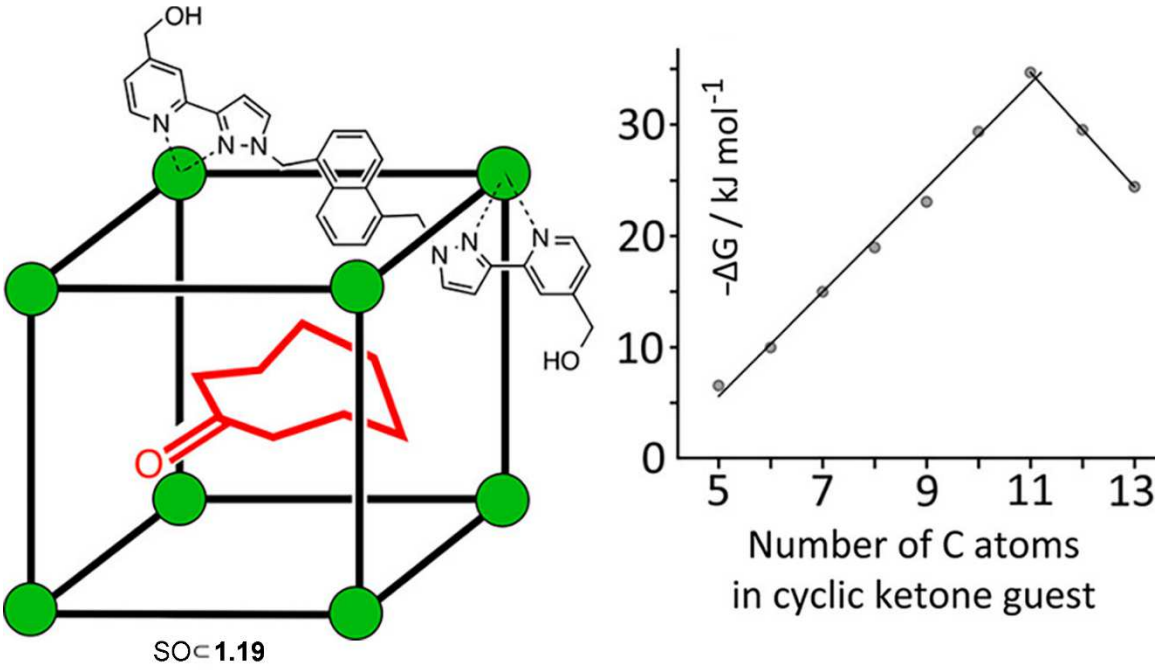

Figure 1.19: a) The structure of cage **1.19** with internally bound guest suberone (SO) and b) the plot of binding free energy vs. the number of carbon atoms in aliphatic cyclic ketone guests in water.[20]

1.6 Conclusion

The iminopyridine cage motif has been well-documented to show how cage components behave synergistically. This architecture allows for fine-tuning of various properties such as functionality, stoichiometry, and shape. While much is known about iminopyridine cages. displaying paramagnetism within this motif is still novel. Self-assembled cage complexes are presently an established field, with a myriad of diamagnetic cages, but there are relatively few examples of SCO or strongly paramagnetic cages. Many studies focus simply on synthesis and characterization of these complexes, somewhat understandably as they tend to be less stable than their diamagnetic counterparts and are more limited in what spectroscopic data can obtained. The intrinsic limitations for paramagnetic complexes can also be their strengths as the stretched NMR range allows visibility of signals that would otherwise overlap and possibly be indecipherable. This subsection of cage complexes has wide room for growth to include cage functionalization and applications. Much of the current literature regarding paramagnetic cages focusing on the synthesis of these novel structures and only a few articles exploring the opportunities for applications in sensing and other reactivity.

1.7 References

1. Young, M. C.; Holloway, L. R.; "Johnson, A. M.; Hooley, R. J. A Supramolecular Sorting Hat: Stereocontrol in Metal-Ligand Self-Assembly by Complementary Hydrogen Bonding." *Angew. Chem. Int Ed.* **2014**, *53*, 9832–9836.

2. Cullen, W.; Hunter, C. A.; Ward, M. D.; "An Interconverting Family of Coordination Cages and a Meso -Helicate; Effects of Temperature, Concentration, and Solvent on the Product Distribution of a Self-Assembly Process." *Inorg. Chem.* **2015**, *54*, 2626–2637.

3. Percástegui, E. G.; Mosquera, J.; Ronson, T. K.; Plajer, A. J.; Kieffer, M.; Nitschke, J. R. “Waterproof Architectures through Subcomponent Self-Assembly.” *Chem. Sci*. **2019**, *10*, 2006–2018.

4. Bolliger, J. L.; Ronson, T. K.; Ogawa, M.; Nitschke, J. R. “Solvent Effects upon Guest Binding and Dynamics of a $FeII_4L_4$ Cage.” *J. Am. Chem. Soc.* **2014**, *136*, 14545–14553.

5. Percástegui, E. G.; Mosquera, J.; Nitschke, J. R. “Anion Exchange Renders Hydrophobic Capsules and Cargoes Water-Soluble.” *Angew. Chem Int. Ed.* **2017**, *56*, 9136–9140.

   Zarra, S.; Clegg, J. K.; Nitschke, J. R. “Selective Assembly and Disassembly of a Water-Soluble Fe_{10} L_{15} Prism.” *Angew. Chem Int Ed.* **2013**, *52*, 4837–4840.

6. Bolliger, J. L.; Belenguer, A. M.; Nitschke, J. R. “Enantiopure Water-Soluble $[Fe_4L_6]$ Cages: Host-Guest Chemistry and Catalytic Activity.” *Angew. Chem Int Ed.* **2013**, *52*, 7958–7962.

   Grommet, A. B.; Bolliger, J. L.; Browne, C.; Nitschke, J. R. “A Triphasic Sorting System: Coordination Cages in Ionic Liquids.” *Angew. Chem Int Ed.* **2015**, *54*, 15100–15104.

   McConnell, A. J. “Spin-State Switching in Fe(II) Helicates and Cages.” *Supramol. Chem*. **2018**, *30*, 858–868.

   Ronson, T. K.; Giri, C.; Kodiah Beyeh, N.; Minkkinen, A.; Topië, F.; Holstein, J. J.; Rissanen, K.; Nitschke, J. R. “Size-Selective Encapsulation of Hydrophobic Guests by Self-Assembled M_4L_6 Cobalt and Nickel Cages.” *Chem. Eur. J.* **2013**, *19*, 3374–3382.

   Zhang, D.; Ronson, T. K.; Lavendomme, R.; Nitschke, J. R. “Selective Separation of Polyaromatic Hydrocarbons by Phase Transfer of Coordination Cages.” *J. Am. Chem. Soc.* **2019**, *141*, 18949–18953.

7. Wood, D. M.; Meng, W.; Ronson, T. K.; Stefankiewicz, A. R.; Sanders, J. K. M.; Nitschke, J. R. “Guest-Induced Transformation of a Porphyrin-Edged $Fe^{II}_4L^6$ Capsule into a $Cu^{I}FeII_2L_4$ Fullerene Receptor.” *Angew. Chem Int Ed.* **2015**, *54*, 3988–3992.

8. Amouri, H.; Mimassi, L.; Rager, M. N.; Mann, B. E.; Guyard-Duhayon, C.; Raehm, L. “Host-Guest Interactions: Design Strategy and Structure of an Unusual Cobalt

Cage That Encapsulates a Tetrafluoroborate Anion." *Angew. Chem Int Ed.* **2005**, *44*, 4543–4546.

Saalfrank, R. W.; Maid, H.; Scheurer, A. Supramolecular Coordination Chemistry: "The Synergistic Effect of Serendipity and Rational Design." *Angew. Chem Int Ed.*, **2008**, *47,* 8794–8824.

Cook, T. R.; Stang, P. J. Recent "Developments in the Preparation and Chemistry of Metallacycles and Metallacages via Coordination." *Chem. Rev*. **2015**, *115*, 7001–7045.

Fujita, M.; Tominaga, M.; Hori, A.; Therrien, B. "Coordination Assemblies from a Pd(II)-Cornered Square Complex." *Acc. Chem. Res*. **2005**, *38*, 369–378.

9. Ward, M. D.; R. Raithby, P. "Functional Behavior from Controlled Self-Assembly: Challenges and Prospects." *Chem. Soc. Rev.* **2013**, *42*, 1619–1636.

Smulders, M. M. J.; Riddell, I. A.; Browne, C.; Nitschke, J. R. "Building on Architectural Principles for Three-Dimensional Metallosupramolecular Construction." *Chem. Soc. Rev.* **2013**, *42*, 1728–1754.

Ren, D. H.; Qiu, D.; Pang, C. Y.; Li, Z.; Gu, Z. G. "Chiral Tetrahedral Iron(II) Cages: Diastereoselective Subcomponent Self-Assembly, Structure Interconversion and Spin-Crossover Properties." *ChemComm* **2015**, *51*, 788–791.

10. Tidmarsh, I. S.; Faust, T. B.; Adams, H.; Harding, L. P.; Russo, L.; Clegg, W.; Ward, M. D. "Octanuclear Cubic Coordination Cages." *J. Am. Chem. Soc*. **2008**, *130*, 15167–15175.

11. Bogie, P. M.; Holloway, L. R.; Ngai, C.; Miller, T. F.; Grewal, D. K.; Hooley, R. J. "A Self-Assembled Cage with Endohedral Acid Groups Both Catalyzes Substitution Reactions and Controls Their Molecularity." *Chem. Eur. J.* 2019, 25 (43).

12. Holloway, L. R.; Young, M. C.; Beran, G. J. O.; Hooley, R. J. "High Fidelity Sorting of Remarkably Similar Components via Metal-Mediated Assembly." *Chem. Sci.* **2015**, *6*, 4801–4806.

13. Holloway, L. R.; Bogie, P. M.; Lyon, Y.; Julian, R. R.; Hooley, R. J. "Stereoselective Postassembly CH Oxidation of Self-Assembled Metal-Ligand Cage Complexes." *Inorg. Chem.* **2017**, *56*, 11435–11442.
Byrne, K.; Zubair, M.; Zhu, N.; Zhou, X. P.; Fox, D. S.; Zhang, H.; Twamley, B.; Lennox, M. J.; Düren, T.; Schmitt, W. "Ultra-Large Supramolecular Coordination

Cages Composed of Endohedral Archimedean and Platonic Bodies." *Nat. Commun*. **2017**, *8*, 1–9.

14. Kryschenko, Y. K.; Seidel, S. R.; Muddiman, D. C.; Nepomuceno, A. I.; Stang, P. J. "Coordination-Driven Self-Assembly of Supramolecular Cages: Heteroatom-Containing and Complementary Trigonal Prisms." *J. Am. Chem. Soc.* **2003**, *125*, 9647–9652.

15. Zhang, Z.; Zhao, Z.; Wu, L.; Lu, S.; Ling, S.; Li, G.; Xu, L.; Ma, L.; Hou, Y.; Wang, X.; Li, X.; He, G.; Wang, K.; Zou, B.; Zhang, M. "Emissive Platinum(II) Cages with Reverse Fluorescence Resonance Energy Transfer for Multiple Sensing." *J. Am. Chem. Soc.* **2020**, *142*, 2592–2600.

16. Browne, C.; Brenet, S.; Clegg, J. K.; Nitschke, J. R. "Solvent-Dependent Host-Guest Chemistry of an Fe_8L_{12} Cubic Capsule." *Angew. Chem Int Ed.* **2013**, *52*, 1944–1948.

Caulder, D. L.; Powers, R. E.; Parac, T. N.; Raymond, K. N. "The Self□Assembly of a Predesigned Tetrahedral M_4L_6 Supramolecular Cluster." *Angew. Chem Int Ed.* **1998**, *37*, 1840–1843.

Tominaga, M.; Suzuki, K.; Murase, T.; Fujita, M. "24-Fold Endohedral Functionalization of a Self-Assembled $M_{12}L_{24}$ Coordination Nanoball." *J. Am. Chem. Soc.* **2005**, *127*, 11950–11951.

Ward, M. D. "Polynuclear Coordination Cages." *ChemComm* **2009**, *30*, 4487–4499.

Holloway, L. R.; McGarraugh, H. H.; Young, M. C.; Sontising, W.; Beran, G. J. O.; Hooley, R. J. "Structural Switching in Self-Assembled Metal-Ligand Helicate Complexes: Via Ligand-Centered Reactions." *Chem. Sci.* **2016**, *7*, 4423–4427.

17. Bogie, P. M.; Holloway, L. R.; Lyon, Y.; Onishi, N. C.; Beran, G. J. O.; Julian, R. R.; Hooley, R. J. "A Springloaded Metal-Ligand Mesocate Allows Access to Trapped Intermediates of Self-Assembly." *Inorg. Chem.* **2018**, *57*, 4155–4163.
18. Riddell, I. A.; Smulders, M. M. J.; Clegg, J. K.; Hristova, Y. R.; Breiner, B.; Thoburn, J. D.; Nitschke, J. R. "Anion-Induced Reconstitution of a Self-Assembling System to Express a Chloride-Binding $Co_{10}L_{15}$ Pentagonal Prism." *Nat. Chem.* **2012**, *4*, 751–756.
19. Ousaka, N.; Grunder, S.; Castilla, A. M.; Whalley, A. C.; Stoddart, J. F.; Nitschke, J. R. "Efficient Long-Range Stereochemical Communication and Cooperative Effects in Self-Assembled Fe_4L_6 Cages." *J. Am. Chem. Soc.* **2012**, *134*, 15528–15537.

20. Murase, T.; Nishijima, Y.; Fujita, M. “Cage-Catalyzed Knoevenagel Condensation under Neutral Conditions in Water.” *J. Am. Chem. Soc.* **2012**, *134*, 162–164.

21. Murase, T.; Otsuka, K.; Fujita, M. “Pairwise Selective Formation of Aromatic Stacks in a Coordination Cage.” *J. Am. Chem. Soc.* **2010**, *132*, 7864–7865.

22. Kusukawa, T.; Fujita, M. “‘Ship-in-a-Bottle’ Formation of Stable Hydrophobic Dimers of Cis- Azobenzene and -Stilbene Derivatives in a Self-Assembled Coordination Nanocage.” *J. Am. Chem. Soc.* **1999**, *1212,* 1397–1398.

23. Ronson, T. K.; Meng, W.; Nitschke, J. R. “Design Principles for the Optimization of Guest Binding in Aromatic-Paneled $FeII_4L_6$ Cages.” *J. Am. Chem. Soc.* **2017**, *139*, 9698–9707.

24. Holloway, L. R.; Bogie, P. M.; Hooley, R. J. “Controlled Self-Sorting in Self-Assembled Cage Complexes.” *Dalton Trans.* **2017**, *46*, 14719–14723.

25. Meng, W.; Ronson, T. K.; Nitschke, J. R. “Symmetry Breaking in Self-Assembled M_4L_6 Cage Complexes.” *Proc. Natl. Acad. Sci.* **2013**, *110*, 10531–10535.

26. Kieffer, M.; Pilgrim, B. S.; Ronson, T. K.; Roberts, D. A.; Aleksanyan, M.; Nitschke, J. R. “Perfluorinated Ligands Induce Meridional Metal Stereochemistry to Generate M_8L_{12}, $M_{10}L_{15}$, and $M_{12}L_{18}$ Prisms.” *J. Am. Chem. Soc.* **2016**, *138*, 6813–6821.

27. Rebek, J. “Molecular Behavior in Small Spaces.” *Acc. Chem. Res.* **2009**, *42*, 1660–1668.

28. Mecozzi, S.; Julius Rebek, J. “The 55 % Solution: A Formula for Molecular Recognition in the Liquid State.” *Chem. Eur. J.* **1998**, *4*, 1016–1022.

29. Ams, M. R.; Ajami, D.; Craig, S. L.; Yang, J. S.; Rebek, J. “Too Small, Too Big, and Just Right - Optical Sensing of Molecular Conformations in Self-Assembled Capsules.” *J. Am. Chem. Soc.* **2009**, *131*, 13190–13191.

30. Bao, L. Y.; Hao, S. J.; Xi, S. F.; Yan, X.; Zhang, H. X.; Shen, R.; Gu, Z. G. “Chiral Supramolecular Coordination Cages as High-Performance Inhibitors against Amyloid-β Aggregation.” *ChemComm* **2018**, *54*, 8725–8728.

31. Ma, S.; Smulders, M. M. J.; Hristova, Y. R.; Clegg, J. K.; Ronson, T. K.; Zarra, S.; Nitschke, J. R. “Chain-Reaction Anion Exchange between Metal-Organic Cages.” *J. Am. Chem. Soc.* **2013**, *135*, 5678–5684.

32. Rizzuto, F. J.; Pröhm, P.; Plajer, A. J.; Greenfield, J. L.; Nitschke, J. R. "Hydrogen-Bond-Assisted Symmetry Breaking in a Network of Chiral Metal-Organic Assemblies." *J. Am. Chem. Soc.* **2019**, *141*, 1707–1715.

33. Smulders, M. M. J.; Jiménez, A.; Nitschke, J. R. "Integrative Self-Sorting Synthesis of a $Fe_8Pt_6L_{24}$ Cubic Cage." *Angew. Chem Int Ed.* **2012**, *51*, 6681–6685.

34. Rizzuto, F. J.; Nitschke, J. R. "Narcissistic, Integrative, and Kinetic Self-Sorting within a System of Coordination Cages." *J. Am. Chem. Soc.* **2020**, *142*, 7749–7753.

35. Bilbeisi, R. A.; Ronson, T. K.; Nitschke, J. R. "A Self-Assembled $[Fe(II)_{12}L_{12}]$ Capsule with an Icosahedral Framework." *Angew. Chem Int Ed.* **2013**, *52*, 9027–9030.

36. Castilla, A. M.; Ramsay, W. J.; Nitschke, J. R. "Stereochemistry in Subcomponent Self-Assembly." *Acc. Chem. Res.* **2014**, *47*, 2063–2073.

37. Riddell, I. A.; Ronson, T. K.; Clegg, J. K.; Wood, C. S.; Bilbeisi, R. A.; Nitschke, J. R. "Cation- and Anion-Exchanges Induce Multiple Distinct Rearrangements within Metallosupramolecular Architectures." *J. Am. Chem. Soc*. **2014**, *136*, 9491–9498.

38. Riddell, I. A.; Hristova, Y. R.; Clegg, J. K.; Wood, C. S.; Breiner, B.; Nitschke, J. R. "Five Discrete Multinuclear Metal-Organic Assemblies from One Ligand: Deciphering the Effects of Different Templates." *J. Am. Chem. Soc.* **2013**, *135*, 2723–2733.

39. Wiley, C. A.; Holloway, L. R.; Miller, T. F.; Lyon, Y.; Julian, R. R.; Hooley, R. J. "Electronic Effects on Narcissistic Self-Sorting in Multicomponent Self-Assembly of Fe-Iminopyridine Meso-Helicates." *Inorg. Chem*. **2016**, *55*, 9805–9815.

40. Grommet, A. B.; Hoffman, J. B.; Percástegui, E. G.; Mosquera, J.; Howe, D. J.; Bolliger, J. L.; Nitschke, J. R. "Anion Exchange Drives Reversible Phase Transfer of Coordination Cages and Their Cargoes." *J. Am. Chem. Soc.* **2018**, *140*, 14770–14776.

41. Grommet, A. B.; Nitschke, J. R. "Directed Phase Transfer of an FeII4L4 Cage and Encapsulated Cargo." *J. Am. Chem. Soc.* **2017**, *139*, 2176–2179.

42. Zhang, D.; Ronson, T. K.; Nitschke, J. R. "Functional Capsules via Subcomponent Self-Assembly." *Acc. Chem. Res.* **2018**, *51*, 2423–2436.

43. Saalfrank, R. W.; Glaser, H.; Demleitner, B.; Hampel, F.; Chowdhry, M. M.; Schünemann, V.; Trautwein, A. X.; Vaughan, G. B. M.; Yeh, R.; Davis, A. V.;

Raymond, K. N. “Self-Assembly of Tetrahedral and Trigonal Antiprismatic Clusters $[Fe_4(L^4)_4]$ and $[Fe_6(L^5)_6]$ on the Basis of Trigonal Tris-Bidentate Chelators.” *Chem. Eur. J.* **2002**, *8*, 493–497.

44. Krivokapic, I.; Zerara, M.; Daku, M. L.; Vargas, A.; Enachescu, C.; Ambrus, C.; Treganna-Piggott, P.; Amstutz, N.; Krausz, E.; Hauser, A. “Different Structural Motifs in Co(II) Complexes with Dicyanamide or Tricyanomethanide Anions.” *Coord. Chem. Rev.* **2007**, *251*, 364–378.

45. Gutlich, P.; Goodwin, H. A. *Spin Crossover in Transition Metal Compounds II*; Springer: Berlin, Heidelberg, 2004.

46. Miller, R. G.; Narayanaswamy, S.; Tallon, J. L.; Brooker, S. “Spin Crossover with Thermal Hysteresis in Cobalt(II) Complexes and the Importance of Scan Rate.” *New J. Chem.* **2014**, *38.* 1932–1941.

47. Kläui, W.; Eberspach, W.; Gütlich, P. “Spin-Crossover Cobalt(III) Complexes: Steric and Electronic Control of Spin State.” *Inorg. Chem.* **1987**, *26*, 3977–3982.

48. Venkataramani, S.; Jana, U.; Dommaschk, M.; Sönnichsen, F. D.; Tuczek, F.; Herges, R. Magnetic “Bistability of Molecules in Homogeneous Solution at Room Temperature.” *Science* **2011**, *331*, 445–448.

49. Nihei, M.; Shiga, T.; Maeda, Y.; Oshio, H. “Spin Crossover Iron(III) Complexes.” *Coord. Chem. Rev*. **2007**, *251,* 2606–2621.

50. Dommaschk, M.; Peters, M.; Gutzeit, F.; Schütt, C.; Näther, C.; Sönnichsen, F. D.; Tiwari, S.; Riedel, C.; Boretius, S.; Herges, R. “Photoswitchable Magnetic Resonance Imaging Contrast by Improved Light-Driven Coordination-Induced Spin State Switch.” *J. Am. Chem. Soc.* **2015**, *137*, 7552–7555.

51. Phonsri, W.; Harding, P.; Murray, K. S.; Moubaraki, B.; Harding, D. J. “Spin Crossover in Mixed Ligand Iron(III) Complexes.” *New J. Chem.* **2017**, *41*, 13747–13753.

52. Isley, W. C.; Zarra, S.; Carlson, R. K.; Bilbeisi, R. A.; Ronson, T. K.; Nitschke, J. R.; Gagliardi, L.; Cramer, C. J. “Predicting Paramagnetic ^{1}H NMR Chemical Shifts and State-Energy Separations in Spin-Crossover Host-Guest Systems.” *Phys. Chem. Chem. Phys.* **2014**, *16*, 10620–10628.

53. Miller, T. F.; Holloway, L. R.; Nye, P. P.; Lyon, Y.; Beran, G. J. O.; Harman, W. H.; Julian, R. R.; Hooley, R. J. “Small Structural Variations Have Large Effects on the Assembly Properties and Spin State of Room Temperature High Spin Fe(II) Iminopyridine Cages.” *Inorg. Chem.* **2018**, *57*, 13386–13396.

54. McConnell, A. J.; Aitchison, C. M.; Grommet, A. B.; Nitschke, J. R. "Subcomponent Exchange Transforms an $Fe^{II}_4L_4$ Cage from High- to Low-Spin, Switching Guest Release in a Two-Cage System." *J. Am. Chem. Soc.* **2017**, *139*, 6294–6297.

55. Tidmarsh, I. S.; Taylor, B. F.; Hardie, M. J.; Russo, L.; Clegg, W.; Ward, M. D. "Further Investigations into Tetrahedral M_4L_6 Cage Complexes Containing Guest Anions: New Structures and NMR Spectroscopic Studies." *New J. Chem*. **2009**, *33*, 366–375.

56. Brooker, S. "Spin Crossover with Thermal Hysteresis: Practicalities and Lessons Learnt." *Chem. Soc. Rev.* **2015**, *44*, 2880–2892.

57. Tuna, F.; Lees, M. R.; Clarkson, G. J.; Hannon, M. J. "Readily Prepared Metallo-Supramolecular Triple Helicates Designed to Exhibit Spin-Crossover Behaviour." *Chem. Eur. J*. **2004**, *10*, 5737–5750.

58. Garcia, Y.; Grunert, C. M.; Reiman, S.; van Campenhoudt, O.; Gütlich, P. "The Two-Step Spin Conversion in a Supramolecular Triple Helicate Dinuclear Iron(II) Complex Studied by Mössbauer Spectroscopy." *Eur. J. Inorg. Chem.* **2006**, *2006*, 3333–3339.

59. Darawsheh, M.; Barrios, L. A.; Roubeau, O.; Teat, S. J.; Aromí, G. "Guest-, Light- and Thermally-Modulated Spin Crossover in $[Fe^{II}_2]$ Supramolecular Helicates. *Chem. Eur. J.* **2016**, *22*, 8635–8645.

60. Ward, M. D.; Hunter, C. A.; Williams, N. H. "Coordination Cages Based on Bis(Pyrazolylpyridine) Ligands: Structures, Dynamic Behavior, Guest Binding, and Catalysis." *Acc. Chem. Res.* **2018**, *51*, 2073–2082.

Chapter 2 Synthetic Parameters for Paramagnetic High Spin Fe(II) Iminopyridine Cages

2.1 Introduction

In this study, we look at determining the parameters necessary to synthesize paramagnetic high spin Fe(II) iminopyridine cages. Spin state at Fe(II) centers is determined by how the metal interacts with the ligand and perturbs the octahedral coordination. To create a library of paramagnetic Fe(II) complexes, we must first determine how to create a metal-ligand coordination capable of forming high spin self-assembled cages. Many diamines have been used to create iminopyridine complexes, but changing the diamine has very little effect on the spin state of the metal when using 2-formylpyridine as aldehyde component. When the aldehyde is altered, however, it can greatly affect the metal's spin state. There has been some exploration of adding groups to the pyridyl aldehyde at the remote 5-position, resulting in slight changes in the rate of formation of the iminopyridine cage complex, but ultimately no effects on spin state.[1] Adding bulk at the 6-position of the pyridyl aldehyde, which is adjacent to the nitrogen binding to the metal, can cause steric interactions with the metal center. Steric interactions can change the coordination angle of the ligand to the Fe(II) center and may force the formation of high spin complexes, which have longer and weaker Fe-N bonds.[2] However, if too much bulk is added, complexation becomes unfavorable and the assembly will not form. Thus, we need to determine the limit of formation for high spin cages, as too much bulk will result in cage complex formation being unfavorable, leading to aggregate formation or no

reaction at all. Altering the Fe(II) coordination center will also affect cage stability and other properties of the complex.[2]

2.2 Synthesis and Basic Characterization of Paramagnetic Iminopyridine Cage Complexes

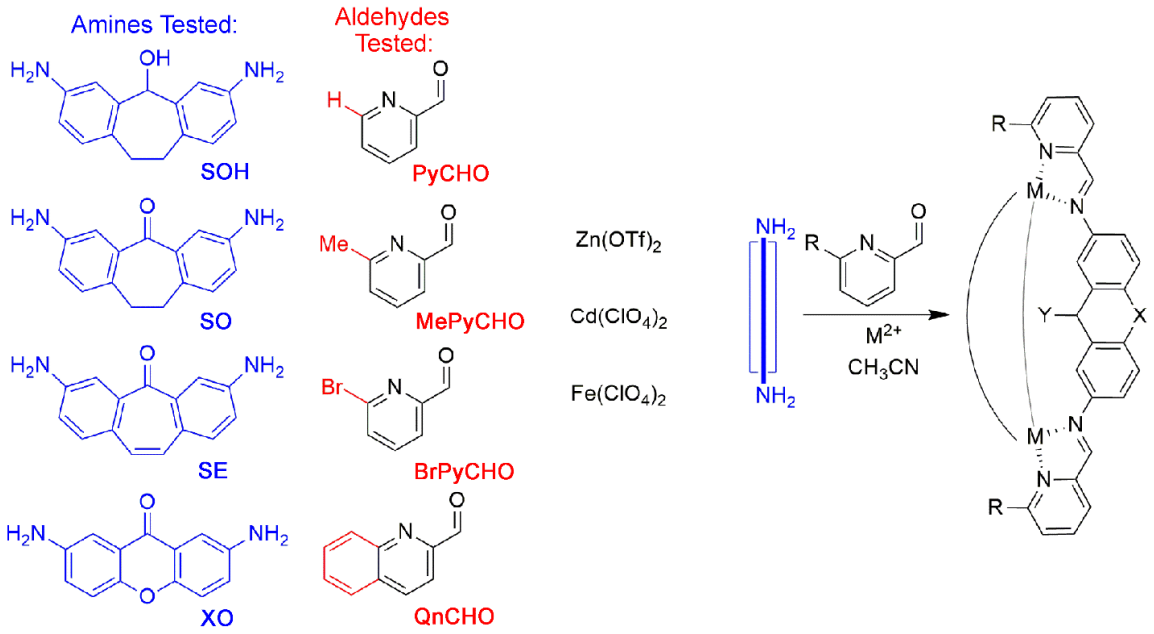

Figure 2.1: Initial combinatorial library of subcomponents tested for self-assembly of cage complexes.

To find conditions necessary for assembly, we iteratively changed the ligand backbone, the metal, and the metal center coordinating groups (Figure2.1). We started with ligand cores that were well-precedented to form diamagnetic Fe_2L_3 *meso*-helicates to determine what conditions favor the formation of a paramagnetic cage. A library was formed consisting of four diamines (3,7- diamino-suberol (**SOH**),[3] -suberone (**SO**),[3] -suberenone (**SE**), and 2,7-diamino-xanthone (**XO**),[4] four aldehydes (PyCHO, MePyCHO, BrPyCHO, or QnCHO), and three metals (Fe(II), Zn(II), and Cd(II)). The four diamines incrementally

increase in rigidity: the **SOH** diamine has a seven-membered ring with two CH_2 groups, (hereinafter referred to as "feet"), at the rear of the ligand and an sp^3 carbon between the two aromatic rings. **SO** has a carbonyl between the benzene rings, which reduces ligand flexibility, and **SE** has the C=O and a double bond between the feet. The xanthone diamine **XO** has a wider diamine coordination angle and additionally increased rigidity with a six-membered ring between the aromatic rings, removing the slight twist seen in the suberyl scaffold. These amines were combined with four aldehydes that each had varying substituents at the 6-position. PyCHO was used as the control, to allow comparison with other more bulky termini. The three more bulky formylpyridines all have slightly different coordination properties. MePyCHO and BrPyCHO have weakly electron donating and electron withdrawing groups, respectively, but these effects themselves should not affect assembly of the cage complex.[1] QnCHO has a secondary aromatic ring attached at the 5 and 6 positions limiting the degrees of freedom of the steric bulk. Varying degrees of bulk determines the limit of delirious steric "clash" that can be tolerated in the formation of high spin Fe(II). A distorted octahedral coordination environment often results in high spin Fe(II), thus paramagnetism and longer Fe-N bond lengths than low spin Fe(II). The paramagnetism alters the chemical shifts in ^{1}H NMR spectra when compared to typical diamagnetic complexes, making assignment more difficult. Zn(II) and Cd(II) have analogous M-N bond lengths to low spin and high spin Fe(II), respectively, and may aid in predicting which cages are likely to form with Fe(II), while remaining simple to assign via NMR. Zn is a good substitute for diamagnetic low-spin Fe(II) bond length and Cd(II) has a similar bond length to high-spin Fe(II).

Table 2.1: Library of components used and complexation result.

	PyCHO	**QnCHO**	**MePyCHO**
SOH•Fe	Yes	Yes	Yes
SOH•Zn	Aggregate Unreacted starting materials	Aggregate	--
SOH•Cd	Yes	Yes	--
SO•Fe	Yes	No Reaction	No Reaction
SO•Zn	Yes	Aggregate Unreacted starting materials	--
SO•Cd	Yes	Yes	--
SE•Fe	Yes	No Reaction	--
SE•Zn	Yes	Aggregate	--
Se•Cd	Yes	Yes	--
XO•Fe	Yes	Unclear	Aggregate
XO•Zn	Yes	Yes	--
XO•Cd	Aggregate	Aggregate	--

Each cage in the library was synthesized using one molar equivalent of diamine, an aldehyde (2 eq.), and a metal salt (0.66 eq) in refluxing acetonitrile for 16 h. Initially, we focused on the effect of replacing PyCHO with QnCHO. From ^{1}H NMR analysis of each cage, there are two main successful aldehyde/metal combinations that can be observed for the majority of diamines used: 1) Fe(II) and PyCHO, and 2) Cd(II) and QnCHO. Both combinations form diamagnetic complexes, with the Fe(II) and PyCHO complexes already known [4]. The Cd(II) and QnCHO combination favorably forms complexes as Cd has a

longer bond length so the metal can have an unperturbed octahedral coordination and does not require steric strain from the quinoline rings being in close proximity. Only two combinations displayed no reaction at all (i.e. only starting material shown in the ^{1}H NMR): 1) **SO**, Fe(II), and QnCHO; and 2) **SE**, Fe(II), and QnCHO. This is most likely due to the inflexibility of the diamine ligand preventing metal coordination. The combination of **XO**, Fe(II), and QnCHO was difficult to analyze as low signal:noise and broad peaks were seen in the ^{1}H NMR spectrum, with no obvious high shift peaks. Aggregate formation occurs several times when using Zn(II) and QnCHO, which may point towards unfavorable *fac* coordination due to the large steric bulk of QnCHO and short Zn-N bonds, instead favoring unorganized aggregate formation.

The only discrete paramagnetic cage from the initial library was the suberol-quinoline self-assembly complex **SOH•Fe•QnCHO**. The complex was made by combining $Fe(NTf_2)_2$ (0.66 mol eq.), QnCHO (2 mol eq.) and, **SOH**, refluxing in CH_3CN for 48 h, to yield paramagnetic complex **SOH•Fe•QnCHO**. The complex was only formed in low yields (30%) after dissolving impurities with ether, and removing excess salt with an ether-methanol wash. Excessive washing of complex resulted in decomposition, seen in ^{1}H NMR and ESI-MS, likely due to the low stability of the high spin Fe(II) coordination. The ^{1}H NMR spectrum (Figure 2.2b) was consistent with a paramagnetic complex (and some decomposition byproducts). ESI-MS analysis showed peaks consistent with the expected Fe_2L_3 *meso*-helicate **SOH•Fe•QnCHO**, with significant decomposition the longer cage was left in solution. The instability of the complex prevented formation of X-ray quality crystals for further structural analysis.

Next, aldehydes MePyCHO and BrPyCHO were combined with selected diamines and Fe(II). The excess bulk at the 6-position of MePyCHO was the correct size to favor forming paramagnetic complex **SOH•Fe•MePyCHO** without destabilizing the assembly, however BrPyCHO was not an effective complexation partner. All reactions with BrPyCHO resulted in no discrete complexes, instead forming brown solids with broad NMR signals regardless of the diamine ligand or Fe salt used, time reacted, or even performing the reaction in an inert environment to prevent iron oxidation. Assembly **SOH•Fe•MePyCHO** is not as strained as **SOH•Fe•QnCHO** since the methyl group is more flexible than the quinoline ring, and so was not as susceptible to degradation. This leads to a drastic increase in isolable material, with cage **SOH•Fe•MePyCHO** formed in 91% yield. Formation of **XO•Fe•MePyCHO**, however, was less successful. The ^{1}H NMR spectrum clearly displays broad paramagnetic peaks, indicating some assembly (possibly aggregate or coordination polymer), but no discrete cage formation. The MePyCHO coordinator was by far the most successful terminus used.

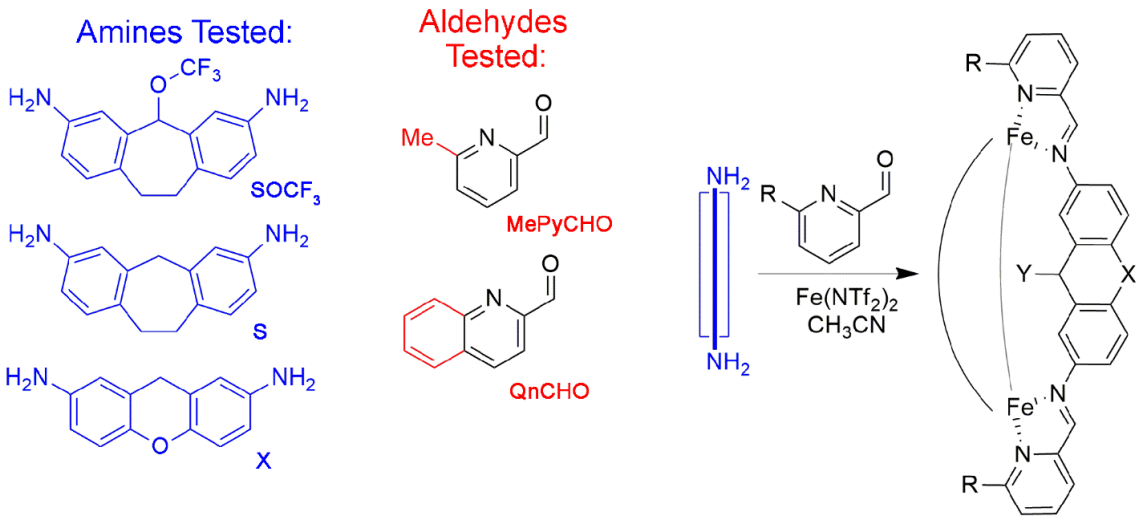

Figure 2.2: Extended combinatorial library of subcomponents tested for self-assembly of high spin cage Fe(II) complexes.

After paramagnetic cages **SOH•Fe•QnCHO** and **SOH•Fe•MePyCHO** were formed, more amines were added to the library to further determine their effect on forming high spin complexes. As **SOH** was the only diamine tested that successfully made a paramagnetic complex, more diamines with sp^3 centers were synthesized and tested. Lauren Holloway had previously synthesized other relevant diamines such as the suberyl ether (**SOCF$_3$**),[4] suberene (**S**), and xanthene (**X**),[5] which were all combined with Fe(II) and Me/QnPyCHO to determine whether they formed paramagnetic self-assemblies (Figure 2.2). Both **SOCF$_3$** and **S** could create paramagnetic complexes with QnCHO and Fe(II), making cages **SOCF$_3$•Fe•QnCHO** and **S•Fe•QnCHO**. **SOCF$_3$** was also combined with MePyCHO and Fe(II) to make **SOCF$_3$•Fe•MePyCHO**. These results suggested that an internal sp^3 carbon in the ligand core was necessary to introduce enough flexibility to accommodate the bulk from QnCHO upon assembly. The **S•Fe•QnCHO** complex was not attempted on a larger scale due to the difficulty of synthesizing suberene ligand **S**. The

SOCF$_3$ diamine gave an opportunity to explore how removing internal hydrogen bonding would affect assembly. The ether complex **SOCF$_3$•Fe•MePyCHO** was attempted several times, but results were irreproducible, giving different responses each time. The ^{1}H NMR spectra of the complex yielded inconclusive results, showing only one isomer, multiple isomers, or no complex at all in various iterations, with no obvious change in reaction conditions.

Reacting **X** with MePyCHO (2 mol eq.) and Fe(NTf$_2$)$_2$ (0.66 mol eq.) in refluxing acetonitrile resulted in a stable, isolable, paramagnetic self-assembled cage complex **X•Fe•MePyCHO**, as shown via ^{1}H NMR (Figure 2.3). Paramagnetic complexes were visually different than their diamagnetic counterparts, displaying a soft red color versus the dark purple typically exhibited by low-spin, diamagnetic Fe(II)-iminopyridine cages. These paramagnetic cage complexes also needed 2-3 days of heating to fully assemble. Paramagnetic self-assembly was unsuccessful with **SO** and inconsistently achieved with **SE**, as expected from our experience with their lack of reaction with QnCHO.

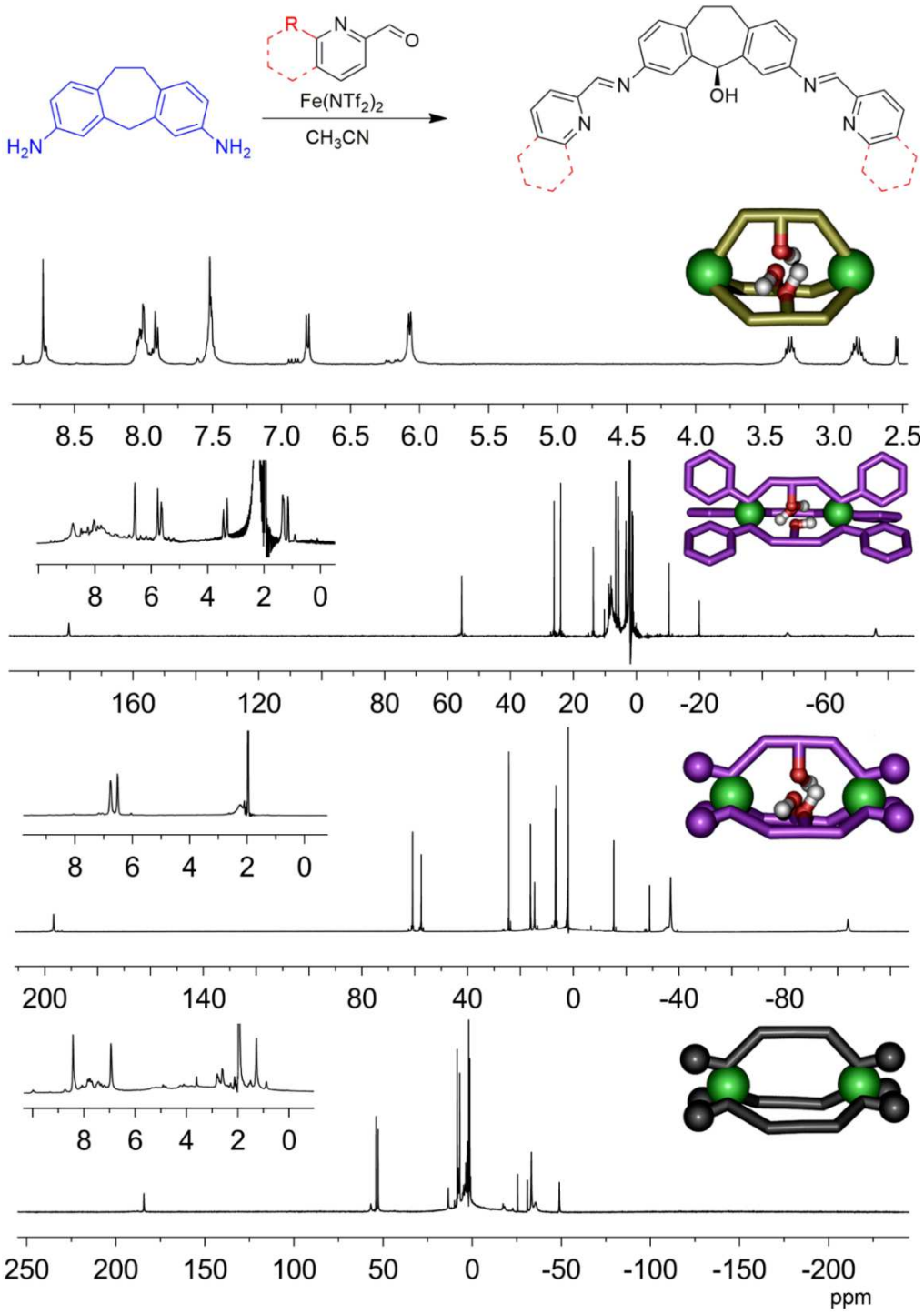

Figure 2.3: Diastereocontrolled assembly of Fe_2L_3 *meso*-helicates. ^{1}H NMR spectra of a) **SOH•Fe•PyCHO**; b) **SOH•Fe•QnCHO** with inset of diamagnetic region (0-10 ppm); c) **SOH•Fe•MePyCHO** with inset of diamagnetic region; d) **X•Fe•MePyCHO** with inset of diamagnetic region (400 MHz, 298 K, CD_3CN).

The ^{1}H NMR spectra of suberol-containing complexes **SOH•Fe•PyCHO**, **SOH•Fe•QnCHO**, and **SOH•Fe•MePyCHO** are quite different (Figure 2.3). By analyzing these spectra, the effect of steric bulk at the 6-position becomes immediately apparent. Whereas diamagnetic cage complexes show peaks from 0-8.5 ppm in ^{1}H NMR, the ^{1}H NMR spectra for **SOH•Fe•QnCHO**, and **SOH•Fe•MePyCHO** show peaks in chemical shift ranges from −100 to +190 ppm, which is typical for high spin complexes. ESI-MS analysis confirms the presence of Fe_2L_3 assembly stoichiometries for all three complexes. All paramagnetic complexes in Figure 2.3 display the same number of peaks as their respective diamagnetic counterparts. The "assignability" of the paramagnetic complex signals is not as straightforward as that of their diamagnetic counterparts. The protons close to the metal centers are the most greatly affected by the magnetic field of the metal, and as a result will have the most highly shifted signals.[6,7] The protons in the middle of the ligand, furthest from the metal center, are still affected by the metal's magnetic field, but shifted to a much lesser extent. While reaction of the xanthene ligand **X** with $Fe(NTf_2)_2$ and QnCHO yielded limited product, when **X** is reacted with MePyCHO and either $Fe(NTf_2)_2$ or $Fe(ClO_4)_2$, yield again increased substantially. The ^{1}H NMR characterization of **X•Fe•MePyCHO** showed a broad range from -60 to +180 ppm, similar to the spectra of **SOH•Fe•MePyCHO**.

2.3 Fe_2L_3 *Meso*-Helicate Crystal Structure Analysis

Crystallographic analysis of the assembly structures allows comparison of the coordination angles and bond lengths at the Fe centers in the diamagnetic and paramagnetic

complexes, making it possible to understand why complexes with QnCHO and MePyCHO show paramagnetic behavior. Lauren Holloway was able to grow X-ray quality crystals the triflimide salt, using slow diffusion of ether into a CH_3CN solution of **X•Fe•MePyCHO•(NTf$_2$)$_4$**. The perchlorate salt, however, had limited solubility, making crystal growth unsuccessful. The solid state structure of **X•Fe•MePyCHO•(NTf$_2$)$_4$** was determined by X-ray diffraction analysis, and Figure 2.4 shows the comparison between **X•Fe•MePyCHO** and a DFT-minimized structure of **X•Fe•PyCHO**, as well as between X-ray structures of **SOH•Fe•PyCHO**, **SO•Fe•PyCHO**, and **X•Fe•MePyCHO**.

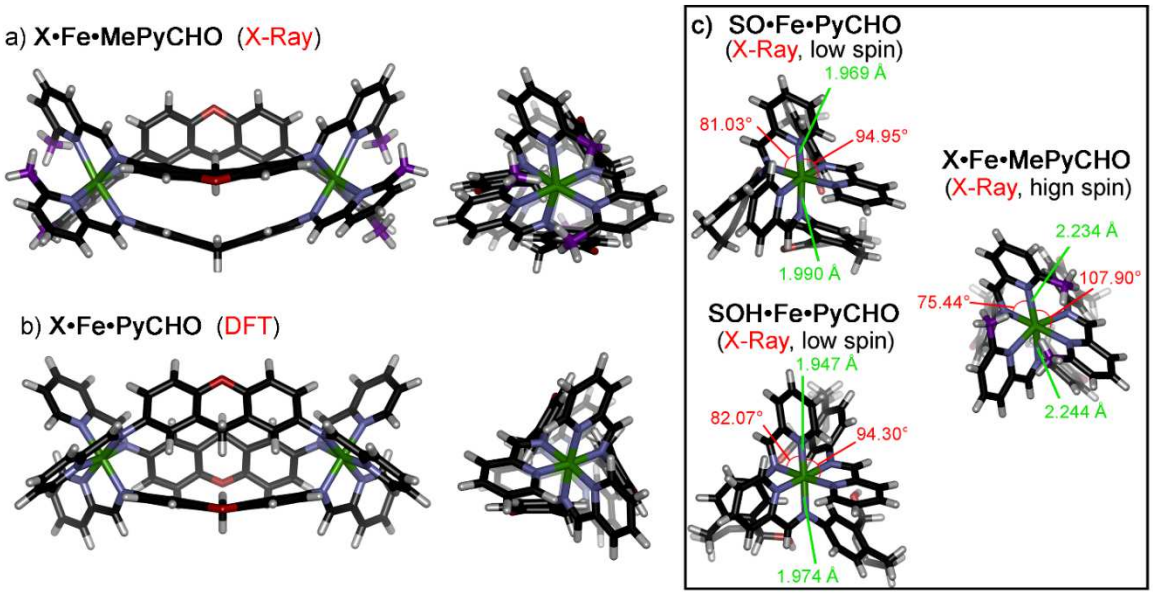

Figure 2.4: Structural variations in Fe_2L_3 *meso*-helicates. a) solid state structure of **X•Fe•MePyCHO •(NTf$_2$)$_4$**, obtained via X-ray diffraction analysis (counterions and disordered solvent omitted for clarity); b) Minimized structure of **[X•Fe•PyCHO]**$^{4+}$ (B3LYP-D3(BJ)/6-31G(d), restricted spin); c) N-Fe-N angle and length comparisons between the solid state structures of **SO•Fe•PyCHO•(ClO$_4$)$_4$**,[3] **SOH•Fe•PyCHO •(ClO$_4$)$_4$**,[3] and **X•Fe•MePyCHO •(NTf$_2$)$_4$** obtained via X-ray diffraction analysis (truncated structures shown for clarity, containing only one Fe center).

Analysis of crystal structure data demonstrates that the major differences lie in the N-Fe-N bond angles and the N-Fe bond lengths (Shown in Figure 2.4). The diamagnetic

complexes **SOH•Fe•PyCHO** and **SO•Fe•PyCHO** show bond angles that are similar and the Fe coordination centers are close to octahedral. The internal N-Fe-N angles (in a single iminopyridine 5-membered ring) are 81.03° and 82.07° for **SO•Fe•PyCHO** and **SOH•Fe•PyCHO** respectively, and the interligand N-Fe-N angles (between two pyridyl N) are 94.95° and 94.30°. Only two angles are discussed here, but they are representative of their other equivalents. By contrast, the high spin Fe(II) centers display longer Fe-N bond lengths and a relatively significant distortion in the ligand field compared to their low-spin counterparts.

The coordination around the Fe centers in the paramagnetic **X•Fe•MePyCHO•$(NTf_2)_4$** is far more distorted (see Figures 2.4a, 2.4c). The internal N-Fe-N angle is 75.44°, and the interligand N-Fe-N angle (between two pyridyl N) is 107.90°. This distortion in the Fe ligand field is complemented by an increase in Fe-N bond length of almost 0.3 Å. The pyridyl N-Fe bond lengths for **SO•Fe•PyCHO** and **SOH•Fe•PyCHO** are 1.969 Å and 1.947 Å and the imine N-Fe lengths are 1.990 Å and 1.974 Å, respectively. In contrast, those bond lengths are 2.234 Å and 2.244 Å in the more strained **X•Fe•MePyCHO**. The longer bond lengths and distorted octahedral coordination environment allows high spin Fe(II) to better accommodate the additional steric bulk from MePyCHO. High spin Fe(II) has longer bond lengths and distorted octahedral coordination to accommodate bulky ligands of asymmetric coordination around the metal, these properties make high spin Fe(II) less energetically favorable than low spin Fe(II). The high energy system is much less stable due to the strain at the Fe vertices.

The solid state structures of **SO•Fe•PyCHO**, **SOH•Fe•PyCHO**, and **X•Fe•MePyCHO** illustrate why paramagnetism is present in the methylpyridine assemblies, but does not account for why the three relatively similar cores vary so greatly in their ability to form high spin cage complexes. The suberol diamine is known to assemble with PyCHO to form the diamagnetic complex **SOH•Fe•PyCHO** and is also able to form high spin complexes with MePyCHO and QnCHO. However, we were unsuccessful in growing suitable X-ray quality crystals of the high spin complexes **SOH•Fe•QnCHO** and **SOH•Fe•MePyCHO**, so their DFT-minimized structures were compared to the solid state structure of **SOH•Fe•PyCHO** obtained by X-ray diffraction (Figure 2.5).[3] The structural variations between **SOH•Fe•PyCHO**, **SOH•Fe•QnPyCHO**, and **SOH•Fe•MePyCHO** nicely illustrate why **SOH** is an effective internal core for assembly with both QnCHO and MePyCHO, and why the **SOH•Fe•QnCHO** and **SOH•Fe•MePyCHO** helicates are paramagnetic. The N-Fe-N angles and N-Fe bond lengths in **SOH•Fe•QnCHO** and **SOH•Fe•MePyCHO** are consistent with those observed in the solid-state structure of **X•Fe•MePyCHO**, with large (>105°) interligand N-Fe-N angles and small (<76°) iminopyridine angles, as well as long (>2.25 Å) N-Fe bond lengths. By analyzing the structures, we can see that the Fe-Fe distances are 9.85 Å and 9.99 Å in **SOH•Fe•QnCHO** and **SOH•Fe•MePyCHO**, whereas the Fe-Fe distance in **SOH•Fe•PyCHO** is only 9.70 Å, meaning that the suberol ligand is less puckered in the high spin complexes. This longer Fe-Fe distance is accommodated because the bend angle (defined as $2\theta_b$, Figure 2.5d) of the CHOH center is lowered in the paramagnetic complexes. This ligand bending angle $2\theta_b$ = 107.0° and 107.5° in **SOH•Fe•QnCHO** and **SOH•Fe•MePyCHO**, but is far wider in

SOH•Fe•PyCHO, with $2\theta_b$ = 114.4°. The ligand coordination angle ($2\theta_c$) changes also, with $2\theta_c$ = 79.9° and 81.6° in **SOH•Fe•QnCHO** and **SOH•Fe•MePyCHO**, and $2\theta_c$ = 79.0° in **SOH•Fe•PyCHO**. Suberol was distinctly more flexible, compared to the other rigid diamines, due to the sp^3 center and 7-membered central ring in **SOH**. We believe that the ease of complex formation with **SOH** is due to the ligand's ability to flex and bend, which better accommodates the excess bulk near the metal center in **SOH•Fe•QnCHO** and **SOH•Fe•MePyCHO**, than diamines **SO** or **X**.

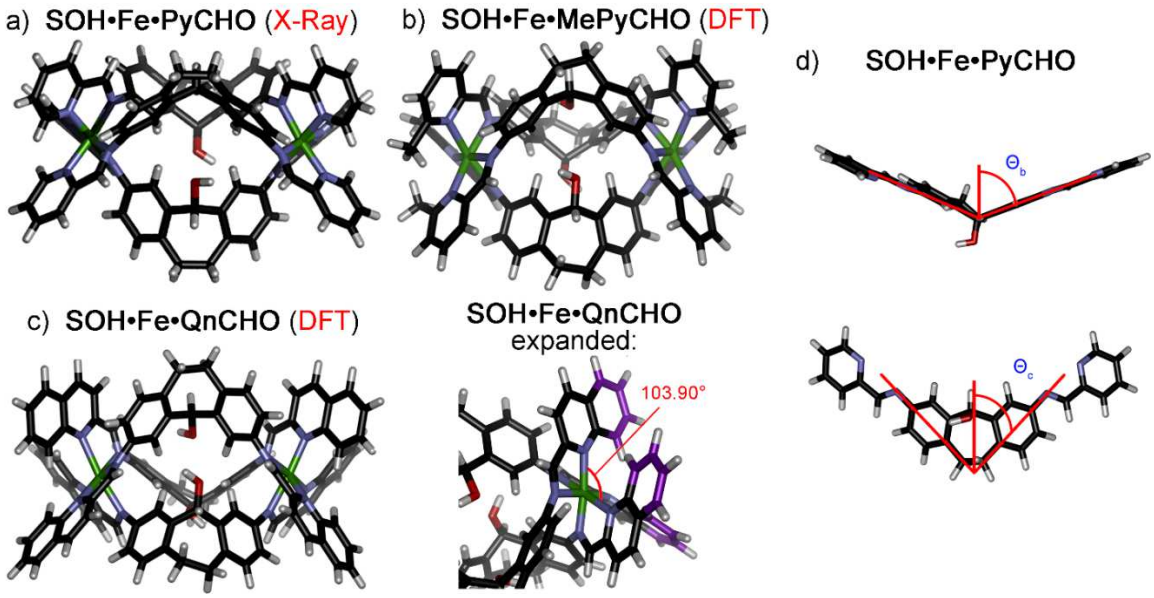

Figure 2.5: Structures of a) solid state structure of **SOH•Fe•PyCHO•$(ClO_4)_4$**[3] obtained via X-ray diffraction analysis (counterions and disordered solvent omitted for clarity), and the DFT optimized structures of b) [**SOH•Fe•MePyCHO**]$^{4+}$; c) [**SOH•Fe•QnCHO**]$^{4+}$ (B3LYP-D3(BJ)/6-31G*, unrestricted spin (i.e. 4 unpaired spins per Fe)). d) Illustration of the coordination angles used to describe the assembly structures (using ligand **Py•SOH** as example).

The variable bend in the ligand has a secondary effect of changing the O-O distances between the alcohol groups on adjacent ligands, which are 4.0 Å, 4.1 Å in **SOH•Fe•QnCHO** and **SOH•Fe•MePyCHO**, and 4.4 Å in **SOH•Fe•PyCHO**. This

secondary effect likely contributes to the higher diastereoselectivity in assembly of **SOH•Fe•QnCHO** and **SOH•Fe•MePyCHO**, compared to **SOH•Fe•PyCHO**. The internal CHOH group is prochiral, and four possible isomers can form upon assembly

Interestingly, upon further analysis, a second isomer of **SOH•Fe•MePyCHO** could be seen. The CHOH group in suberol **SOH** is a prochiral center, so four isomers of **SOH•Fe** complexes are possible upon assembly (for the *meso*-helicate structure with fac-ΛΔ stereochemistry at the metal centers),[8,9] with the OH groups either *all-in*, *all-out*, out_2in or in_2out. For the diamagnetic complex **SOH•Fe•PyCHO**, the self-complementary H-bonding between the OH groups favors the *all-in* isomer, but a dissymmetric isomer is also present (~10% of the sample, as shown by ^{1}H NMR analysis, Figure 2.3a). However, in the spectra of **SOH•Fe•QnCHO** and **SOH•Fe•MePyCHO** there is only one isomer present. The DFT-minimized models suggest that the OH groups are closer, and therefore can more effectively H-bond in **SOH•Fe•QnCHO** and **SOH•Fe•MePyCHO** complexes, favoring the *all-in* conformation more so than in_2out seen in the ^{1}H NMR of cage complex **SOH•Fe•MePyCHO**.

2.4 Synthesis and Characterization of Paramagnetic Fe_4L_6 Cage Complexes

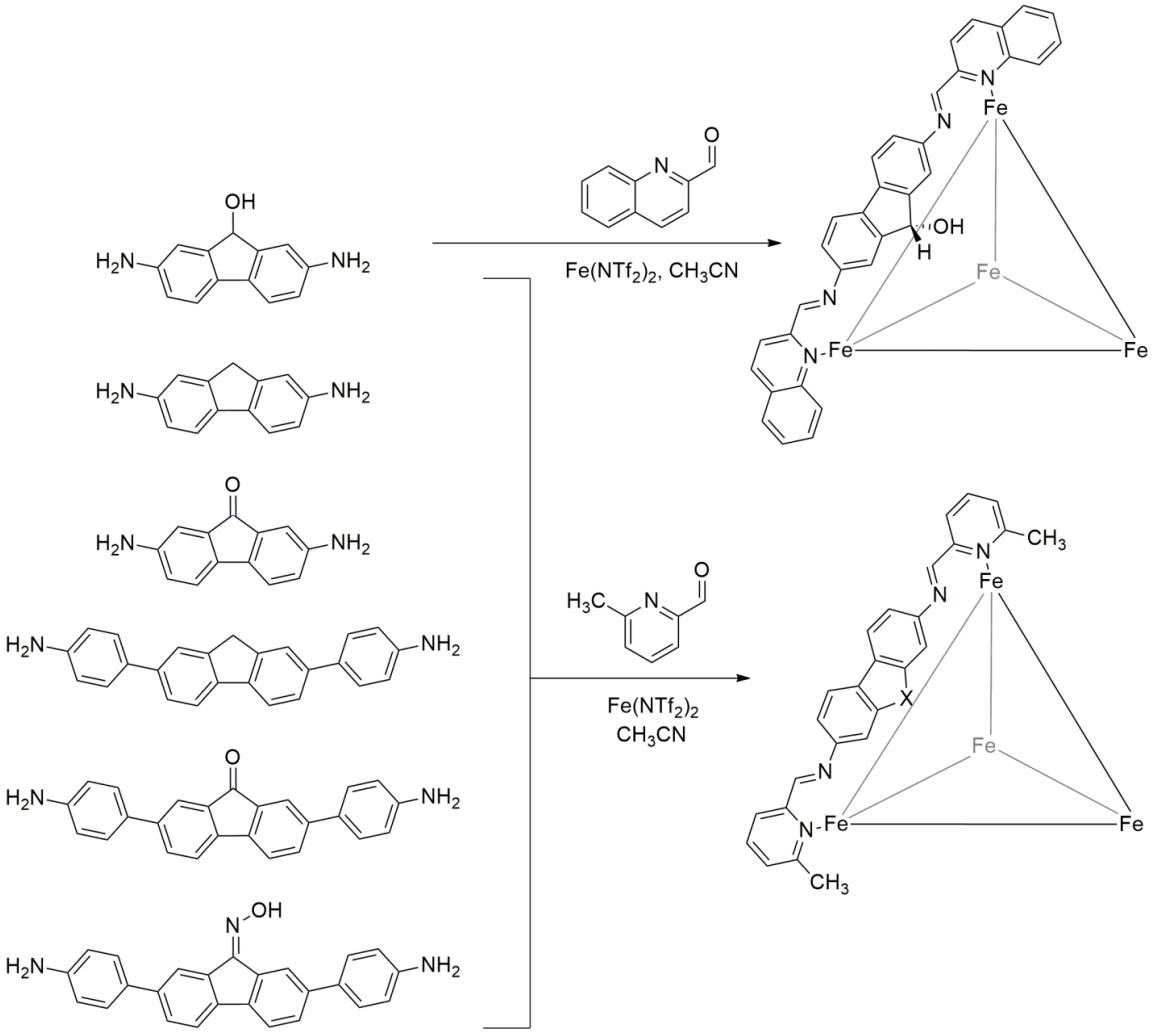

Figure 2.6: Extended Fluorenyl Library for synthesis of paramagnetic cage.

The formation of M_2L_3 *meso*-helicates is moderately facile and tolerant of excess bulk around the metal centers when the flexibility of the ligand backbone is sufficient to allow distortion upon assembly. As the ligand bends to accommodate this bulk the octahedral coordination environment becomes distorted (Figures 2.4 and 2.5). Unfortunately, one of the requirements in forming larger M_4L_6 complexes is that the ligands need to be more linear and rigid than the V-shaped diamine ligands shown previously, which initially seems

diametrically opposed to the conditions necessary to form high spin, paramagnetic complexes **SOH•Fe•MePyCHO** and **X•Fe•MePyCHO**. Attempts made with ligands with limited flexibility (i.e. **XO**, **SO**, and **SE**) had led to unsuccessful assembly. However, a rigid diamine ligand with a more linear coordination angle could be able to form paramagnetic polyhedra, such as M_4L_6 tetrahedral cage complexes.

Table 2.2: Reactivity table for fluorenyl-based ligands.

	MePyCHO	**QnCHO**
F•Fe	No	--
FOH•Fe	Yes	Yes
FO•Fe	No	--
Ph_2F•Fe	No	--
Ph_2FO•Fe	No	--
Ph_2FOX•Fe	No	--

Attempting to couple rigid fluorene-based ligands **F**, **FOH**, **FO**, **EF**, **EFO**, and **EFOX** (2,7-diaminofluorene, 2,7-diaminofluorenol, and 2,7-diaminofluorenone, 2,7-bis(4-aminophenyl) fluorene, 2,7-bis(4-aminophenyl) fluorenone, 2,7-bis(4-aminophenyl) fluoryl oxime), Figure 2.6 with Fe(II) and bulky aldehydes QnCHO or MePyCHO was generally unsuccessful, resulting in few self-assemblies. Not surprisingly, the results showed that assembly with fluorenyl ligands was far less favorable than that of the M_2L_3 *meso*-helicates, with only **FOH** yielding product consistently. Complex **F•Fe•MePyCHO** was able to form once at 5 mg scale, but results were unable to be replicated, either at the

same or larger scale. All extended ligands were unable to form paramagnetic complexes. However, heating together **FOH**, MePyCHO, $Fe(NTf_2)_4$, and $NaClO_4$ in CH_3CN for 72 h yielded the paramagnetic cage **FOH•Fe•MePyCHO•ClO_4•$(NTf_2)_7$** in good yield. The ^1H NMR of the complex showed peaks ranging from -100 to +200 ppm. ESI-MS analysis corroborated an M_4L_6 stoichiometry (Figure 2.8). The presence of ClO_4^- anion was found to be important, as the anion was used as a template in assembly to form only one diastereomer.

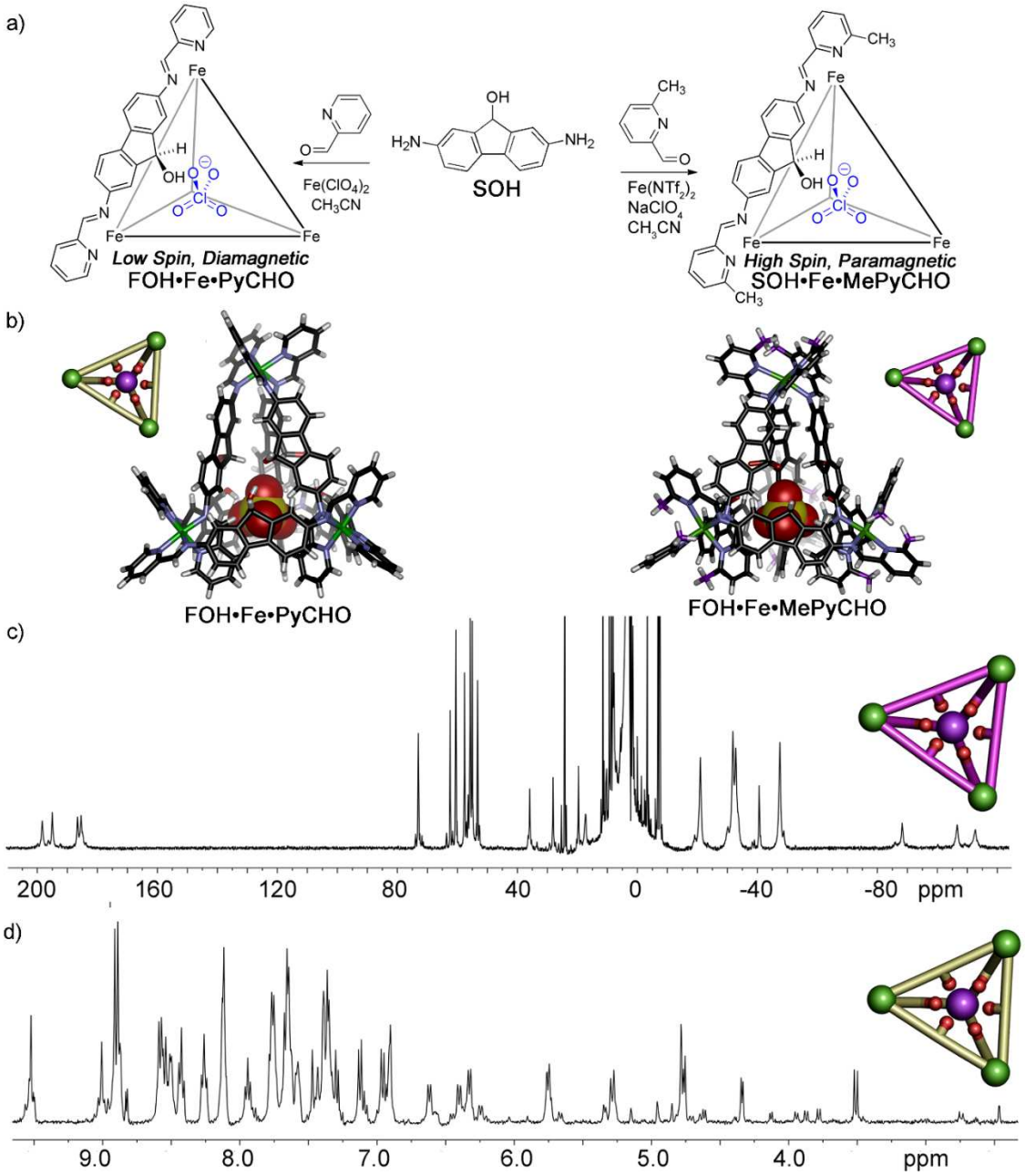

Figure 2.7: a) Diastereocontrolled assembly of Fe_4L_6 cages **FOH•Fe•PyCHO** and **FOH•Fe•MePyCHO**. b) Solid state structures of **FOH•Fe•PyCHO •$(ClO_4)_8$**[10] and **FOH•Fe•MePyCHO •ClO_4•$(NTf_2)_7$**, obtained via X-ray diffraction analysis (external counterions and disordered solvent omitted for clarity); ^{1}H NMR spectra of c) **FOH•Fe•MePyCHO•ClO_4•$(NTf_2)_7$**; d) **2.8•$(ClO_4)_8$** (400 MHz, 298 K, CD_3CN).

Anion templation for cage **FOH•Fe•MePyCHO•ClO_4•$(NTf_2)_7$** had precedent, as the same phenomena occurs in cage **FOH•Fe•PyCHO•$(ClO_4)_8$**, which forms as only one diastereomer with a *mer*$_3$*fac* arrangement at the metals, with overall C_3 symmetry (Figure 2.7b).[10] The reason for templation is favorable hydrogen bonding whereby the OH groups hydrogen bond with the ClO_4^- anion favoring the *mer*$_3$*fac* isomer. Additionally, this particular isomer allows hydrogen bonding not only to the ClO_4^- anion, but also between all axial ligands (those connected to the *fac* center) and between axial and base ligands, whereas other isomers would force at least one OH group outwards making a less stable complex. Without the addition of the ClO_4^- anion, the high spin complex was unable to assemble into a discrete cage. Instead, testing with other possible hydrogen bonding anions such as TfO^- or SO_4^{2-} resulted in a non-discrete aggregate showing broad mounds in the ^{1}H NMR spectra.[10] While the $Fe(ClO_4)_2$ salt could be used to form **FOH•Fe•MePyCHO**, its low solubility in acetonitrile was an issue. While some ClO_4^- anion is necessary for formation, other Fe(II) salts can be used to increase or decrease solubility. We tested anions NTf_2^-, BF_4^-, and SO_4^{2-}, and found that NTf_2^- was the only anion that increased solubility. Increased solubility became necessary for good signal:noise in the ^{1}H NMR experiments as well as aiding in crystallization. An increase in yield was also observed, from ClO_4 at 24% to NTf_2 at 76%, thus the best anion choice for **FOH•Fe•MePyCHO** is a mixture of NTf_2^- to aid solubility, and ClO_4^- as a template for self-assembly.

The hydrogen bonding control of assembly with **FOH** also helps explain why fluorene and fluorenone ligands were unsuccessful, as there is no H-bonding or anion templation that can be exploited in those cases. The ^{1}H NMR spectrum of

FOH•Fe•MePyCHO•ClO$_4$•(NTf$_2$)$_7$ is complex, but it is consistent with the ^{1}H NMR spectrum **FOH•Fe•MePyCHO•(ClO$_4$)$_8$**. The *mer$_3$fac* structure is dissymmetric, easily noted by the four discrete peaks for imine CH (one *mer*, three *fac*) protons observed in both cage complexes. The more obvious peak separation in the paramagnetic **FOH•Fe•MePyCHO•ClO$_4$•(NTf$_2$)$_7$** further supports this assignment, with peak clusters split into sets of four, notably at 180-200 ppm and -85 − -100 ppm.

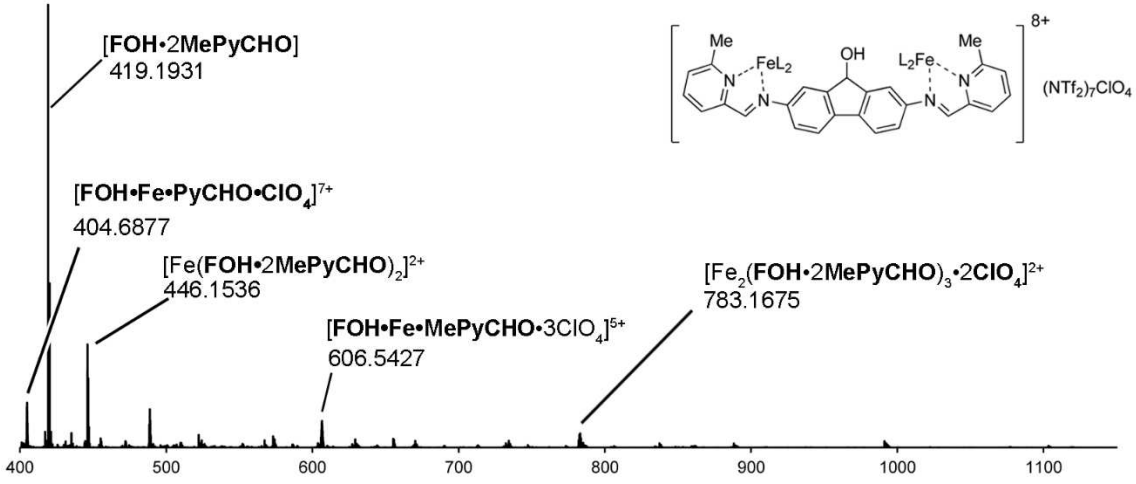

Figure 2.8: Full ESI-MS of cage **FOH•Fe•MePyCHO** (CH_3CN).

2.5 Fe$_4$L$_6$ Crystal Structure Analysis

Having only one diastereomer made producing X-ray quality crystals of **FOH•Fe•MePyCHO•ClO$_4$•(NTf$_2$)$_7$** possible thanks to Lauren Holloway, and in turn the crystal structure validated that only the *mer$_3$fac* structure was present (Figure 2.7b). While crystallization was possible, the crystals were extremely complex and polymorphic. There were four **FOH•Fe•MePyCHO** cations, 16 NTf_2^- and 5 ClO_4^- anions, plus 15 solvent molecules present in the asymmetric unit of the unit cell. The crystals display weak

scattering and solvent/counterion disorder, the crystals cracked at low temperatures (presumably due to a spin transition at low temperature), and so the acquisition was performed at 150 K. However, the basic structure and connectivity of the complex could be unambiguously determined: all four cations in the unit cell showed the Fe_4L_6 *mer*$_3$*fac* **FOH•Fe•MePyCHO** structure.

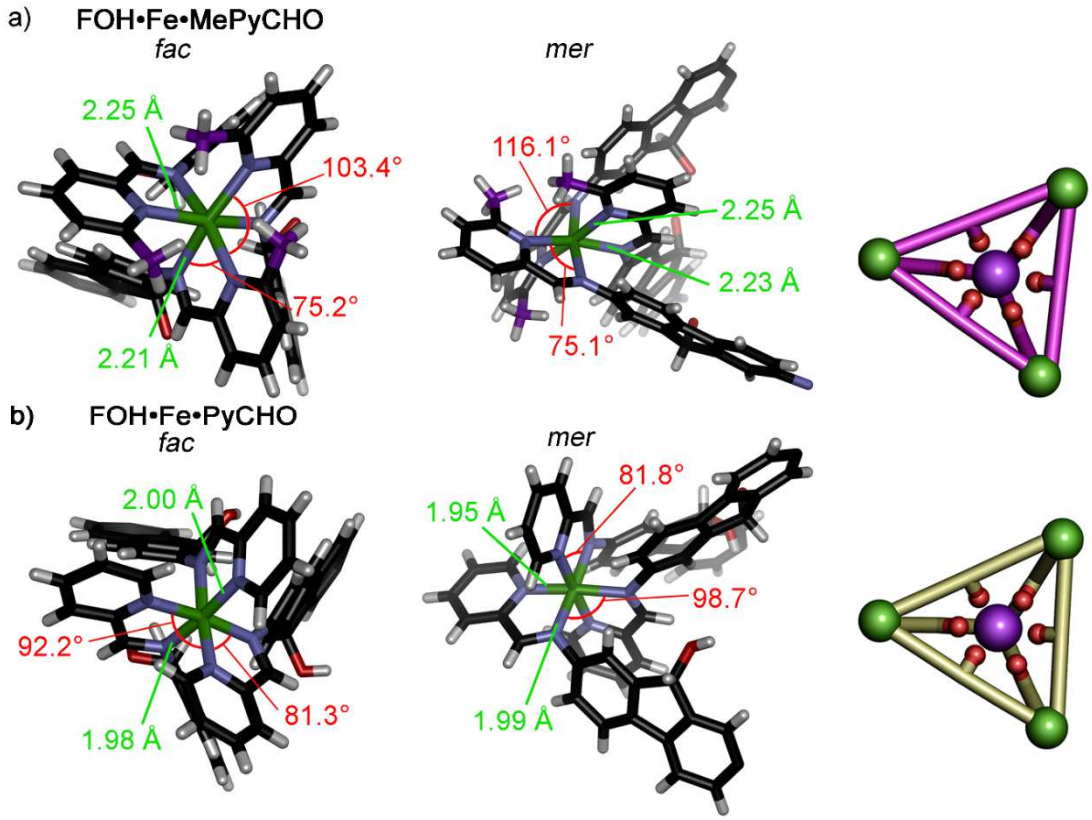

Figure 2.9: Structural variations in Fe_4L_6 cages. N-Fe-N angle and length comparisons between the solid state structures of *fac* and *mer* Fe centers in a) **FOH•Fe•MePyCHO •ClO$_4$•(NTf$_2$)$_7$**; b) **FOH•Fe•PyCHO •(ClO$_4$)$_8$**[48] obtained via X-ray diffraction analysis (truncated structures shown for clarity, containing only one Fe center).

The solid-state structure allowed analysis of the coordination environment, and a comparison of the Fe(II) centers in the diamagnetic and paramagnetic Fe_4L_6 cage variants. Importantly, as **FOH•Fe•MePyCHO•ClO$_4$•(NTf$_2$)$_7$** has a much lower resolution

compared to data from the previously discussed M_2L_3 high spin complexes, care should be taken when analyzing bond angles and lengths. The internal/interligand N-Fe-N bond angles and Fe-N bond lengths (Figure 2.9) have similar values with those seen in **X•Fe•MePyCHO**. The solid state structure is also able to reveal why, despite having no flexibility in ligand backbone and no observed ligand bending, **FOH•Fe•MePyCHO•ClO$_4$•(NTf$_2$)$_7$** forms a stable high spin Fe(II) assembly. The **FOH•Fe•MePyCHO•ClO$_4$•(NTf$_2$)$_7$** assembly has *mer* centers which are able to accommodate high levels of distortion than *fac* centers in pyridyl cage **FOH•Fe•PyCHO•ClO$_4$**, and even greater distortion in **FOH•Fe•MePyCHO•ClO$_4$•(NTf$_2$)$_7$**. The N-Fe bond distances are longer in **FOH•Fe•MePyCHO•ClO$_4$**, at ~2.25 Å in both the *fac* and *mer* centers, as opposed to N-Fe bond distances of ~2.00 Å in **FOH•Fe•PyCHO•ClO$_4$**. The greatest distortion occurs at the *mer* centers in **FOH•Fe•MePyCHO•ClO$_4$**, with very large (116°) interligand N-Fe-N angles and very small (75°) iminopyridine angles. The *fac* center is still distorted (N-Fe-N = 103°, 75°), but less so. The *mer* Fe centers are able aid in the assembly of the M_4L_6, being able to better accommodate the bulky methylpyridine groups of the high spin Fe(II) cage complex.

2.6 Spin State Determination of Paramagnetic Cage Complexes

Cage complexes **SOH•Fe•MePyCHO**, **X•Fe•MePyCHO**, and **FOH•Fe•MePyCHO** are all paramagnetic, but this does not necessarily mean that they are truly "high" spin, as intermediate spin states are possible. To determine the spin state of the Fe(II) centers

(intermediate or high spin) requires the determination of the cage complexes' magnetic susceptibility (Full spectra Figure 6.33-36). Magnetic susceptibility was determined using Evans' method[11–14] variable temperature ^{1}H NMR experiments on the four paramagnetic complexes **SOH•Fe•QnCHO**, **SOH•Fe•MePyCHO**, **X•Fe•MePyCHO**, and **FOH•Fe•MePyCHO** (Table 2.3 and Figure 2.10). The spectra show paramagnetic signals persisting from 313 K – 233 K for all four complexes in CD_3CN solution.

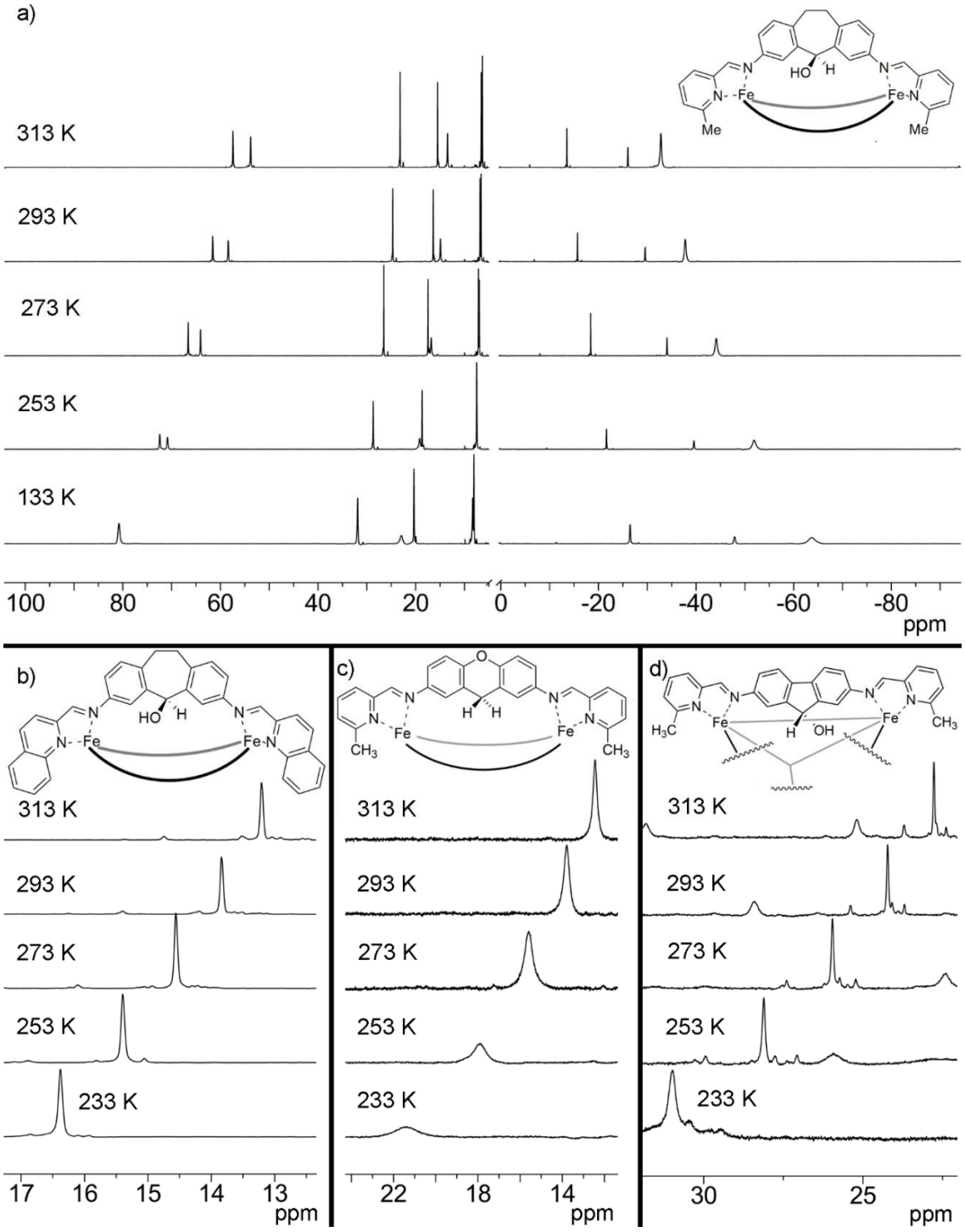

Figure 2.10: Full spectral sweep width of the ^{1}H NMR spectra for a) **SOH•Fe•MePyCHO**, and downfield regions of b) **SOH•Fe•QnCHO**, c) **X•Fe•MePyCHO** and d) **FOH•Fe•MePyCHO•ClO$_4$•(NTf$_2$)$_7$** at various temperatures, illustrating the high spin nature of the complexes in solution from 313 K to 233 K (CD_3CN, 500 MHz).

The $\chi_M T$ values rise with decreasing temperature, which matches with data from similar self-assembled Fe(II) cage complexes, although this behavior is different to that of the majority of mononuclear Fe(II) paramagnetic complexes.[7] The observed and corrected χ_M values are shown in Table 1: as the M_w of the complexes is large, the diamagnetic contribution was calculated and applied in the correction, not ignored (as is common for small M_W complexes).[7,14] The data for each cage complex correlates to high spin Fe(II) centers that exhibit significant magnetic coupling. The corrected magnetic susceptibilities $\chi_{M'}$ of **SOH•Fe•QnCHO**, **SOH•Fe•MePyCHO**, and **X•Fe•MePyCHO** are all very similar, as would be expected for their similar coordination environment. There is no significant difference between QnCHO and MePyCHO, as they result in similar coordination environments, and as such, similar effects on the spin state of the Fe(II) centers. The larger **FOH•Fe•MePyCHO•ClO_4•$(NTf_2)_7$** displays an overall larger susceptibility as the value is per Fe center, not per complex, and there are four Fe atoms in this complex.

Table 2.3: Molar Susceptibility (χ_M), corrected molar susceptibility ($\chi_{M'}$), and effective magnetic moment (μ_{eff}) for cages **SOH•Fe•QnCHO**, **SOH•Fe•MePyCHO**, **X•Fe•MePyCHO**, and **FOH•Fe•MePyCHO** at 293 K.

Cage	Δf (Hz)	χ_M ($cm^3\ mol^{-1}$)	$\chi_{M'}$ ($cm^3\ mol^{-1}$)	μ_{eff}
SOH•Fe•QnCHO	154.2	0.021	0.023	7.1
SOH•Fe•MePyCHO	201.6	0.025	0.026	7.7
X•Fe•MePyCHO	184.8	0.023	0.024	7.4
FOH•Fe•MePyCHO	180.0	0.042	0.044	9.9

2.7 Anion Exchange and Post-Assembly Reactivity in Paramagnetic Complexes

The **FOH** complexes with ClO_4^- anions form only one isomer due to anion templation, which directs hydrogen bonding of the –OH groups to a ClO_4^- anion in the internal cavity. This in turn makes the internal cavity fully occupied by the ClO_4^- anion. For a guest to replace the perchlorate ion in the cavity of the cage, the guest has to be more favorable than the ClO_4^- anion, even though it perfectly occupies the internal space. However, when $Fe(NTf_2)_2$ is used to form the complex, a cage is formed with multiple isomers, as shown by the ^1H NMR spectrum (Figure 2.11). This suggests that the cavity could be filled with a suitable guest, most likely something that emulated the characteristics of the ClO_4^- anion and have protons that could be affected by the paramagnetism of the cage. With these characteristics in mind, sodium dodecanesulfonate (SDS) was chosen as the anion portion has similar size and charge density properties as the ClO_4^- anion.

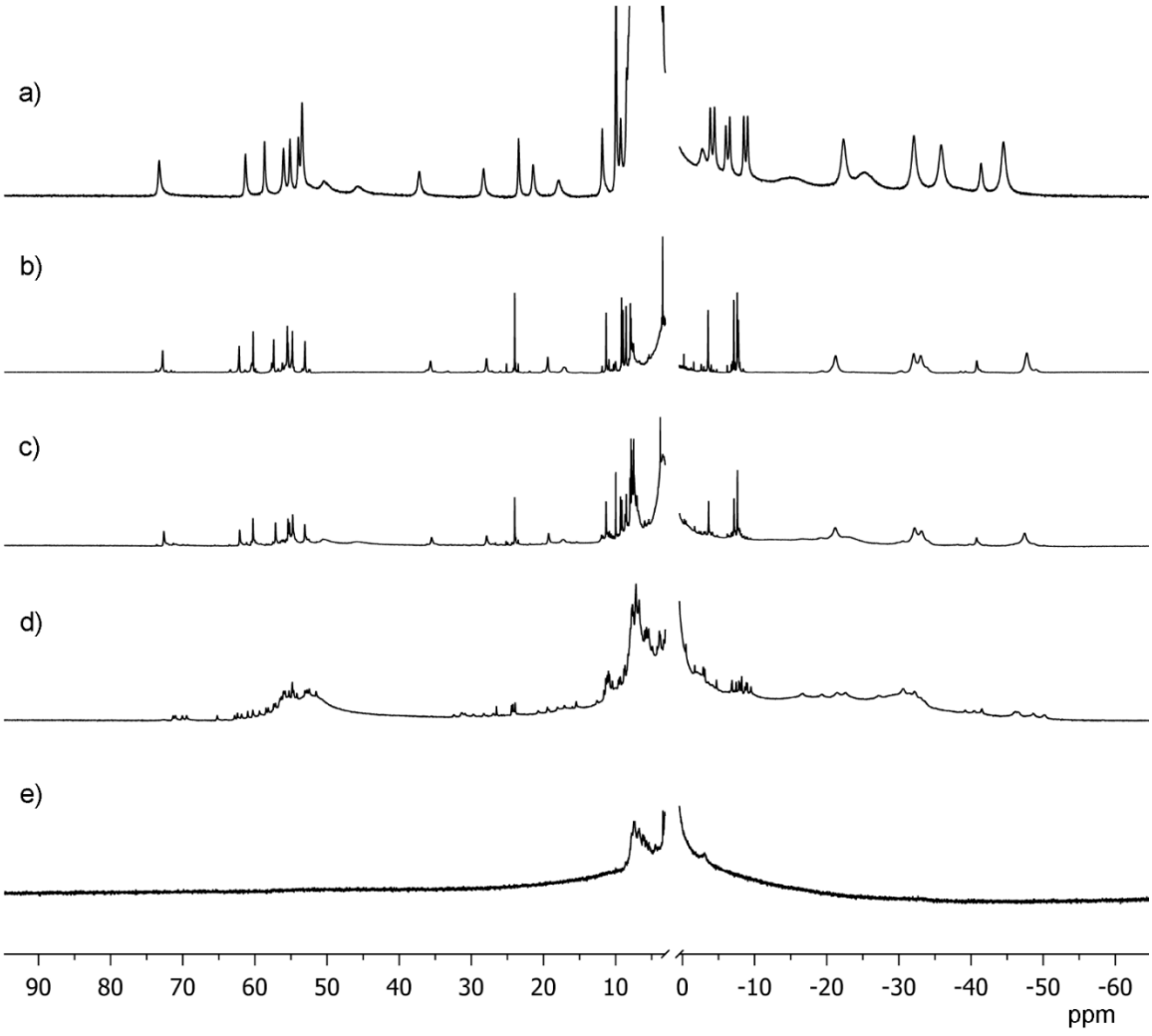

Figure 2.11: ^{1}H NMR spectra of a) **F•Fe•MePyCHO**, b) **FOH•Fe•MePyCHO**, c) **FOH•Fe•MePyCHO** and 10 eq. SDS in CD_3CN heated at reflux for 24 hr, d) **FOH**, $Fe(NTf_2)_2$, MePyCHO, and SDS reacted together and heated at reflux for 24 hr, and e) **FOH•Fe•MePyCHO** and 10 eq. butyl isocyanate in CD_3CN heated at reflux for 24 hr (400 MHz, 298 K, CD_3CN).

Unfortunately, SDS is insoluble in organic solvents and needs a fair amount of water to aid solubility in acetonitrile, and as more SDS was added to a solution of **FOH•Fe•MePyCHO** in acetonitrile, material started to precipitate out of solution. The ^{1}H

NMR of the solution showed only complex **FOH•Fe•MePyCHO** (Figure 2.11). The precipitate could not be redissolved in CD_3CN.

With SDS being, at best, inconclusive about being able to displace ClO_4^-, a different approach to post-assembly modification was attempted. Butyl isocyanate had been previously reacted with diamagnetic cage **SOH•Fe•PyCHO** to create a novel complex, but this was difficult to assign due to peak clustering in the ^1H NMR. The paramagnetic cages have far more spread out peaks, however, so they were promising targets and may show a more readily decipherable ^1H NMR spectra. The reaction was tested with **SOH•Fe•MePyCHO** and **FOH•Fe•MePyCHO**, separately. Reacting butyl isocyanate (18 eq.) with either **SOH•Fe•MePyCHO** (1 eq.) or **FOH•Fe•MePyCHO** (1 eq.) in acetonitrile unfortunately resulted in the destruction of both cages, showing indecipherable peaks, and only in the diamagnetic region. This is likely due to the destabilized paramagnetic cages, with the longer, weaker Fe-N bonds less tolerant to further reaction.

2.8 Amine Exchange and Comparison of Stability to Diamagnetic Counterparts

The diamagnetic pyridyl *meso*-helicates show high fidelity self-sorting.[4] For example, when **SOH** and **SO** are combined with PyCHO and Fe(II) in a one-pot reaction, only complexes **SOH•Fe•PyCHO** and **SO•Fe•PyCHO** are seen, with no heterocomplexes. The strongly self-sorting assembly properties are a result of the relative energy required to distort the ligand backbone upon assembly. Suberone *meso*-helicate **SO•Fe•PyCHO** is relatively more stable than the suberol equivalent **SOH•Fe•PyCHO**, thus it is formed selectively with no heterocomplexes observed.[4] Introducing steric bulk at the pyridyl

centers changes the Fe(II) coordination, altering both the Fe-N bond lengths and the N-Fe-N bond angles: this leads to the question of whether the paramagnetic cages are capable of similarly effective self-sorting when multiple ligands are assembled at once.

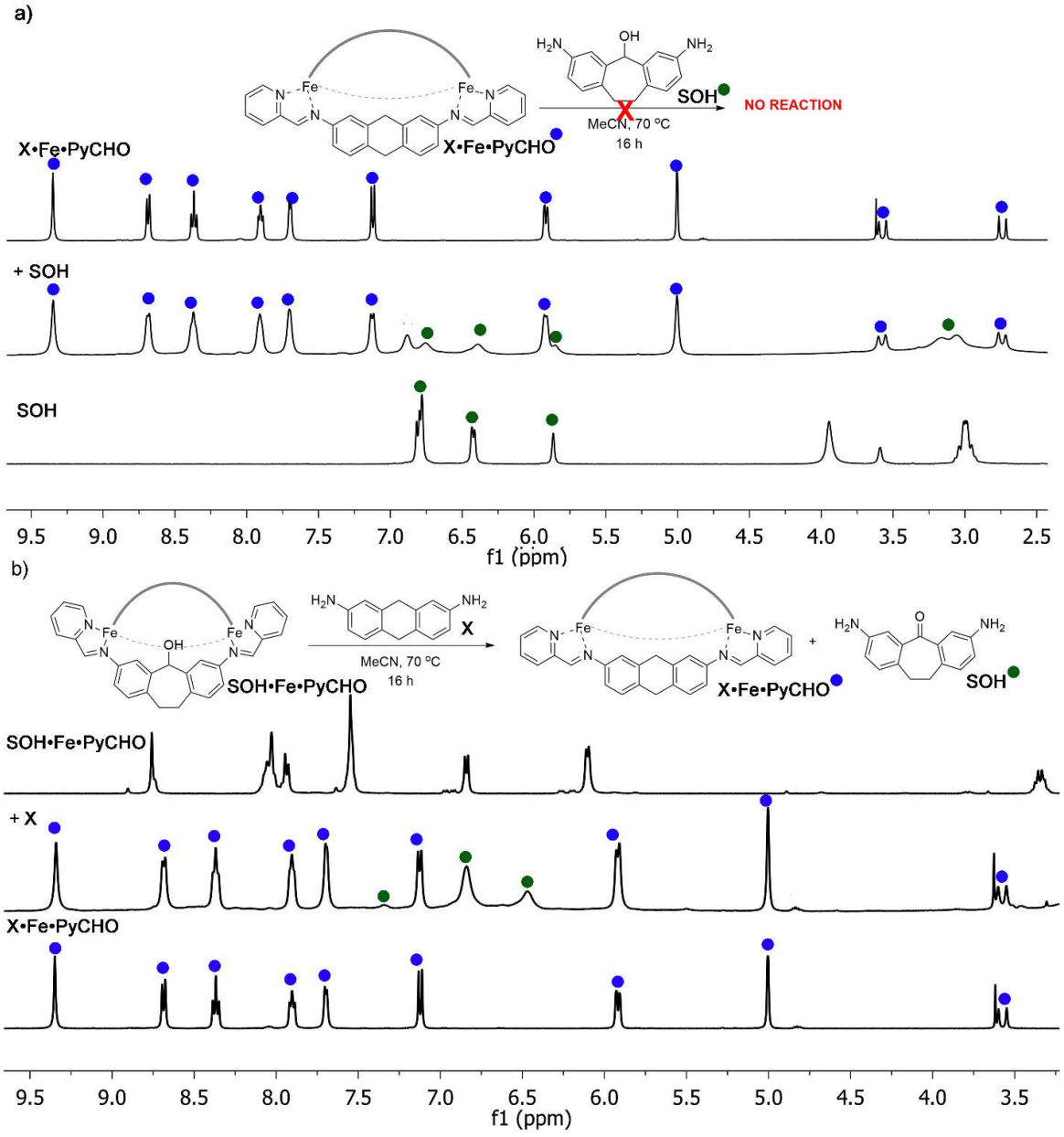

Figure 2.12: Variable self-sorting behavior in diamagnetic helicates. Displacement experiments with a) **X** with **SOH•Fe•MePyCHO**, and b) **X** with **SOH•Fe•PyCHO** (400 MHz, 298 K, CD_3CN).

The change in Fe coordination added uncertainty towards whether or not selective sorting would be possible between **SOH•Fe•MePyCHO**, and **X•Fe•MePyCHO**. Given that **SO** would not self-assemble with MePyCHO, it is evident that the relative stabilities of the complexes will change when the pyridyl group is altered. First, the relative favorability of **SO•Fe•PyCHO**, **SOH•Fe•PyCHO**, and **X•Fe•PyCHO** needed to be determined, as xanthene had not been previously tested for its sorting proclivities. Therefore diamine **X** (3 eq., 0.021 mmol) was added to a solution of **SOH•Fe•PyCHO** (1 eq., 0.007 mmol) and CD_3CN, and after heating at 77°C for 2 h complete displacement of **SOH** from **X•Fe•PyCHO** was observed, with only **X** remaining and no heterocomplex according to ^1H NMR (Figure 2.8d).The reverse process, adding **SOH** (3 eq., 0.021 mmol) to **X•Fe•PyCHO** (1 eq., 0.007 mmol) in CD_3CN solution, resulted in no reaction even after heating at reflux for 24 h (Figure 2.8f).

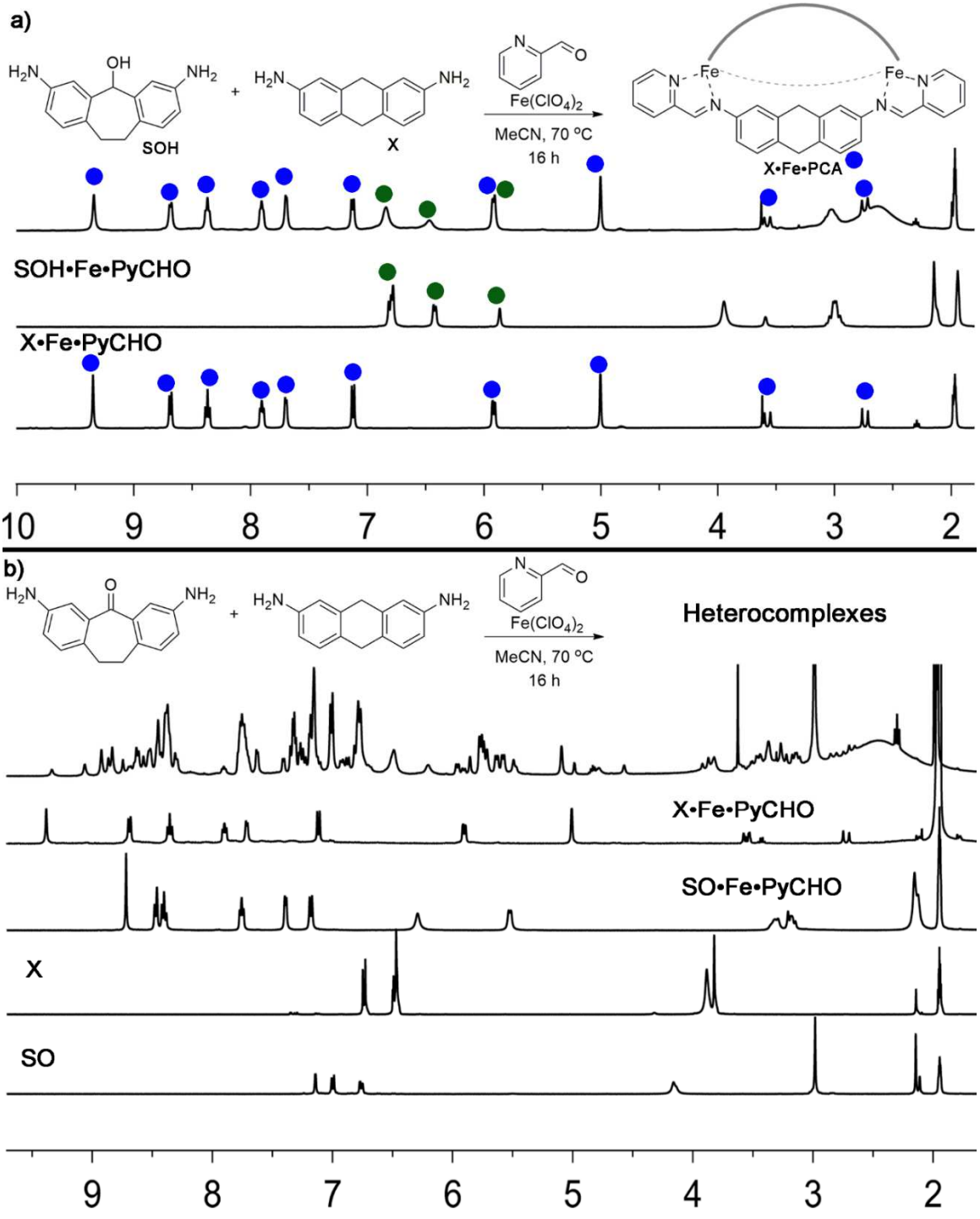

Figure 2.13: Competition experiment to determine favored cage of a) **SOH**, **X**, **Fe**, and **PyCHO**. Hetercomplexes formed upon the mixture of b) **SO**, **X**, **Fe**, and PyCHO (400 MHz, 298 K, CD_3CN).

Finally, combining diamines **X** (1 eq., 0.02 mmol) and **SOH** (1 eq., 0.02 mmol) in CD_3CN with PyCHO (2 eq., 0.04 mmol) and Fe(II) (0.066 eq., 0.013 mmol), showed the formation of only **X•Fe•PyCHO**, indicating that **X•Fe•PyCHO** is more stable than **SOH•Fe•PyCHO** (Figure 2.13). Interestingly, competition experiments between **SO•Fe•PyCHO** and **X•Fe•PyCHO** did not show self-sorting: mixtures of **SO•Fe•PyCHO**, **X•Fe•PyCHO**, and heterocomplexes were observed (Figure 2.13), indicating that there is little difference in favorability between **SO•Fe•PyCHO** and **X•Fe•PyCHO**.

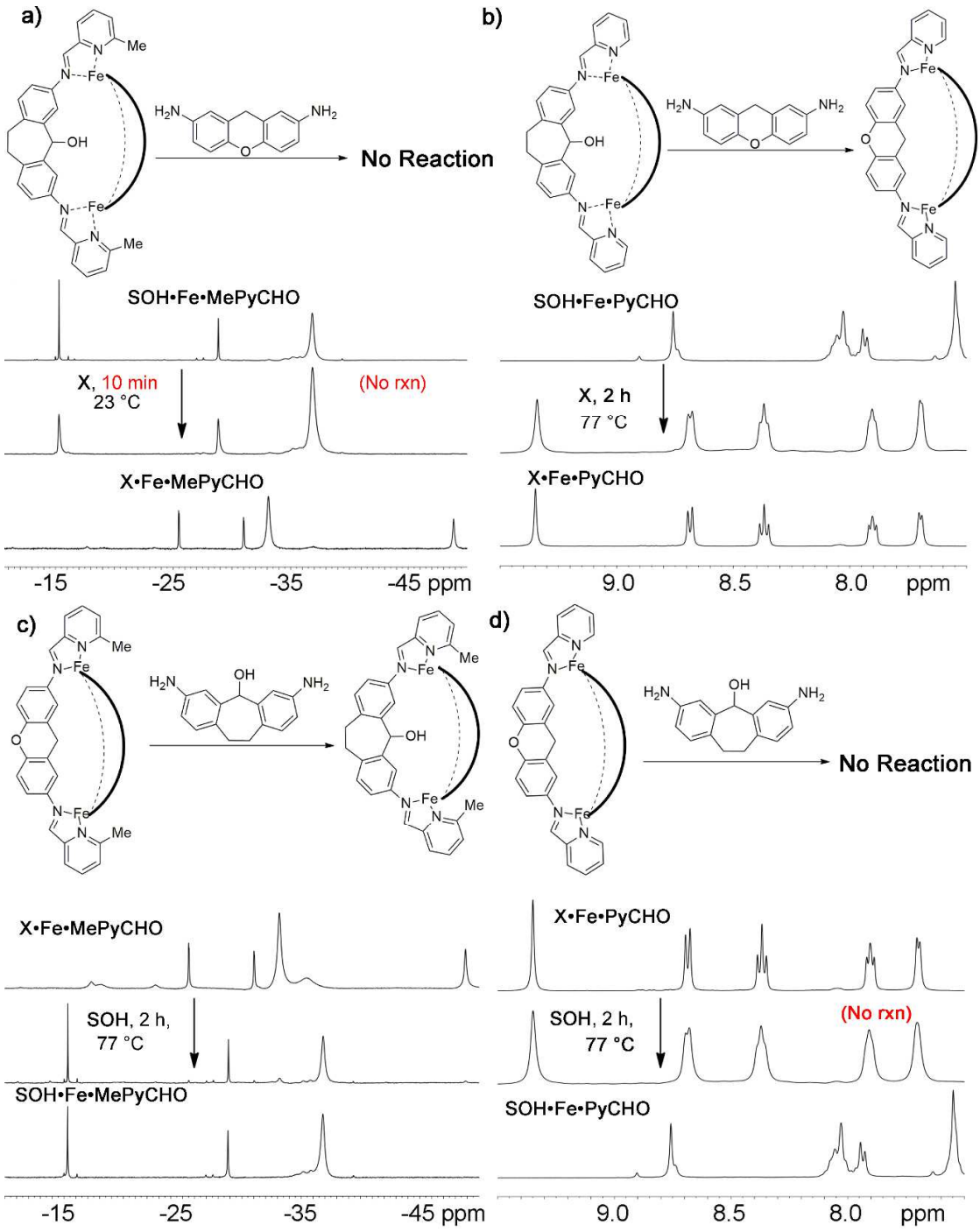

Figure 2.14: Selected regions of the ^{1}H NMR spectra of the reaction in CD_3CN at the noted temperature of a) **X** with **SOH•Fe•MePyCHO**; b) **X** with **SOH•Fe•PyCHO**; c) **SOH** with **X•Fe•MePyCHO**; and d) **SOH** with **X•Fe•PyCHO** (CD_3CN, 400 MHz, 298K). See Figure 6.6, Figure 6.42, and refs 3 and 4 for NMR peak assignment of cages **SOH•Fe•PyCHO** and **X•Fe•MePyCHO** (400 MHz, 298 K, CD_3CN).

Analogous component exchange experiments were performed to determine complex favorability of paramagnetic complexes. The **SOH** diamine (3 eq., 0.0039 mmol) was added to a solution of **X•Fe•MePyCHO** (1 eq., 0.012 mmol), displacement occurred rapidly within 10 min at room temperature showing only peaks for **SOH•Fe•MePyCHO** and displaced **X** ligand. The reverse process, adding **X** (3 eq, 0.0039) to a **SOH•Fe•MePyCHO** (1 eq, 0.012) solution, showed no reaction after 4 h at 77°C showing only **SOH•Fe•MePyCHO** and **X** diamine in the ^{1}H NMR spectrum. Since the suberol-based **SOH•Fe•PyCHO** cage complex is present after both sets of reactions, we can conclude that it is the most favorable complex, followed by **X•Fe•MePyCHO**, then **SO•Fe•MePyCHO**, which did not assemble. In summation, the order of stability of the high spin complexes suberol, suberone, and xanthene is reversed from that of their diamagnetic counterparts (Figure 2.15). Therefore, changing the pyridyl coordinator changes the relative order of favorability and factors that affect selectivity, but it does not preclude self-sorting. The most important factor is that the ligand core is able to accommodate the bulky MePyCHO groups around the Fe centers. Varying the terminal aldehyde also changes the transimination rate. Full equilibration of pyridyl-terminated helicates requires heating for multiple hours to affect full transimination, but the less strongly coordinating MePyCHO variants react in minutes at room temperature. High spin Fe-N bonds are longer and have a more distorted coordination environment, making paramagnetic complexes less stable than their diamagnetic counterparts.

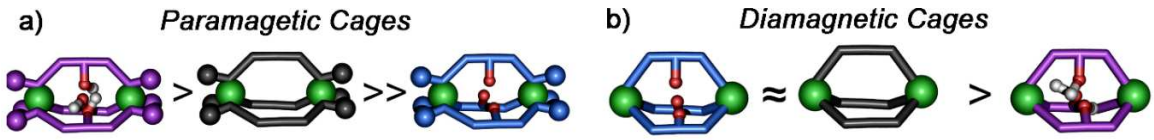

Figure 2.15: Variable self-sorting behavior in paramagnetic helicates. a) Order of favorability of **SO/SOH/X•Fe•PyCHO** and b) **SO/SOH/X•Fe•MePyCHO**.

2.9 Altering Spin State via Subcomponent Exchange

The notable stability differences between high spin **SOH•Fe•MePyCHO**, **X•Fe•MePyCHO**, and **FOH•Fe•MePyCHO** complexes and low spin **SOH•Fe•PyCHO**, **SO•FePyCHO**, **X•Fe•PyCHO**, and **FOH•Fe•MePyCHO** complexes introduce the possibility of interconverting the complexes, effectively "switching off" the paramagnetism.[7] Aldehyde exchange is possible in iminopyridine complexes by heating the complex with an excess of the new aldehyde and a small amount of water to aid in imine solvolysis.[1,7] In the case of our cage complexes, this means when paramagnetic **SOH•Fe•MePyCHO**, **X•Fe•MePyCHO**, and **FOH•Fe•MePyCHO** are combined with PyCHO, the reaction results in the formation of diamagnetic counterparts **SOH•Fe•MePyCHO**, **X•Fe•MePyCHO**, and **FOH•Fe•MePyCHO**. This particular reaction provides a window through which to view the mechanism of subcomponent exchange. As PyCHO switches out the MePyCHO, additional peaks are observed in the ^{1}H NMR spectra, which belong to the intermediates of the reaction and are able to be easily identified since paramagnetic complexes are more highly separated in the NMR spectrum than diamagnetic their diamagnetic counterparts. Aldehyde exchange for **SOH•Fe•MePyCHO** is shown in Figure 2.16. When PyCHO and water are added to **SOH•Fe•MePyCHO** in a CD_3CN solution and heated to 343 K, to observe diamagnetic

cage formation and loss of the intermediates. After 15 mins, the NMR changes from the symmetrical spectrum of **SOH•Fe•MePyCHO** to an unsymmetrical spectrum, where each peak in the paramagnetic region is converted multiple equivalents. During the exchange, 6 PyCHO molecules are added to **SOH•Fe•MePyCHO**, and as they are iteratively added intermediates can be seen in the ^{1}H NMR spectrum. If the complex has more MePyCHO "caps" than PyCHO in the system, it will retain paramagnetism with the dissymmetric **SOH•MePyCHO$_{6-x}$•PyCHO$_{x}$** intermediates able to be clearly observed. After 2 h the aldehyde exchange is completed and diamagnetic complex **SOH•Fe•PyCHO** can be isolated via precipitation and washing. The challenge when performing the same test with the Fe_4L_6 cages is that the ^{1}H NMR spectra of both **FOH•Fe•MePyCHO** and **FOH•Fe•PyCHO** are complicated, which made identifying exchange components quite challenging. Monitoring the reaction was not practical, but loss of paramagnetism does occur under the same conditions.

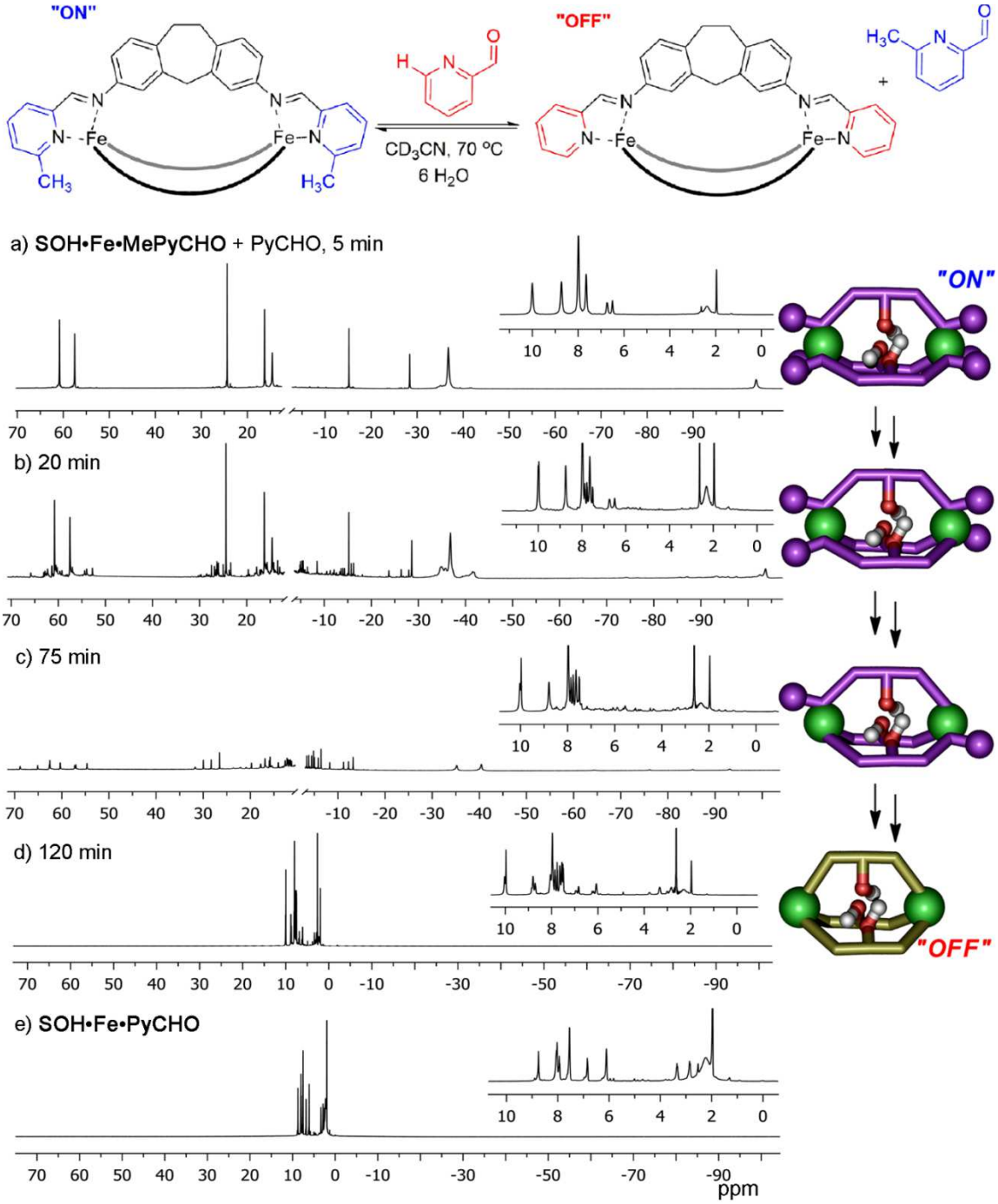

Figure 2.16: Spin state changes upon aldehyde interconversion. Wide range (paramagnetic) region of the ^{1}H NMR spectra with insets of diamagnetic region (0-10 ppm) of a) **SOH•Fe•MePyCHO**; and PyCHO, H_2O (6 eq.) , heat at 77°C for 5 min b) 20 min; c) 75 min; d) 120 min; e) independently synthesized **SOH•Fe•PyCHO** (400 MHz, 298 K, CD_3CN).

2.10 Conclusion

With this work, we have investigated varying component structure on the assembly properties of room temperature, high spin Fe(II)-iminopyridine self-assembled cages. By varying the steric bulk of the aldehyde component, we can favor the formation of high spin cages. From these studies we have learned that the self-assembly of high spin complexes with bulky aldehydes is highly sensitive to ligand rigidity and the coordination angle around high spin Fe(II). High spin Fe(II) assembly can only form with ligands that can accommodate a twisted octahedral geometry. The assembly of paramagnetic helicates is only possible if the ligand is flexible enough to twist around the Fe vertices. If the ligand is too rigid (e.g.: diamino-xanthene, -suberone, -suberenone) or the pyridyl aldehyde is excessively bulky (i.e.: BrPyCHO, QnCHO in certain cases), assembly fails. To form high spin cage complexes, added bulk must be properly matched with ligands that can either sufficiently bend and twist to accommodate the distorted Fe(II) octahedral geometry, or can access the less common *mer* configureuration at the metal center. The large ligand bend in suberol or the inclusion of *mer* coordination centers, like in **FOH•Fe•MePyCHO** allows the bulky aldehydes to pack around the Fe center, even for more rigid QnCHO. Self-assembly would fail to yield discrete complexation if the aldehyde was too bulky, or if the diamine was too rigid and inflexible. Successfully assembled high spin Fe_2L_3 *meso*-helicates and Fe_4L_6 cages could be synthesized in good yield and remain paramagnetic in the temperature window observable by ^{1}H NMR. High spin assemblies have been characterized by X-ray crystallographic and computational methods, showing longer N-Fe

bond distances and larger interligand N-Fe-N bond angles than their diamagnetic counterparts.

Structural changes of high spin complexes were found to have effects on stability, self-sorting, and subcomponent exchange rates compared to diamagnetic complexes. In diamagnetic iminopyridine cages, selective self-sorting is controlled by ligand deformation energy, however paramagnetic narcissistic self-sorting is controlled by the coordination environment around the metal center. Ligands with high levels of flexibility are better suited for paramagnetic *meso*-helicate assembly, which results in inverted ligand selectivity with respect to the diamagnetic counterparts. Transamination rates of paramagnetic cages are highly accelerated, and via aldehyde exchange they can be smoothly interconverted to their diamagnetic counterparts. Aldehyde exchange intermediates can be visualized in situ by NMR analysis and demonstrate that paramagnetism can be conferred on the assembly by the presence of only a small number of bulky ligand components.

2.11 References

1. Wiley, C. A.; Holloway, L. R.; Miller, T. F.; Lyon, Y.; Julian, R. R.; Hooley, R. J. "Electronic Effects on Narcissistic Self-Sorting in Multicomponent Self-Assembly of Fe-Iminopyridine Meso-Helicates." *Inorg. Chem*. **2016**, *55*, 9805–9815.

2. Rodríguez-Jiménez, S.; Yang, M.; Stewart, I.; Garden, A. L.; Brooker, S. "A Simple Method of Predicting Spin State in Solution." *J. Am. Chem. Soc.* **2017**, *139*, 18392–18396.

3. Young, M. C.; Johnson, A. M.; Hooley, R. J. "Self-Promoted Post-Synthetic Modification of Metal-Ligand M_2L_3 Mesocates." *Chem. Commun*. **2014**, *50*, 1378–1380.

4. Holloway, L. R.; Young, M. C.; Beran, G. J. O.; Hooley, R. J. "High Fidelity Sorting of Remarkably Similar Components via Metal-Mediated Assembly." *Chem. Sci.* **2015**, *6*, 4801–4806.

5. Holloway, L. R.; Bogie, P. M.; Lyon, Y.; Julian, R. R.; Hooley, R. J. "Stereoselective Postassembly CH Oxidation of Self-Assembled Metal-Ligand Cage Complexes." *Inorg. Chem*. **2017**, *56*, 11435–11442.

6. Tidmarsh, I. S.; Taylor, B. F.; Hardie, M. J.; Russo, L.; Clegg, W.; Ward, M. D. "Further Investigations into Tetrahedral M_4L_6 Cage Complexes Containing Guest Anions: New Structures and NMR Spectroscopic Studies." *New J. Chem*. **2009**, *33*, 366–375.

7. McConnell, A. J.; Aitchison, C. M.; Grommet, A. B.; Nitschke, J. R. "Subcomponent Exchange Transforms an FeII4L4 Cage from High- to Low-Spin, Switching Guest Release in a Two-Cage System." *J. Am. Chem. Soc*. **2017**, *139*, 6294–6297.

8. Meng, W.; Ronson, T. K.; Nitschke, J. R. "Symmetry Breaking in Self-Assembled M_4L_6 Cage Complexes." *Proc. Natl. Acad. Sci. U. S. A.* **2013**, *110*, 10531–10535.

9. Meng, W.; Clegg, J. K.; Thoburn, J. D.; Nitschke, J. R. "Controlling the Transmission of Stereochemical Information through Space in Terphenyl-Edged Fe_4L_6 Cages." *J. Am. Chem. Soc.* **2011**, *133*, 13652–13660.

10. Young, M. C.; Holloway, L. R.; Johnson, A. M.; Hooley, R. J. "A Supramolecular Sorting Hat: Stereocontrol in Metal-Ligand Self-Assembly by Complementary Hydrogen Bonding." *Angew. Chemie Int. Ed.* **2014**, *53*, 9832–9836.

11. Evans, D. F. “The Determination of the Paramagnetic Susceptibility of Substances in Solution by Nuclear Magnetic Resonance.” *J. Chem. Soc*. **1959**, *81*, 2003–2005.

12. Löliger, J.; Scheffold, R. “Paramagnetic Moment Measurements by NMR: A Micro Technique.” *J. Chem. Educ.* **1972**, *49,* 646–647.

13. Piguet, C. Paramagnetic Susceptibility by NMR: “The “Solvent Correction” Removed for Large Paramagnetic Molecules.” *J. Chem. Educ*. **1997**, *74*, 815–816.

14. Bain, G. A.; Berry, J. F. “Diamagnetic Corrections and Pascal’s Constants.” *J. Chem. Educ.* **2008**, *85*, 532–536.

Chapter 3 Synthesis of Novel Paramagnetic High Spin Fe(II) Cage Complexes

3.1 Introduction

The iminopyridine scaffold has been used to create many cages with a wide range of functional properties. By implementing quinoline carboxaldehyde (**QnCHO**) and 6-methyl-2-formyl pyridine (**MePyCHO**) into the iminopyridine scaffold we were able to create paramagnetic cage complexes. Whereas unhindered **PyCHO** formed low spin Fe(II) cage complexes, **QnCHO** and **MePyCHO** formed high spin Fe(II) cage complexes because of the additional steric bulk surrounding the metal center. While the iminopyridine scaffold has been and continues to be investigated, its success has meant other termini have been largely ignored. We would like to explore the application of other heterocyclic compounds for cage termini and investigate their properties.

3.2 Synthesis of New Cage Complexes

Initially, we continued to explore complexes with the **MePyCHO** terminus, examining complex formation with a flexible ditopic ligand and a tritopic ligand. Tritopic ligands are ligands that attach to three separate metals and can be used to create M_4L_4 cages. Diaminodiphenylmethane (**DPM**) is a V-shaped ligand which has no central ring and makes very energetically favorable M_2L_3 helicate complexes.[1] When **DPM** was combined with $Fe(NTf_2)_2$ and **MePyCHO** resulting in cage **DPM•Fe•MePyCHO**. The ^1H NMR spectrum of **DPM•Fe•MePyCHO** revealed a clean spectrum of a single discrete cage complex. Using triamines such as tris(aminophenyl) amine (**APA**) force a tetrahedral geometry on the cage complex.[2] This kind of ligand would be on the face of the complex

rather than the edge when combined as 1 eq. **APA**, 1 eq. $Fe(NTf_2)_2$, and 3 eq. **MePyCHO** in acetonitrile at reflux. The ^1H NMR spectrum confirms only one isomer is formed.

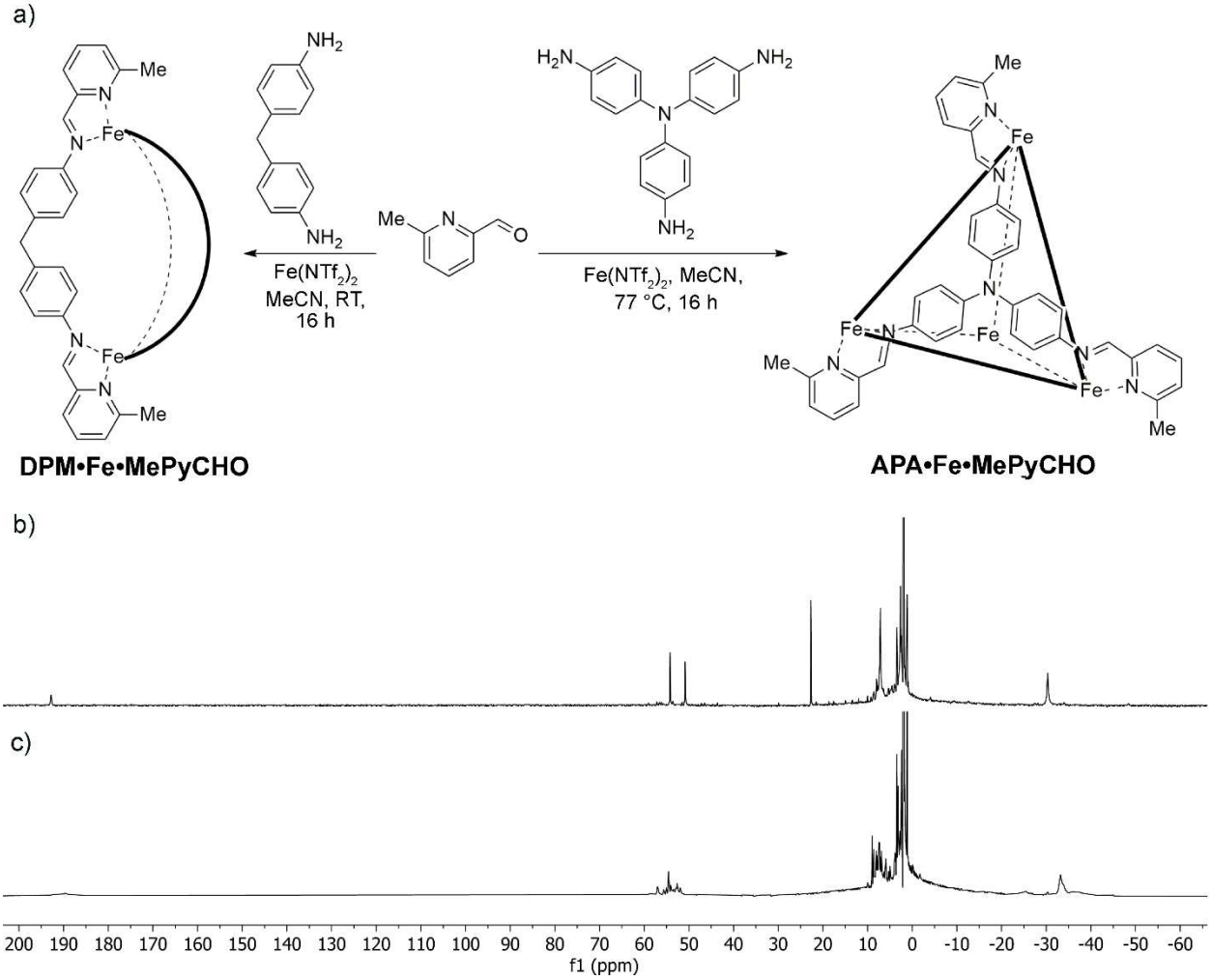

Figure 3.1: a) The Synthetic scheme for cage complexes **DPM•Fe•MePyCHO** and **APA•Fe•MePyCHO**, and b) the ^1H NMR spectrum for complex **DPM•Fe•MePyCHO** and c) complex **APA•Fe•MePyCHO** (400 MHz, 298 K, CD_3CN).

Cages formed with **MePyCHO** decomposed in solution within minutes regardless of the amine used. This showed a clear lack of stability compared to diamagnetic cages, which can be stable in solutions for months or greater. We became interested in pursuing alternative termini that would be capable of creating more stable paramagnetic complexes

and are capable of forming cages through imine condensation. Formyl imidazoles have been known to create high spin Fe(II) complexes in both mononuclear complexes[3] and metal-organic cages[4] because they have a weaker ligand field strength.[5] As such, we tested various formyl imidazoles as the second generation of paramagnetic cages to determine if using imidazole instead of **MePyCHO** would create a more stable complex. Three formyl imidazoles were chosen to test complex synthesis: **4ImCHO**, **2ImCHO**, and **MeImCHO**. The three imidazoles allow testing of slightly different bite angles and electronics.

Figure 3.2: Structures of the imidazoles tested for cage formation.

The **DPM** diamine was chosen to test imidazole coordinating groups because it can create the most energetically favorable helicate, giving it the highest likelihood for success. **DPM** and $Fe(NTf_2)_2$ were combined in acetonitrile with either **2ImCHO**, **4ImCHO**, or **MeImCHO**. These experiments yielded paramagnetic M_2L_3 complexes **DPM•Fe•2ImCHO** and **DPM•Fe•4ImCHO**; **MeImCHO** was unable to complex with **DPM**. The ^{1}H NMR spectrum of the **MeImCHO** reaction mixtures only showed peaks that correlated to starting materials. Complexes **DPM•Fe•2ImCHO** and **DPM•Fe•4ImCHO** confirmed that formyl imidazoles could be used as termini to form novel paramagnetic complexes. **APA** was already known to complex with **MeImCHO**,[4] and when combined with $Fe(NTf_2)_2$ and either **2ImCHO** or **4ImCHO** open to atmospheric conditions resulted in paramagnetic M_4L_4 cages **APA•Fe•2ImCHO** or **APA•Fe•4ImCHO**, respectively.

Combination with **MePyCHO** under identical conditions resulted in no reaction, requiring inert atmosphere to react. The ^{1}H NMR spectra of the imidazole cages all showed peaks over a broad range (200 to - 10 ppm) and the relative number and size of peaks present in the spectra indicated only one isomer formed for each possible product. Additionally, the imidazole cages proved to be more stable than those capped with **MePyCHO** showing no evidence of degradation in solution via monitoring by ^{1}H NMR or MS.

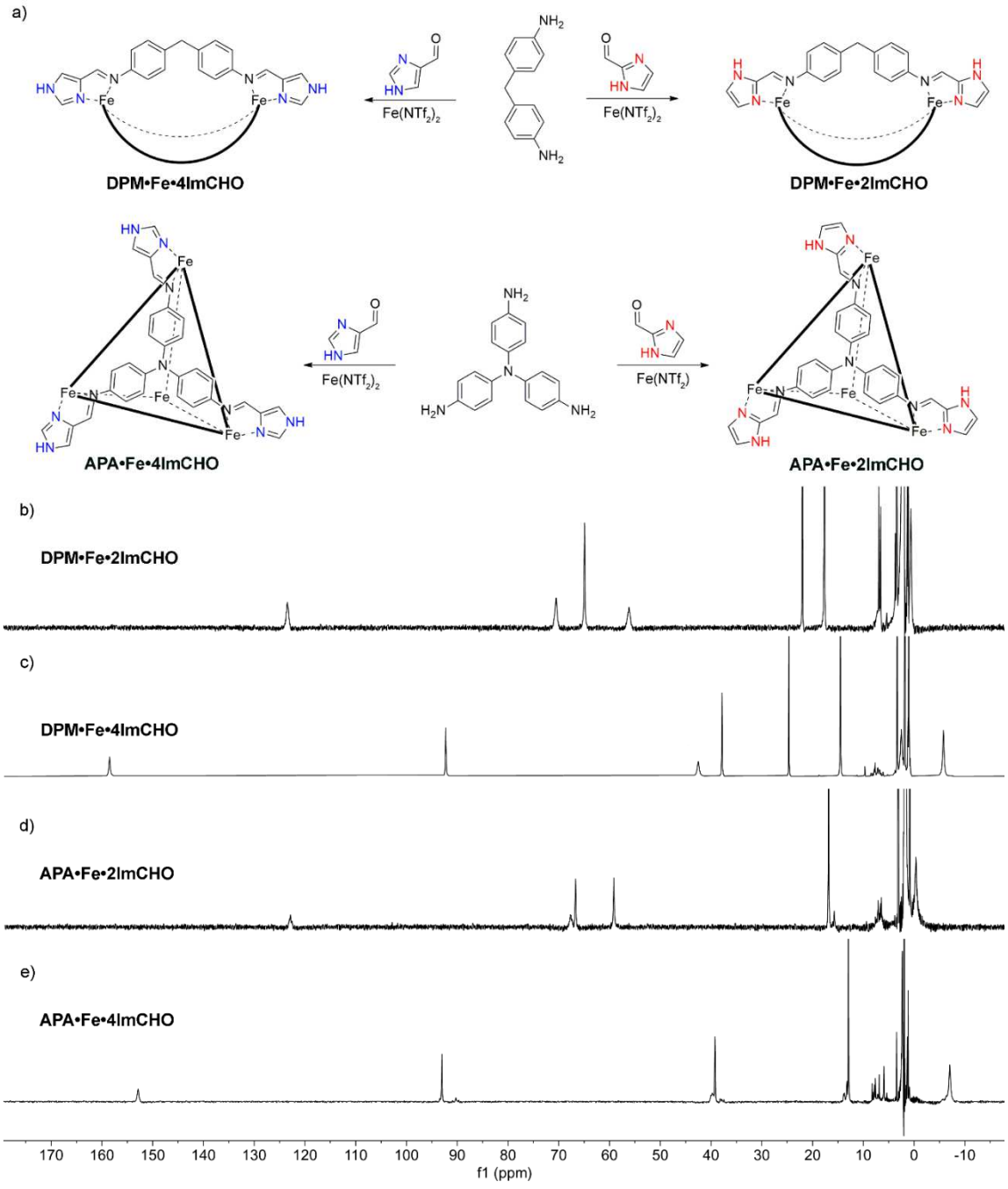

Figure 3.3: a) Synthetic scheme for the formation of cages **DPM•Fe•2ImCHO, DPM•Fe•4ImCHO**, **APA•Fe•2ImCHO** and **APA•Fe•4ImCHO**, and their respective ^{1}H NMR spectra (b-e) (600 MHz, 298 K, CD_3CN).

Previous work with the triamine **APA** has been used to make stable and discrete complexes with $Fe(ClO_4)_2$ and **PyCHO** of both M_2L_3 and M_4L_4 stoichiometries.[6] The formation of the M_4L_4 complex included formation of an M_2L_3 intermediate. The helicate M_2L_3 cage was able to be formed as a discrete assembly by kinetically trapping the M_2L_3 intermediate with exposed amines by reacting for 2 h at 50°C.[6] Since high spin paramagnetic Fe(II) cages have a higher energy level associated with the Fe(II) centers, it was unclear how the weaker metal coordination from using **4ImCHO** would affect the stability of the M_2L_3 intermediate. Regardless of component ratio used, either 1 eq. **APA**, 2 eq. **4ImCHO**, 0.66 eq. $Fe(NTf_2)_2$ (M_2L_3 ratio) or 1 eq. **APA**, 3 eq. **4ImCHO**, 1 eq. $Fe(NTf_2)_2$ (M_4L_4 ratio), the product resulted in only the M_4L_4 cage being present. When the 1:2:0.66 eq. ratio was tested and analyzed over time at room temperature (at 50°C the reaction mixture formed the M_4L_4 complex too quickly), peaks representative of the M_2L_3 appeared and equilibrated to form the M_4L_4 complex. This is determined by the disappearance of the amine peak at 75 ppm and after 6 days of heating at 75°C the spectrum changed to match the spectrum of pre-formed M_4L_4 **APA•Fe•4ImCHO**.

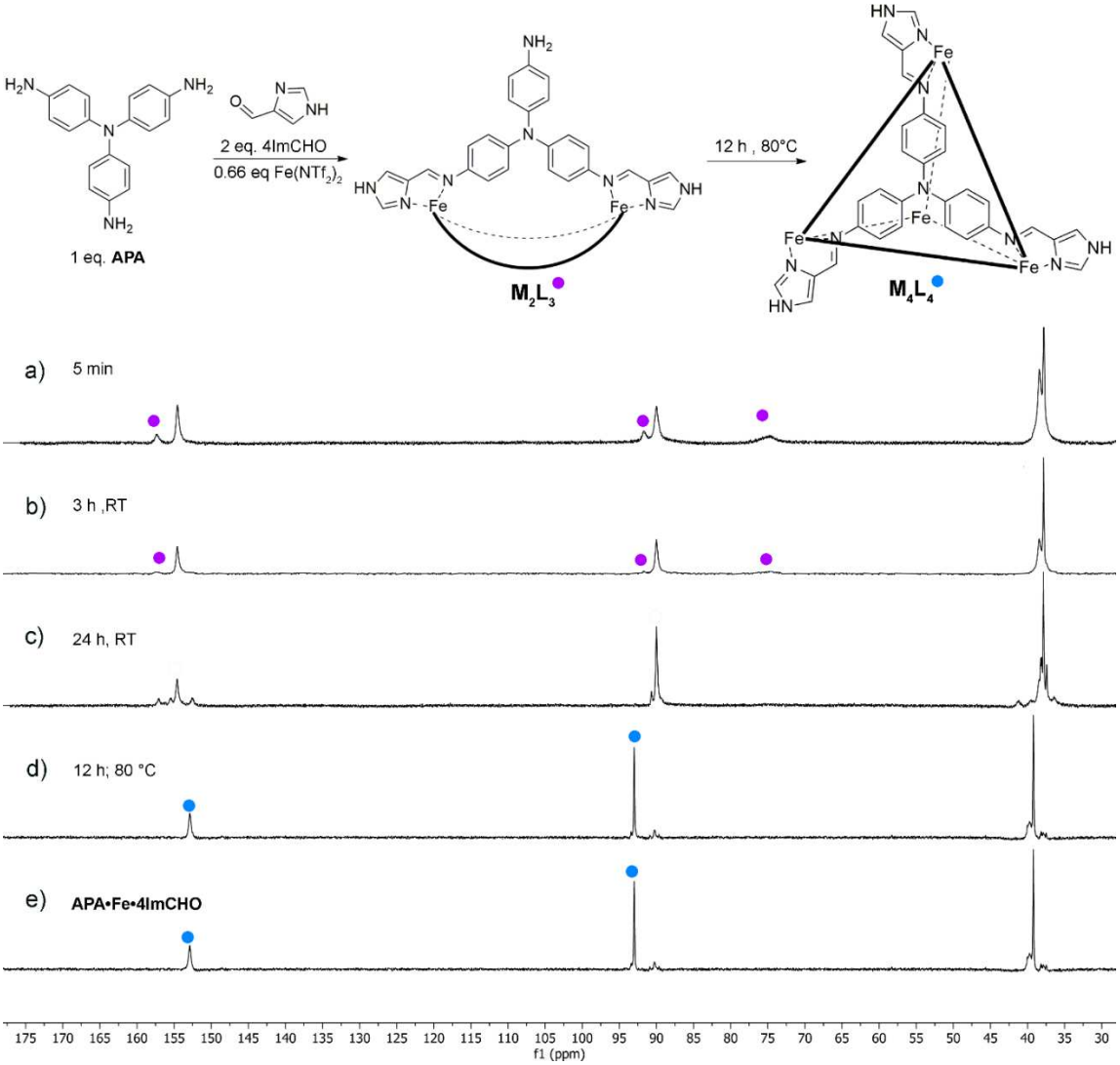

Figure 3.4: The combination of 1 eq. **APA**, 2 eq. **4ImCHO**, 0.66 eq $Fe(NTf_2)_2$ heated at reflux at time a) 5 minutes, b) 1 h, c) 3 h, d) 6 days. and e) preformed cage **APA•Fe•4ImCHO** (400 MHz, 298 K, CD_3CN).

3.3 Self-Sorting and Component Favorability

Combining two or more versions of the same component type into a self-assembled cage gives two possible results: narcissistic sorting or social (integrative) sorting.[7] Narcissistic self-sorting occurs when combination of the components forms only homo-

selective complexes (all ligands are the same) and multiple homocomplexes can be formed out of the reaction mixture.[8] Alternatively, social sorting is the incorporation of many ligands to form a single assembly. Testing of component favorability and how to control self-sorting behavior is a well-researched topic and continues to be relevant when examining new complex scaffolds to determine relative energetic favorability.

3.3.1 Aldehyde Favorability

With formyl pyridine, the aldehyde is limited to placement at the 2-position in order to create a favorable bidentate ligand upon imine formation. Imidazole has two positions that can accommodate the favorable imino-imidazole coordination. Both **2ImCHO** and **4ImCHO** can make clean, discrete imino-imidazole complexes with only one isomer. Between **2ImCHO** and **4ImCHO** it is not obvious if there will be preference for the incorporation of one formyl imidazole over the other. Small changes in the ligand can have drastic effects on the outcomes of self-assembly.[9] We wanted to determine we could have selective incorporation between both of these components, and whether it is possible to tease out favorability between the formyl imidazoles or if combining the two would result in social sorting.

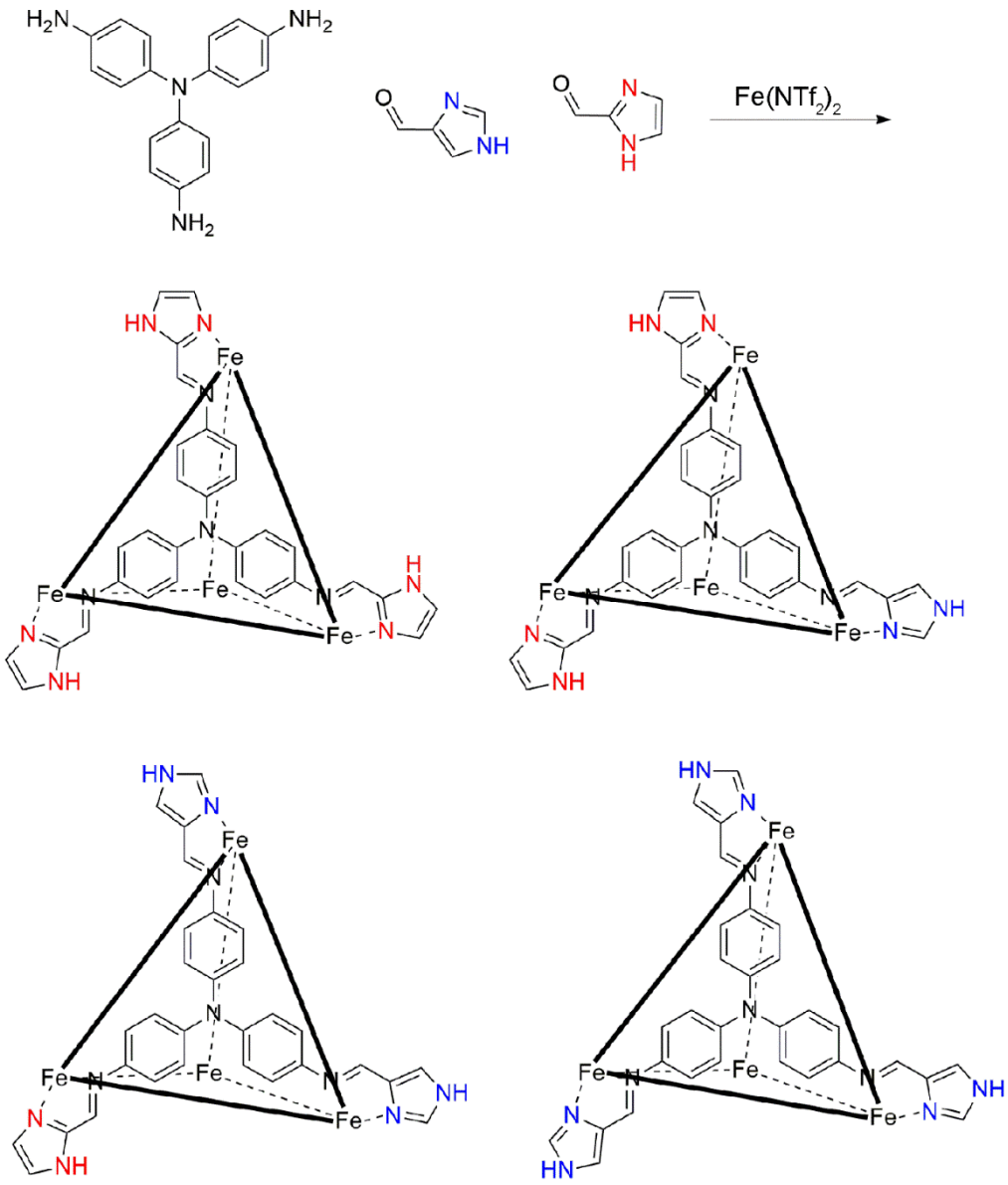

Figure 3.5: Possible ligands for **APA** cage using both **2ImCHO** and **4ImCHO**.

Testing was performed two ways: either each component was combined during initial reactivity or a pre-formed complex was combined in solution with the other aldehyde. These studies relied heavily on NMR, as MS would be unable to discern any difference between the different isomeric complexes as they have the same mass. For these

experiments, **APA** was chosen to be the amine core since it has a larger cavity size as an M_4L_4 than **DPM•Fe•2ImCHO**, for example, and the M_4L_4 complex may be used for sensing experiments later. The ^{1}H NMR spectra of **APA•Fe•2ImCHO** and **APA•Fe•4ImCHO** are visibly distinct from each other, especially peaks in the highly shifted region, which should correspond to protons on the imidazole which are closer in proximity to the Fe(II) centers. The **APA•Fe•4ImCHO** cage has a wider range, with the most downfield proton being the imine proton due to proximity of the metal center and the peak is broad, most likely due to deuterium exchange. The proton at the 2-position is deshielded and therefore shifted more downfield to 92 ppm than the proton at the 3-position which shows at 39 ppm, and the N-H amine proton is shifted to -7 ppm. The furthest downfield shifted proton of cage **APA•Fe•2ImCHO** will also be the imine proton due to proximity to the metal. The peaks at 67 ppm and 59 ppm of the spectra correlate to the C-H protons of **2ImCHO** based on height, shape, and shift, and the broad peak at 68 ppm is the NH peak. (**Figure 3.6**). When 1 eq, **APA**, 1 eq. $Fe(NTf_2)_2$, 3 eq. **2ImCHO**, and 3 eq. **4ImCHO** were combined and reacted at room temperature for 12 h the result shows peaks indicative of **APA•Fe•2ImCHO** and **APA•Fe•4ImCHO** present in solution and a few peaks that correlated to neither cage, indicating possible heterocomplex. The product of the reaction seemed to favor synthesis of complexes including **4ImCHO**. We were interested in determining if varying the concentrations of **2ImCHO** and **4ImCHO** in the reaction solution could result in the formation with more **2ImCHO** incorporated. The combination of various ratios of **4ImCHO** to **2ImCHO** with 1 eq. **APA** and 1 eq.

$Fe(NTf_2)_2$ show **4ImCHO** continuing to be the preferred aldehyde, and **2ImCHO** only being incorporated in majority if there is an insufficient amount of aldehyde in solution.

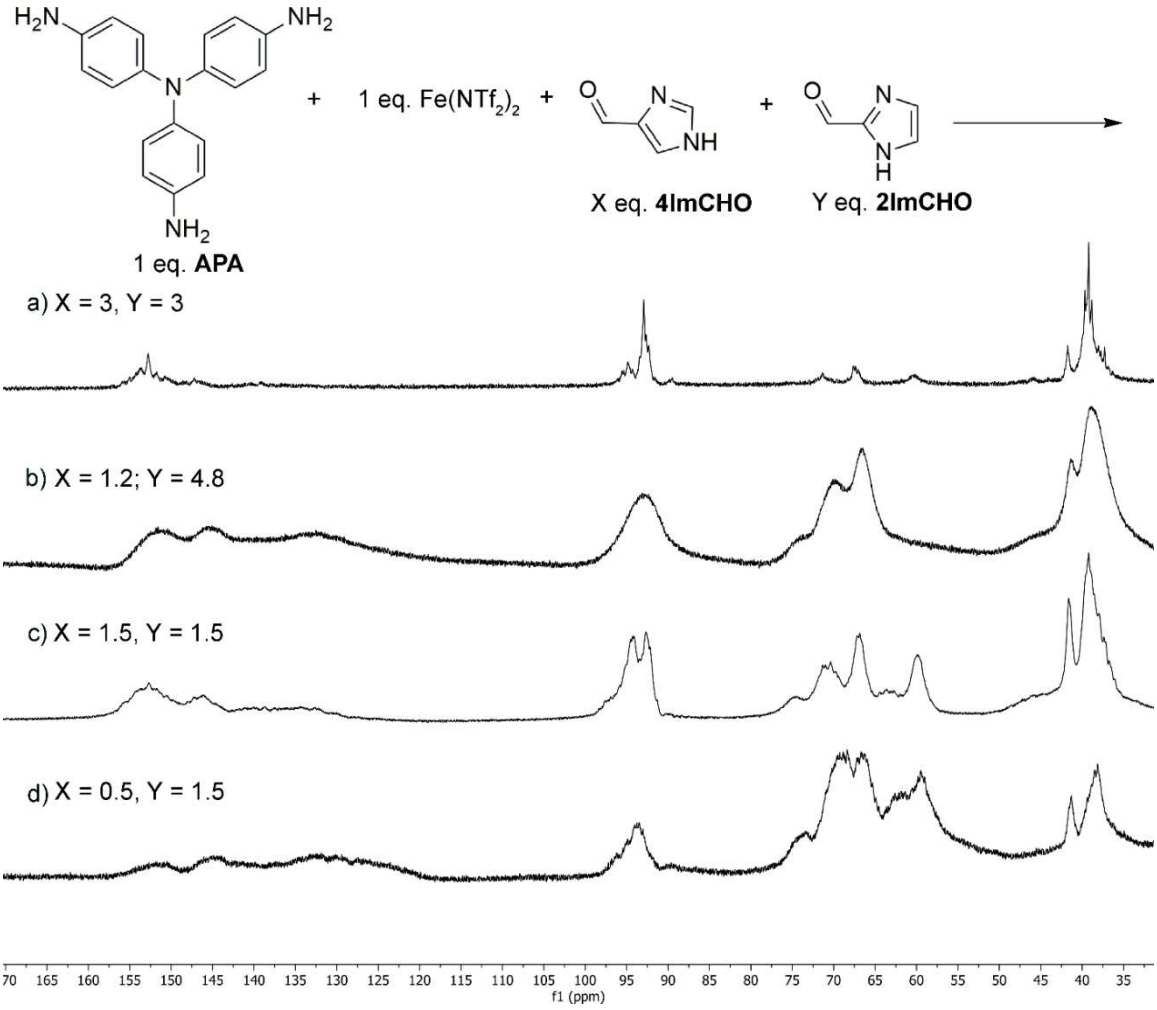

Figure 3.6: Varying ratios of **4ImCHO**:**2ImCHO** a) 3:3, b) 1.2:4.8, c) 1.5:1.5, and d) 0.5:1.5 (400 MHz, 298 K, CD_3CN).

Since heterocomplex formation is evident from the ^1H NMR spectra, component exchange with preformed cages was attempted. Component exchange with preformed cages is used to analyze how susceptible cages are to exchange and whether products would differ based on order of addition. Cage complex **APA•Fe•2ImCHO** and 12 eq. of **4ImCHO** were combined in acetonitrile and brought to reflux. The reaction was observed

via ^{1}H NMR over two days to monitor changes. After two days, the reaction mixture showed the presence of paramagnetic structures incorporating both **2ImCHO** and **4ImCHO**. The ^{1}H NMR spectrum revealed a result similar to the ^{1}H NMR spectrum of individual component addition reaction reflecting position and relative ratio. However, when **2ImCHO** is added to **APA•Fe•4ImCHO** the peaks corresponding complexes incorporating **2ImCHO** appear at a much smaller ratio than in either of the other cases. When the reaction was repeated the results were consistent, displaying a low amount of incorporation of **2ImCHO** into the system. Both displacement tests and the combination reaction all show similar spectra favoring formation of complex **APA•Fe•4ImCHO**. This seemed to indicate that once formed, paramagnetic cage **APA•Fe•4ImCHO** is slightly more stable and less susceptible to component exchange than compounds involving **2ImCHO**.

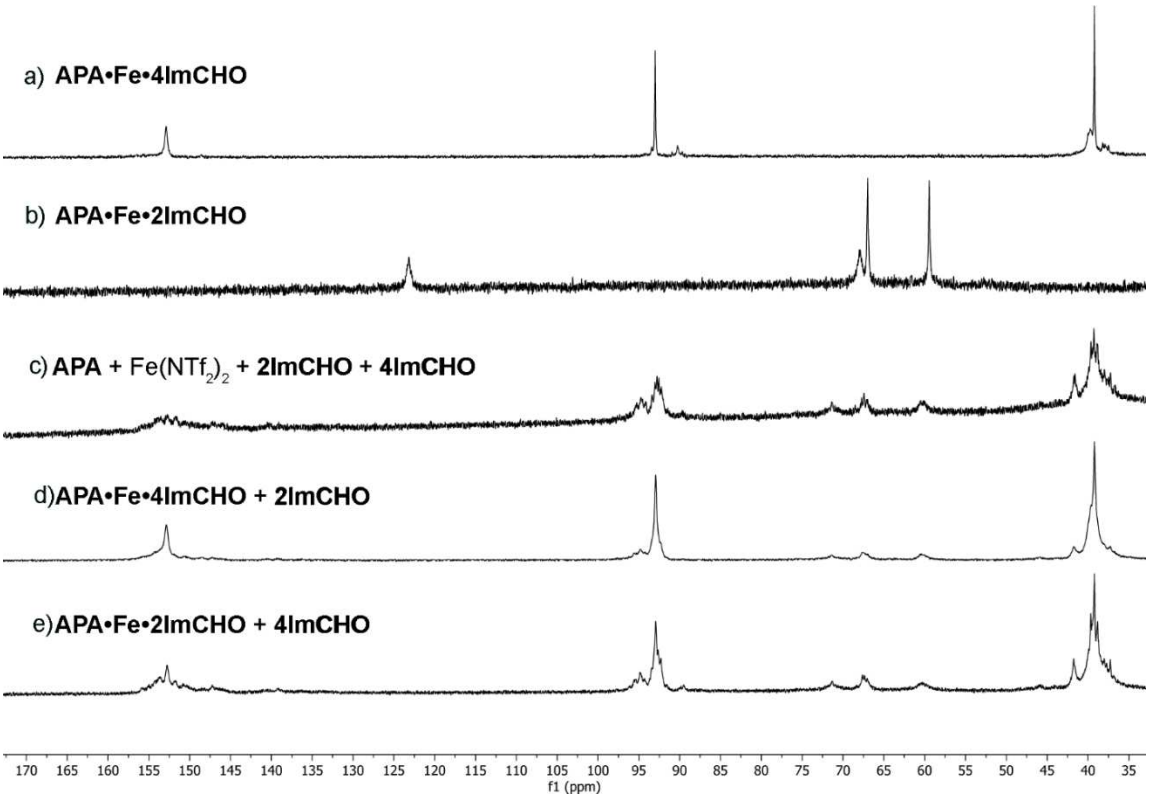

Figure 3.7: a) **APA•Fe•2ImCHO**, b) **APA•Fe•4ImCHO**, c) Combination of 1 eq. APA, 1 eq. $Fe(NTf_2)_2$, 3 eq. **2ImCHO**, and 3 eq. **4ImCHO**, d) 1eq. **APA•Fe•2ImCHO** cage and 12 eq. **4ImCHO**, e) 1 eq. **APA•Fe•4ImCHO** cage and 12 eq. **2ImCHO** (400 MHz, 298 K, CD_3CN).

3.3.2 Amine Favorability

The properties of iminopyridyl cages which allowed reversibility and amine switching to occur should be relevant for iminoimidazole cages as well. We wanted to confirm that amine exchange is still possible and can be used to transfer from one discrete complex into another with imidazole termini. Ideally, the first test would be from a cage with one stoichiometry to another with the same stoichiometry, so that the component ratio would remain the same. Cage **X•Fe•4ImCHO** was synthesized to test the hypothesis, and an ^1H

NMR spectrum of cage **X•Fe•4ImCHO** showed a discrete complex. The spectrum also validated that peaks between 160-38 ppm correspond to the protons from **4ImCHO**.

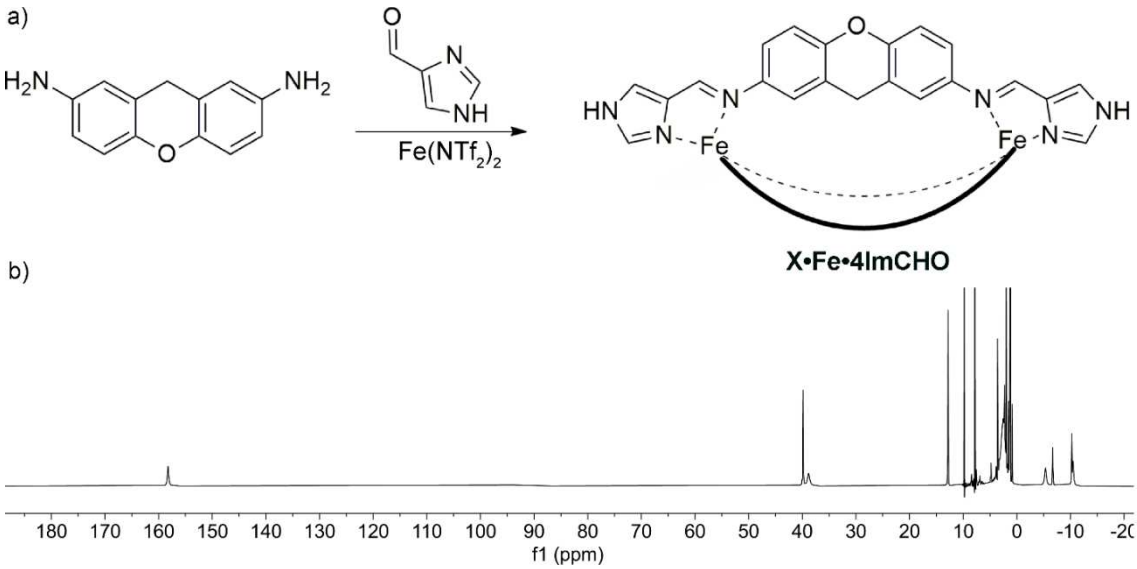

Figure 3.8: a) Synthesis of cage **X•Fe•4ImCHO** and b) the ^{1}H NMR spectrum (400 MHz, 298 K, CD_3CN).

Combination of **X**, **DPM**, $Fe(NTf_2)_2$, and **4ImCHO** after heating at reflux for 12 h resulted in a mixture of products including the formation of heterocomplexes. Heterocomplexes occur when ligands have similar coordinating angles. Analysis of NMR data alone makes it unclear if the peaks seen demonstrate social sorting or statistical mixture. Social sorting results in one favorable heterocomplex being formed, opposed to a statistical mixture which has no control for organization of components. Some peaks have the same shifts as those of cage **X•Fe•4ImCHO**, however there are additional sharp peaks that do not correlate to either complex. Diamine **DPM** was added to cage **X•Fe•4ImCHO** for 12 h resulted in a very similar spectrum to the combination of all components indicating a new complex formed rather than trapped intermediates. The three peaks at 94 ppm had different height ratios, but all peaks showed at the same shifts, indicating favorable

heterocomplex formation. The ESI-MS spectrum of this reaction presented peaks matching to both **DPM•Fe•4ImCHO** and **$(DPM)_2$X•Fe•4ImCHO** (Figure 6.55). The reverse reaction, combining cage **DPM•Fe•4ImCHO** and **X**, shows again a very similar ^{1}H NMR spectrum with the only outlier being one very broad peak at 94 ppm, instead of three sharp peaks. Together these results indicate that **DPM•Fe•4ImCHO** and **$(DPM)_2$X•Fe•4ImCHO** is the most favorable outcome from the combination of these components and can occur regardless of order of addition.

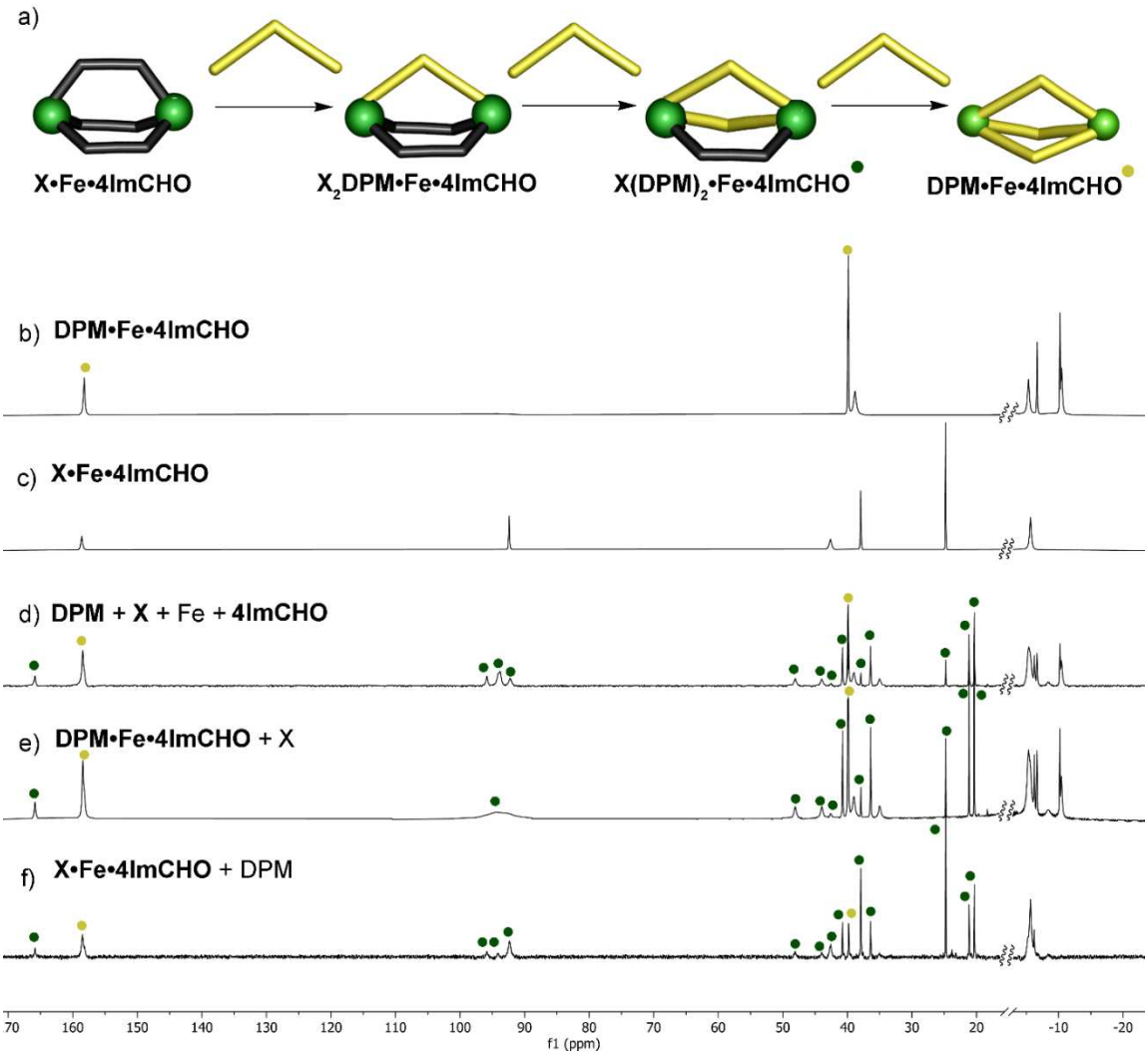

Figure 3.9: a) Cartoon of ligand exchange adding **DPM** to cage **X•Fe•4ImCHO**, b) **DPM•Fe•4ImCHO** cage, c) **X•Fe•4ImCHO** cage, d) the combination of **DPM**, **X**, **Fe(NTf$_2$)$_2$**, and **4ImCHO**, e) 1 eq. **DPM•Fe•4ImCHO** cage and 3 eq. **X**, and f) 1 eq. **X•Fe•4ImCHO** cage and 3 eq. **DPM** (400 MHz, 298 K, CD_3CN).

A second amine exchange was attempted with amines **DPM** and **APA**. Their cages have different stoichiometries when using the **4ImCHO** aldehyde cap. This study aimed to determine the most energetically favorable complex with a secondary goal to see if the **APA** ligand could be forced into an M_2L_3 configuration or if it would only form M_4L_4 complexes. Peaks corresponding to the imine and imidazole ring in **DPM•Fe•4ImCHO**

and **APA•Fe•4ImCHO** show at approximately the same shifts, but when the two amines are combined either through competition (**APA**, **DPM**, $Fe(NTf_2)_2$, and **4ImCHO** all combined at the same time) or displacement (1 eq. **DPM•Fe•4ImCHO** and 4 eq. **APA** or 1 eq.**APA•Fe•4ImCHO** and 4 eq. **DPM**) reactions, multiple peaks become present and do not go away after continued reaction. The additional peaks and the very broad peak at 75 ppm suggest that M_2L_3 heterocomplexes have formed in solution. The heterocomplex formed is the most favorable result as the ^1H NMR spectrum is the same in cases of the competition and both displacement reactions.

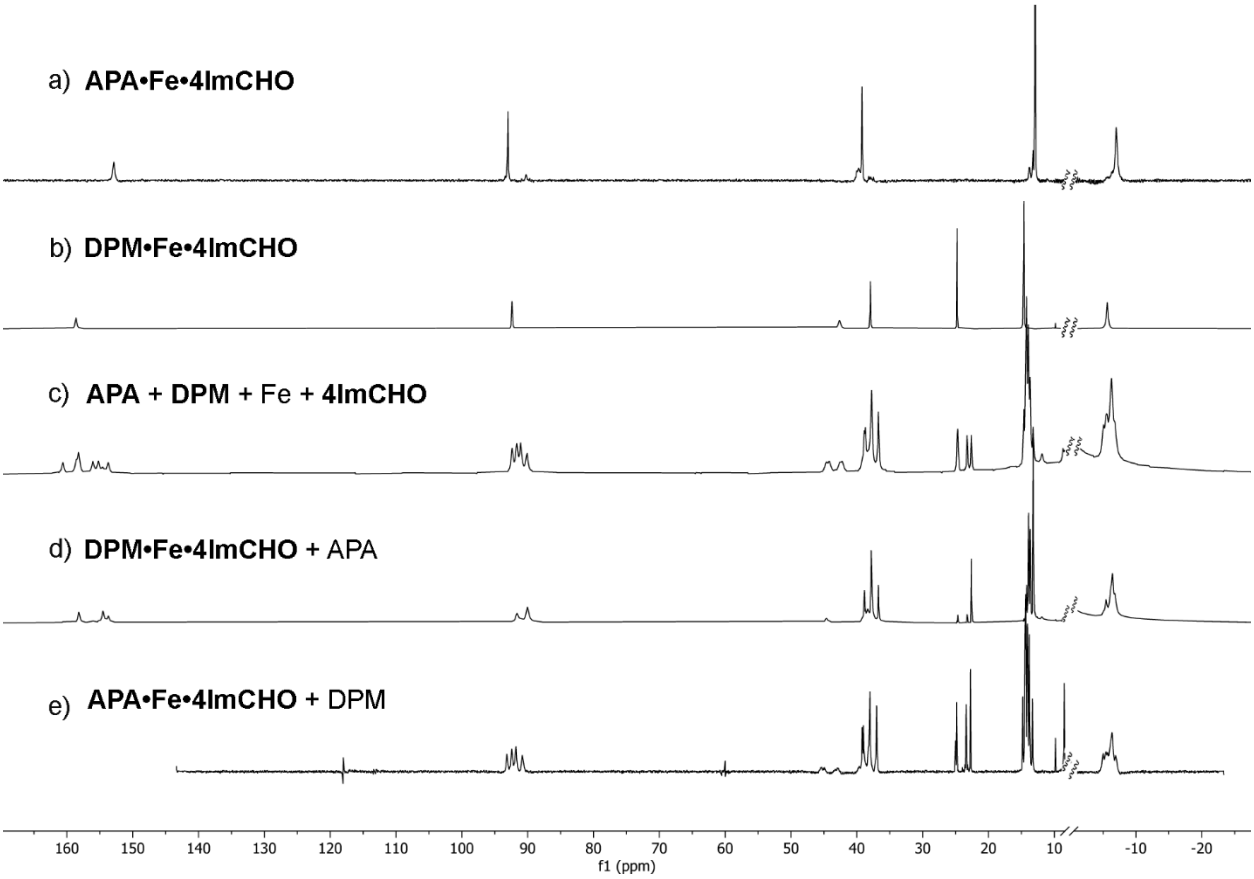

Figure 3.10: a) **DPM•Fe•4ImCHO**, b) **APA•Fe•4ImCHO**, c) the combination of 1.5 eq. **DPM**, 1 eq. **APA**, 1 eq. **$Fe(NTf_2)_2$**, and 3 eq. **4ImCHO**, d) **DPM•Fe•4ImCHO** and 2 eq. **APA**. e) **APA•Fe•4ImCHO** and 6 eq. **DPM** (400 MHz, 298 K, CD_3CN).

3.4 Anion Exchange

Counterions are known to greatly affect the properties of cage complexes such as solubility. Cage complex **APA•Fe•4ImCHO** seemed to be a good candidate for testing an anion screen to analyze the effects of counterions on the imino-imidazole assemblies. **APA•Fe•4ImCHO** was synthesized with iron salts $Fe(NTf_2)_2$, $Fe(ClO_4)_2$, $Fe(BF_4)_2$ and $FeSO_4$. $Fe(NTf_2)_2$ was used as a standard since synthesis and properties of cage **APA•Fe•4ImCHO** incorporating the NTf_2^- anion are already well known. $Fe(ClO_4)_2$ is well known to facilitate the synthesis of iminopyridine cages, and it was unclear if solubility was simply correlated with iminopyridine cages or if the low solubility was caused by the perchlorate anion. The BF_4^- anion is not typically used as a counterion for self-assembled cages and showed a decreased solubility in polar organic solvents. Lastly, $FeSO_4$ is possibly the most interesting salt, as the inclusion of the SO_4^{2-} counterion is the simplest way to make an Fe-iminopyridyl or Fe-iminoimidazole cage water-soluble, however it is unknown if that effect applies to all complexes. The water-solubility of cages comes at the cost of lowering the solubility of the cage complex in organic solvents.

Regardless of counterion used to synthesize **APA•Fe•4ImCHO**, each product showed peaks representative of the self-assembled cage complex in the ^{1}H NMR spectra. The cage was formed as a flaky brown solid in each case. If the reaction mixture was not heated to a high enough temperature a tacky brown substance was formed and no peaks corresponding to the cage were present in the ^{1}H NMR spectrum. The **APA•Fe•4ImCHO** cages showed different paramagnetic ^{1}H NMR peak ranges with each of the four anions. The ^{1}H NMR

spectra for **APA•Fe•4ImCHO•BF_4** and **APA•Fe•4ImCHO•SO_4** are missing peaks, however this may be due the anions causing signals to show at a broader rangeThe **APA•Fe•4ImCHO•$(SO_4)_4$** product formed from this reaction had remarkably low solubility in acetonitrile. The cage often strongly colors the solution, however the complex solution with the SO_4 anion remained almost clear despite the sample being saturated. The sample of **APA•Fe•4ImCHO•$(SO_4)_4$** with D_2O demonstrated even less solubility than that with CD_3CN, but peaks corresponding to a cage complex were present in both ^1H NMR spectra using CD_3CN and D_2O. Despite the low solubility, the ^1H NMR spectrum validated that we did have a water-soluble cage complex due the solvation effects of the sulfate anion.

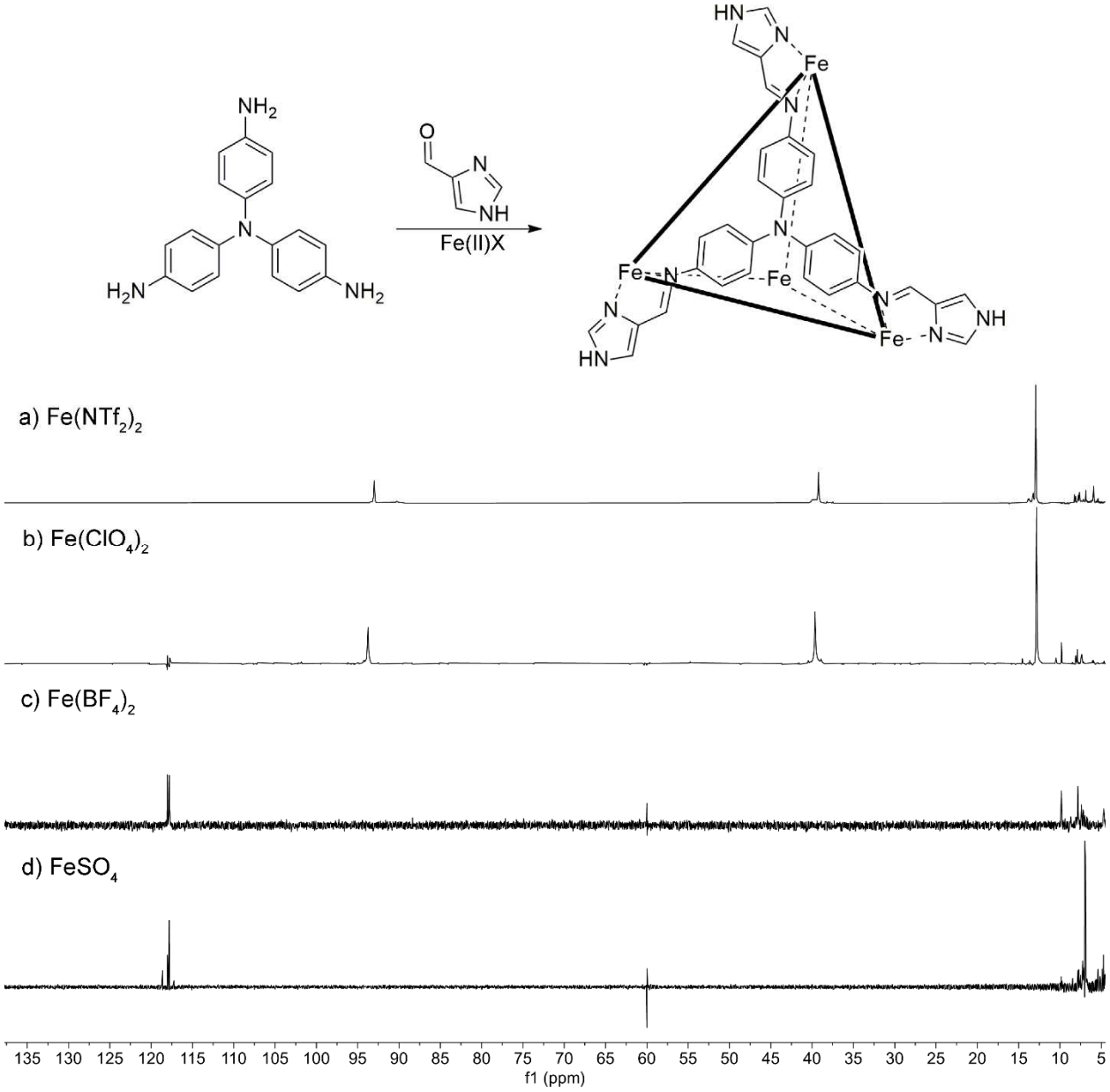

Figure 3.11: Cage **APA•Fe•4ImCHO** synthesized with Fe salts a) $Fe(NTf_2)_2$, b) $Fe(ClO_4)_2$, c) $Fe(BF_4)_2$ and d) $FeSO_4$ (600 MHz, 298 K, CD_3CN).

Since cage **APA•Fe•4ImCHO** has been synthesized with a variety of different Fe salts, it is possible to distinguish how the anion affects the cage. Anion effects for this complex seem to be limited to solubility. The anions choice does not seem to affect whether the cage

forms, only the solubility properties. Cage **APA•Fe•4ImCHO** incorporating the NTf_2^- anion had the highest solubility in polar organic solvents. The cage complex with using BF_4^- or ClO_4^- as the counterion had intermediate solubility in polar organic solvents. When cage **APA•Fe•4ImCHO** had SO_4^{2-} as the counterion, the complex was barely soluble in acetonitrile but gained slight solubility in water. This screen showed a direct comparison on how anions affect the properties of the cage which we had not previously seen. It is important to keep anion choice in mind to determine desired properties with NTf_2 increasing solubility, SO_4^{2-} giving water solubility.

3.5 Synthesis of Other Imidazole Capped Cages

The stability of the paramagnetic cages with imidazole aldehyde caps is a great improvement from **MePyCHO**, making them more useful for binding small molecules. The **APA**-imidazole cages would be ideal for guest-binding however, the cavities of these cages are too small for guest molecules to bind in the interior space. The **4ImCHO**-Fe motif can be applied to create a cage with any appropriate amine capable of undergoing imine condensation. This idea was initially tested by synthesizing cages with **X**, **DPM**, and **APA** to create **X•Fe•4ImCHO**, **DPM•Fe•4ImCHO**, and **APA•Fe•4ImCHO**. Larger amines were selected to determine if they would be able to form assemblies. 2,7-bis(4-aminophenyl) fluorene, **Ph_2F**, was not able to consistently complex with **MePyCHO**, so cage complexation with **4ImCHO** was attempted.

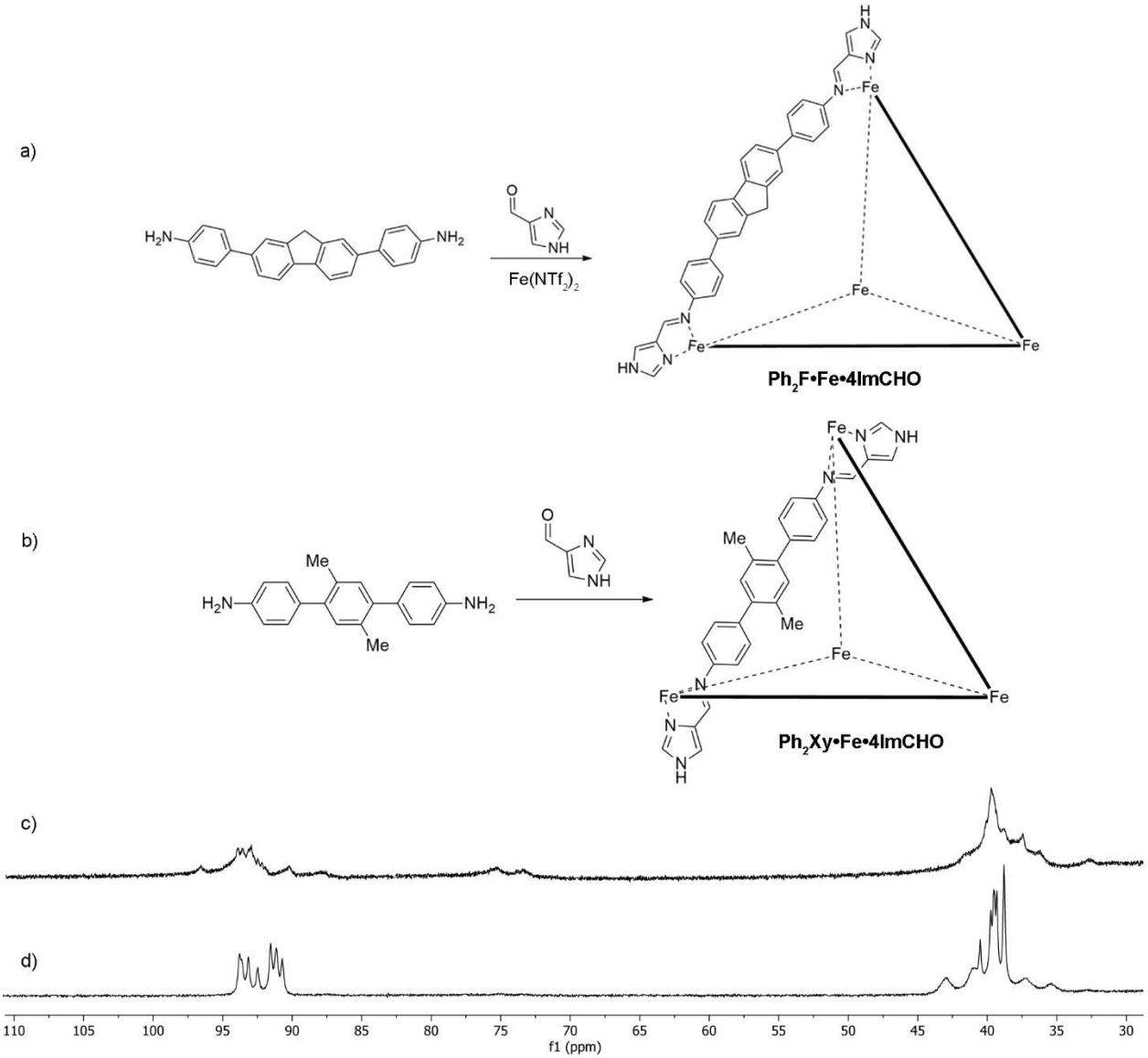

Figure 3.12: Synthetic pathway for a) **Ph_2F•Fe•4ImCHO** and b) **Ph_2Xy•Fe•4ImCHO**. ^1H NMR expansion of range 160-30 ppm for cages c) **Ph_2F•Fe•4ImCHO** and d) **Ph_2Xy•Fe•4ImCHO** (400 MHz, 298 K, CD_3CN).

Combining **Ph_2F**, $Fe(NTf_2)_2$, and **4ImCHO** in acetonitrile at reflux overnight resulted in novel paramagnetic complex **Ph_2F•Fe•4ImCHO**. Peaks corresponding to **4ImCHO** in **Ph_2F•Fe•4ImCHO** can be seen at 93.1 and 39.8 ppm, similar to other cages formed with **4ImCHO**. There is an additional peak expected around 150 ppm, but the NMR instrument

was unable to take a spectrum with wide enough range to accommodate viewing all signals. The ^{1}H NMR spectrum for cage **Ph$_2$F •Fe•4ImCHO** has much broader peaks than other imidazole capped complexes. The paramagnetic signals indicate that there are multiple isomers present or that the symmetry group of the M_4L_6 cage is more complex than a tetrahedral symmetry group. These results reflect similar responses seen for previously published **Ph$_2$F •Fe•PyCHO**, which has the three symmetry groups with an isomeric ratio of 11% T, 48% *C$_3$*, and 41% *S$_4$*.[10] As the structures are similar it is likely that the isomeric ratio is similar, if not the same.

Phil Dietz synthesized previously published the diamine linear terphenyl, **Ph$_2$Xy**,[11] which I combined with $Fe(NTf_2)_2$, and **4ImCHO** to form paramagnetic cage **Ph$_2$Xy•Fe•4ImCHO**. The ^{1}H NMR spectrum has peaks corresponding to **4ImCHO** in a paramagnetic cage. The ^{1}H NMR signals for cage **Ph$_2$Xy•Fe•4ImCHO** indicate multiple isomers present. The diamagnetic cage **Ph$_2$Xy•Fe•PyCHO** has been previously synthesized and the isomeric ratio has been determined to be 33% T, 33% *C$_3$*, and 34% *S$_4$*.[11] The peaks of cage **Ph$_2$Xy•Fe•4ImCHO** appear more symmetrical than those of **Ph$_2$F•Fe•4ImCHO**. For more structural information a crystal structure would need to be obtained. Studies performed with a similar cage, **Ph$_2$F•Fe•PyCHO**, suggest that the large windows and large cavity do not limit binding abilities. Paul Bogie synthesized a porphyrin with four pendant amines for use as an internal amine in cage synthesis. The porphyrin ring would act as a wall rather than an edge seen with amines like **Ph$_2$F** and **Ph$_2$Xy**.

3.6 Conclusion

In this work, we have determined another terminal aldehyde that can be used to make novel paramagnetic cages. The **4ImCHO** terminus creates a more stable complex than complexes with **MePyCHO** termini which quickly degrade in solution. The weak ligand field of imidazole is more energetically favorable than the distortion of the metal center from **MePyCHO** which is caused by steric bulk used to form paramagnetic cages. The addition of steric interactions around the metal center caused by **MePyCHO** makes complexation less preferred, than the imidazole termini which innately have a weaker ligand field which favors high spin Fe. The enhanced stability allows for large cage complexes to be formed as there are not as many unfavorable interactions preventing complexation. Two imidazole termini were tested to successfully form many paramagnetic cages. The **2ImCHO** and **4ImCHO** termini have similar favorability which allows for heterocomplexes but **4ImCHO** is more likely to be incorporated into complexation than **2ImCHO**. Heterocomplexes were readily able to form by mixing amines (i.e. **DPM** and **X** or **DPM** and **APA)** to create a variety of M_2L_3 heterocomplexes. Cage **APA•Fe•4ImCHO** was used to explore how anion choice affects solubility, using SO_4^{2-} anion to create a paramagnetic water-soluble cage. While solubility was poor for **APA•Fe•4ImCHO•SO_4** the issue may be alleviated by using an amine with polar groups to aid in solubility.

3.7 References

1. Hotze, A. C. G.; Hodges, N. J.; Hayden, R. E.; Sanchez-Cano, C.; Paines, C.; Male, N.; Tse, M. K.; Bunce, C. M.; Chipman, J. K.; Hannon, M. J. "Supramolecular Iron Cylinder with Unprecedented DNA Binding Is a Potent Cytostatic and Apoptotic Agent without Exhibiting Genotoxicity." *Chem. Biol.* **2008**, *15*, 1258–1267.
2. Bilbeisi, R. A.; Clegg, J. K.; Elgrishi, N.; Hatten, X. De; Devillard, M.; Breiner, B.; Mal, P.; Nitschke, J. R. "Subcomponent Self-Assembly and Guest-Binding Properties of Face-Capped $Fe_4L_4^{8+}$ Capsules." *J. Am. Chem. Soc.* **2012**, *134*, 5110–5119.
3. Kläui, W.; Eberspach, W.; Gütlich, P. "Spin-Crossover Cobalt(III) Complexes: Steric and Electronic Control of Spin State." *Inorg. Chem.* **1987**, *26*, 3977–3982.
4. Bilbeisi, R. A.; Zarra, S.; Feltham, H. L. C.; Jameson, G. N. L.; Clegg, J. K.; Brooker, S.; Nitschke, J. R. "Guest Binding Subtly Influences Spin Crossover in an $Fe^{II}_4L_4$ Capsule." *Chem. Eur. J.* **2013**, *19*, 8058–8062.
5. McConnell, A. J. "Spin-State Switching in Fe(II) Helicates and Cages." *Supramol. Chem*. **2018**, *30*, 858–868.
6. Roberts, D. A.; Castilla, A. M.; Ronson, T. K.; Nitschke, J. R. "Post-Assembly Modification of Kinetically Metastable $Fe^{II}_2L_3$ Triple Helicates." *J. Am. Chem. Soc.* **2014**, *136*, 8201–8204.
7. Holloway, L. R.; Bogie, P. M.; Hooley, R. J. "Controlled Self-Sorting in Self-Assembled Cage Complexes." *Dalton Trans*. **2017**, *43,* 14719–14723.
8. Holloway, L. R.; Young, M. C.; Beran, G. J. O.; Hooley, R. J. "High Fidelity Sorting of Remarkably Similar Components via Metal-Mediated Assembly." *Chem. Sci*. **2015**, *6*, 4801–4806.
9. Wiley, C. A.; Holloway, L. R.; Miller, T. F.; Lyon, Y.; Julian, R. R.; Hooley, R. J. "Electronic Effects on Narcissistic Self-Sorting in Multicomponent Self-Assembly of Fe-Iminopyridine Meso-Helicates." *Inorg. Chem*. **2016**, *55*, 9805–9815.
10. Holloway, L. R.; Bogie, P. M.; Lyon, Y.; Ngai, C.; Miller, T. F.; Julian, R. R.; Hooley, R. J. "Tandem Reactivity of a Self-Assembled Cage Catalyst with Endohedral Acid Groups." *J. Am. Chem. Soc*. **2018**, *140*, 8078-8081.
11. Meng, W.; Clegg, J. K.; Thoburn, J. D.; Nitschke, J. R. "Controlling the Transmission of Stereochemical Information through Space in Terphenyl-Edged Fe_4L_6 Cages." *J. Am. Chem. Soc.* **2011**, *133*, 13652–13660.

Chapter 4: Paramagnetic Cobalt Cages

4.1 Introduction

Our exploratory work in paramagnetic cages, specifically that dealing with imidazoles, gave us a new opportunity to invert the ligand assembly. An inverted assembly is desirable because an aldehyde-containing core can couple to a much larger library of amines. The vast number of amines available allows new avenues of research and novel properties for cages, such as water solubility,[1,2] covalent cages,[3] and chirality.[4] The imidazole rings can be attached to alkyl di- or tri-halides via nucleophilic substitution to create novel cage cores.

4.2 Synthesis and Characterization of Novel Complexes

Besides being simply used as an aldehyde cap in traditional iminoimidazole complexes, formylimidazole has been previously reacted with simple alkyl halides to form dialdehyde ligand candidates.[4,5] Creation of novel cages with aldehyde cores is possible by using an S_N2 reaction to couple 2ImCHO and an alkyl bromide, followed by imine condensation. Alkyl dibromides used in synthesis would ideally have properties such as ligand rigidity and the opportunity for a large cavity upon metal-mediated assembly. Dibromobutane has been used as an alkyl dibromide previously,[4,5] however it has more degrees of freedom and is more flexible than we desired. To form a more linear ligand, α,α-dibromo-*p*-xylene was applied, which should theoretically form a linear ligand once coupled with **2ImCHO**.

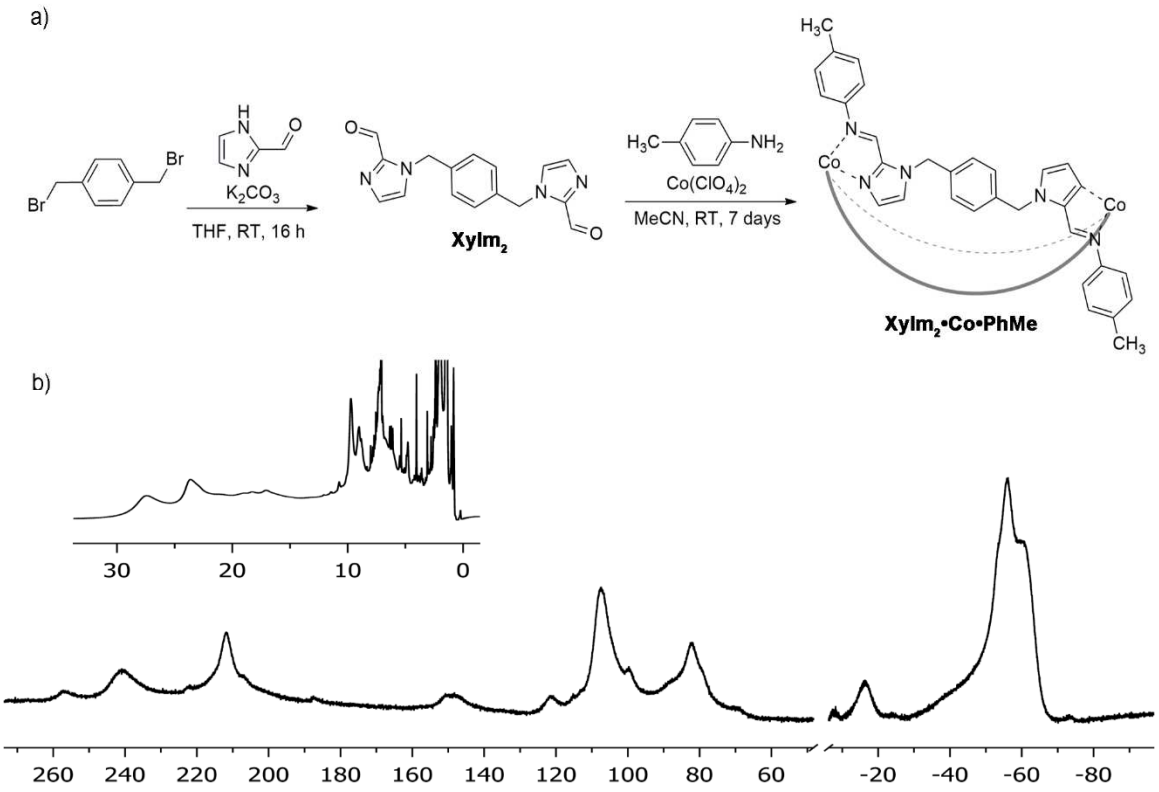

Figure 4.1: a) The synthesis of ditopic aldehyde cage **XyIm$_2$•Co•PhMe** and b) the ^{1}H NMR of **XyIm$_2$•Co•PhMe**, inset of diamagnetic region (400 MHz, 298 K, CD_3CN).

Ligand precursor **XyIm$_2$** was formed via an S_N2 reaction with α,α-dibromo-*p*-xylene and 2-formylimidazole. Cage assembly was initially attempted by combining **XyIm$_2$** and *p*-anisidine with $Fe(NTf_2)_2$ in refluxing acetonitrile, however this formed no product. Cage complex **XyIm$_2$•Co•PhMe** was formed from the combination of **XyIm$_2$**, $Co(ClO_4)_2$, and *p*-toluidine. Using cobalt salts, either $Co(ClO_4)_2$ or $Co(NTf_2)_2$, resulted in broad peaks in ^{1}H NMR from 260 to -75ppm (Figure 4.1), indicative of paramagnetism. The peak broadness prevents accurate structural analysis, this occurs due to multiple fragments or free cobalt in solution. This complex is very strained, making cage formation less favorable than fragments or free components. The high strain increases the likelihood for free cobalt

to exist in solution when solvated and paramagnetic fragments to be present which can be confirmed in ESI-MS. ESI-MS can be used to validate the stoichiometry of the complex, which has found **XyIm$_2$•Co•Ph Me** to show the Co_2L_3 stoichiometry present at the 2+ and 3+ charge states, but larger stoichiometries for prism-type geometries are not present. The ESI-MS additionally shows many fragments such as M_2L_2 and ML_3, most likely because the cage is very strained and easily decomposes in the MS.

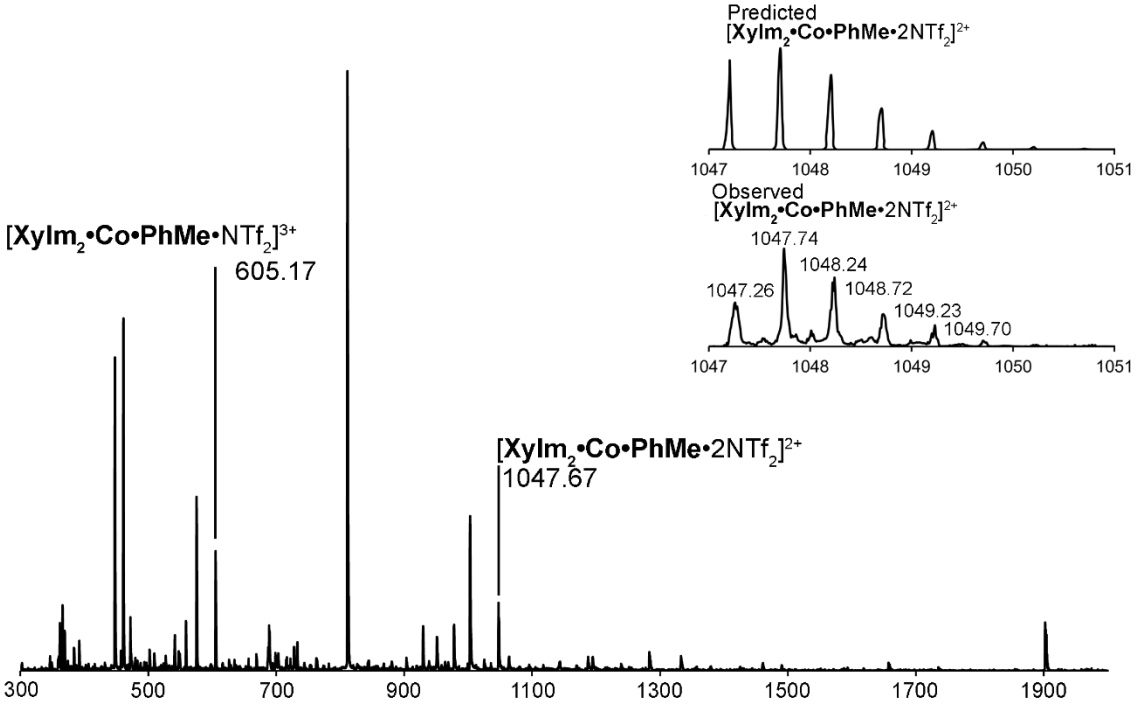

Figure 4.2: The ESI MS data of cage **XyIm$_2$•Co•PhMe**, and expansion of the 2+ charge state.

The "linear" ditopic ligand was not optimal for cage formation due to strain and fragmentation. Moreover, despite attempting to create a ligand that could allow tetrahedral M_4L_6 complexes, an M_2L_3 helicate was formed. Helicate formation implies that the ligand more favorably bends rather than holding a linear 180˚ angle between the aldehyde groups

which would form an M_4L_6 or other prism-like shape. The helicate forms only one isomer due formation constraints. The helicate is the most stable cage possible but, the overall strain of the complex results in fragment formation which is seen in the ESI-MS spectrum and can be inferred from the broad signals in the ^1H NMR spectrum.

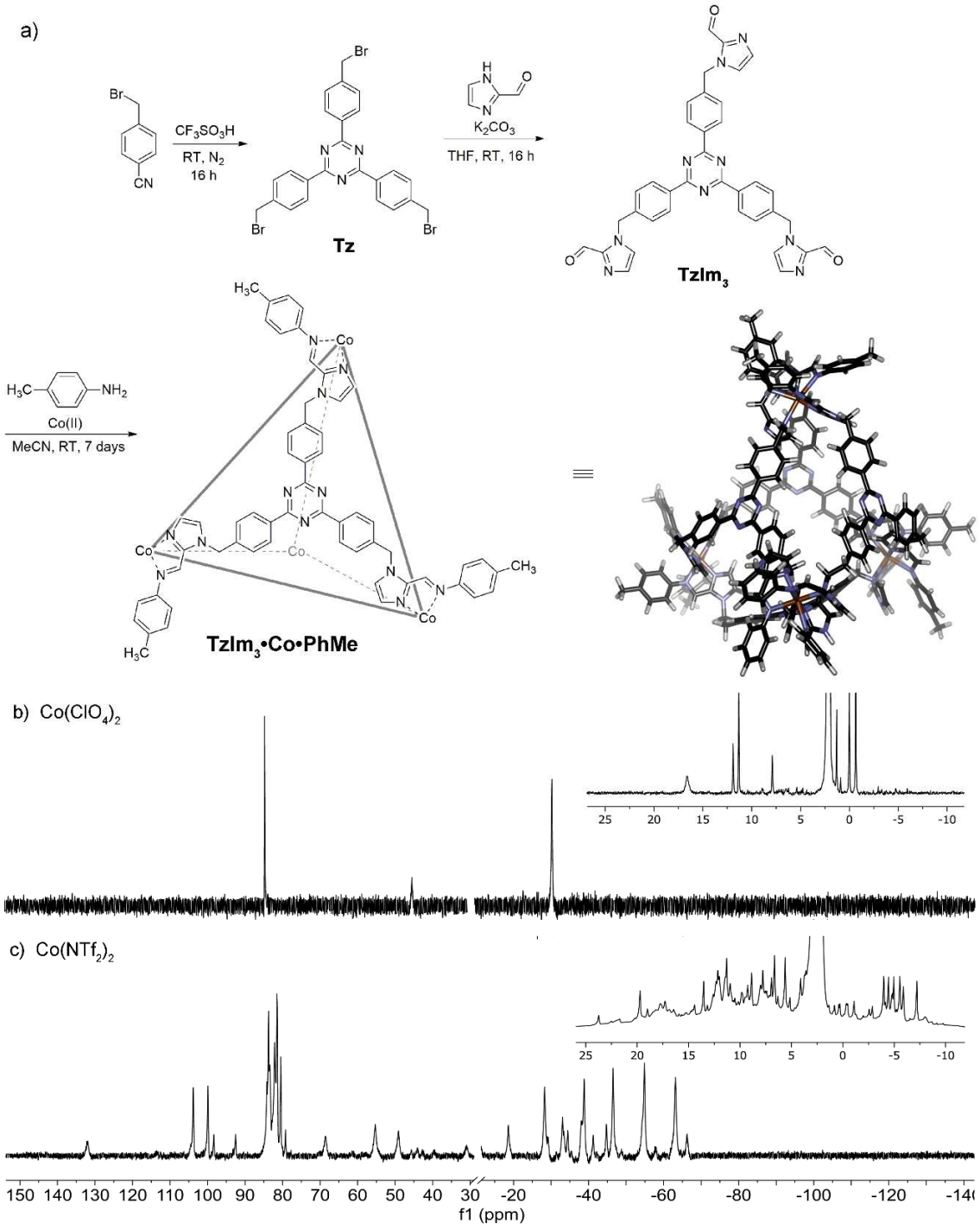

Figure 4.3: The a) synthesis of tritopic aldehyde cage **TzIm3•Co•PhMe** and the b) ^{1}H NMR of **TzIm3•Co•PhMe•ClO4**, inset expansion of diamagnetic region and c) **TzIm3•Co•PhMe•NTf2**,inset expansion of diamagnetic region. (400 MHz, 298 K, CD_3CN).

A tritopic ligand, which attaches to three separate metals, could be an alternative spacer used to create a novel cage that limits the number of isomers the complex can form. A tritopic ligand structure would not accommodate an M_2L_3 or M_4L_6 stoichiometry, but instead would most likely form an M_4L_4 stoichiometry, allowing better organization of components while still forming a tetrahedral shape (Figure 4.3). To make this tritopic ligand, cyanobenzyl bromide and trifluoromethanesulfonic acid were combined, and reacted at room temperature for 16 h to form stable triazine ring **Tz**, which has three alkyl bromide positions around the ring. After ring formation, 2-formyl imidazole was attached via S_N2 reaction to the alkyl bromide positions on **Tz** to form tri-aldehyde **TzIm$_3$**. Imine condensation with tri-aldehyde **TzIm$_3$** and *p*-toluidine in the presence of $Co(ClO_4)_2$ resulted in the formation of M_4L_4 cage **TzIm$_3$**.

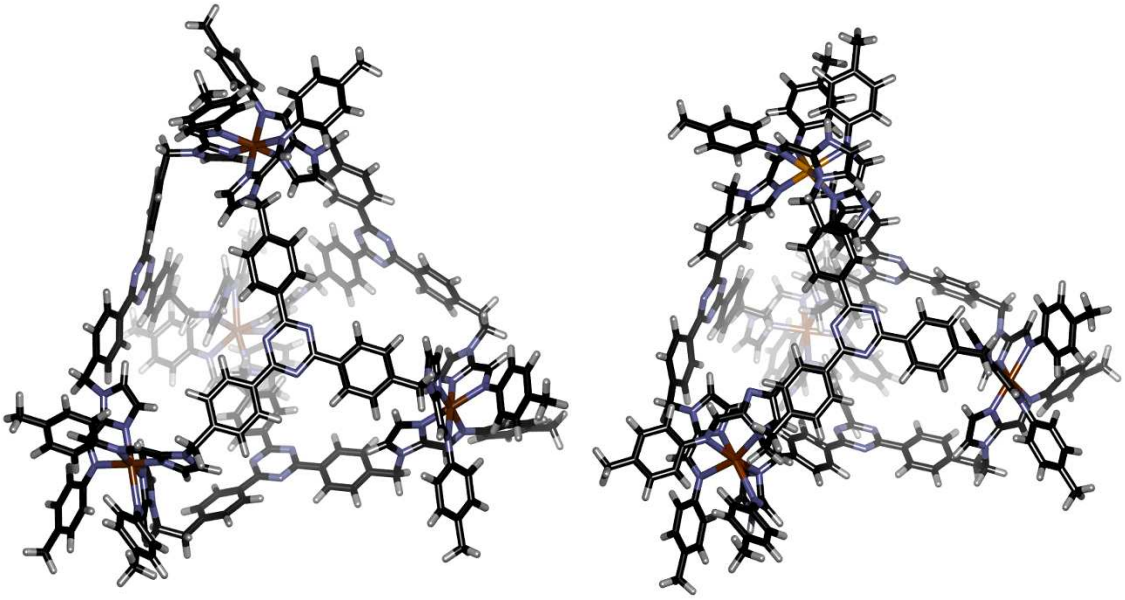

Figure 4.4: Energy minimized models of **TzIm$_3$•Co•PhMe** with *T*-symmetry (left) and C_3-symmetry ΔΔΔΛ, the Λ metal coordination is denoted with an orange metal center (right).

In contrast to the M_2L_3 cage **XyIm$_2$•Co•PhMe**, the ^{1}H NMR spectrum of cage **TzIm$_3$•Co•PhMe** has sharp and distinguishable peaks. There is a possibility for multiple diastereomers from *mer* and *fac* coordination around the metal center and multiple symmetries including *T* (ΔΔΔΔ or ΛΛΛΛ), *C$_3$* (ΔΔΔΛ or ΛΛΛΔ), and *S$_4$* (ΛΛΔΔ). However, only *T* and *C$_3$* symmetry have been observed for M_4L_4 cages.[6–9] From these factors there should be many isomers present in the ^{1}H NMR spectrum however, the ^{1}H NMR spectrum of cage **TzIm$_3$•Co•PhMe•ClO$_4$**, it is apparent that there are few peaks present indicating only one isomer is forming as there are no clusters of peaks (Figure 4.3).

Cage **TzIm$_3$•Co•PhMe•ClO$_4$** was formed in low yield, and had limited solubility which made crystallization attempts difficult, therefore $Co(NTf_2)_2$ was employed to increase solubility of the complex. When **TzIm$_3$•Co•PhMe** is formed with $Co(NTf_2)_2$ the ^{1}H NMR spectrum is remarkably different from **TzIm$_3$•Co•PhMe•ClO$_4$**. The ^{1}H NMR spectrum of **TzIm$_3$•Co•PhMe•NTf$_2$** displayed additional peaks with many peaks showing in multiples of six. It was unclear if the ClO_4 complex and the NTf_2 complex are the same cage as there can be multiple symmetry groupings possible such as *T* or *C$_3$*.[6] Many of the peaks are in groupings of six, which may indicate that there are multiple diastereomers present. The expansion of diamagnetic regions of **TzIm$_3$•Co•PhMe•ClO$_4$** and **TzIm$_3$•Co•PhMe•NTf$_2$** echoes the distinct difference in the number of peaks present, again in multiples of six. To determine that different structures were indeed formed, rather than a one-off outlier, the cages **TzIm$_3$•Co•PhMe•ClO$_4$** and **TzIm$_3$•Co•PhMe•NTf$_2$**, were synthesized multiple times under different conditions which varied temperature (room temperature or 60 ˚C) and time (overnight up to a week). Despite varying conditions, the

results were unchanged, and beige solids were formed in each case, with no change in ^{1}H NMR spectrums of either complex. According to ESI-MS, the stoichiometries of the cage complexes are equivalent, showing the M_4L_4 complex, indicating the cages are similar in general assembly structure. Analysis of the ESI-MS data shows that the complexes of the same mass are being formed and are seen in various charge states. Cage **TzIm$_3$•Co•PhMe•ClO$_4$** seems to favor cage over any fragments and therefore shows fewer side products or fragments present in the ESI-MS spectrum.

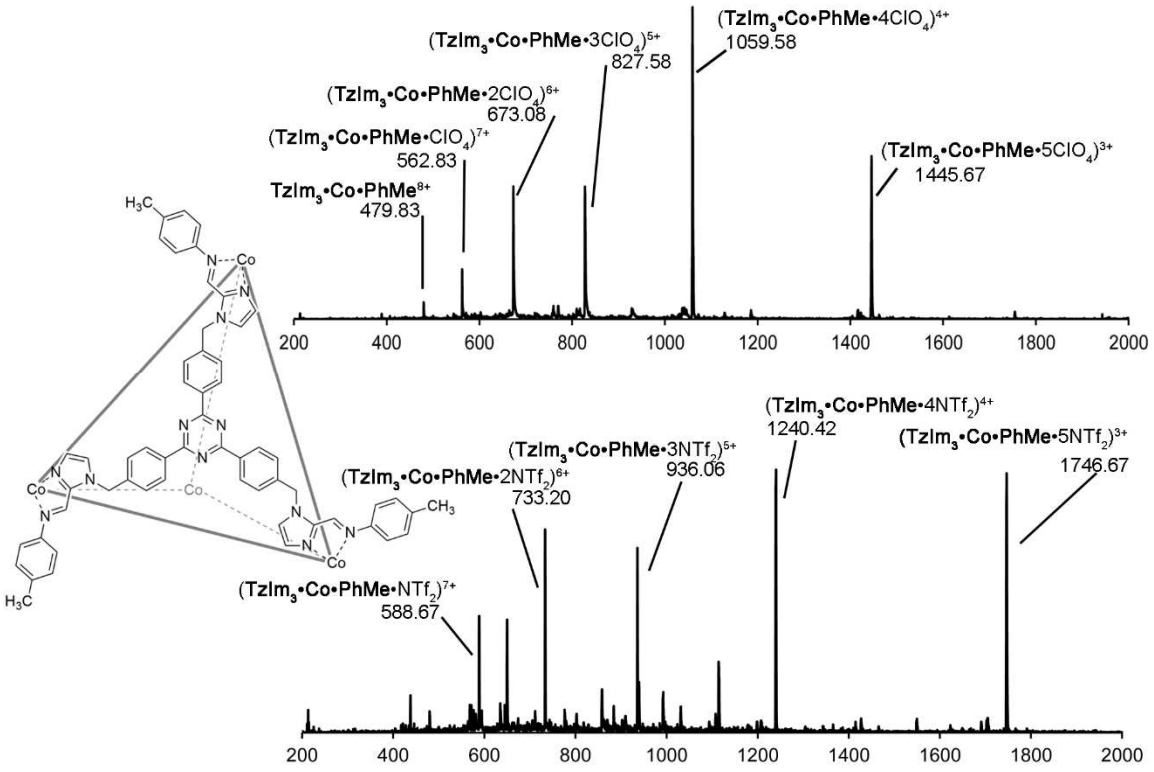

Figure 4.5: The ESI MS data of cages a) **TzIm$_3$•Co•PhMe•ClO$_4$** and b) **TzIm$_3$•Co•PhMe•NTf$_2$**.

To definitively show that these two cages are not the same, we would ideally determine the structures from single crystals via X-Ray diffraction analysis, which would clearly

identify the symmetry of both cages and aid in explaining the ^{1}H NMR. To access crystals of **TzIm$_3$•Co•PhMe•NTf$_2$**, slow vapor diffusion of isopropyl ether into a solution of **TzIm$_3$•Co•PhMe•NTf$_2$** and acetonitrile was performed. The crystals produced were needle-like and unsuitable for XRD (Figure 4.6a). The needle-like crystals could be separated from the Co(NTf$_2$)$_2$ salt that also crystallized out of solution, and this could be exploited as a method of purification. After multiple iterative recrystallizations, three different types of crystalline structures were formed: needles (thicker than those initially formed), hexagonal plates, and small prisms (Figure 4.5b). However, while each crystal type seemed like a good candidate for XRD, Dr. Charlene Tsay tested each type and determined none were able to diffract. Lack of diffraction also indicated that none of the crystals were Co(NTf$_2$)$_2$ salt either, as tightly packing salt crystals are well-known to diffract. Crystallization attempts are ongoing for **TzIm$_3$•Co•PhMe•ClO$_4$**.

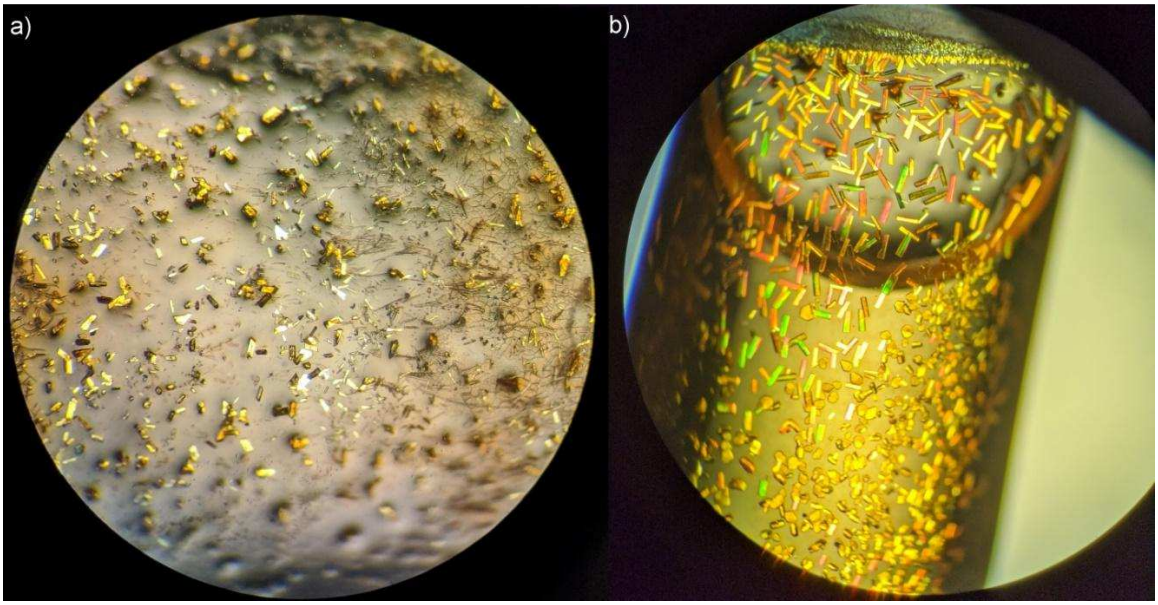

Figure 4.6: Images of the crystals produced from the slow vapor diffusion of isopropyl ether into acetonitrile solution, a) the initial needle-like crystals produced and b) the three types of crystals produced after iterative recrystallization.

The magnetic susceptibility of Co(II) paramagnetic complexes **XyIm$_2$•Co•PhMe**, **TzIm$_3$•Co•PhMe•ClO$_4$**, and **TzIm$_3$•Co•PhMe•NTf$_2$** was determined using Evans' method[8,10–12] variable temperature ^{1}H NMR experiments. The spectra show paramagnetic signals persisting from 313 K – 233 K for **XyIm$_2$•Co•PhMe**, **TzIm$_3$•Co•PhMe•ClO$_4$**, and **TzIm$_3$•Co•PhMe•NTf$_2$** in CD_3CN solution (data can be seen in Figure 4.7). These complexes displayed temperature dependent signal shifts in the same directionality of the Fe(II) paramagnetic cages **SOH•Fe•QnCHO**, **SOH•Fe•MePyCHO**, **X•Fe•MePyCHO**, and **FOH•Fe•MePyCHO**, where the $\chi_M T$ values decrease with decreasing temperature. (Full spectra can be seen in Figures 6.68-6.70.)

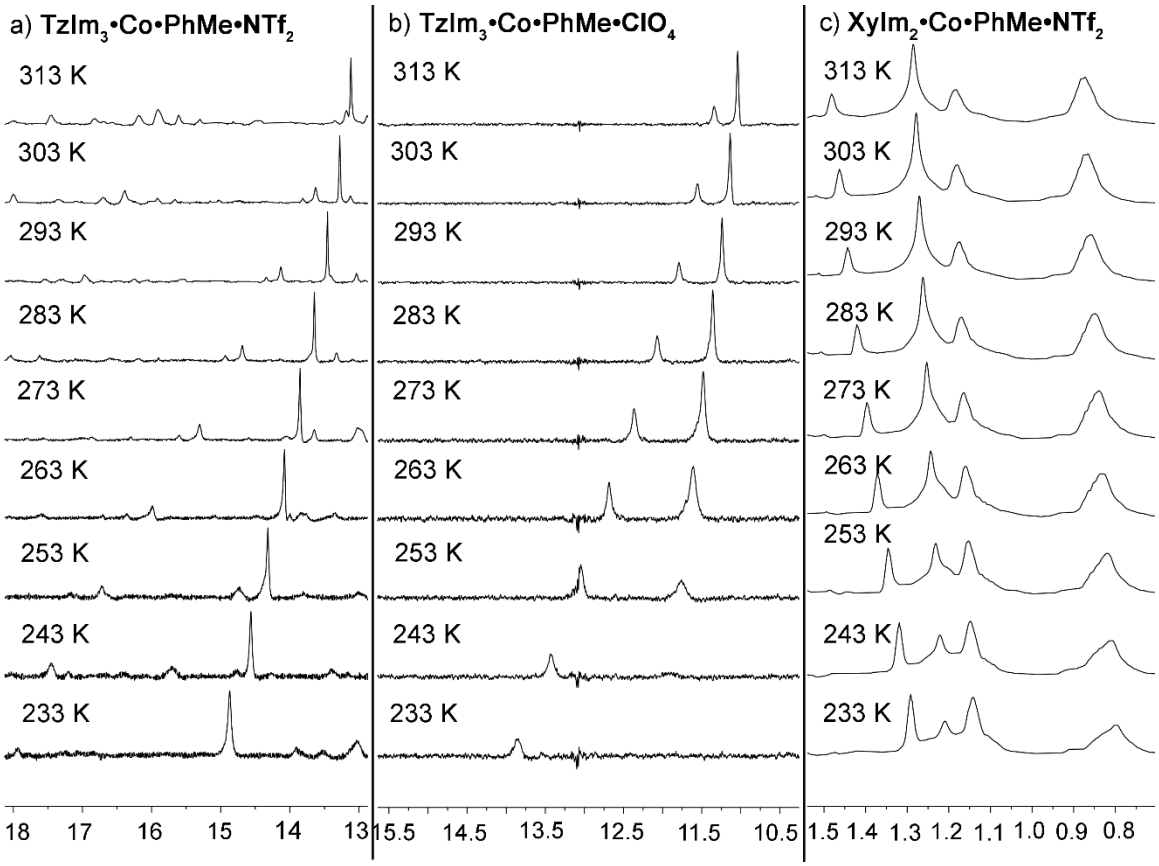

Figure 4.7: ^{1}H NMR spectra of selected ranges, taken from 313-233 K in 10 degree increments with a dichloroethane standard for magnetic moment data of cages a) **TzIm$_3$•Co•PhMe•NTf$_2$**, b) **TzIm$_3$•Co•PhMe•ClO$_4$**, and c) **XyIm$_2$•Co•PhMe•NTf$_2$** (600 MHz, CD_3CN).

The $\chi_M T$ values rise with decreasing temperature, which matches with data trends from complexes in Chapter 2, although this behavior is different to that of the majority of mononuclear Fe(II) paramagnetic complexes.[8] The observed and corrected χ_M values are shown in Table 4.1: as the M_w of the complexes is large, the diamagnetic contribution was calculated and applied in the correction, not ignored (as is common for small M_W complexes).[8,12] The data for each cage complex correlates to high spin Co(II) centers that exhibit significant magnetic coupling.

Table 4.1: Molar Susceptibility (χ_M), corrected molar susceptibility ($\chi_{M'}$), and effective magnetic moment (μ_{eff}) for cages **XyIm$_2$•Co•PhMe**, **TzIm$_3$•Co•PhMe•ClO$_4$**, and **TzIm$_3$•Co•PhMe•NTf$_2$** at 293 K.

Cage	Δf (Hz)	χ_M (cm^3 mol^{-1})	$\chi_{M'}$ (cm^3 mol^{-1})	μ_{eff}
XyIm$_2$•Co•PhMe	312.72	0.0273	0.0282	8.01
TzIm$_3$•Co•PhMe•ClO$_4$	107.40	0.00187	0.00190	6.67
TzIm$_3$•Co•PhMe•NTf$_2$	326.22	0.0283	0.0292	8.15

4.3 Anion Exchange

Complexes **TzIm$_3$•Co•PhMe•ClO$_4$** and **TzIm$_3$•Co•PhMe•NTf$_2$** are similar complexes, but the reasons for why **TzIm$_3$•Co•PhMe•NTf$_2$** has multiple isomers present and **TzIm$_3$•Co•PhMe•ClO$_4$** forms only one isomer remains unknown. We were curious if it would be possible to interconvert complexes by adding the anion. In this vein, a comparative study was performed to determine if there was any apparent favorability between anions, what effects the anion used would have on the complex, and if it would be possible to gain any identifying information about what was happening to enable these differences seen. The wide range of the ^{1}H NMR spectrum allows peaks that would otherwise overlap or be unseen to be discrete, aiding in the determination of anion favorability. The ^{1}H NMR spectrum of **TzIm$_3$•Co•PhMe•NTf$_2$** looks like it has many isomeric possibilities including a mixture of *mer* and *fac* coordination around the metal center or multiple symmetries including *T*, C_3, and S_4, whereas **TzIm$_3$•Co•PhMe•ClO$_4$** appears to only have one isomer present. UV-vis absorbance spectrometry is also a viable

method for visualizing anion exchange. The complexes are similar, but the anion used in synthesis makes the UV-vis spectra discernable from each other.

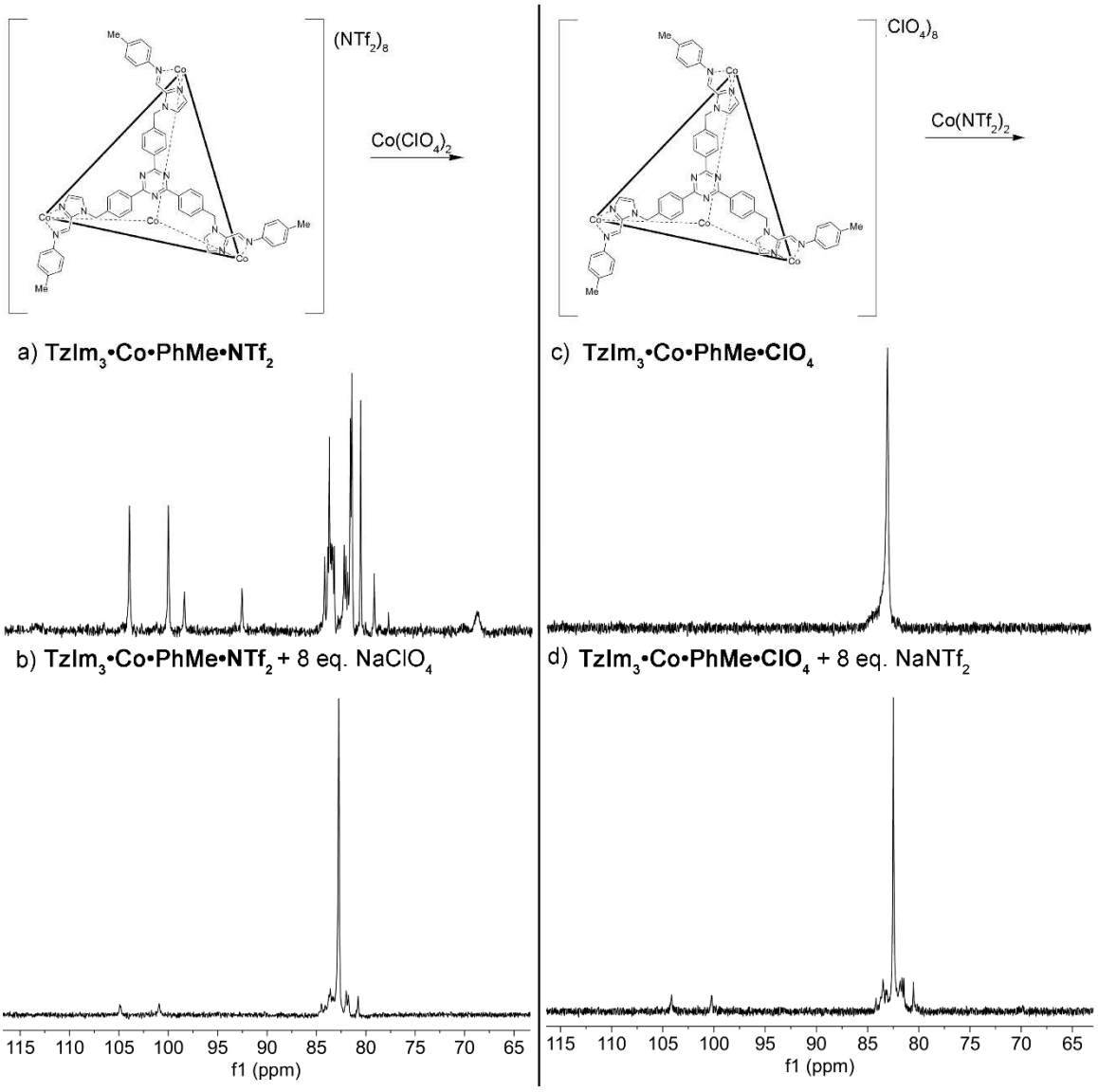

Figure 4.8: Anion exchange observed via ^{1}H NMR with a) showing **TzIm3•Co•PhMe•NTf2** only, b) **TzIm3•Co•PhMe•NTf2** and 8 eq. $NaClO_4$ after 5 minutes at room temperature, c)showing **TzIm3•Co•PhMe•ClO4** only, and d) **TzIm3•Co•PhMe•ClO4** and 8 eq. $NaNTf_2$ after 5 days at room temperature (400 MHz, 298 K, CD_3CN).

The initial hypothesis was that ClO_4^- would be the more favorable anion, compared to NTf_2^-, as it is able to form only one isomer of cage **TzIm$_3$•Co•PhMe**. The addition of ClO_4^- anion to **TzIm$_3$•Co•PhMe•(NTf$_2$)$_8$** resulted in immediate changes in the ^{1}H NMR spectrum due to some formation of **TzIm$_3$•Co•PhMe•(ClO$_4$)$_8$**. This immediate change is worth noting as isomer interconversion usually happens on a scale of days.[13] After the addition of 8 eq. $NaClO_4$ many peaks drop out, and cage decomposition products start to form at 6.5-7.5 ppm (Figure 4.8).

The reverse reaction, adding $NaNTf_2$ to **TzIm$_3$•Co•PhMe•(ClO$_4$)$_8$**, resulted in a much cleaner transition with no evidence of decomposition products. Five minutes after the addition of 10 eq. $NaNTf_2$, the ^{1}H NMR spectrum showed that peaks corresponding to **TzIm$_3$•Co•PhMe•ClO$_4$** were drastically reduced and new paramagnetic peaks corresponding to **TzIm$_3$•Co•PhMe•NTf$_2$** had grown in. The reversibility indicates that there is not a strong preference based on energetic favorability, but rather an equilibrium of the two anions.

The complexes were also analyzed via UV-vis spectrometry to determine if either complex could exchange into the other. However, neither spectrum coalesces into the alternate complex. Both spectra show changes in the absorbance after the alternate anion is added indicating that there is something happening to the complex, but whether it is decomposition or transition to another complex is unclear.

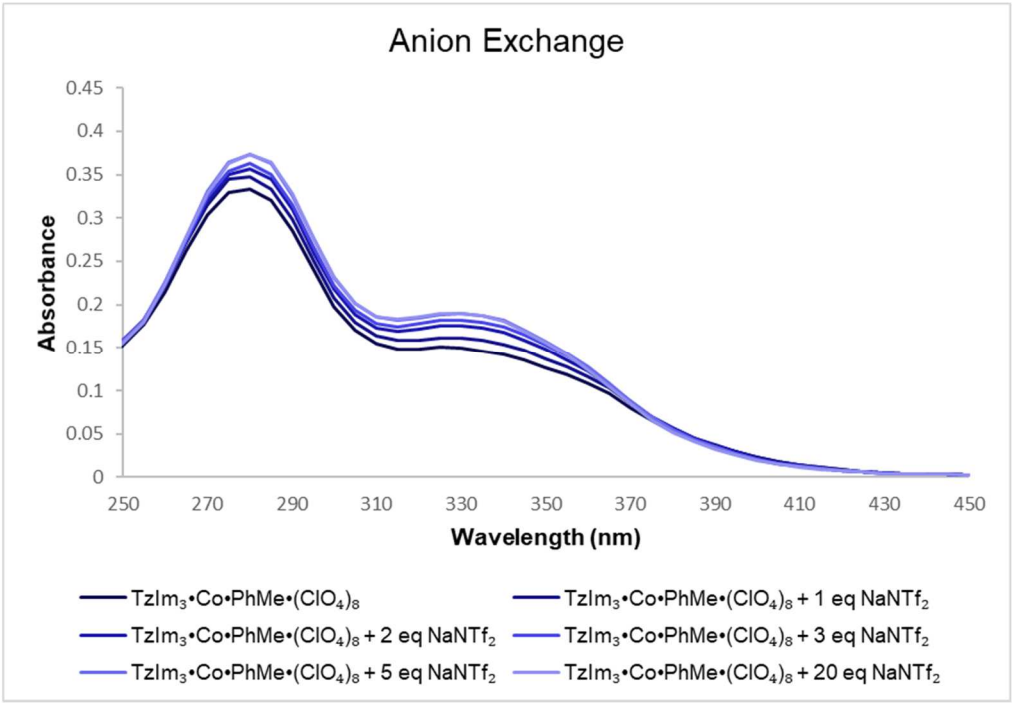

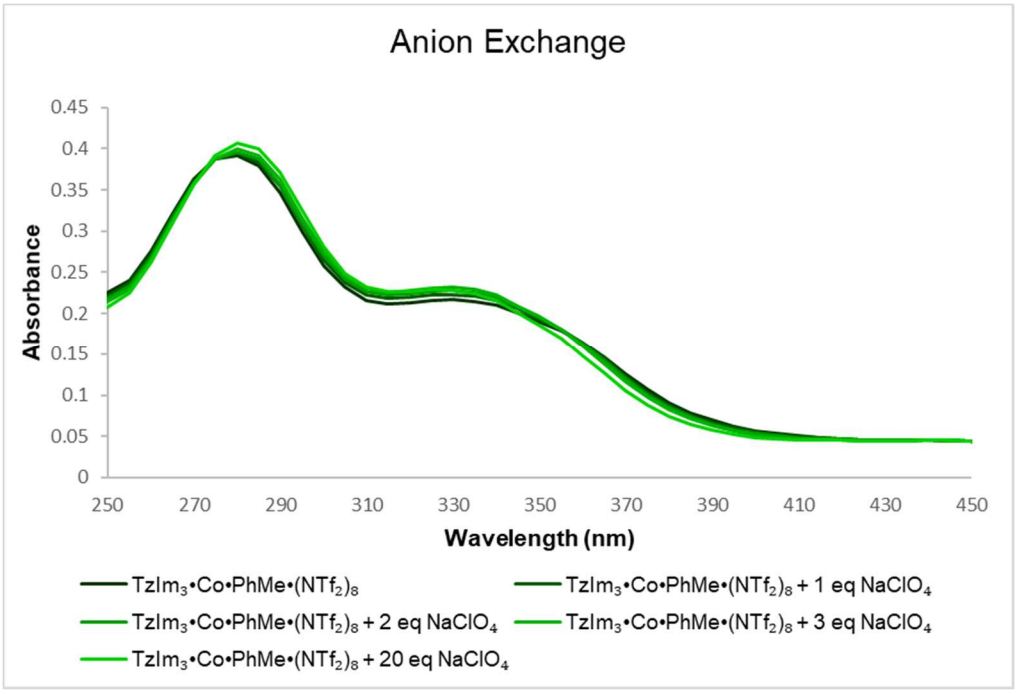

Figure 4.9: a) UV-Vis absorption spectrum of the titration of $NaNTf_2$ into a 5 µM solution of cage **TzIm3•Co•PhMe** in CH_3CN. $NaNTf_2$ was added in 1 µL aliquots from a 5 mM stock solution in CH_3CN. b) UV-Vis absorption spectrum of the titration of $NaClO_4$ into a 5 µM solution of cage **TzIm3•Co•PhMe** in CH_3CN. $NaClO_4$ was added in 1 µL aliquots from a 5 mM stock solution in CH_3CN.

4.4 Subcomponent Exchange

With previous cages, both aldehyde ends and amine cores could be switched out if a more favorable complex could be formed. With tritopic cage **TzIm$_3$•Co•PhMe** there are many amines suitable for synthesis and exchange which can enable new properties such as water solubility and chirality. After the initial synthesis of cage **TzIm$_3$•Co•PhMe**, other amines were tested to evaluate synthetic compatibility and determine the scope of possible complexes. Testing either *p*-anisidine or bromoanline with Co(II) and trialdehyde **TzIm$_2$** in acetonitrile at 60 ˚C resulted in paramagnetic complex **TzIm$_3$•Co•PhOMe** using *p*-anisidine and **TzIm$_3$•Co•PhBr** using 4-bromoaniline.

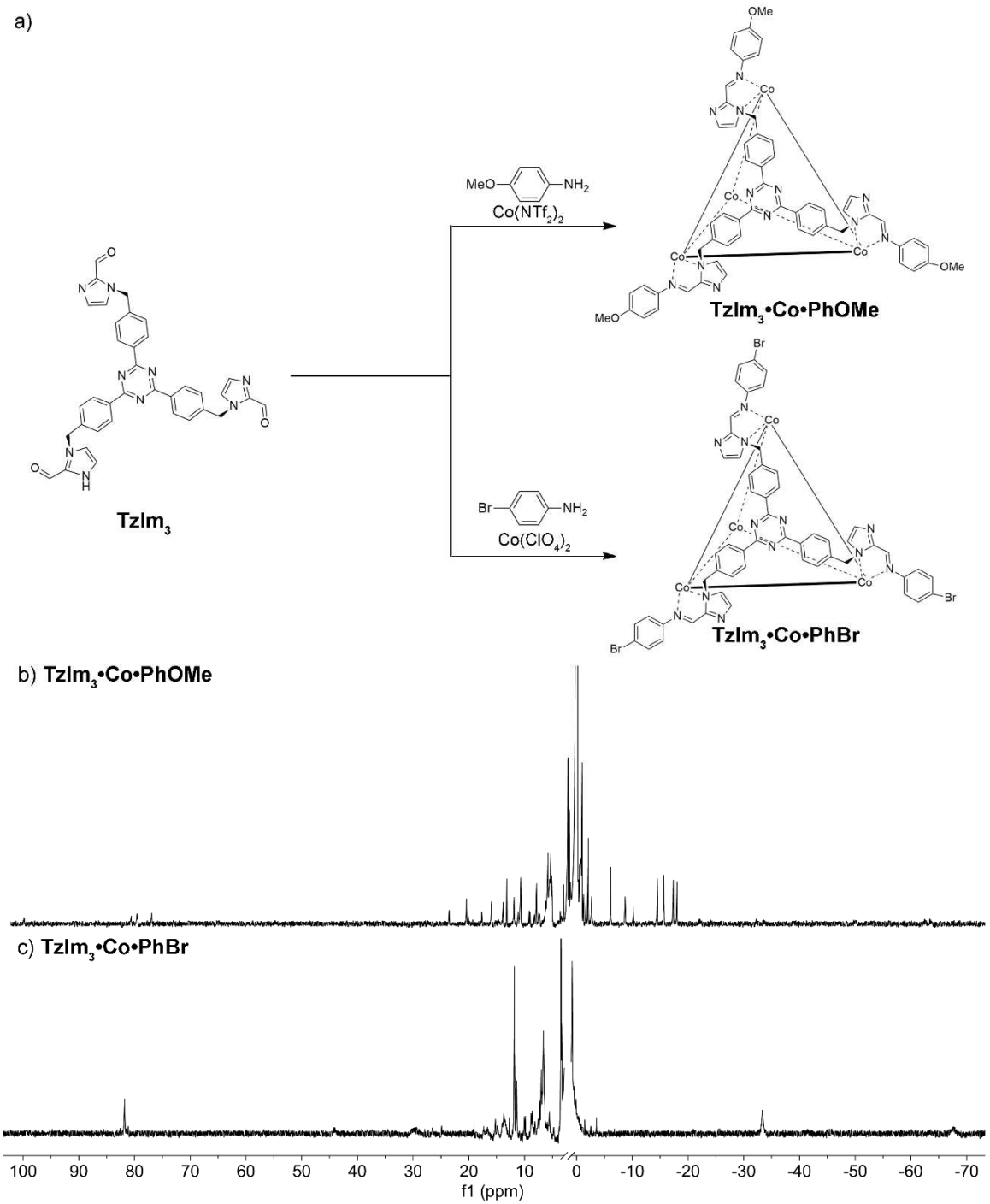

Figure 4.10: a) Synthesis of cages **TzIm3•Co•PhOMe** and **TzIm3•Co•PhBr** and the ^{1}H NMR spectra of b) **TzIm3•Co•PhOMe** and c) **TzIm3•Co•PhBr** (400 MHz, 298 K, CD_3CN).

Amine exchange is used to determine whether complexation was possible using preformed complex **TzIm$_3$•Co•PhMe** and either *p*-anisidine or butylamine to determine if a new self-assembly would form. When *p*-anisidine was added to **TzIm$_3$•Co•PhMe** the resulting ^{1}H NMR spectra had very few differences from the **TzIm$_3$•Co•PhMe** spectrum, making it difficult to discern if any change took place. However, the doublet at 6.6 ppm had shape similar to what you would expect from *p*-anisidine. The coupling constant for the doublet around 6.6 ppm, which appears when *p*-anisidine is added is skewed due to the magnetic field of the cage interacting with compounds in solution. From the peaks immediately growing in after 3 eq. of *p*-anisidine being added and having the same peaks be present throughout the experiment, it can be logically assumed that *p*-anisidine is not displacing p-toluidine.

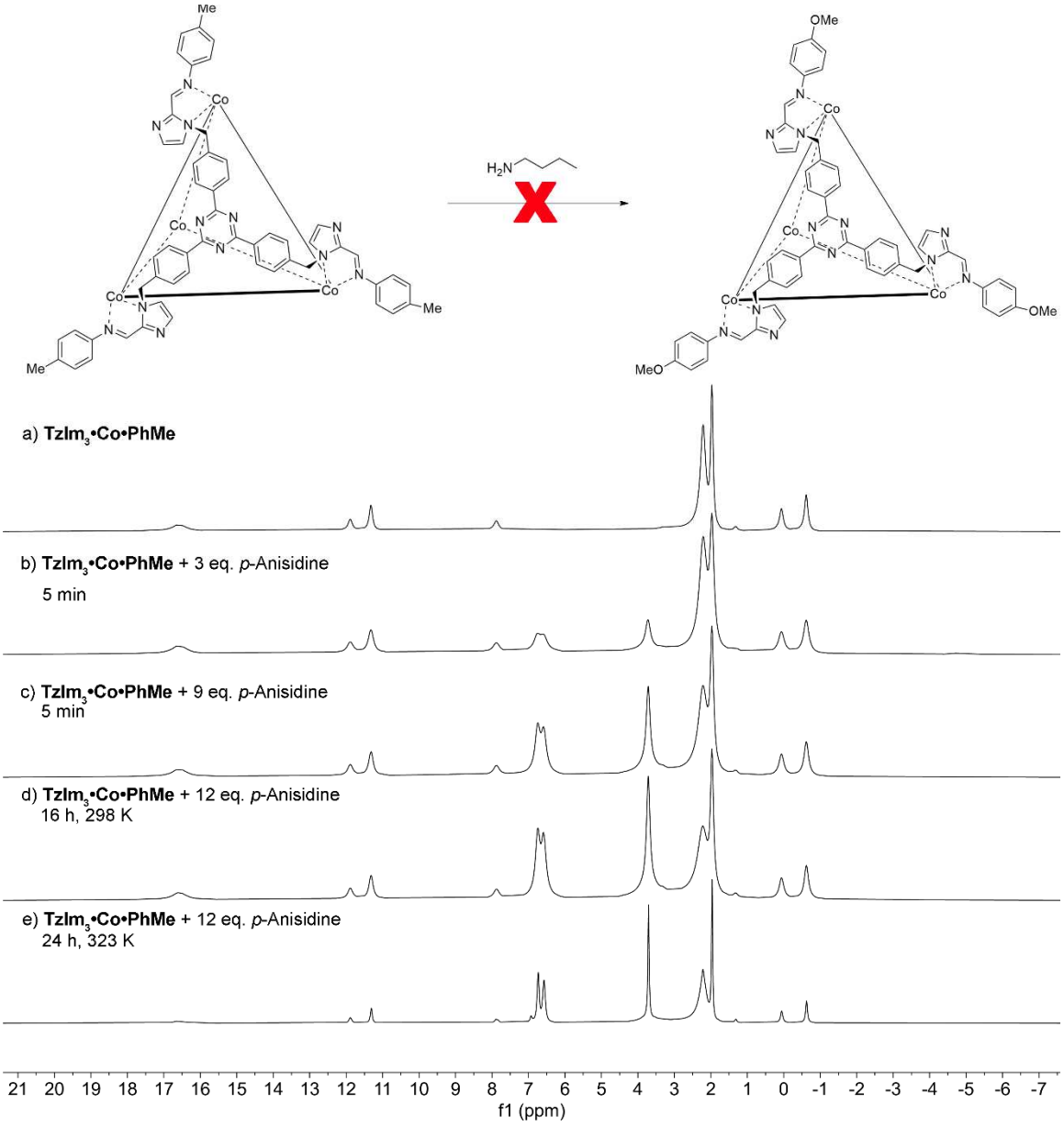

Figure 4.11: Amine exchange with *p*-anisidine and **TzIm$_3$•Co•PhMe** a) addition of 3 eq. *p*-anisidine to cage **TzIm$_3$•Co•PhMe**, b) addition of 12 eq. *p*-anisidine to cage **TzIm$_3$•Co•PhMe**, addition of 12 eq. *p*-anisidine to cage **TzIm$_3$•Co•PhMe** after 16 h at 25°C and d) after heating at 50°C for 24 h.

In the case of butylamine, even with heating, amine exchange proved to be unsuccessful. Not only did no new complexes form, but the pre-existing cage was also

destroyed. The ^{1}H NMR spectrum after interaction, regardless, shows significant decrease in the concentration of paramagnetic complex and new peaks corresponding to amine and ligand fragmentation.

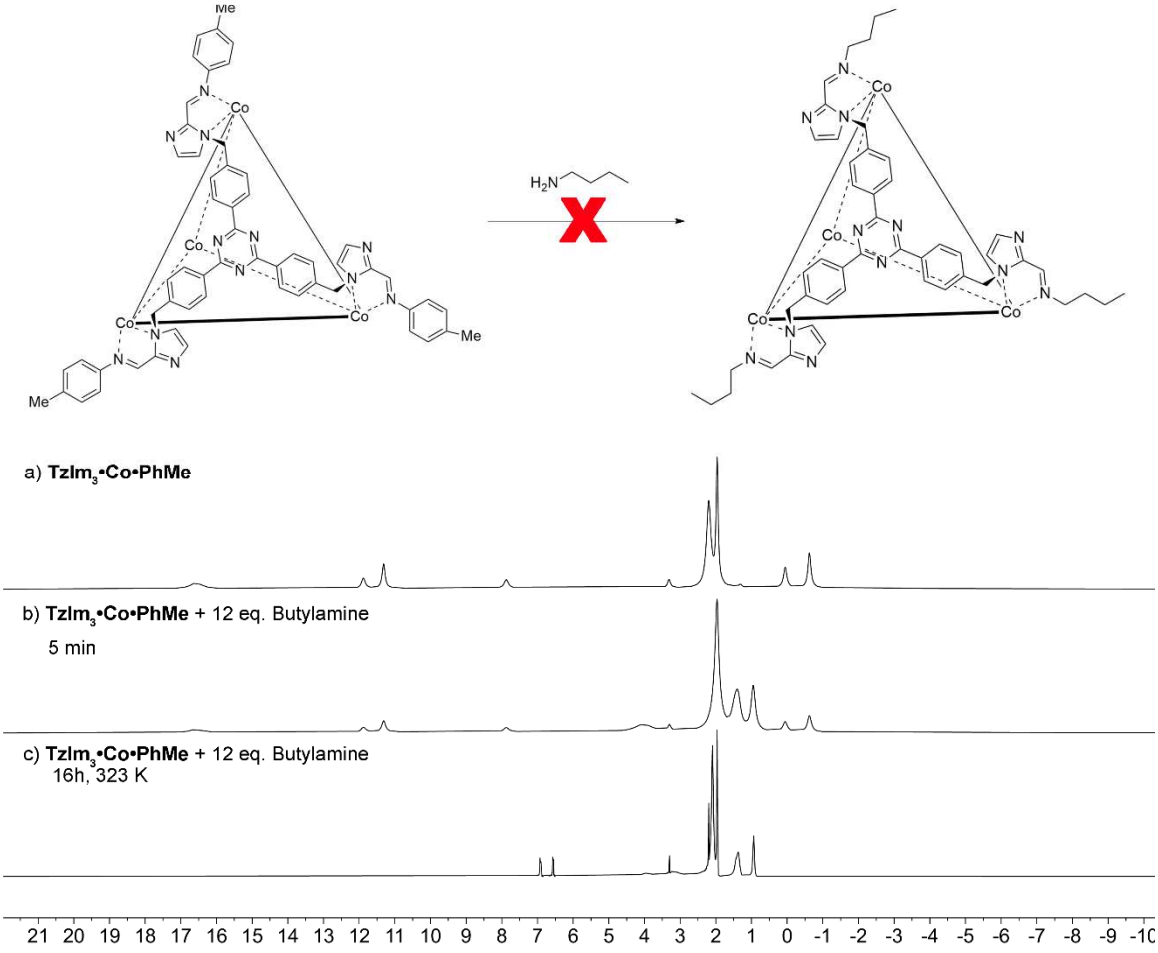

Figure 4.12: Amine exchange with *p*-anisidine and **TzIm$_3$•Co•PhMe**, starting with cage **TzIm$_3$•Co•PhMe** (top), 5 min after adding 12 eq. *p*-anisidine (middle), and after 16 h at 50°C (bottom). Amine exchange butylamine and **TzIm$_3$•Co•PhMe**, starting with cage **TzIm$_3$•Co•PhMe** (top), 5 min after adding 12 eq. butylamine (middle), and after 16 h at 50°C (bottom) (400 MHz, 298 K, CD_3CN).

4.5 Guest Binding Studies Monitored via UV-vis titration

Cage **TzIm$_3$•Co•PhMe** provided a novel scaffold with a relatively sizable internal cavity for binding small molecules. An energy optimized model (SPARTAN semi-

empirical, AM1 forcefield) of the complex with all *fac* vertices was created to determine which small molecules would be able bind to the cage. A range of organic aromatic planar molecules (pyrene, 2-aminopyrene, anthracene), and steroids (progesterone, estrone, and estradiol) small molecules were tested to determine what would bind in the cavity. Most compounds did not show any evidence of binding, displaying only the spectrum of the cage complex. Progesterone and estrone presented isosbestic points, which are indicative of binding to the cage, Figure 4.13.

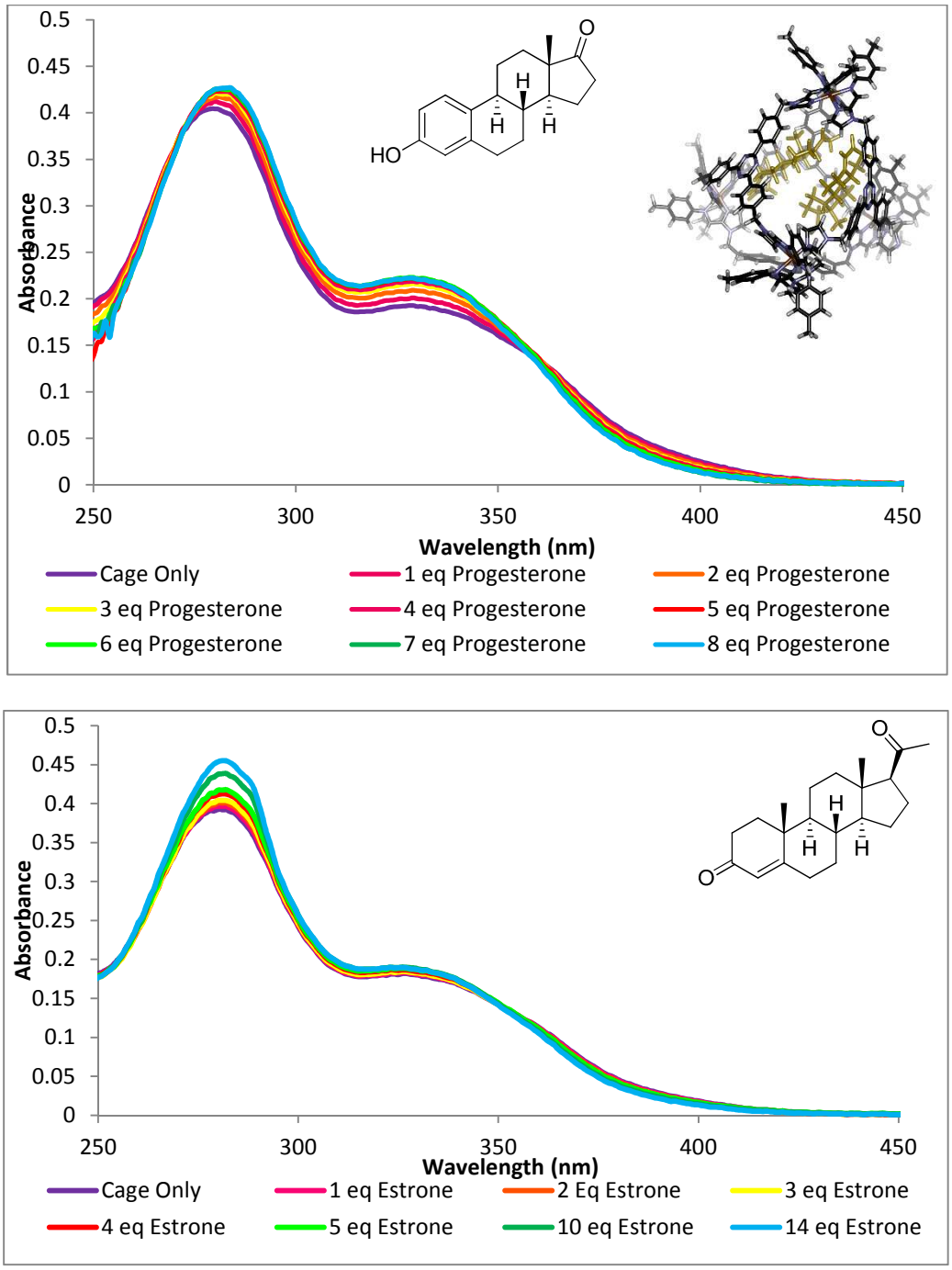

Figure 4.13: UV-Vis absorption spectrum of the titration of progesterone into a 5 μM solution of cage **TzIm$_3$•Co•PhMe•NTf$_2$** in CH_3CN. progesterone was added in 1 μL aliquots from a 5 mM stock solution in CH_3CN. An energy minimized spartan model of two progesterone molecules inside cage **TzIm$_3$•Co•PhMe**. b) UV-Vis absorption spectrum of the titration of estrone into a 5 μM solution of cage **TzIm$_3$•Co•PhMe•NTf$_2$** in CH_3CN. progesterone was added in 1 μL aliquots from a 5 mM stock solution in CH_3CN.

The UV/Vis titrations were used to determine the binding affinity of the various components of the reaction. Binding affinities were calculated by linear regression analysis (Nelder–Mead method) from the change in cage **TzIm$_3$•Co•PhMe•NTf$_2$** absorbance at two points (330 and 380 nm) upon guest titration.[14,15] The host-guest complex was determined to demonstrate 1:2 host-guest binding, as 1:1 binding resulted in large percent error and unrealistic K_1 values. The affinities were fit to 1:2 models, and the binding constants for **TzIm$_3$•Co•PhMe•NTf$_2$**⊃progesterone and **TzIm$_3$•Co•PhMe•NTf$_2$**⊃estrone are presented in Table 4.2. These values indicate a moderately strong binding affinity between host and guest.

Table 4.2: Binding Affinities of Hormones in Cage **TzIm3•Co•PhMe.**

Guest	$K_1 \times 10^3$ M^{-1}	$K_2 \times 10^3$ M^{-1}
Progesterone	1.95 ± 0.092	78.1 ± 3.7
Estrone	0.285 ± 0.066	78.0 ± 23

When progesterone was added to **TzIm$_3$•Co•PhMe•ClO$_4$** there was no evidence of binding. The UV-vis spectra showed only cage present, with no change as progesterone aliquots added. Cage **TzIm$_3$•Co•PhMe•ClO$_4$** shows only one isomer, likely due to some sort of anion templation, where ClO_4^- is directing the ligands in the cavity. There is precedence for ClO_4^- acting as a templating ion with ligands containing hydrogen bonding.[4,13,16,17] The O in ClO_4 anion directs from the C-H bonds of the alkyl chain towards itself aiding in organizing the cage. However, Cage **TzIm$_3$•Co•PhMe** is dissimilar to cage **FOH•Fe•MePyCHO**, as it does not have as the cavity is much larger able to two

progesterone molecules whereas **FOH•Fe•MePyCHO** could only encapsulate the ClO_4^- anion. The size discrepancies of the cavities indicate whatever type of anion templation is occurring is occurring through a different pathway than previously seen. The occupation of ClO_4^- anions in the internal cavity is more favorable guest than progesterone, which makes it difficult for the complex to bind to interesting species.

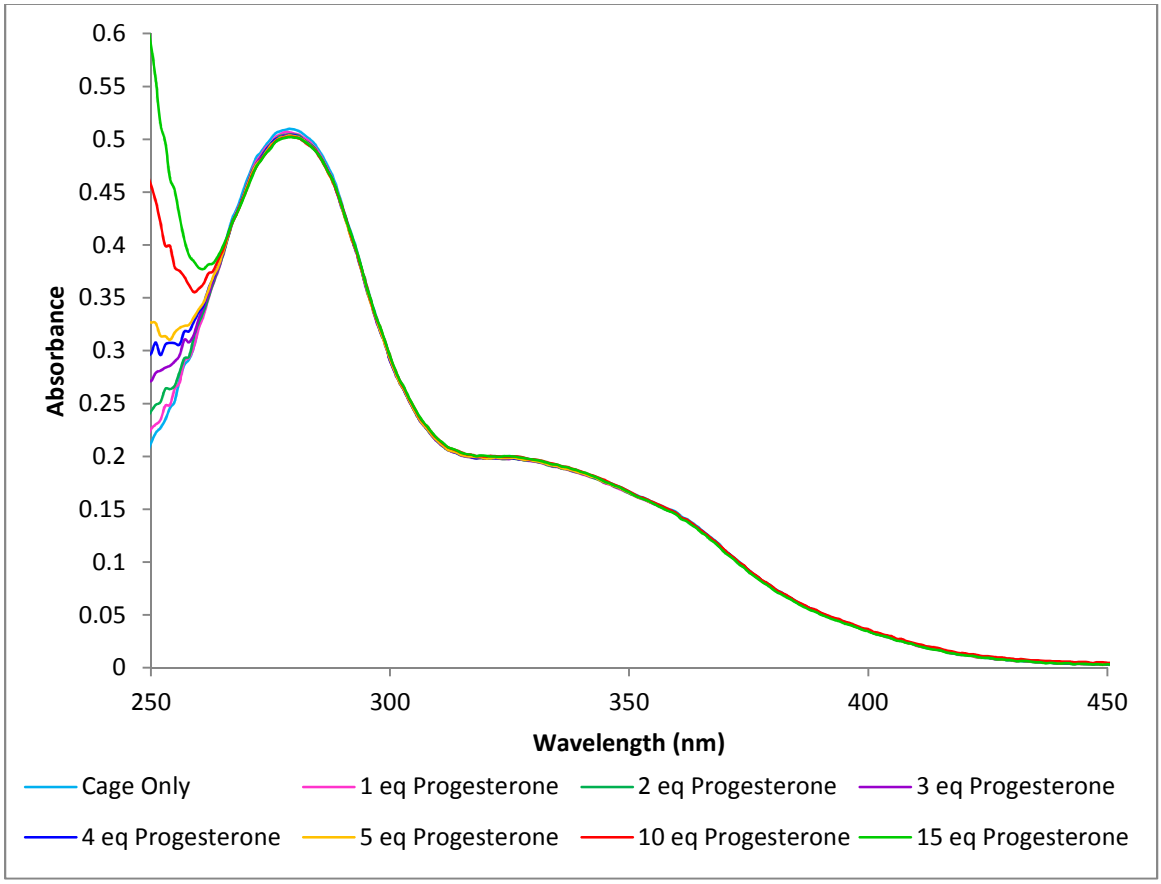

Figure 4.14: UV-Vis absorption spectrum of attempted titration of progesterone into a 5 µM solution of cage **TzIm$_3$•Co•PhMe•ClO$_4$** in CH_3CN. progesterone was added in 1 µL aliquots from a 5 mM stock solution in CH_3CN. b) UV-Vis absorption spectrum of the titration of estrone into a 5 µM solution of cage **TzIm$_3$•Co•PhMe•ClO$_4$** in CH_3CN. progesterone was added in 1 µL aliquots from a 5 mM stock solution in CH_3CN.

4.6 Conclusions

In these studies, novel aldehyde ended cores for cage complexation have been synthesized

with several options for functionalization. The paramagnetic tritopic complex **TzIm$_3$•Co•PhMe** gives an opportunity to study how anions affect cage formation and properties. The paramagnetic nature of the cage increases the range of the ^{1}H NMR by spreading the peaks further out allowing isomeric peaks to be more visible. Since we were unable to get a crystal structure of the complex, were used other spectroscopic methods to obtain an understanding of the structure and extrapolate properties to rationalize and determine how anions are interacting with the cage. Results of the anion exchange experiments show that an equilibrium can be reached between the anions and the result does not show direct replacement of one anion in favor of another. The anion used is able to alter many properties of the cage including solubility and number of isomers formed, although the reason is relatively ambiguous. It is likely that there is some anion templation occurring which is evidenced in the host-guest binding experiments where **TzIm$_3$•Co•PhMe•NTf$_2$** is able to bind to progesterone but **TzIm$_3$•Co•PhMe•ClO$_4$** cannot, most likely because there is already something more preferred in the cavity.

4.7 References

1. Percástegui, E. G.; Mosquera, J.; Ronson, T. K.; Plajer, A. J.; Kieffer, M.; Nitschke, J. R. "Waterproof Architectures through Subcomponent Self-Assembly." *Chem. Sci*. **2019**, *10*, 2006–2018.

2. Percástegui, E. G.; Mosquera, J.; Nitschke, J. R. "Anion Exchange Renders Hydrophobic Capsules and Cargoes Water-Soluble." *Angew. Chemie Int. Ed.* **2017**, *56*, 9136–9140.

3. Greenaway, R. L.; Santolini, V.; Bennison, M. J.; Alston, B. M.; Pugh, C. J.; Little, M. A.; Miklitz, M.; Eden-Rump, E. G. B.; Clowes, R.; Shakil, A.; Cuthbertson, H. J.; Armstrong, H.; Briggs, M. E.; Jelfs, K. E.; Cooper, A. I. "High-Throughput

Discovery of Organic Cages and Catenanes Using Computational Screening Fused with Robotic Synthesis." *Nat. Commun.* **2018**, *9*, 1–11.

4. Ren, D. H.; Qiu, D.; Pang, C. Y.; Li, Z.; Gu, Z. G. "Chiral Tetrahedral Iron(II) Cages: Diastereoselective Subcomponent Self-Assembly, Structure Interconversion and Spin-Crossover Properties." *Chem. Commun.* **2015**, *51*, 788–791.

5. Bao, L. Y.; Hao, S. J.; Xi, S. F.; Yan, X.; Zhang, H. X.; Shen, R.; Gu, Z. G. "Chiral Supramolecular Coordination Cages as High-Performance Inhibitors against Amyloid-β Aggregation." *Chem. Commun*. **2018**, *54*, 8725–8728.

6. Zhang, D.; Ronson, T. K.; Greenfield, J. L.; Brotin, T.; Berthault, P.; Leónce, E.; Zhu, J. L.; Xu, L.; Nitschke, J. R. "Enantiopure $[Cs^{+}/Xe\subset Cryptophane]\subset Fe^{II}_{4}L_{4}$ Hierarchical Superstructures." *J. Am. Chem. Soc*. **2020**, *141*, 8339–8345.

7. Zhang, D.; Ronson, T. K.; Mosquera, J.; Martinez, A.; Guy, L.; Nitschke, J. R. "Anion Binding in Water Drives Structural Adaptation in an Azaphosphatrane-Functionalized $Fe^{II}_{4}L_{4}$ Tetrahedron." *J. Am. Chem. Soc*. **2017**, *139*, 6574–6577.

8. McConnell, A. J.; Aitchison, C. M.; Grommet, A. B.; Nitschke, J. R. "Subcomponent Exchange Transforms an FeII4L4 Cage from High- to Low-Spin, Switching Guest Release in a Two-Cage System." *J. Am. Chem. Soc.* **2017**, 139, 6294–6297.

9. Bilbeisi, R. A.; Zarra, S.; Feltham, H. L. C.; Jameson, G. N. L.; Clegg, J. K.; Brooker, S.; Nitschke, J. R. "Guest Binding Subtly Influences Spin Crossover in an $Fe^{II}_{4}L_{4}$ Capsule." *Chem. Eur. J.* **2013**, *19*, 8058–8062.

10. Evans, D. F. "The Determination of the Paramagnetic Susceptibility of Substances in Solution by Nuclear Magnetic Resonance." *J. Chem. Soc*. **1959**, *81*, 2003–2005.

11. Piguet, C. "Paramagnetic Susceptibility by NMR: The "Solvent Correction" Removed for Large Paramagnetic Molecules." *J. Chem. Educ.* **1997**, *74*, 815–816.
12. Bain, G. A.; Berry, J. F. "Diamagnetic Corrections and Pascal's Constants." *J. Chem. Educ*. **2008**, *85*, 532–536.

13. Riddell, I. A.; Ronson, T. K.; Clegg, J. K.; Wood, C. S.; Bilbeisi, R. A.; Nitschke, J. R. "Cation- and Anion-Exchanges Induce Multiple Distinct Rearrangements within Metallosupramolecular Architectures." *J. Am. Chem. Soc.* **2014**, *136*, 9491–9498.

14. Thordarson, P. "Determining Association Constants from Titration Experiments in Supramolecular Chemistry." *Chem. Soc. Rev.* **2011**, *40*, 1305–1323.

15. Brynn Hibbert, D.; Thordarson, P. “The Death of the Job Plot, Transparency, Open Science and Online Tools, Uncertainty Estimation Methods and Other Developments in Supramolecular Chemistry Data Analysis.” *Chem. Commun.* **2016**, *52*, 12792–12805.

16. Turega, S.; Cullen, W.; Whitehead, M.; Hunter, C. A.; Ward, M. D. “Mapping the Internal Recognition Surface of an Octanuclear Coordination Cage Using Guest Libraries.” *J. Am. Chem. Soc.* **2014**, *136*, 8475–8483.

17. Ward, M. D.; Hunter, C. A.; Williams, N. H. “Coordination Cages Based on Bis(Pyrazolylpyridine) Ligands: Structures, Dynamic Behavior, Guest Binding, and Catalysis.” *Acc. Chem. Res.* **2018**, *51*, 2073–2082.

Chapter 5: Investigations into the Synthesis of Novel Ligand Scaffolds

5.1 Introduction

New ligand systems are desired for forming complexes with interesting geometries and functionalities. Complexes with aldehyde cores are highly appealing as they can react with a wide variety of amines that have more interesting and valuable properties than previous diamine-based ligands. Aldehyde-ended cores take on a variety of different structures and can incorporate different metals, amine caps, and functional groups to create new assemblies with useful applications. Aldehyde-ended cores do not have to be limited to an "inverse" iminopyridine motif as they can be formed from formyl imidazole or an oxidized alkyl group. New ligand systems allow the opportunity for a variety of different geometries and novel properties. Aldehyde cores are highly desirable for their ability to undergo imine condensation with amines that have water soluble properties such as polyethylene glycol (PEG) or amino acids in hopes that the amine cap will confer its properties onto the complex. Described herein are the attempts to synthesize novel aldehyde ended ligands and some their complexes for new reactivity.

5.2 Mixed Tetrahedron

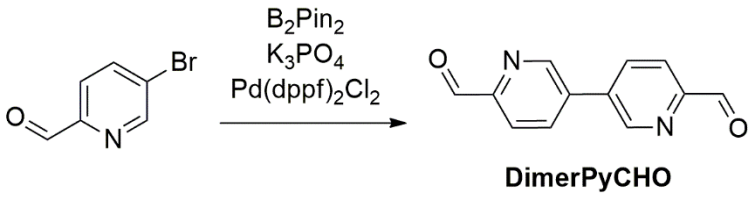

Figure 5.1: The synthesis of **DimerPyCHO**.

Dialdehyde ligand [3,3'-bipyridine]-6,6'-dicarboxaldehyde (**DimerPyCHO**) was initially synthesized by Calvin Wiley *via* literature methods.[1] **DimerPyCHO** was created by dimerizing 5-bromopyridine carboxaldehyde with itself *via* an initial borylation,[2] followed by Suzuki reaction to create the linear dialdehyde.[3] The synthesis of **DimerPyCHO** spawned multiple possible routes for novel cage complexes whereby diamine and dialdehyde ligands could be combined in one assembly system, hopefully showing social self-sorting (Figure 5.1).

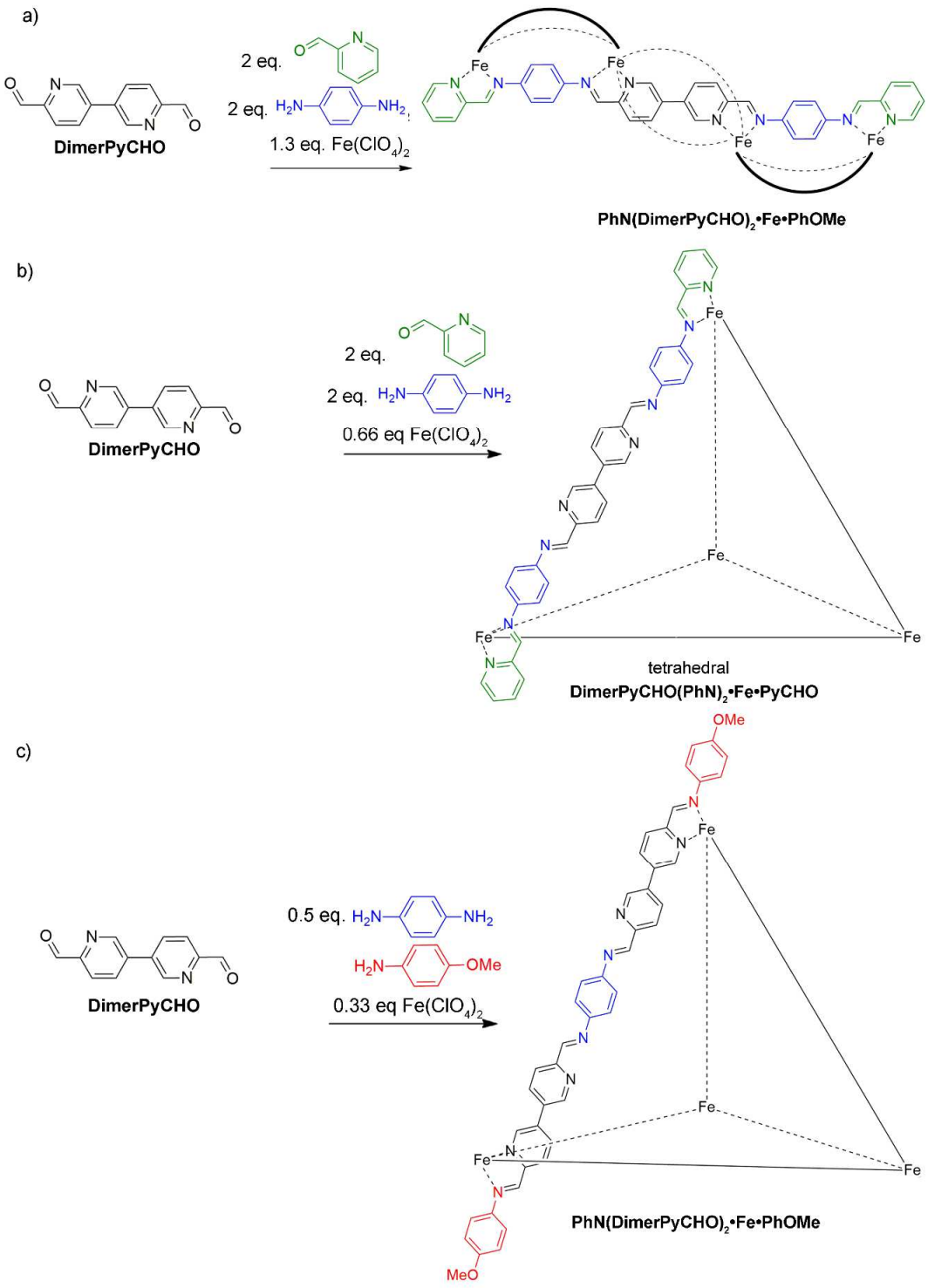

Figure 5.2: Synthetic routes for possible cage complexes with alternating amine and aldehyde components.

Attempts at creating these complexes ultimately failed. It was unclear if complexation was simply not possible or if **DimerPyCHO** had failed to be synthesized, as **DimerPyCHO** and 5-bromo-2-pyridine carboxaldehyde starting material have very similarly shifted ^{1}H NMR signals.

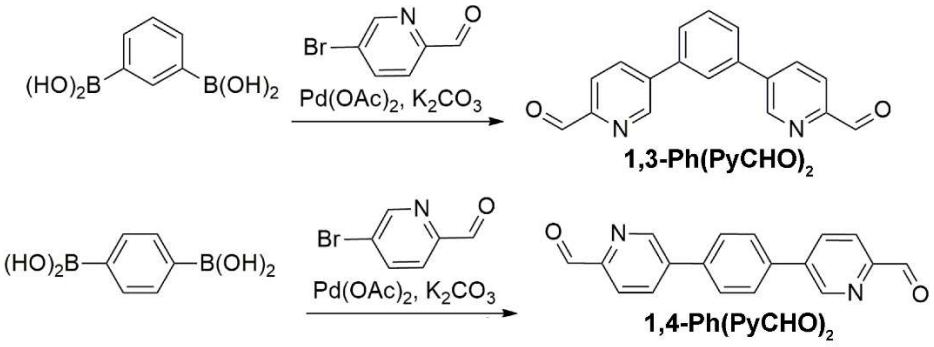

Figure 5.3: Synthetic pathways for dialdehyde ligand cores **1,3-Ph(PyCHO)$_2$•Fe•PhOMe** and **1,4-Ph(PyCHO)$_2$•Fe•PhOMe**.

The internal dialdehyde (**PhPyCHO**) was synthesized by coupling 1,3-phenyldiboronic acid or 1,4-phenyldiboronic acid with 5-bromo-2-pyridine carboxaldehyde *via* Suzuki reaction to create **1,3-Ph(PyCHO)$_2$** and **1,4-Ph(PyCHO)$_2$**, respectively.[1] The new **1,3-Ph(PyCHO)$_2$** core was tested to see if it would form a simple cage when combined with *p*-anisidine and $Fe(ClO_4)_2$. The synthesis was attempted both open to air and under inert atmosphere, however both sets of conditions resulted in no cage complex forming. Combining **1,4-Ph(PyCHO)$_2$** with $Fe(ClO_4)_2$ and *p*-anisidine under inert atmosphere at 50°C for 16 h created the tetrahedral cage **1,4-Ph(PyCHO)$_2$•Fe•PhOMe** and the ^{1}H NMR spectrum matched literature precedent.[1,4] Forming the tetrahedral cage complex with linear **1,4-Ph(PyCHO)$_2$** suggested that the bent **1,3-Ph(PyCHO)$_2$** was unable to create a stable cage complex under the same conditions.

We then became interested in seeing if **1,3-Ph(PyCHO)$_2$** and **1,4-Ph(PyCHO)$_2$** would be capable of reacting with other amines. When **1,4-Ph(PyCHO)$_2$** was combined with $Fe(BF_4)_2$ and *o*-toluidine at 50°C for 16 h, the product's ^{1}H NMR spectrum did not resemble a discrete cage, but instead looked more like a polymer had formed.

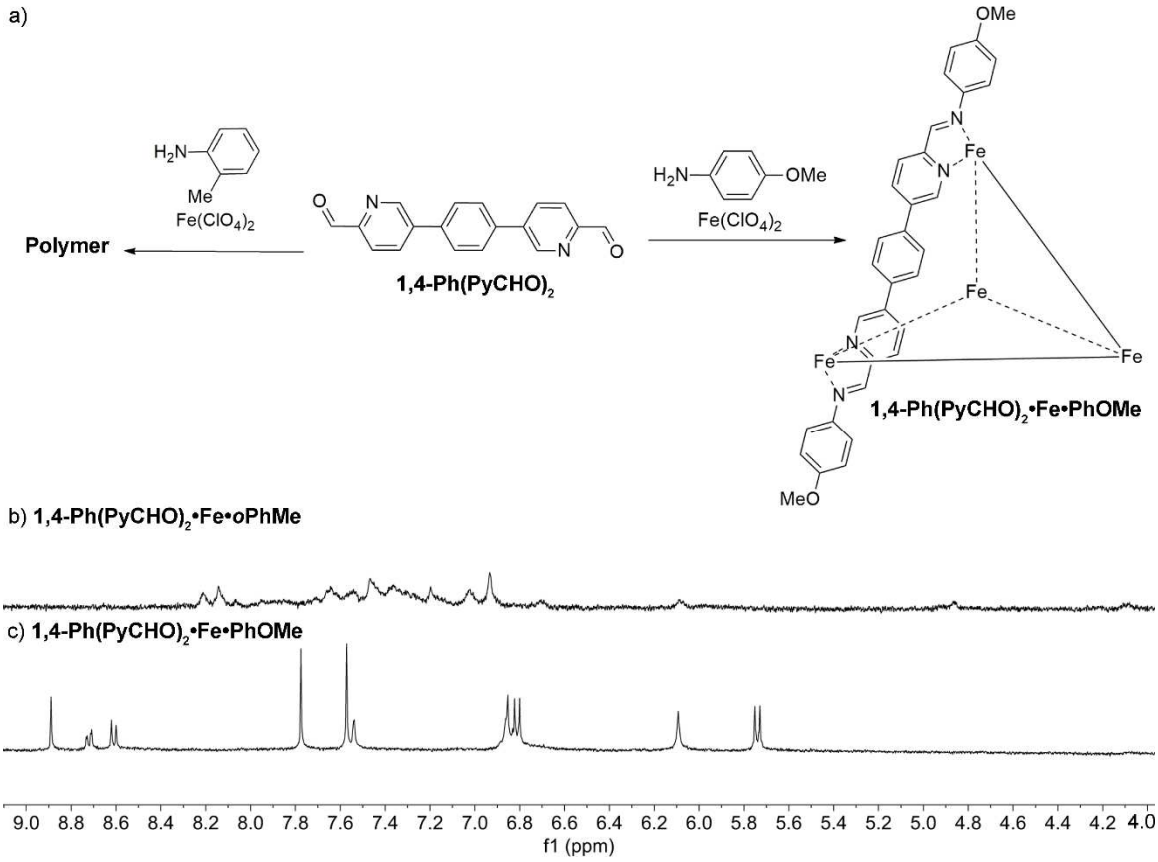

Figure 5.4: a) Synthesis of cages made from linear dialdehyde **1,4-Ph(PyCHO)$_2$**, and the ^{1}H NMR spectra of b) **Ph(PyCHO)$_2$•Fe•*o*PhMe** and c) **Ph(PyCHO)$_2$•Fe•PhOMe** (CD_3CN, 400 MHz, 298 K).

Synthesis of cages using **1,3-Ph(PyCHO)$_2$** with $Fe(BF_4)_2$ and other amines were tested to determine if other complexes could be formed (Figure 5.5). We wanted to create assemblies with alternating diamine and dialdehyde components in order to form longer ligands and obtain a complex with multiple cavities. Beginning with a dialdehyde (either

1,3-Ph(PyCHO)$_2$ or **1,4-Ph(PyCHO)$_2$**), we could perform imine condensation with a diamine and cap the ligand with **PyCHO** in the presence of Fe(II) to create a self-assembled ligand with a ABCBA pattern.

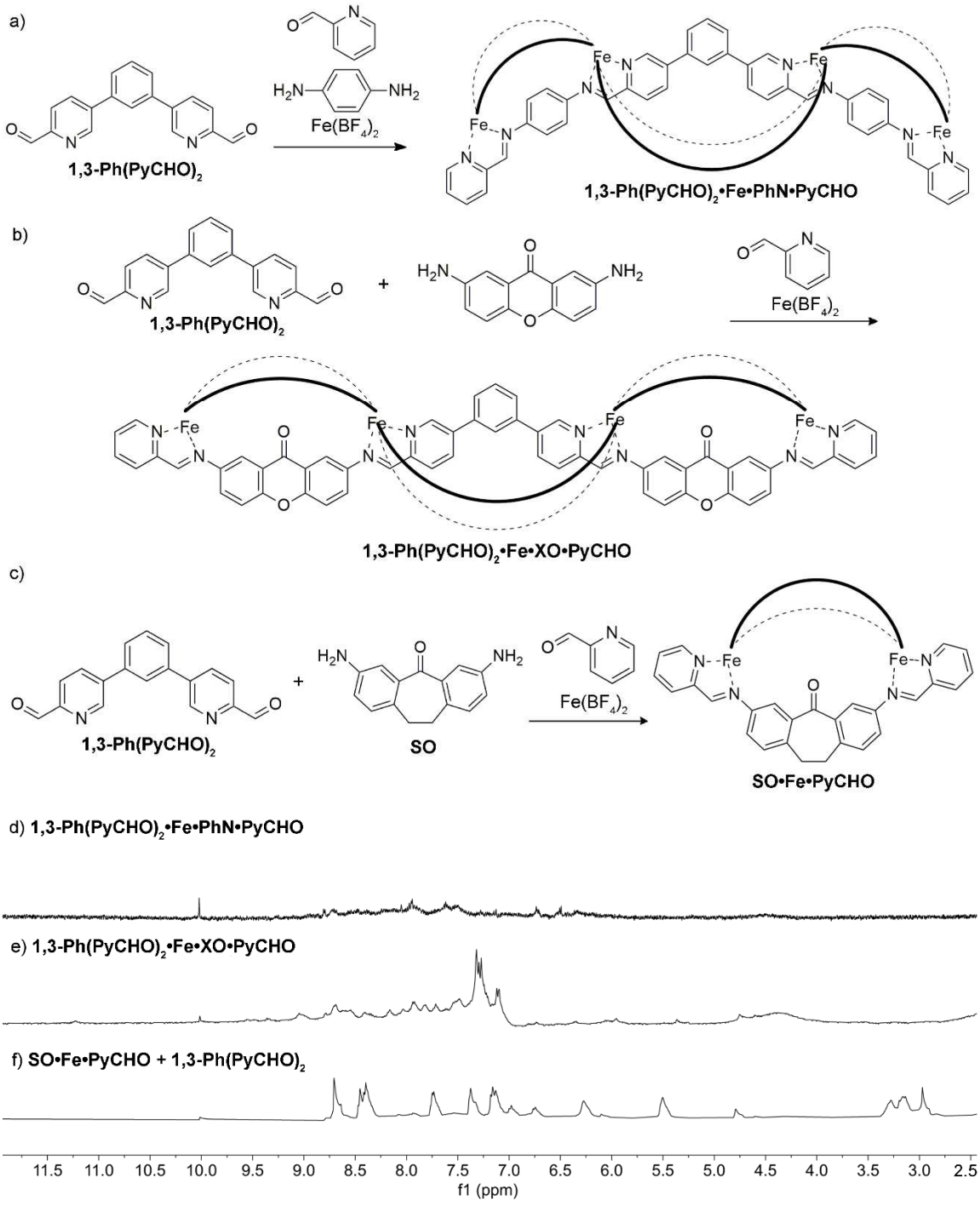

Figure 5.5: Attempted syntheses of cages with multiple cavities for a) **1,3-Ph(PyCHO)$_2$•Fe•PhN•PyCHO**, b) **1,3-Ph(PyCHO)$_2$•Fe•XO•PyCHO**, and failed synthesis attempt for c) **1,3-Ph(PyCHO)$_2$•Fe•SO•PyCHO**. ^{1}H NMR of d) **1,3-Ph(PyCHO)$_2$•Fe•PhN•PyCHO**, e) **1,3-Ph(PyCHO)$_2$•Fe•XO•PyCHO**, and f) the product of **SO**, **1,3-Ph(PyCHO)$_2$**, **PyCHO**, and $Fe(ClO_4)_2$ (CD_3CN, 400 MHz, 298 K).

Most of the diamines we have previously used to make cage complexes would not be suitable for synthesizing a ligand with an ABCBA pattern, as an ABA combination would create a more energetically favorable complex. This theory was confirmed when **1,3-Ph(PyCHO)$_2$**, **PyCHO**, **SO**, and $Fe(BF_4)_2$ were combined in inert atmosphere with dry acetonitrile and reacted at 80°C for 16 h. The product ^{1}H NMR spectrum showed **SO•Fe•PyCHO** and unreacted **1,3-Ph(PyCHO)$_2$** present in solution. Therefore, we were limited to using diamines that were either too small to form complexes on their own, or would create relatively strained complexes, such as **XO** which exhibits some paramagnetic signals in the ^{1}H NMR spectrum of **XO•Fe•PyCHO**. Using phenylenediamine as the diamine source with either **1,3-Ph(PyCHO)$_2$** or **1,4-Ph(PyCHO)$_2$**, $Fe(BF_4)_2$, and PyCHO, resulted in a new set of signals. Due to the increased ligand length and alternating components (see Figure 5.5) there is a much higher likelihood for polymerization to occur. The ^{1}H NMR spectra for these products are consistent with polymer formation, with both product solutions showing no discrete complex formed. As **XO** creates a strained complex with **PyCHO**, the diamine was expected to be a good candidate for complexation with **PyCHO**, **1,3-Ph(PyCHO)$_2$**, and $Fe(BF_4)_2$. When the components were combined and reacted together the product again resembled a polymer, more than a discrete complex, however these peaks were sharp and distinctly different from the signals of the **XO•Fe•PyCHO** cage complex.

5.3 Tetrazine Ligands

Creating new ligands with unique properties for cage complexation can be as simple as altering a functional group on a known ligand, however creating more novel ligands can allow for new reactivity such as post assembly modification. Ring-forming reactions can be used to combine components and integrate new functional groups into the ligand backbone. Using tetrazine rings in ligand synthesis allowed for a new pathway to form aldehyde-ended cores. If successful, a large variety of ligands with tetrazine rings could be easily synthesized due to the wide library of nitrile compounds commercially available.

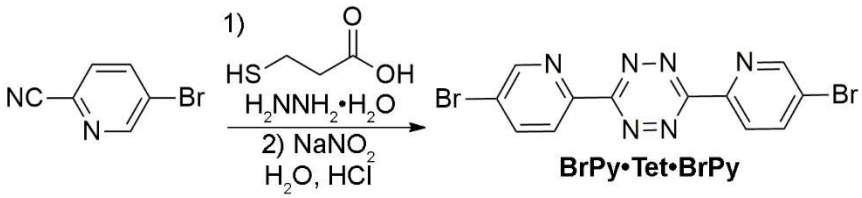

Figure 5.6: Tetrazine formed from pyridinecarbonitrile.

Tetrazine rings are made through a facile cyclization reaction from two cyano groups. Our initial tetrazine ring was dimer of pyridinecarbonitrile synthesized via literature methods.[5] The success of the reaction allowed us to look at synthesizing longer aromatic backbones incorporating tetrazine rings, by using combinations of acrylonitrile (**VCN**), acetonitrile (**MeCN**), terephthalonitrile (**TPCN**), and *p*-chlorobenzonitrile (**BnClCN**). **VCN** is attractive because it could be subsequently oxidized to produce the dialdehyde. **MeCN** could create tetrazine rings and the methyl group from **MeCN** becomes an activated carbon capable of radical bromination which can then be further reacted to produce the aldehyde. **TPCN** has two cyano groups and can react to create two tetrazine

rings, so depending on what other nitriles are present can create at least a three-ring system. **ClBnCN** was used for control reactions, reacting with either **VCN** or **MeCN**.

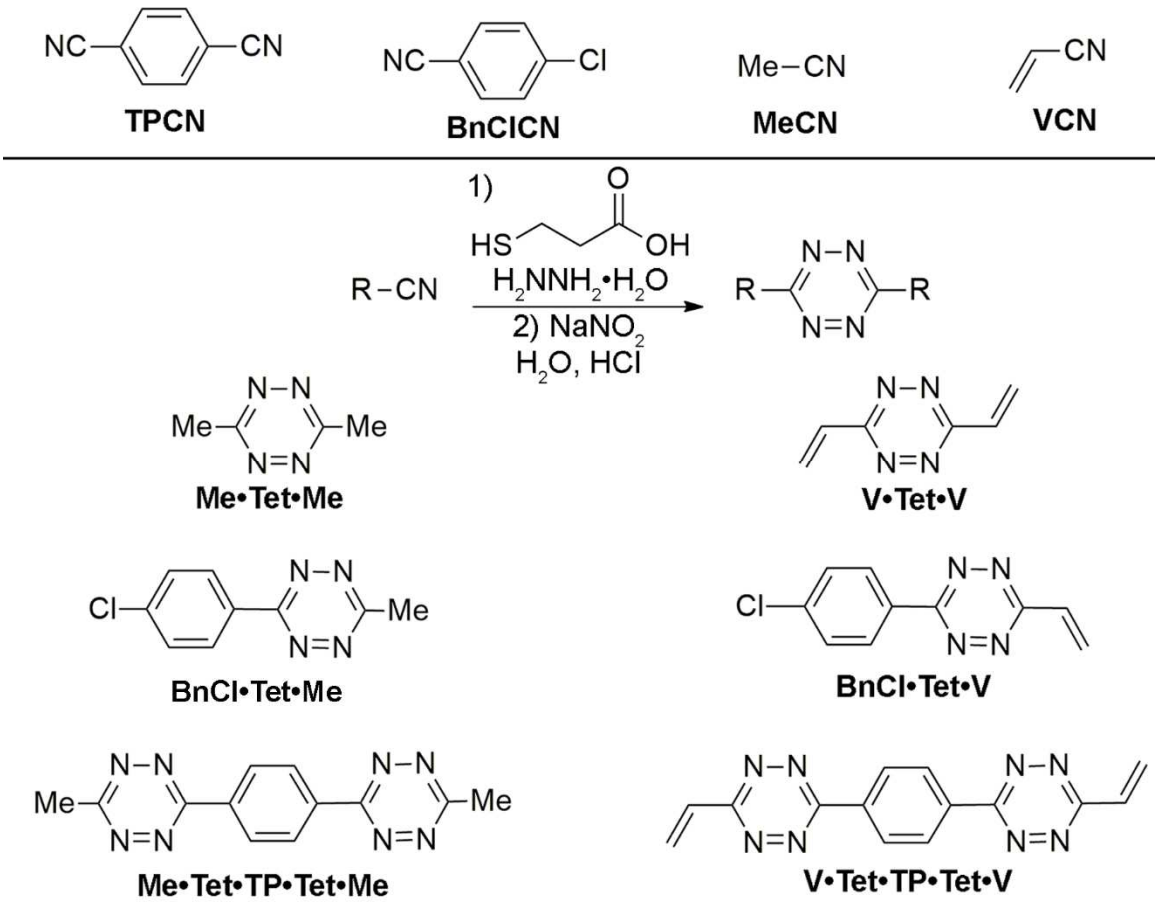

Figure 5.7: Nitriles used for novel tetrazine synthesis and the library of tetrazine compounds formed.

The target complex shown in Figure 5.7 involved using either **Me•Tet•TP•Tet•Me**, or **V•Tet•TP•Tet•V** as they are all symmetric. Both the methyl group and vinyl group can be reacted form aldehydes and make the dialdehyde core for a cage complex. The methyl group can undergo radical bromination to form **$BrCH_2$•Tet•TP•Tet•$BrCH_2$**, followed by an S_N2 reaction with NaOH to produce the alcohol **CH_2OH•Tet•TP•Tet•CH_2OH**, which then oxidized to form the dialdehyde **CHO•Tet•TP•Tet•CHO**. Whereas the vinyl group

can undergo an oxidation reaction, such as ozonolysis, to form dialdehyde **CHO•Tet•TP•Tet•CHO**. The dialdehyde then can be reacted with *p*-anisidine and Fe(II) to obtain the desired cage.

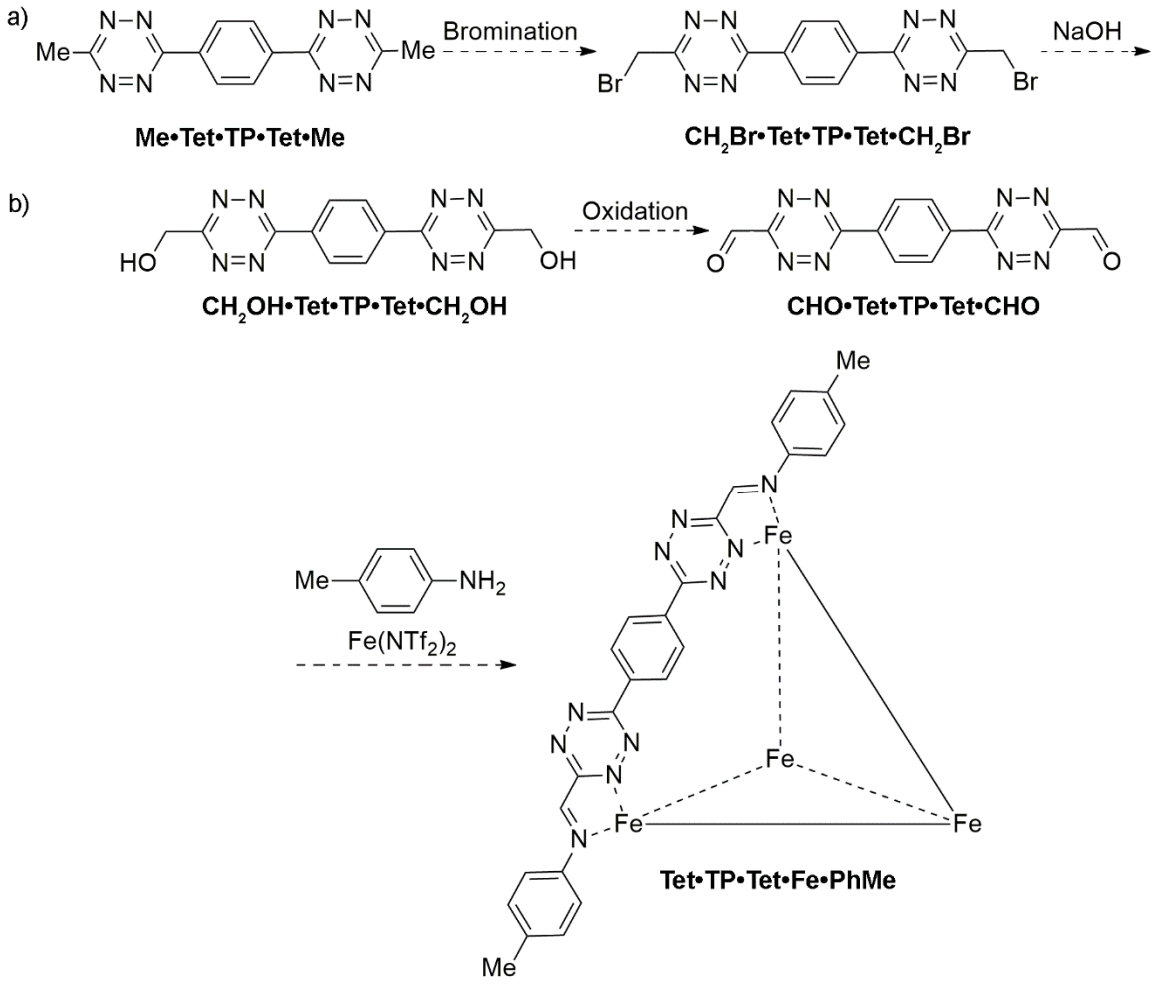

Figure 5.8: Projected possible synthesis to create dialdehyde core and cage complex *via* tetrazine containing compounds. a) Synthesis of **CHO•Tet•TP•Tet•CHO** from **Me•Tet•TP•Tet•Me**. b) Synthesis of **CHO•Tet•TP•Tet•CHO** from **V•Tet•TP•Tet•V**. c) Synthesis of target cage *via* imine condensation of **CHO•Tet•TP•Tet•CHO** and **PhMe**.

To create ligands that are capable of making cage complexes we would need to focus on the tetrazine compounds made with **TPCN**. The **TPCN** ligands long enough to accommodate metal coordination, unlike the dimers, and have either methyl or vinyl

groups on both ends. Using either **Me•Tet•TP•Tet•Me** or **V•Tet•TP•Tet•V** as the ligand precursor should allow for the creation of symmetrical dialdehyde core **CHO•Tet•TP•Tet•CHO**. However, with multiple methyl or vinyl groups there is higher likelihood for side products to occur which can make testing new reactions conditions difficult. Therefore, tetrazine rings made with **BnClCN** were used as a control for testing new reaction conditions. Using **BnClCN** to form **BnCl•Tet•Me** or **BnCl•Tet•V** results in only one methyl or vinyl group available to undergo further reations. The benzyl chloride substituent should be unaffected by reaction conditions allowing **BnCl•Tet•Me** or **BnCl•Tet•V** to proceed fully to the formation of the aldehyde. Unfortunately, **VCN** proved difficult to work with, because while it could successfully be used to create **V•Tet•V**, **V•Tet•TP•Tet•V**, and **BnCl•Tet•V**, the double bond was prone to undergo side reactions, resulting in the formation of multiple products that were difficult to separate. **MeCN** was able to form rings **Me•Tet•Me**, **Me•Tet•TP•Tet•Me**, and **BnCl•Tet•Me** cleanly. Each of the products from the tetrazine ring syntheses resulted varying shades of vibrant pink powders.

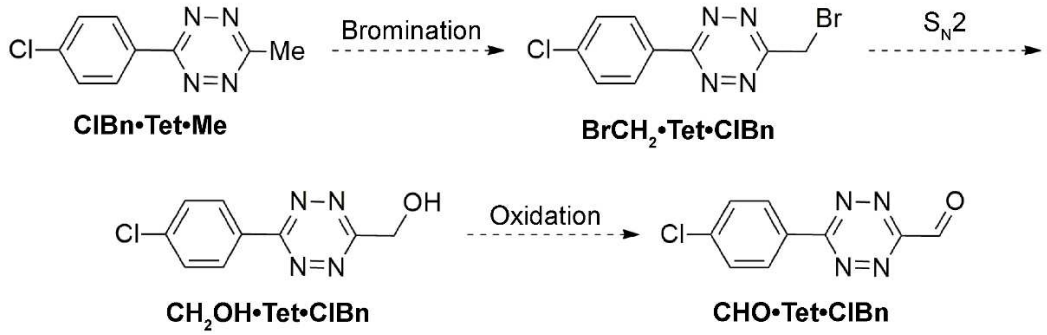

Figure 5.9: Projected possible synthesis from tetrazine to aldehyde. a) The tetrazine rings synthesized from **MeCN** could be brominated to form **BrCH₂•Tet•ClBn**, which can be reacted *via* S_N2 reaction with NaOH to for alcohol **CH₂OH•Tet•ClBn**, and finally oxidized to form the desired aldehyde **CHO•Tet•BnCl**.

Tetrazine rings were formed with **BnClCN** to be used in control reactions to show proof-of-concept for aldehyde formation. Compound **Me•Tet•BnCl** has only one methyl group which limits the number of products that can be produced. Tetrazine ring **Me•Tet•BnCl** was able to be synthesized and produce clean product with little to no side products present which is very desirable as the next step is a radical bromination. Three different sets of radical bromination reaction conditions were attempted on **Me•Tet•BnCl**, and none of these condition sets were able to generate the desired product. Reaction conditions were either too weak and did not affect the starting material or affected sites on the molecule other than the benzylic position, ultimately producing no **BrCH$_2$•Tet•BnCl** in any case. One set of conditions did seem to form some brominated compound in low yield, but the yield was not able to be increased when reaction conditions were altered to encourage reactivity. If a more appropriate set of brominating conditions can be found for this compound it may be possible to produce desired dialdehyde ligands.

5.4 Linear Dialdehyde Ligands

An alternative to introducing multiple aldehyde groups on a premade ligand is to incorporate components that already contain aldehyde functional groups such as formylimidazole or formylpyridine. Formylpyridine can be limiting as there is only one position on the ring for the aldehyde that would allow chelation, post-assembly, and electrophilic aromatic substitution to formylate pyridine is very difficult, due to the electron poor nature of the ring. Imidazole, on the other hand, can be used in coupling reactions such as the Chan-Lam-Buchwald reaction. The Chan-Lam-Buchwald reaction can be used

to couple imidazole to an aromatic dibromide:[6] this leads to the question of whether formyl-imidazole is a suitable coupling partner, which would create a linear dialdehyde core.

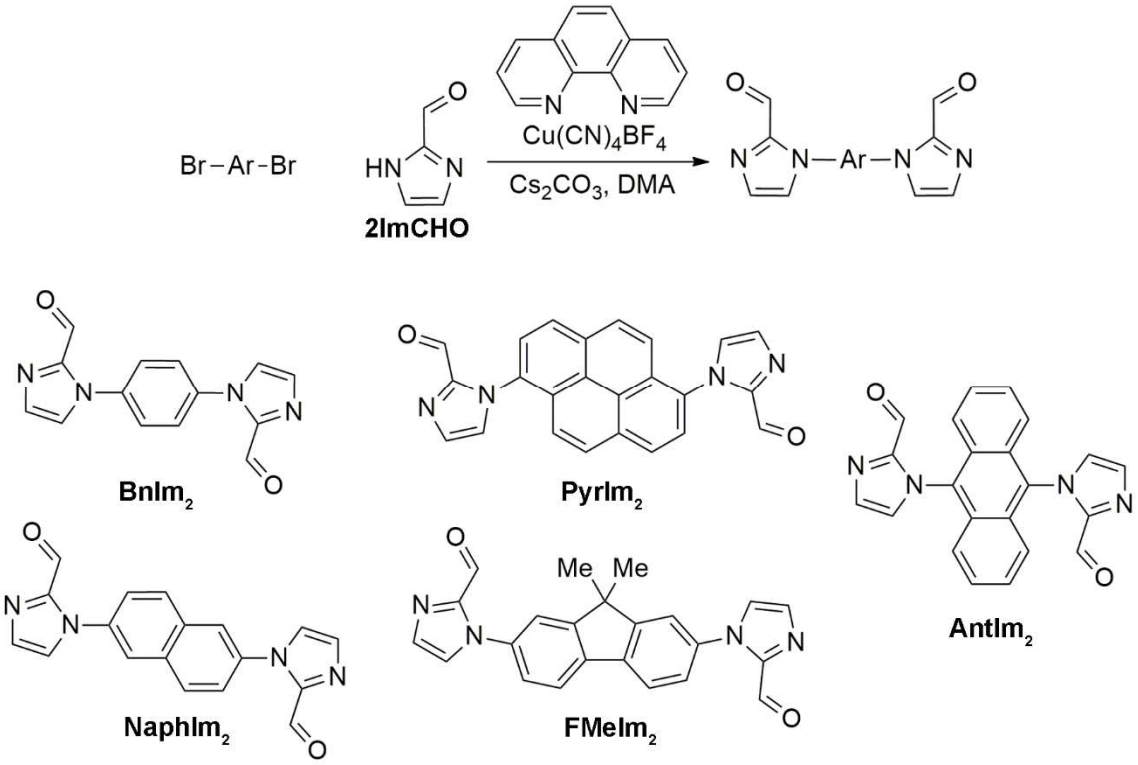

Figure 5.10: Synthetic scheme of diimidazoles produced from the Chan-Lam-Buchwald reaction.

Between the two possible choices of formylimidazoles, **2ImCHO** or **4ImCHO**, **2ImCHO** was chosen for this set of reactions. **B**ased on literature precedence groups at either the 2- or 4-position should not affect the reaction from occurring, but using **2ImCHO** resulted in fewer side products occurring. The Chan-Lam-Buchwald reaction can successfully incorporate a wide range of aromatic molecules with various functional groups.[6] The reaction is also amenable to being performed twice on the same aromatic substrate. The aromatic compounds that we have successfully coupled to **2ImCHO** *via* the Chan-Lam-Buchwald reaction are benzene (**Bn**), pyrene (**Pyr**), anthracene(**Ant**),

naphthalene(**Naph**), and dimethylfluorene(**FMe**). Complexation experiments have yet to be performed to determine best metal to complex with and determine any parameters for amine caps. Metals that are likely for these aromatic dialdehydes to form cage complexes would be Co (II) and Cd (II), based on what is known about **TzIm$_3$•Co•PhMe**. Amine caps give the opportunity to introduce new functionality to the complex such as water solubility, so we are interested in testing water soluble amine such as PEG amines.

5.5 Triazine Ligands

Complex **TzIm$_3$•Co•PhMe** was the first successful triazine ligand cage complex we had created. The triazine core offers many opportunities for functionalization on the phenyl rings surrounding the triazine ring and either amine or aldehyde ends. While we had success with the **TzIm$_3$•Co•PhMe** complex, we were interested in how adding functional groups or changing the chelator would affect complexation, properties, and trends in binding.

One of the simplest derivatizations of the **TzIm$_3$•Co•PhMe** cage complex is to create a ligand without the benzylic carbon. One of the reasons for creating this ligand would be to limit the number of possible isomers formed and definitively determine that the number of isomers seen in chapter 4 for **TzIm$_3$•Co•PhMe** is due to coordination around the metal center as stated in section 4.2 not an effect of the ligand itself. To create the more rigid triazine ligand 4-bromobenzonitrile was used to create triazine **RTz** (Figure 5.9). Using the Chan-Lam-Buchwald reaction **RTz** was coupled to **2ImCHO** to produce **RTzIm$_3$**. Triimidazole **RTzIm$_3$** was complexed with *p*-toluidine and $Co(NTf_2)_2$ to create

RTzIm$_3$•Co•PhMe. The ^{1}H NMR spectrum of **RTzIm$_3$•Co•PhMe** was very similar to the spectrum of **TzIm$_3$•Co•PhMe**, showing that there were still multiple isomers present due to coordination around the metal center not the flexibility of the ligand.

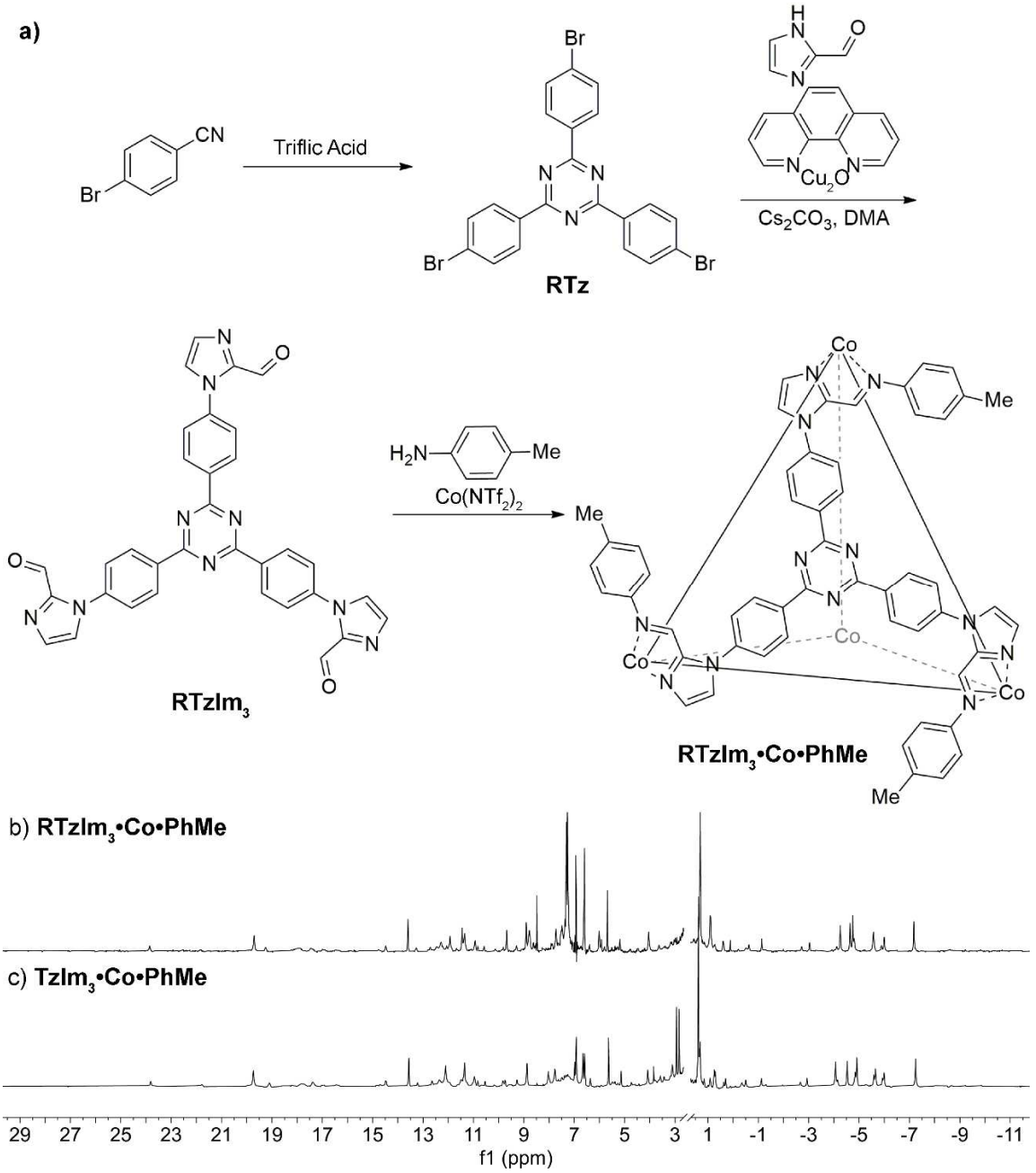

Figure 5.11: a) Synthesis of rigid triazine complex **RTzIm$_3$•Co•PhMe** the ^{1}H NMR spectrum of b) **RTzIm$_3$•Co•PhMe** and c) **TzIm$_3$•Co•PhMe** (400 MHz, 298 K, CD_3CN).

Novel triazine cores can be created using functionalized benzonitrile rings and may allow us to create new complexes with different properties. The 2- and 4-position can accommodate the presence of various functional groups so long as they do not prevent complexation and using protecting groups as needed. Novel triazine rings would then further reacted to obtain new tetrahedral complexes. The first step to new triazine ligands is ensuring that the new functional groups do not impair triazine formation. When 2-hydroxy-4-methylbenzonitrile was used to make triazine **Tz(OHMe)3** ring under the same conditions as the 4-cyanobenzyl bromide cyclization, it did not proceed to form clean product. Side reactions occurred due to the alcohol interfering during ring cyclization. Further reactions may be probed by installing a protecting group on the 2-hydroxy-4-methylbenzonitrile such as CBz, and proceeding with cyclization (Figure 5.12).

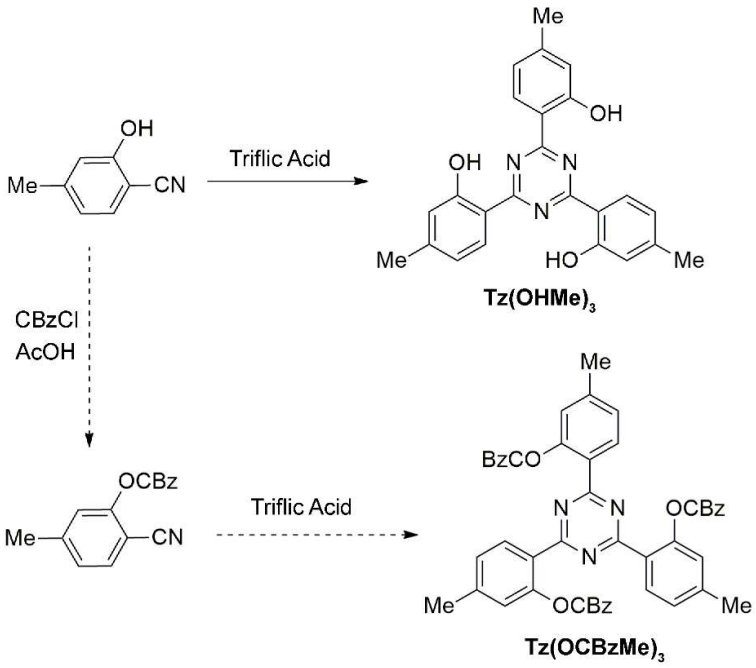

Figure 5.12: Projected synthesis of triazine ring with alcohol and secondary synthetic route using the CBz protecting group on the alcohol.

An alternative synthetic route for making a triazine with alcohols uses cyanuric chloride as the triazine source. The three chlorides on cyanuric chloride can be used to perform either coupling or substitution reactions. One possible synthetic pathway for adding alcohol functional groups uses the chloride for Friedel-Crafts benzylation, where resorcinol reacts with cyanuric chloride to form **Tz(OH)$_3$**. While the reactivity of the alcohols from resorcinol is very similar, there is some literature precedent for differentiating the alcohols and selectively reacting at one of the positions.[7] We expect to either selectively acetalize or react the alcohol in the 4-position with triflate to produce **TzOHOAc** or **TzOHTf**, respectively. Either option would allow for selective reactivity and desirable intermediate. The triflate on **TzOHTf** would then undergo a Chan-Lam-Buchwald reaction with **2ImCHO** to give the tris(2-hydroxy-4-(2-formylimidazole)) triazine, **TzOHIm$_3$** seen in Figure 5.10. Triazine **TzOHIm$_3$** has the same backbone as triazine **TzIm$_3$**, which allows us to see how adding the alcohol at the 2-position of the benzyl would affect complexation and binding of the complex.

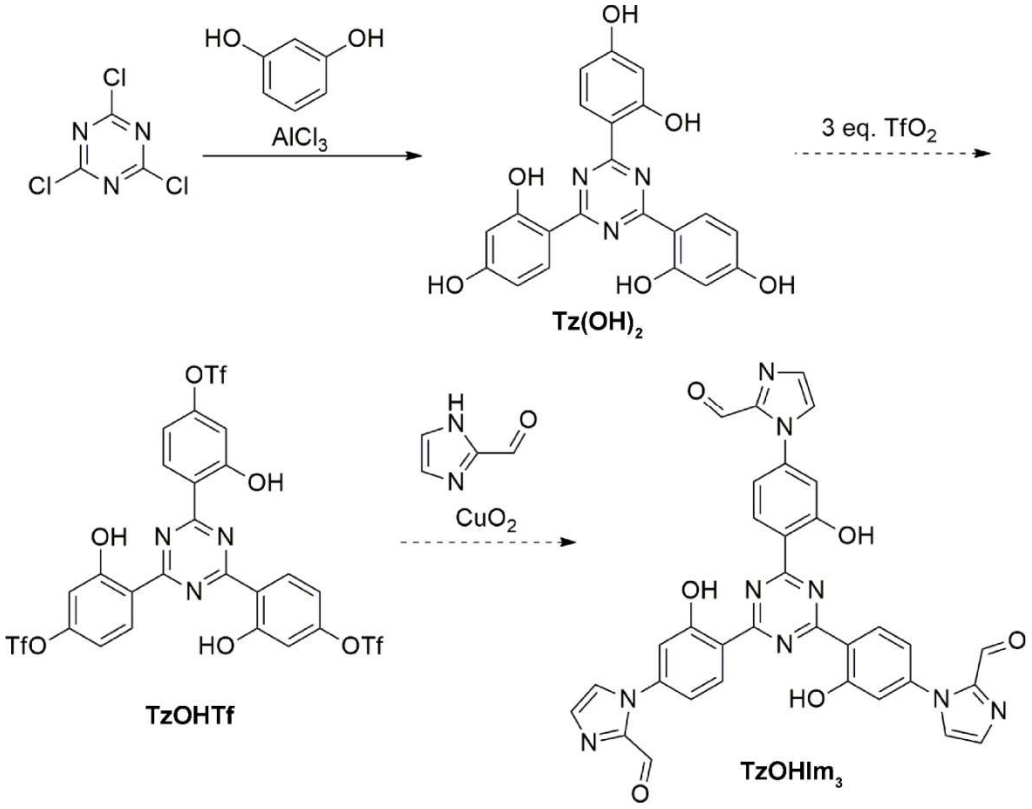

Figure 5.13: Alternative reaction pathway to form an alcohol containing triazine ring using resorcinol.

To make an iminopyridyl triazine complex we used a different approach to making triazine rings. As opposed to coupling formylimidazole to the triazine ring, a triazine ring would be formed containing pendant amine groups. After the success of this reaction we can now try various combinations of metal salts and **PyCHO** to make a cage complex. To first create the triamine triazine ring, a melt reaction was performed with 4-nitrobenzylnitrile, potassium hydroxide, and 18-crown-6 to give, **NO_2Tz**, which would then be reduced using Raney nickel to form triamine triazine **AmTz**. Triazine **AmTz** would then ideally be coupled to either **2ImCHO**, **4ImCHO**, or **PyCHO** to produce comparable diamagnetic or paramagnetic complexes. Creating a diamagnetic counterpart is also of

interest as paramagnetism complicates NMR spectroscopy because of the shifted and broadened signals. However, when complexation was attempted with any of the aldehydes and $Fe(NTf_2)_2$, no cage complex was produced, even after varying conditions including temperature (50°C or 80°C) or ambient or inert atmosphere. Further testing with alternate metals such as Cd(II) or Co(II) may generate cage complexes.

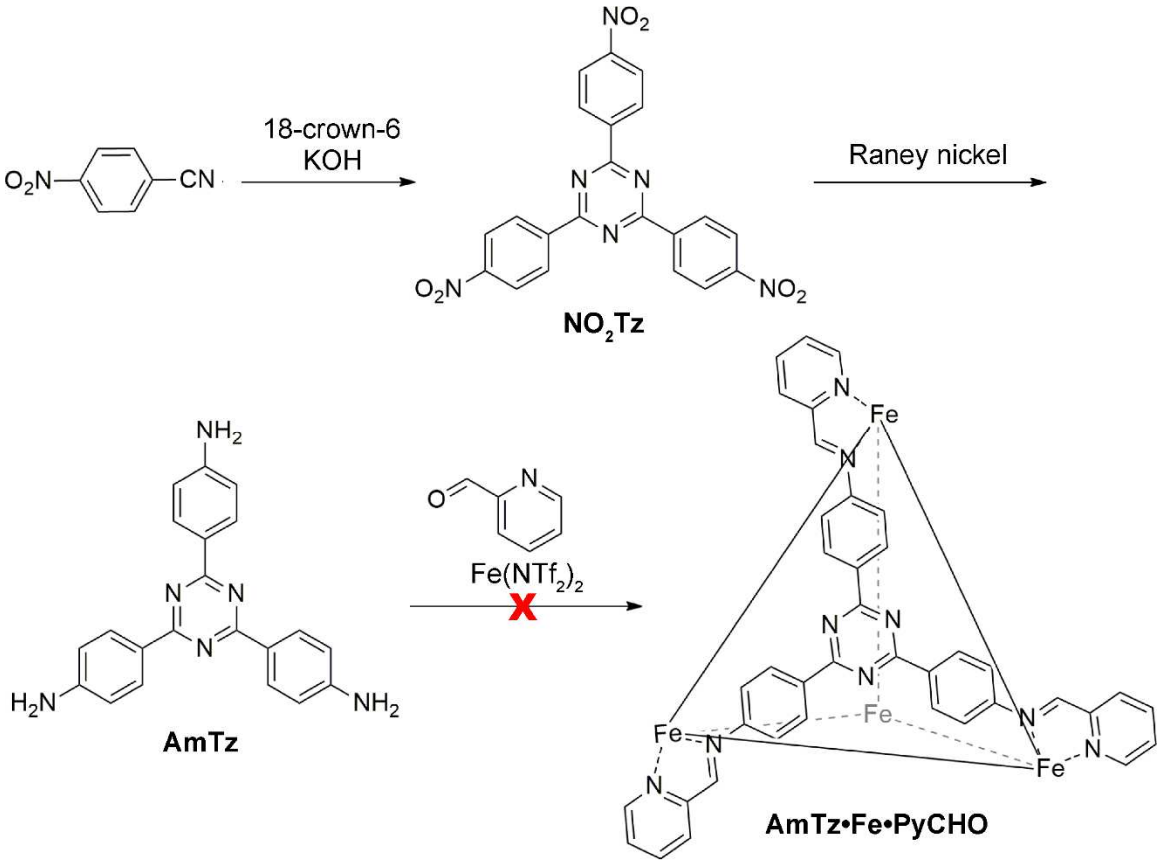

Figure 5.14: Synthetic pathway of **AmTz•Fe•PyCHO** from 4-nitrobenzonitrile.

5.6 Conclusion

Aldehyde ligands are a highly desirable target because of the seemingly limitless applications that can be performed from using amine caps. In this research we have shown

several attempts and promising pathways for creating aldehyde ended cores. Initially, small dialdehydes were used in attempt to extend ligands and create multiple small pockets in a single complex. The small dialdehydes were able to successfully undergo imine condensation with diamines but instead creating ligands of desired length polymerized. Tetrazine containing compounds seemed to be a promising synthesis to create longer ligands with aldehyde ended cores for new coordinators. However, bromination of the methyl group proved difficult to get a significant yield to move to the next step.

Integrating imidazole rings into ligand synthesis created a new way to add aldehydes to the ligand core without having to perform oxidization reactions. The most promising synthetic routes to more aldehyde ended cores result from either coupling or substituting formylimidazole onto aromatic compounds. The linear dialdehyde cores formed from the Chan-Lam-Buchwald reaction can create complexes with varying geometries and complexity dependent on the aromatic dibromide used. The triazine motif is limited to the tetrahedral geometry and has shown promise as the **TzIm$_3$•Co•PhMe** in binding bioactive compounds. We are interested in adding functional groups to the benzene rings of the triazine core to see if new trends in bind or synthesis occur. Work will continue in this lab to generate new aldehyde ended cores to form complexes with amine caps. With these new chelators we desired to create water-soluble complexes and create covalent organic cages.

5.7 References

(1) Ousaka, N.; Grunder, S.; Castilla, A. M.; Whalley, A. C.; Stoddart, J. F.; Nitschke, J. R. “Efficient Long-Range Stereochemical Communication and Cooperative

Effects in Self-Assembled Fe_4L_6 Cages." *J. Am. Chem. Soc*. **2012**, *134*, 15528–15537.

(2) Erb, W.; Hellal, A.; Albini, M.; Rouden, J.; Blanchet, J. "An Easy Route to (Hetero)Arylboronic Acids." *Chem. Eur. J*. **2014**, *20,* 6608–6612.

(3) Butters, M.; Harvey, J. N.; Jover, J.; Lennox, A. J. J.; Lloyd-Jones, G. C.; Murray, P. M. "Aryl Trifluoroborates in Suzuki-Miyaura Coupling: The Roles of Endogenous Aryl Boronic Acid and Fluoride." *Angew. Chemie. Int. Ed*. **2010**, *49*, 5156–5160.

(4) Ma, S.; Smulders, M. M. J.; Hristova, Y. R.; Clegg, J. K.; Ronson, T. K.; Zarra, S.; Nitschke, J. R. "Chain-Reaction Anion Exchange between Metal-Organic Cages." *J. Am. Chem. Soc.* **2013**, *135*, 5678–5684.

(5) Roberts, D. A.; Pilgrim, B. S.; Cooper, J. D.; Ronson, T. K.; Zarra, S.; Nitschke, J. R. "Post-Assembly Modification of Tetrazine-Edged $Fe^{II}_4L_6$ Tetrahedra." *J. Am. Chem. Soc.* **2015**, *137*, 10068–10071

(6) Altman, R. A.; Koval, E. D.; Buchwald, S. L. "Copper-Catalyzed N-Arylation of Imidazoles and Benzimidazoles." *J. Org. Chem.* **2007**, *72*, 6190–6199.

(7) Miyazawa, T.; Hamada, M.; Morimoto, R.; Maeda, Y. "Candida Antarctica Lipase B-Mediated Regioselective Acylation of Dihydroxybenzenes in Organic Solvents." *Tetrahedron* **2015**, *71*, 3915–3923.

Chapter 6 Experimental

6.1 General Information

^{1}H and ^{13}C NMR spectra were recorded on either a Varian Inova 400 MHz NMR spectrometer, an Avance NEO 400 MHz spectrometer or a Bruker 600 MHz spectrometer and processed using MestReNova by Mestrelab Research S.L. gCOSY NMR were recorded on a an Avance NEO 400 MHz spectrometer or Bruker 600 MHz spectrometer equipped with TopSpin. Proton (^{1}H) chemical shifts are reported in parts per million (ppm) with respect to tetramethylsilane (TMS, $\delta = 0$). ^{1}H and ^{13}C spectra are referenced internally with respect to the solvent residual peak. Deuterated NMR solvents were obtained from Cambridge Isotope Laboratories, Inc., Andover, MA, and used without further purification. Mass spectra were recorded on an Agilent 6210 LC TOF mass spectrometer using electrospray ionization with fragmentation voltage set at 115 V and processed with an Agilent MassHunter Operating System for data collected in chapters 2-4. Mass spectrometric analysis for Chapter 2-4 was performed using a Thermo LTQ linear ion trap with a standard electrospray ionization source (Thermo Fisher Scientific, San Jose, CA, USA). Samples were directly infused at 3 μL/min in 100% MeCN, with the source voltage set to 3 kV, tube lens at 75 kV and the capillary temperature at 270°C. CID spectra were collected in ZoomScan mode where the isolation window = 5 m/z, normalized collision energy (nCE) = 30 and activation time = 30 ms. MS data was analyzed using Thermo XCalibur. Mass spectroscopic samples for cages in Chapter 2 were infused into an Orbitrap Velos Pro mass spectrometer with the standard HESI source at a flow rate of 3 μL/min. The spray voltage was 3 kV, capillary temperature was set to 170°C and an S-lens RF level

of 45% was applied. Full FTMS were acquired with a resolution of r = 30,000, and ambient ions were used as internal lock mass calibrants. CID spectra were collected in ZoomScan mode where the isolation window = 5 m/z, normalized collision energy (nCE) = 30 and activation time = 30 ms. MS data was analyzed using Thermo XCalibur. Predicted isotope patterns were prepared using ChemCalc.1 X-Ray diffraction data was obtained and the crystal structure of **X•Fe•MePyCHO** was solved at the UC Riverside ACIF facility. Data collection, solution, and refinement were routine. X-ray intensity data were collected at 100(2) K on a Bruker APEX2 platform-CCD X-ray diffractometer system (fine focus Mo-radiation, λ = 0.71073 Å, 50KV/30mA power). The structure was deposited at the CCDC (#1848253). The diffraction data for **FOH•Fe•MePyCHO•ClO_4•$(NTf_2)_7$** was obtained at the UC San Diego X-ray Crystallography Facility, and the structure was solved at the UC Riverside ACIF facility. X-ray intensity data were collected at 150(2) K on a Bruker Rotating Anode generator with APEX2 platform-CCD X-ray diffractometer system (Mo-radiation, λ = 0.71073 Å, 50KV/24mA rotating anode power). The structure was deposited at the CCDC (#1848254). All other materials were obtained from Aldrich Chemical Company, St. Louis, MO and were used as received. Solvents were dried through a commercial solvent purification system (Pure Process Technologies, Inc.). Molecular modeling (semi-empirical calculations) was performed using the AM1 force field using SPARTAN.

6.2 Chapter 2 Experimental

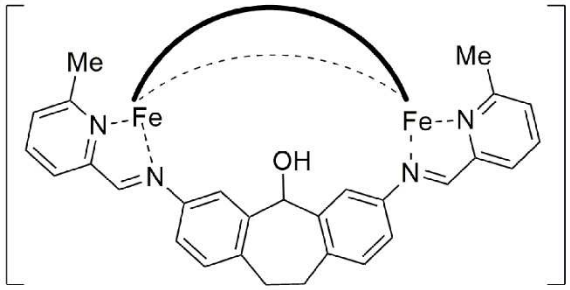

***Meso*-helicate SOH•Fe•MePyCHO:**

2,7-diaminosuberol (**SOH)** (170 mg, 0.71 mmol), 6-methylpyridine-2-carboxaldehyde (171 mg, 1.41 mmol), and $Fe(NTf_2)_2$ (310 mg, 0.47 mmol) were combined in MeCN (10 mL) in a 25 mL round-bottom flask. The solution was then heated at 77°C for 48 h with stirring. The reaction mixture was cooled, and the acetonitrile removed *in vacuo*. The red solid was sonicated with 20 mL of 3:1 Et_2O:MeOH solution and filtered. After drying, the product was isolated as a red powder (572 mg, 91% yield). ^{1}H NMR (400 MHz; CD_3CN) δ 196.64 (s), 60.84 (s), 57.5 (s), 24.34 (s), 16.24 (d, J =9.6 Hz), 14.62 (s), 6.76 (d, 9.2 Hz), 6.50 (s), 2.62 (s), 1.96 (s), -15.27 (s), -28.72 (s), -36.83 (s), -103.82 (s). HRMS (ESI) m/z calcd. for $C_{87}H_{78}Cl_2Fe_2N_{12}O_{11}$ ($[M_2L_3•(ClO_4)_2]^{2+}$) 824.1989, found 824.9617. Elemental Analysis: Calc. for $C_{95}H_{78}F_{24}Fe_2N_{16}O_{19}S_8$ C: 44.36; H: 3.06; N: 8.71; Found: C: 44.68; H: 2.96; N: 8.53.

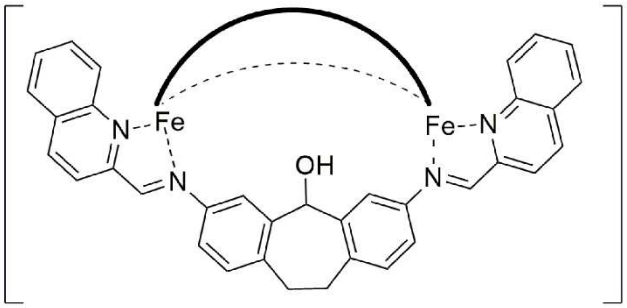

***Meso*-helicate SOH•Fe•QnCHO:**

2,7-Diaminosuberol (**SOH)** (30 mg, 0.13 mmol), 2-quinoline carboxaldehyde (58.8 mg, 0.38 mmol), and $Fe(NTf_2)_2$ (50.8 mg, 0.082 mmol) were combined in MeCN (3 mL) in a 25 mL round bottom flask. The solution was then heated at 77°C for 48 h with stirring. The reaction mixture was cooled, and the acetonitrile removed *in vacuo*. The brown solid was sonicated with 10 mL of 3:1 Et_2O:MeOH solution and filtered. After drying the product was isolated as a brown powder (100.7 mg, 28.9% yield). ^1H NMR (400 MHz; CD_3CN) δ 181.41 (s), 55.48 (s), 26.17 (s), 24.15 (s), 13.68 (d, J= 9.4 Hz), 6.58 (s), 5.77 (s), 5.64 (d, J=9.6 Hz), 3.44 (s), 3.31 (s), 1.34 (s), 1.15 (s), -10.30 (s), -19.93 (s), -48.08 (s), -76.25 (s). HRMS (ESI) m/z calcd. for $C_{109}H_{78}F_{12}Fe_2N_{14}O_{11}S_4$ ($[M_2L_3•(NTf_2)_2^{2+}$) 1113.6694, found 1113.6691. Elemental Analysis: Calc. for $C_{113}H_{78}F_{24}Fe_2N_{16}O_{19}S_8$ C: 48.68; H: 2.82; N: 8.04; Found: C: 48.32; H: 2.70; N: 7.84.

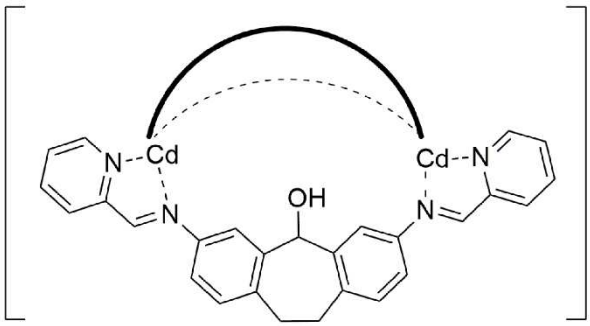

***Meso*-helicate SOH•Cd•PyCHO:**

2,7-diaminosuberol (**SOH)** (20 mg, 0.084 mmol), 2-formyl pyridine (16 µL, 0.17 mmol), and $Cd(ClO_4)_2$ (17.2 mg, 0.055 mmol) were combined in MeCN (3 mL) in a 25 mL round-bottom flask. The solution was then heated at 77°C for 18 h with stirring. The reaction mixture was cooled, and the acetonitrile removed *in vacuo*. The orange solid was sonicated with 10 mL of 3:1 Et_2O:MeOH solution and filtered. After drying, the product was isolated as an orange powder (45 mg, 86% yield). ^{1}H NMR (400 MHz; CD_3CN) δ 8.88 (s, 2H), 8.79 (m, 2H), 8.36 (m, 2H), 8.00 (m 2H), 7.94 (s, 2H), 6.99 (s,4H), 6.14 (d, J=3.2 Hz, 1H), 4.32 (s, 3.6, 1 Hz), 3.54 (dd, J=6.9, 5.0 Hz, 1H), 3.28 (m, 2H), 2.74 (dd, J=15.0, 7.2 Hz, 2H), 2.46 (t, J=5.1 Hz, 1H).

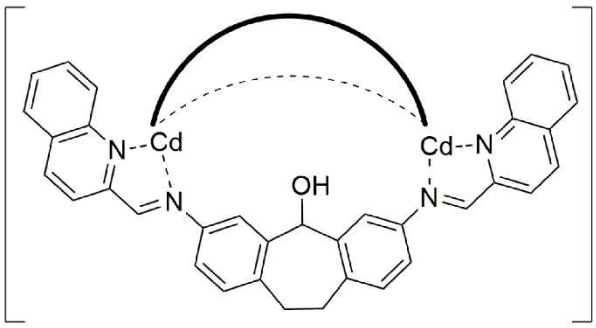

***Meso*-helicate SOH•Cd•QnCHO:**

2,7-diaminosuberol (**SOH)** (200 mg, 0.84 mmol), 2-quinoline carboxaldehyde (262.8 mg, 1.6 mmol), and $Cd(ClO_4)_2$ (171.84 mg, 0.55 mmol) were combined in MeCN (3 mL) in a 25 mL round-bottom flask. The solution was then heated at 77°C for 18 h with stirring. The reaction mixture was cooled, and the acetonitrile removed *in vacuo*. The orange solid was sonicated with 10 mL of 3:1 Et_2O:MeOH solution and filtered. After drying, the product was isolated as an orange powder (457 mg, 93.3% yield). ^{1}H NMR (400 MHz; CD_3CN) δ 8.62 (d, J=8.2 Hz, 2H), 8.30 (s, 1H), 8.18 (d, J=8.2 Hz, 2H), 8.07 (d, J=8.2 Hz, 2H), 7.95 (s, 2H), 7.78 (t, J=7.3 Hz, 2H), 7.57 (d, J=8.2 Hz, 4H), 6.55 (d, J=8.2 Hz, 2H), 6.01 (d, J=5.27 Hz, 2H), 5.25 (d, J=7.3 Hz, 2H), 3.26 (m, 2H), 2.73 (m, 2H).

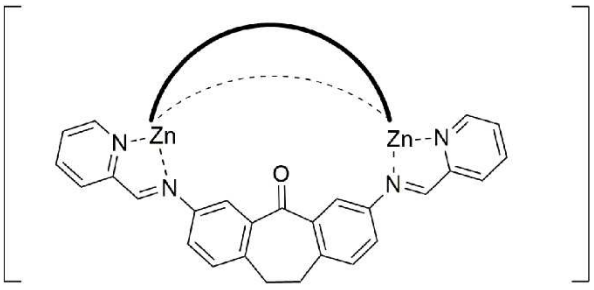

***Meso*-helicate SO•Zn•PyCHO:**

2,7-diaminosuberone (**SO)** (50 mg, 0.21 mmol), 2-formyl pyridine (40 μL, 0.42 mmol), and $Zn(OTf)_2$ (50.5 mg, 0.14 mmol) were combined in MeCN (3 mL) in a 25 mL round-bottom flask. The solution was then heated at 77°C for 18 h with stirring. The reaction mixture was cooled, and the acetonitrile removed *in vacuo*. The orange solid was sonicated with 10 mL of 3:1 Et_2O:MeOH solution and filtered. After drying, the product was isolated as an orange powder (51 mg, 53.5% yield). ^{1}H NMR (400 MHz; CD_3CN) δ 8.49 (t, J=7.7

Hz, 2H), 8.45 (s, 2H), 8.21 (d, J=7.5 Hz, 2H), 8.14 (d, J=4.3 Hz, 2H), 7.94 (t, J=5.2, 2H), 7.21 (d, J=8.0 Hz, 2H), 6.58 (s,2H), 5.98 (d, J=8.11 Hz, 2H), 3.34 (dd, J= 10.2, 14.8 Hz, 2H), 3.17 (dd, J= 10.2,14.8 Hz, 2H).

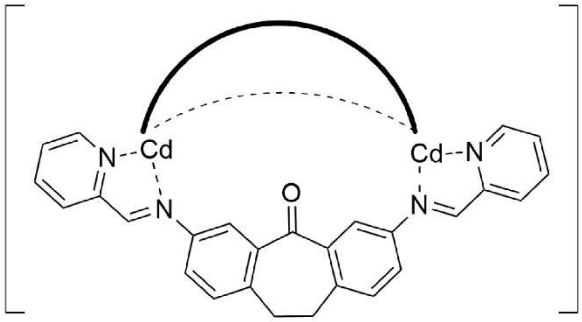

***Meso*-helicate SO•Cd•PyCHO:**

2,7-diaminosuberone (**SO)** (20 mg, 0.084 mmol), 2-formyl pyridine (16 μL, 0.17 mmol), and $Cd(ClO_4)_2$ (17.2 mg, 0.055 mmol) were combined in MeCN (3 mL) in a 25 mL round-bottom flask. The solution was then heated at 77°C for 18 h with stirring. The reaction mixture was cooled, and the acetonitrile removed *in vacuo*. The orange solid was sonicated with 10 mL of 3:1 Et_2O:MeOH solution and filtered. After drying, the product was isolated as an orange powder (21 mg, 51.7% yield). ^{1}H NMR (400 MHz; CD_3CN) δ 8.94 (s, 2H), 8.52 (s, 2H), 8.34 (d, J=7.2 Hz, 2H), 8.16 (d, J=6.8 Hz, 2H), 7.85 (d, J=5.6 Hz, 2H), 7.75 (s, 2H), 7.05 (d, J=7.9 Hz, 2H), 6.78 (d, J=5.9, 2H), 2.84 (d, J=12.6 Hz, 2H), 2.66 (d, J= 12.6 Hz, 2H).

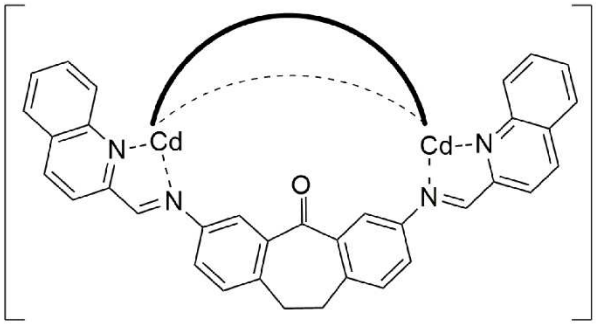

***Meso*-helicate SO•Cd•QnCHO:**

2,7-diaminosuberone (**SO)** (30 mg, 0.13 mmol), 2-quinoline carboxaldehyde (39.6 mg, 0.25 mmol), and $Cd(ClO_4)_2$ (33.7 mg, 0.083 mmol) were combined in MeCN (3 mL) in a 25 mL round-bottom flask. The solution was then heated at 77°C for 18 h with stirring. The reaction mixture was cooled, and the acetonitrile removed *in vacuo*. The orange solid was sonicated with 10 mL of 3:1 Et_2O:MeOH solution and filtered. After drying, the product was isolated as an orange powder (25.0 mg, 33.9% yield). ^{1}H NMR (400 MHz; CD_3CN) δ 9.09 (t, J=8.6 Hz, 2H), 8.85 (dd, J=1.13, 8.5 Hz, 4H), 8.56 (d, J=9.1 Hz, 2H), 8.35 (d, J=7.8 Hz, 2H), 8.19 (m, 6H), 7.97 (m, 4H), 7.79 (m, 10H), 7.42 (m, 4H), 7.17 (t, J=8.2Hz, 2H), 6.95 (d, J= 8.2 Hz, 2H), 6.71 (s, 2H), 6.38 (dd, J=5.9, 1.9 Hz, 2H), 5.91 (dd, J=5.9, 1.9 Hz, 2H), 3.43 (dd, J=9.0, 15.4 Hz, 2H), 3.19 (dd, J=9.0, 15.4 Hz, 4H), 2.86 (m, H), 2.76 (m, 2H).

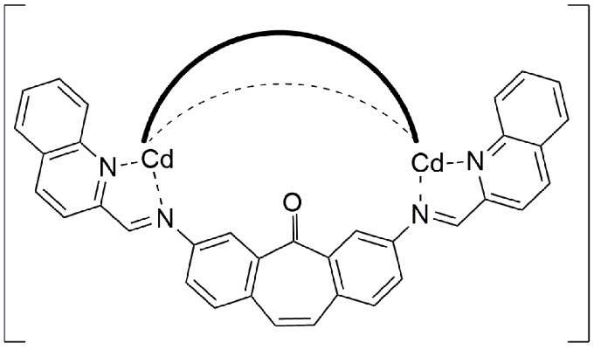

***Meso*-helicate SE•Cd•QnCHO:**

2,7-diaminosuberenone (**SE)** (30 mg, 0.13 mmol), 2-quinoline carboxaldehyde (39.6 mg, 0.25 mmol), and $Cd(ClO_4)_2$ (33.7 mg, 0.083 mmol) were combined in MeCN (3 mL) in a 25 mL round-bottom flask. The solution was then heated at 77°C for 18 h with stirring. The reaction mixture was cooled, and the acetonitrile removed *in vacuo*. The orange solid was sonicated with 10 mL of 3:1 Et_2O:MeOH solution and filtered. After drying, the product was isolated as an orange powder (9 mg, 10% yield). ^{1}H NMR (400 MHz; CD_3CN) δ 8.86 (d, J=3.3 Hz, 2H), 8.80 (s, 1H), 8.28 (d, J=1.6 Hz, 1H), 8.24 (d, J=8.19 Hz, 2H), 8.03 (d, 8.7 Hz, 2H), 7.98 (d, 8.2 Hz, 2H), 7.81 (t, 7.5 Hz, 2H), 7.52 (t, J=7.5 Hz, 2H), 7.29 (d, J= 8.5 Hz, 2H), 6.96 (s, 2H), 6.38 (dd, J=2.0, 8.5 Hz, 2H).

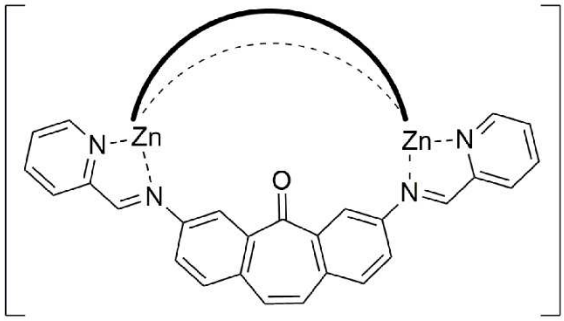

***Meso*-helicate SE•Zn•PyCHO:**

2,7-diaminosuberenone (**SE)** (32.8 mg, 0.13 mmol), 2-formyl pyridine (24 μL, 0.25 mmol), and $Zn(OTf)_2$ (61.2 mg, 0.083 mmol) were combined in MeCN (3 mL) in a 25 mL round-bottom flask. The solution was then heated at 77°C for 18 h with stirring. The reaction mixture was cooled, and the acetonitrile removed *in vacuo*. The orange solid was sonicated with 10 mL of 3:1 Et_2O:MeOH solution and filtered. After drying, the product was isolated as an orange powder (63 mg, 68% yield). ^{1}H NMR (400 MHz; CD_3CN) δ 8.58 (td, J=8.6 Hz, 2H), 8.52 (s, 1H), 8.31 (s, 1H), 8.29 (d, J=2.7 Hz, 2H), 8.05 (ddd, J=1.5, 6.9, 10.5 Hz, 2H), 7.62 (d, 10.5 Hz, 2H), 7.22 (s, 2H), 6.87 (d, J=3.2 Hz, 2H), 6.08 (dd, J=3.2, 10.5 Hz, 2H).

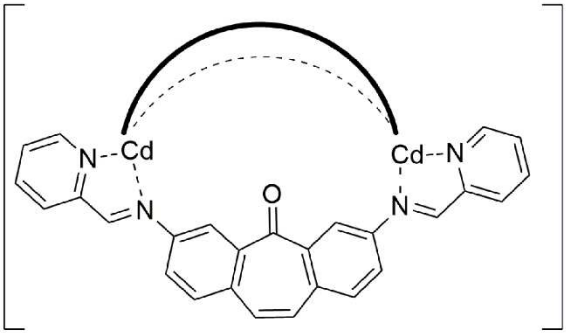

***Meso*-helicate SE•Cd•PyCHO:**

2,7-diaminosuberenone (**SE)** (32.8 mg, 0.13 mmol), 2-formyl pyridine (24 μL,0.25 mmol), and $Zn(OTf)_2$ (61.2 mg, 0.083 mmol) were combined in MeCN (3 mL) in a 25 mL round-bottom flask. The solution was then heated at 77°C for 18 h with stirring. The reaction mixture was cooled, and the acetonitrile removed *in vacuo*. The orange solid was sonicated with 10 mL of 3:1 Et_2O:MeOH solution and filtered. After drying, the product was isolated as an orange powder (13.58 mg, 5% yield). ^{1}H NMR (400 MHz; CD_3CN) δ 8.76 (s, 2H), 8.66 (s, 2H), 8.31 (t, J=10.2 Hz, 2H), 8.24 (s, 2H), 8.04 (d, J=9.9 Hz, 2H), 7.87 (d, J=6.4 Hz, 2H), 7.37 (d, 11.5 Hz, 2H), 6.95 (s, 2H), 6.62 (s, 2H).

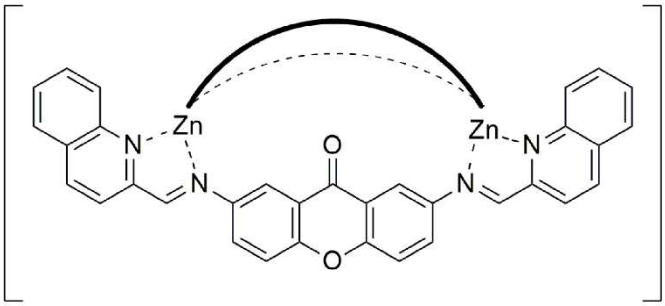

***Meso*-helicate XO•Zn•QnCHO:**

2,7-diaminoxanthone (**XO)** (28.5 mg, 0.13 mmol), 2-quinoline carboxaldehyde (39.6 mg, 0.25 mmol), and $Zn(OTf)_2$ (61.2 mg, 0.083 mmol) were combined in MeCN (3 mL) in a 25 mL round-bottom flask. The solution was then heated at 77°C for 18 h with stirring. The reaction mixture was cooled, and the acetonitrile removed *in vacuo*. The orange solid was sonicated with 10 mL of 3:1 Et_2O:MeOH solution and filtered. After drying, the product was isolated as an orange powder (6.8 mg, 7% yield). ^{1}H NMR (400 MHz; CD_3CN) δ 9.18 (dd, J=2.1,8.2 Hz, 2H), 9.16 (s, 1H), 8.31 (dd, J=2.0, 8.1 Hz, 2H), 8.29 (d, J=8.1 Hz, 2H), 8.08 (d, J=8.5, 2H), 7.91 (d, 7.6 Hz, 2H), 7.69 (t, 8.1 Hz, 3H), 7.57 (dd, J=2.1, 8.9 Hz, 2H), 7.43 (s, 2H).

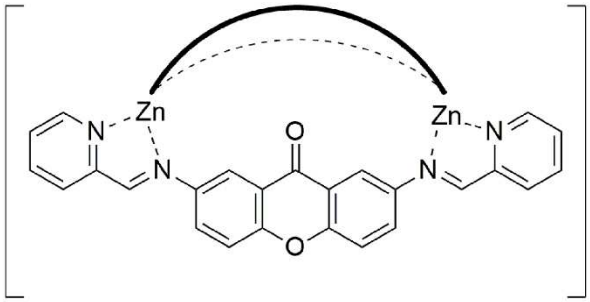

***Meso*-helicate XO•Zn•PyCHO:**

2,7-diaminoxanthone (**XO)** (28.5 mg, 0.13 mmol), 2-formyl pyridine (39.6 mg, 0.25 mmol), and $Zn(OTf)_2$ (61.2 mg, 0.083 mmol) were combined in MeCN (3 mL) in a 25 mL round-bottom flask. The solution was then heated at 77°C for 18 h with stirring. The reaction mixture was cooled, and the acetonitrile removed *in vacuo*. The orange solid was sonicated with 10 mL of 3:1 Et_2O:MeOH solution and filtered. After drying, the product was isolated as an orange powder (10.9 mg, 13% yield). ^{1}H NMR (400 MHz; CD_3CN) δ 8.75 (s, J=8.2 Hz, 2H), 8.49 (t, J=7.4, 2H), 8.31 (d, J=7.6 Hz, 2H), 8.29 (d, J=8.1 Hz, 2H), 8.08 (d, J=8.5, 2H), 7.91 (d, 7.6 Hz, 2H), 7.69 (t, 8.1 Hz, 2H), 7.57 (dd, J=2.1, 8.9 Hz, 2H), 7.43 (s, 2H).

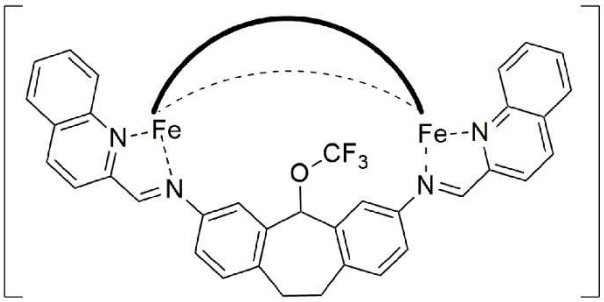

***Meso*-helicate SOCF$_3$•Fe•QnCHO:**

2,7-diaminoxanthone (**SOCF$_3$)** (10 mg, 0.032 mmol), 2-quinoline carboxaldehyde (10 mg, 0.065 mmol), and $Fe(ClO_4)_2$ (5 mg, 0.0214 mmol) were combined in MeCN (3 mL) in a 25 mL round-bottom flask. The solution was then heated at 77°C for 18 h with stirring. The reaction mixture was cooled, and the acetonitrile removed *in vacuo*. The orange solid was sonicated with 10 mL of 3:1 Et_2O:MeOH solution and filtered. After drying, the product was isolated as an orange powder (5.8 mg, 24% yield). ^{1}H NMR (400 MHz; CD_3CN) δ 54.00 (s), 46.48 (s), 33.35 (s), 22.28 (s), 20.13 (s, br), 18.36 (s), 17.32 (s), 15.42 (s), 12.08 (s), 11.79 (s), 10.06 (s), 9.87 (s), 8.09 (s), 7.91 (s), 7.77 (s), 7.65 (s), 3.90 (s), 1.52 (s), 0.29 (s), -1.05 (s), -2.13 (s), -3.98 (s), -4.89 (s), -6.19 (s), -7.10 (s), -8.74 (s), -11.67 (s), -28.22 (s, br), -41.63 (s), -48.62 (s).

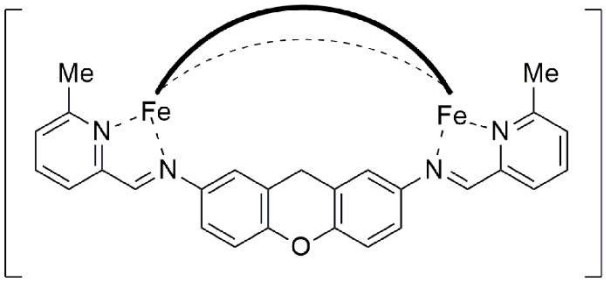

***Meso*-helicate X•Fe•MePyCHO:**

2,7-Diamino-9H-Xanthene (**X**) (150 mg, 0.71 mmol), 6-methylpyridine-2-carboxaldehyde (171 mg, 1.41 mmol) and $Fe(NTf_2)_4$ (310 mg, 0.47 mmol) were combined in MeCN (10 mL) in a 25 mL round-bottom flask. The solution was then heated at 77°C for 48 h with stirring. The reaction mixture was cooled, and the acetonitrile removed *in vacuo*. The red solid was sonicated with 20 mL of 3:1 Et_2O:MeOH solution and the red solid was removed via vacuum filtration. After drying, the product was isolated as a red powder (592 mg, 94% yield). ^{1}H NMR (400 MHz; CD_3CN) δ 184.25, 54.01 (s), 52.89 (s), 13.56 (s), 8.41 (s), 6.87 (s), -25.49 (s), -30.94 (s), -33.24 (s), -48.88 (s). HRMS (ESI) m/z calcd. for $C_{85}H_{66}F_{12}Fe_2N_{14}O_{11}S_4$ (M_2L_3•$(NTf_2)_2^{2+}$) 963.1208, found 963.6368. Elemental Analysis: Calc. for $C_{89}H_{66}F_{24}Fe_2N_{16}O_{19}S_8$ C: 42.97; H: 2.67; N: 9.01; Found: C: 42.78; H: 2.67; N: 9.11.

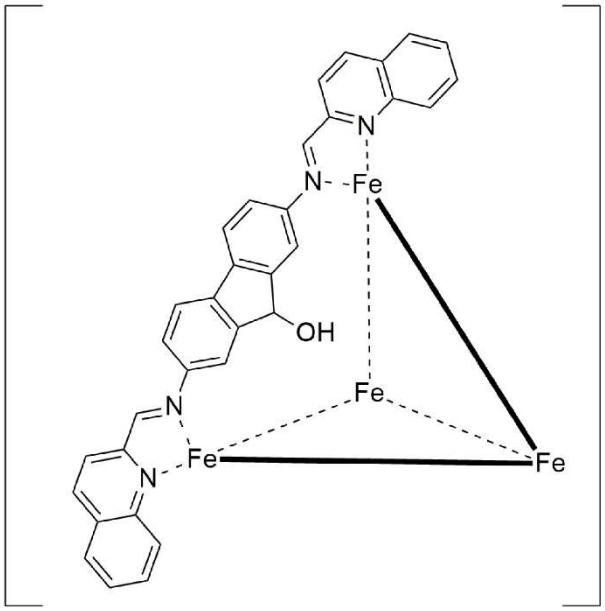

Cage FOH•Fe•QnCHO:

2,7-Diaminofluorenol **(FOH)** (30 mg, 0.14 mmol), 2-quinoline carboxaldehyde (32.2 mg, 0.28 mmol), and $Fe(ClO_4)_2$ (44.4 mg, 0.093 mmol) were combined in MeCN (mL) in a 25 mL round-bottom flask. The solution was then heated at 77°C for 72 h with stirring. The red solid was sonicated with 20 mL of 3:1 Et_2O:MeOH solution and the red solid was removed via vacuum filtration. After drying, the product was isolated as a red solid (570 mg, 76% yield). ^1H NMR (400 MHz; CD_3CN) : δ 73.27 (s), 61.28 (s), 58.66 (s), (s), 56.05 (s), 55.14 (s), 53.76 (d, J= 209.1 Hz), 44.99 (s), 46.42 (s), 37.22 (s), 28.32 (s), 23.45 (s), 21.45 (s), 17.91 (s), 11.78 (s), 9.25 (s), -2.76 (s), -4.16 (d, J=230.4 Hz), -6.30 (d, J=231.7 Hz), -8.76 (d, J=214.2 Hz), -15.19 (s, br), -22.28 (s), -25.43 (s, br), -32.06 (s), -41.41 (s), -44.53 (s), -91.92 (s, br), -108.21 (s, br), 110.41 (s, br).

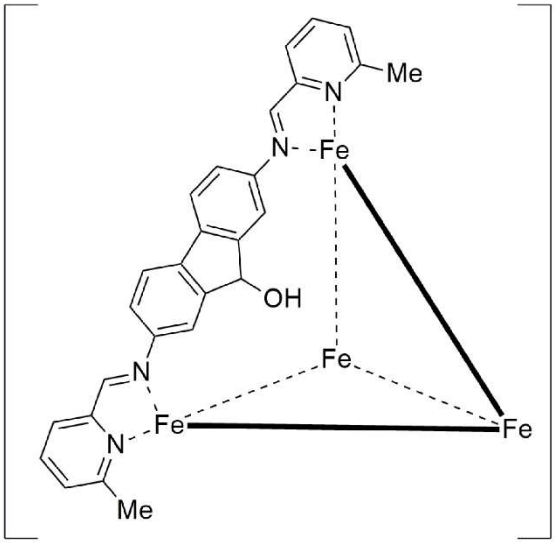

Cage FOH•Fe•MePyCHO:

2,7-Diaminofluorenol **(FOH)** (200 mg, 0.94 mmol), 6-methylpyridine-2-carboxaldehyde (228.29 mg, 1.88 mmol), $Fe(NTf_2)_2$ (412.82 mg, 0.63 mmol) and $NaClO_4$ (24.99 mg, 0.20 mmol) were combined in MeCN (15 mL) in a 25 mL round-bottom flask. The solution was then heated at 77°C for 72 h with stirring. The red solid was sonicated with 20 mL of 3:1 Et_2O:MeOH solution and the red solid was removed via vacuum filtration. After drying, the product was isolated as a red solid (508 mg, 65% yield). ^1H NMR (400 MHz; CD_3CN) : δ 198.17 (s), 194.84 (s), 186.44 (s), 185.28 (s), 72.77 (s), 62.18 (s), 60.26 (s), 57.38 (s), 55.50 (s), 55.41 (s), 54.81 (s), 53.05 (s), 36.65 (s), 27.89 (s), 23.98 (s), 19.40 (s), 17.15 (s), 11.32 (s), 9.17 (s) (s), 8.99 (s), 8.55 (s), 7.96 (s), 3.47 (s), 3.02 (s), 2.60 (s), 1.14 (s), -0.18 (s), -1.54 (s), -3.55 (s), -7.10 (s), -7.57 (s), -7.72 (s), -21.24 (s), -32.07 (s), -33.02 (s), -40.82 (s), -47.73 (s), -88.59 (s), -106.85 (s), -112.94 (s), -324.92 (s). HRMS (ESI) m/z calcd. for $C_{162}H_{132}ClFe_4N_{24}O_{10}$ ($[M_4L_6•ClO_4]^{7+}$) 404.6806, found 404.8304.

General competitive assembly procedure: All mixing experiments were performed in an NMR tube. One equivalent of dianiline **SOH** (0.02 mmol) and one equivalent of dianiline B (0.02 mmol) were placed in an NMR tube. Deuterated acetonitrile (400 μL) was added to the tube and a proton spectrum of the dianiline mixture obtained. 2 equivalents of 6-methyl-2-formyl pyridine were added (0.04 mmol) followed by 0.66 equivalents of $Fe(NTf_2)_2$ (0.013 mmol) in CD_3CN). A spectrum of the mixture was obtained. The tube was heated at 77°C for 1 h. Another spectrum was taken after heating to show the favored cage and the unfavored dianiline ligand.

General amine displacement procedure: All displacement experiments were performed in an NMR tube. One equivalent of preformed cage **SOH•Fe•MePyCHO** (10 mg, 0.0039 mmol), and three equivalents of dianiline **X** (4.3 mg, 0.012 mmol) were placed in an NMR tube. Dry deuterated acetonitrile (400 μL) was added to the tube and a proton spectrum of the starting mixture obtained. The tube was heated at 25°C for paramagnetic complexes or 77°C for diamagnetic complexes for at least 2 h to determine whether the preformed cage was displaced by the free dianiline ligand.

General aldehyde displacement procedure: All displacement experiments were performed in an NMR tube. One equivalent of preformed **SOH•Fe•MePyCHO** (10 mg, 0.0039 mmol) and 6 equivalents of 2-formylpyridine PyCHO (2.22 μL, 0.0233 mmol) were placed in an NMR tube. Dry deuterated acetonitrile (400 μL) was added and the sample

heated at 70°C for a given period of time and subjected to ^{1}H NMR analysis throughout the course of the experiment.

X-Ray Crystallographic Data

a) Xanthene Mesocate X•Fe•MePyCHO (CCDC #1848253). 150 mg of cage **X•Fe•MePyCHO** was dissolved in a minimal amount of acetonitrile and 0.5 mL of the resulting solution was pipetted into an NMR tube. The tube was placed into an 8 oz. glass jar containing 25 mL of diethyl ether. The jar was capped tightly, and the sample was allowed to sit for 5 days, until solvent diffusion was complete and the solution inside the NMR tube was colorless. Red prisms and needles were both observed within the NMR tube.

A red prism fragment (0.488 x 0.136 x 0.030 mm^3) was used for the single crystal X-ray diffraction study of $[C_{81}H_{66}Fe_2N_{12}O_3]^{4+}.[C_2F_6NO_4S_2]^-_4.[CH_3CN]_3$. The crystal was coated with paratone oil and mounted on to a cryo-loop glass fiber. X-ray intensity data were collected at 100(2) K on a Bruker APEX2 platform-CCD x-ray diffractometer system (fine focus Mo-radiation, λ = 0.71073 Å, 50KV/30mA power).[1] The CCD detector was placed at a distance of 5.0600 cm from the crystal.

A total of 3600 frames were collected for a sphere of reflections (with scan width of 0.3^o in ω, starting ω and 2θ angles of –30^o, and φ angles of 0^o, 90^o, 120^o, 180^o, 240^o, and 270^o for every 600 frames, 60 sec/frame exposure time). The frames were integrated using the Bruker SAINT software package[2] and using a narrow-frame integration algorithm. Based on a triclinic crystal system, the integrated frames yielded a total of 109946 reflections at a maximum 2θ angle of 56.564^o (0.75 Å resolution), of which 26638 were independent

reflections (R_{int} = 0.0396, R_{sig} = 0.0366, redundancy = 4.1, completeness = 99.9%) and 20391 (76.5%) reflections were greater than 2σ(I). The unit cell parameters were, **a** = 14.5840(5) Å, **b** = 18.9278(7) Å, **c** = 19.8975(7) Å, **α** =80.8140(6)**, β** = 82.2801(6)°**, γ** = 89.9495(6) V = 5371.8(3) $Å^3$, Z = 2, calculated density D_c = 1.614 g/cm^3. Absorption corrections were applied (absorption coefficient μ = 0.544 mm^{-1}; max/min transmission = 0.984/0.777) to the raw intensity data using the SADABS program.[3]

The Bruker SHELXTL software package[4] (was used for phase determination and structure refinement. The distribution of intensities (E^2-1 = 0.933) and no systematic absent reflections indicated two possible space groups, P-1 and P1. The space group P-1 (#2) was later determined to be correct. Direct methods of phase determination followed by two Fourier cycles of refinement led to an electron density map from which most of the non-hydrogen atoms were identified in the asymmetric unit of the unit cell. With subsequent isotropic refinement, all of the non-hydrogen atoms were identified. There was one cation of $[C_{81}H_{66}Fe_2N_{12}O_3]^{4+}$, four anions of $[C_2F_6NO_4S_2]^-$, and three solvent molecules of CH_3CN present in the asymmetric unit of the unit cell. Three of the four anions of $[C_2F_6NO_4S_2]^-$ were modeled with disorder (disordered site occupancy ratios were 93% / 7%, 62% / 38%, and 46% / 44% / 10%). The alert level B of the short non-bonding inter halogen contact of F2F...F1L is probably due to the disordered anions.

Atomic coordinates, isotropic and anisotropic displacement parameters of all the non-hydrogen atoms were refined by means of a full matrix least-squares procedure on F^2. The H-atoms were included in the refinement in calculated positions riding on the atoms to which they were attached. The refinement converged at R_1 = 0.0443, wR_2 = 0.1000, with

intensity I > 2σ (I). The largest peak/hole in the final difference map was 0.953 / -0.737 e/Å^3.

Table 6.1: Crystal data and structure refinement for **Xanthene Mesocate X•Fe•MePyCHO**.

Empirical formula	$C_{95}H_{75}F_{24}Fe_2N_{19}O_{19}S_8$	
Formula weight	2610.92	
Temperature	100(2) K	
Wavelength	0.71073 Å	
Crystal system	Triclinic	
Space group	P -1	
Unit cell dimensions	*a* = 14.5840(5) Å	α= 80.8140(6)°
	b = 18.9278(7) Å	β= 82.2801(6)°
	c = 19.8975(7) Å	γ = 89.9495(6)°
Volume	5371.8(3) Å^3	
Z	2	
Density (calculated)	1.614 Mg/m^3	
Absorption coefficient	0.544 mm^{-1}	
F(000)	2652	
Crystal size	0.488 x 0.136 x 0.030 mm^3	
Theta range for data collection	1.384 to 28.282°.	
Index ranges	-19<=*h*<=19, -25<=*k*<=25, -26<=*l*<=26	

Reflections collected	109946
Independent reflections	26638 [R(int) = 0.0396]
Completeness to θ = 25.242°	100.0%
Absorption correction	Semi-empirical from equivalents
Refinement method	Full-matrix least-squares on F^2
Data / restraints / parameters	26638 / 1777 / 2028
Goodness-of-fit on F^2	1.017
Final R indices [I>2σ(I)]	R_1 = 0.0443, wR_2 = 0.1000
R indices (all data)	R_1 = 0.0662, wR_2 = 0.1099
Extinction coefficient	n/a
Largest diff. peak and hole	0.953 and -0.737 e.Å^{-3}

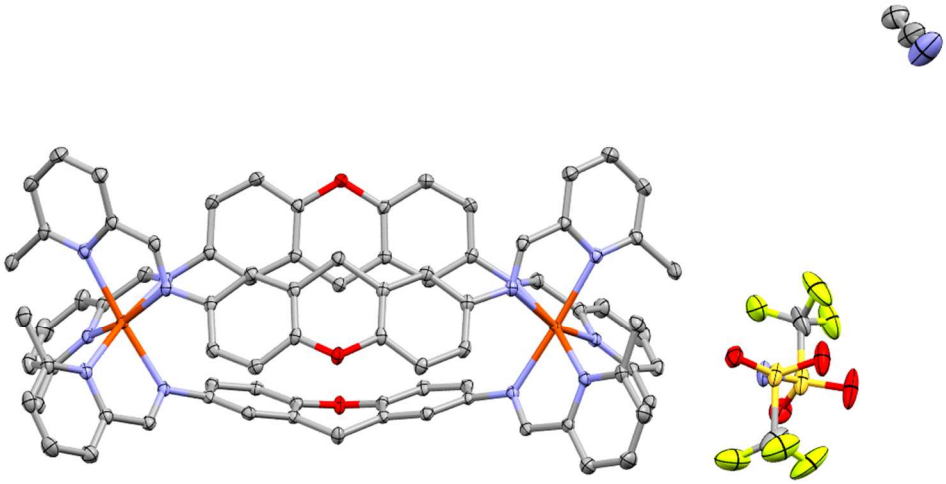

Figure 6.1: ORTEP structure of **X•Fe•MePyCHO•(NTf$_2$)$_4$** (slow diffusion of diethyl ether into acetonitrile, diffracted at 100 K).

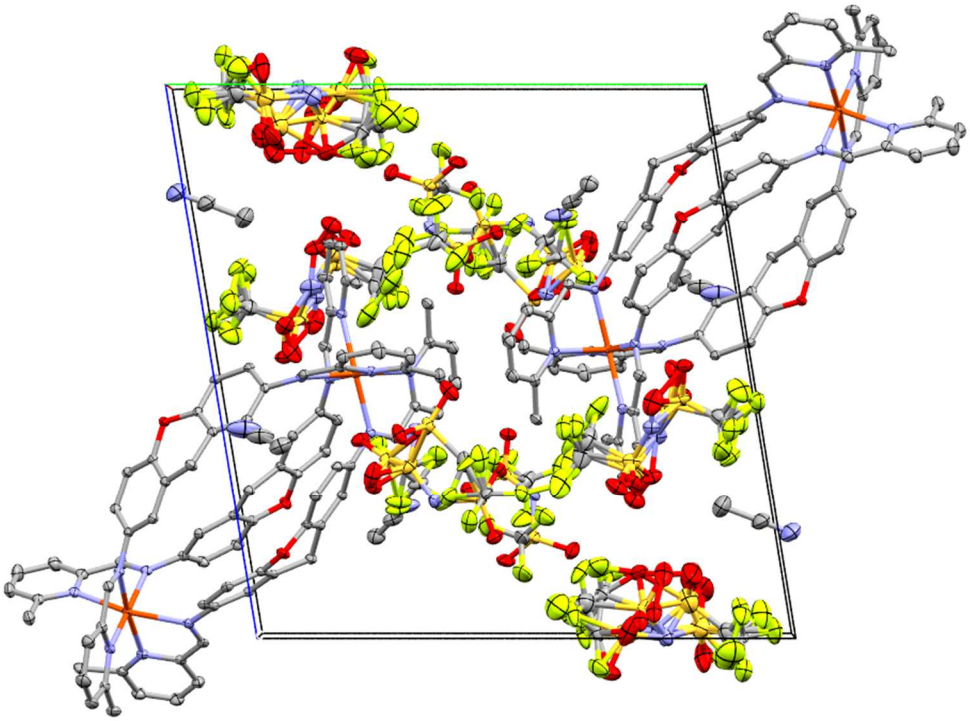

Figure 6.2: Unit cell of **X•Fe•MePyCHO•$(NTf_2)_4$** (slow diffusion of diethyl ether into acetonitrile, diffracted at 100 K).

b) Fluorenol Cage FOH•Fe•MePyCHO (CCDC #1848254)

100 mg of cage **FOH•Fe•MePyCHO** was dissolved in a minimal amount of acetonitrile and 0.5 mL of the resulting solution was pipetted into an NMR tube. The tube was placed into an 8 oz. glass jar containing 25 mL of diethyl ether. The jar was capped tightly, and the sample was allowed to sit for 5 days, until solvent diffusion was complete and the solution inside the NMR tube was colorless. Red prisms and needles were both observed within the NMR tube.

A dark red prism fragment (0.150 x 0.125 x 0.125 mm^3) was used for the single crystal X-ray diffraction study of $[C_{162}H_{132}Fe_4N_{24}O_6]^{8+}.[C_2F_6NO_4S_2]^{-}{}_7.[ClO_4]^{-}$. The crystal was

coated with paratone oil and mounted on to a cryo-loop glass fiber. X-ray intensity data were collected at 150(2) K on a Bruker Rotating Anode generator with APEX2 platform-CCD X-ray diffractometer system (Mo-radiation, λ = 0.71073 Å, 50KV/24mA rotating anode power).[1] The CCD detector was placed at a distance of 7.0000 cm from the crystal.

A total of 2188 frames were collected for a sphere of reflections (with scan width of 0.5° in ω and ϕ, for ω-scan starting ω angle at -15.19°, starting 2θ angle at 11.88°, ϕ angles of 0°, 51°, 153°, and 225° for every 332 frames, for one ϕ scan starting ϕ angle at 266.77°, starting 2θ angle of 11.88°, ω angle of -35.92° for every 760 frames, 60 sec/frame exposure time). The frames were integrated using the Bruker SAINT software package[2] and using a narrow-frame integration algorithm. Based on a monoclinic crystal system, the integrated frames yielded a total of 513139 reflections at a maximum 2θ angle of 33.586° (1.23 Å resolution), of which 49262 were independent reflections (R_{int} = 0.0559, R_{sig} = 0.0332, redundancy = 10.4, completeness = 100%) and 34050 (69.1%) reflections were greater than 2σ(I). The unit cell parameters were, **a** = 45.686(2) Å, **b** = 31.2027(14) Å, **c** = 61.452(3) Å, **β** = 91.4112(10)°, V = 87576(7) Å^3, Z = 16, calculated density D_c = 1.128 g/cm^3 [Note that the calculated density is based on the Empirical Formula and unit cell volume used and it's not the true density of the crystal because of unresolved anions and solvents that are missing]. Absorption corrections were applied (absorption coefficient μ = 0.395 mm^{-1}; max/min transmission = 0.952/0.943) to the raw intensity data using the SADABS program.[3]

The Bruker SHELXTL software package[4] was used for phase determination and structure refinement. The distribution of intensities (E^2-1 = 0.934) and systematic absent reflections

indicated one possible space group, P2(1)/c. The space group P2(1)/c (#14) was later determined to be correct. Direct methods of phase determination followed by two Fourier cycles of refinement led to an electron density map from which most of the non-hydrogen atoms were identified in the asymmetric unit of the unit cell. With subsequent isotropic refinement, all 4 cations, 21 anions and 15 molecules of ether were identified. There were four cations of $[C_{162}H_{132}Fe_4N_{24}O_6]^{8+}$, 16 anions of $[C_2F_6NO_4S_2]^-$, 5 anions of $[ClO_4]^-$ and 15 solvent molecules of $C_4H_{10}O$ present in the asymmetric unit of the unit cell. There are a total of 11 anions and possible solvents of ether/acetonitrile that can't be identified. SQUEEZE for removing unresolved solvent disorder could not be applied because of the missing anions. All the alert levels A through G for the checkcif are due to the poor resolution data, poor crystal quality, and unresolved electron density peaks in the final difference map. The connectivity of all the four cations are clearly resolved.

Atomic coordinates, isotropic and anisotropic displacement parameters of all the non-hydrogen atoms were refined by means of a full matrix least-squares procedure on F^2. The H-atoms were included in the refinement in calculated positions riding on the atoms to which they were attached. The refinement converged at $R_1 = 0.2213$, $wR_2 = 0.5334$, with intensity $I>2\sigma$ (I). The largest peak/hole in the final difference map was 2.584/-0.913 e/Å^3. The high difference electron density peak/hole is mainly due to the unresolved anions and solvents of crystallization.

Table 6.2: Crystal data and structure refinement for **Fluorenol Cage FOH•Fe•MePyCHO**.

Empirical formula	$C_{175.56}H_{153.43}Cl_{1.22}F_{14.96}Fe_4N_{26.49}O_{23.22}S_{4.99}$	
Formula weight	3716.73	
Temperature	150(2) K	
Wavelength	0.71073 Å	
Crystal system	Monoclinic	
Space group	P2(1)/c	
Unit cell dimensions	a = 45.686(2) Å	α = 90°.
	b = 31.2027(14) Å	β = 91.4112(10)°.
	c = 61.452(3) Å	γ = 90°.
Volume	87576(7) $Å^3$	
Z	16	
Density (calculated)	1.128 Mg/m^3	
Absorption coefficient	0.395 mm^{-1}	
F(000)	30676	
Crystal size	0.150 x 0.125 x 0.125 mm^3	
Theta range for data collection	0.663 to 16.793°.	
Index ranges	-37<=*h*<=36, -25<=*k*<=25, -49<=*l*<=49	
Reflections collected	513139	
Independent reflections	49262 [*R*(int) = 0.0559]	
Completeness to theta = 25.242°	31.1%	

Absorption correction	Semi-empirical from equivalents
Refinement method	Full-matrix least-squares on F^2
Data / restraints / parameters	49262 / 17672 / 10141
Goodness-of-fit on F^2	2.758
Final R indices [I>2sigma(I)]	$R_1 = 0.2213$, $wR_2 = 0.5334$
R indices (all data)	$R_1 = 0.2663$, $wR_2 = 0.5687$
Extinction coefficient	n/a
Largest diff. peak and hole	2.584 and -0.913 e.Å^{-3}

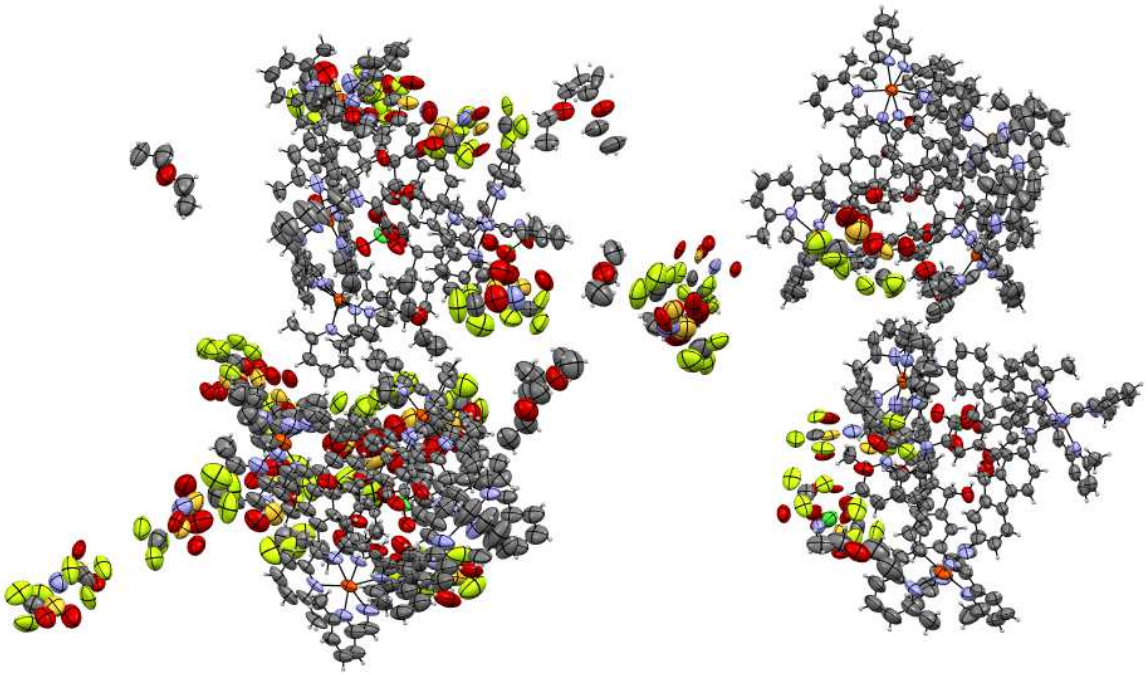

Figure 6.3: ORTEP representation of the unit cell of **FOH•Fe•MePyCHO•ClO_4•$(NTf_2)_7$** (slow diffusion of diethyl ether into acetonitrile, diffracted at 150 K).

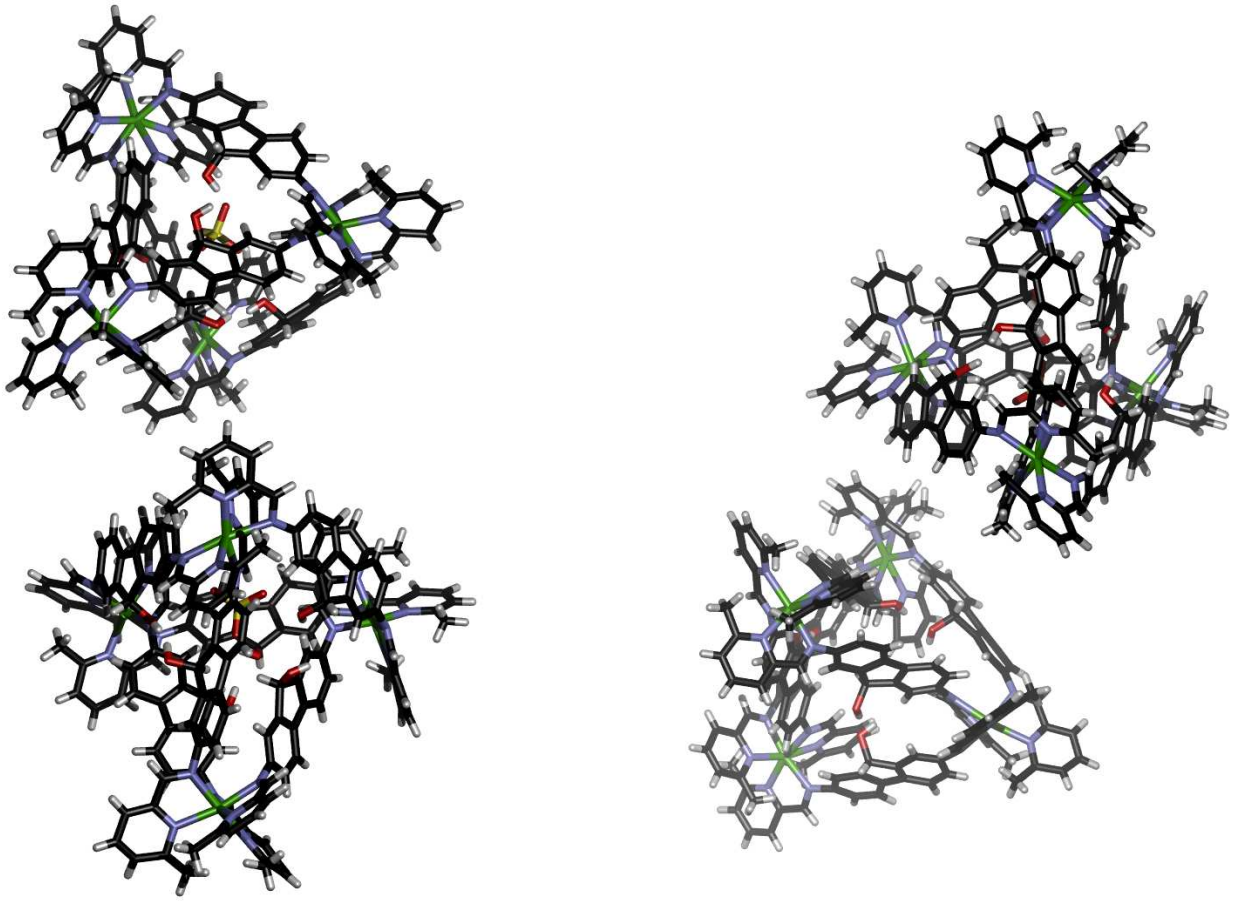

Figure 6.4: View of all four cationic cages **FOH•Fe•MePyCHO•ClO_4** in the unit cell.

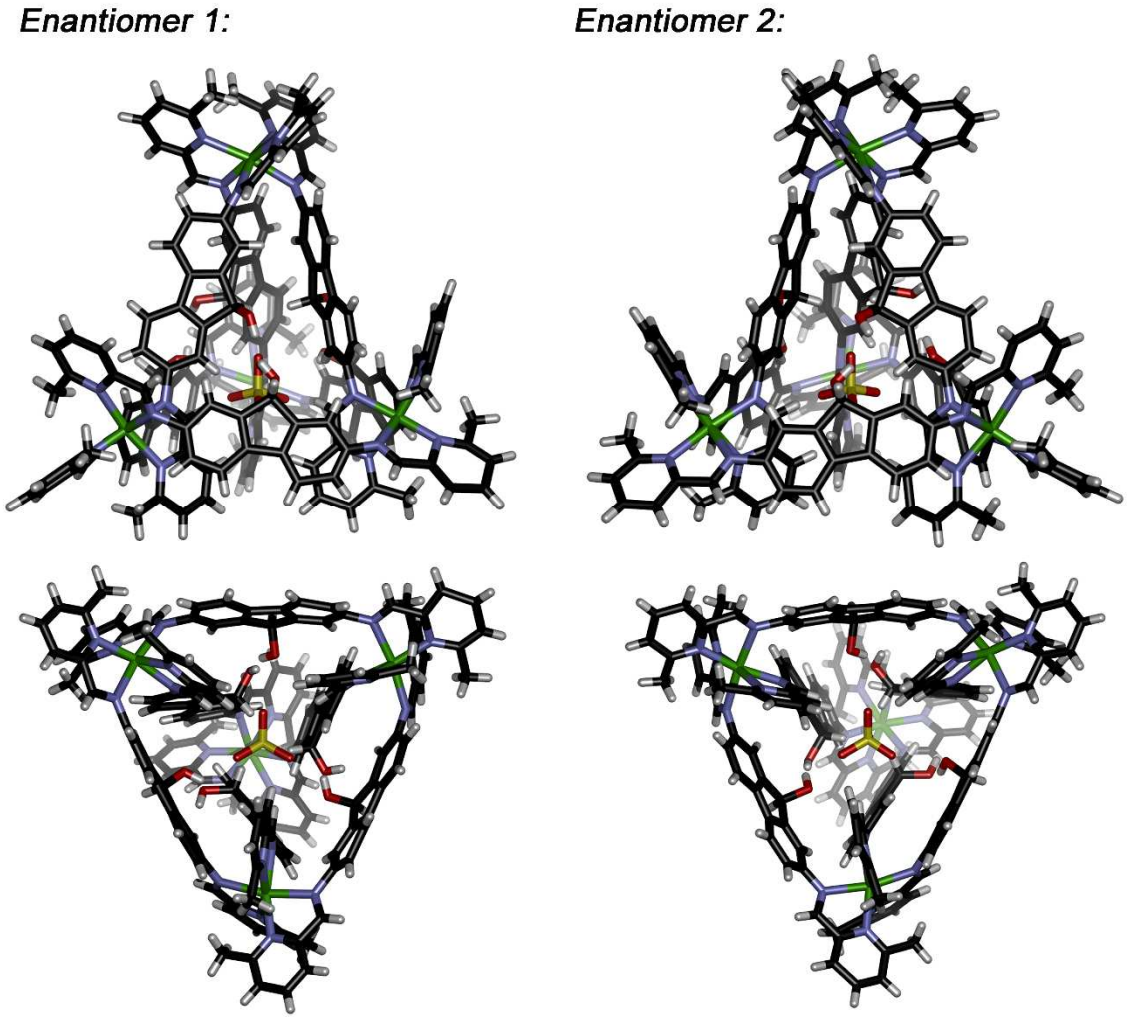

Figure 6.5: Two views of the enantiomeric pairs of **FOH•Fe•MePyCHO•ClO_4** in the unit cell.

6.3 Chapter 3 Experimental

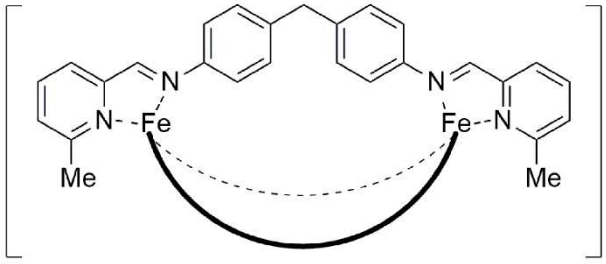

***Meso*-helicate APM•Fe•MePyCHO:**

4,4'-diaminodiphenylmethane (**APM)** (30 mg, 0.15 mmol), 6-methylpyridine-2-carboxaldehyde (36.6 mg, 0.30 mmol), and $Fe(NTf_2)_2$ (61.6 mg, 0.10 mmol) were combined in MeCN (10 mL) in a 25 mL round-bottom flask. The solution was then heated at 77°C for 18 h with stirring. The reaction mixture was cooled, and the acetonitrile removed *in vacuo*. The red solid was sonicated with 20 mL of 3:1 Et_2O:MeOH solution and filtered. After drying, the product was isolated as a red powder (104 mg, 85% yield). ^{1}H NMR (400 MHz; CD_3CN) δ 192.80 (s), 54.20 (s), 50.83 (s), 22.68 (s), 7.14 (s), 3.45 (s), 2.61 (s), 1.14 (s), -30.32 (s).

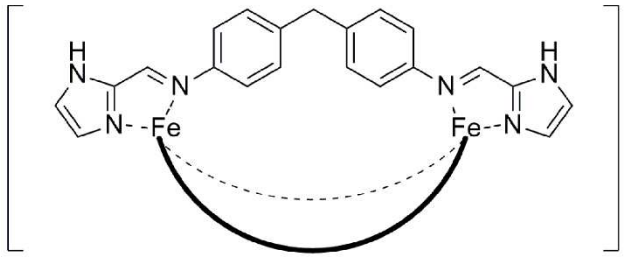

***Meso*-helicate DPM•Fe•2ImCHO:**

4,4'-diaminodiphenylmethane (**APM)** (30.0 mg, 0.15 mmol), 2-formylimidazole (69.59 mg, 0.30 mmol), and $Fe(NTf_2)_2$ (61.6 mg, 0.10 mmol) were combined in MeCN (10 mL)

in a 25 mL round-bottom flask. The solution was then heated at 77°C for 18 h with stirring. The reaction mixture was cooled, and the acetonitrile removed *in vacuo*. The red solid was sonicated with 20 mL of 3:1 Et_2O:MeOH solution and filtered. After drying, the product was isolated as a red powder (100 mg, 90% yield). ^{1}H NMR: (400 MHz; CD_3CN) δ 123.42 (s), 70.51 (s), 64.90 (s), 56.10 (s), 21.98 (s), 17.64 (s), 6.75 (d, J=139, 2H).

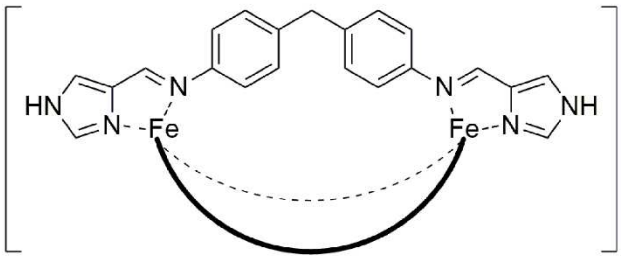

Meso-helicate APM•Fe•4ImCHO:

4,4'-diaminodiphenylmethane (**APM)** (30.0 mg, 0.15 mmol), 4-formylimidazole (69.59 mg, 0.30 mmol), and $Fe(NTf_2)_2$ (61.6 mg, 0.10 mmol) were combined in MeCN (10 mL) in a 25 mL round-bottom flask. The solution was then heated at 77°C for 18 h with stirring. The reaction mixture was cooled, and the acetonitrile removed in vacuo. The red solid was sonicated with 20 mL of 3:1 Et_2O:MeOH solution and filtered. After drying, the product was isolated as a red powder (107 mg, 93% yield). ^{1}H NMR (400 MHz; CD_3CN) δ 160.05 (s), 93.19 (s), 43.28 (s), 38.24 (s), (s), 25.00 (s), 14.81 (s), -5.72 (s).

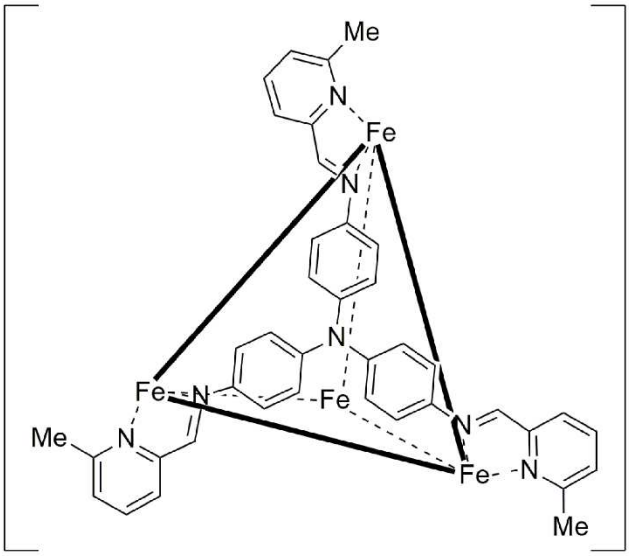

Cage APA•Fe•MePyCHO:

Tris(4-aminophenyl)amine (**APA)** (30.0 mg, 0.10 mmol), 6-methyl-2-pyridinecarboxaldehyde (24.2 mg, 0.20 mmol), and $Fe(NTf_2)_2$ (72.0 mg, 0.10 mmol) were combined in MeCN (10 mL) in a 25 mL round-bottom flask. The solution was then heated at 77°C for 18 h with stirring. The reaction mixture was cooled, and the acetonitrile removed in vacuo. The red solid was sonicated with 20 mL of 3:1 Et_2O:MeOH solution and filtered. After drying, the product was isolated as a red powder (49 mg, 40% yield). ^1H NMR (400 MHz; CD_3CN) δ 189.67 (s), 186.97 (s), 182.55 (s), 54.55 (m), 7.47 (m), -33.22 (s).

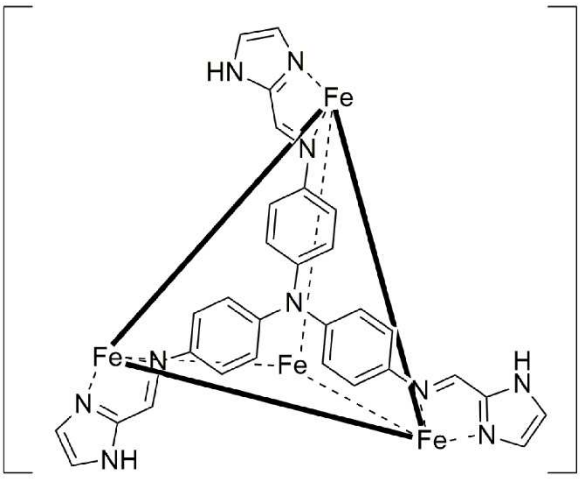

Cage APA•Fe•2ImCHO:

Tris(4-aminophenyl)amine (**APA)** (30.0 mg, 0.10 mmol), 2-formylimidazole (30.0 mg, 0.20 mmol), and $Fe(NTf_2)_2$ (72.0 mg, 0.10 mmol) were combined in MeCN (10 mL) in a 25 mL round-bottom flask. The solution was then heated at 77°C for 18 h with stirring. The reaction mixture was cooled, and the acetonitrile removed in vacuo. The red solid was sonicated with 20 mL of 3:1 Et_2O:MeOH solution and filtered. After drying, the product was isolated as a red powder (79.9 mg, 70% yield). ^{1}H NMR (400 MHz; CD_3CN) δ 123.17 (s, br), 67.00 (s), 59.47 (s), 17.13 (s), 3.45 (s), 1.14 (s).

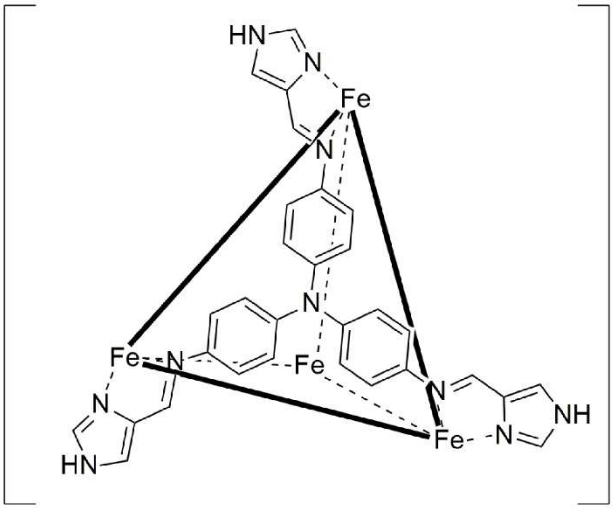

CageAPA•Fe•4ImCHO:

Tris(4-aminophenyl)amine (**APA)** (30.0 mg, 0.10 mmol), 4-formylimidazole (30.0 mg, 0.20 mmol), and $Fe(NTf_2)_2$ (72.0 mg, 0.10 mmol) were combined in MeCN (10 mL) in a 25 mL round-bottom flask. The solution was then heated at 77°C for 18 h with stirring. The reaction mixture was cooled, and the acetonitrile removed in vacuo. The red solid was sonicated with 20 mL of 3:1 Et_2O:MeOH solution and filtered. After drying, the product was isolated as a red powder (74.1 mg, 65% yield). ^{1}H NMR (400 MHz; CD_3CN) δ 152.85 (s), 93.00 (s), 39.20 (s), 24.34 (s), 1.12 (s), -7.04 (s).

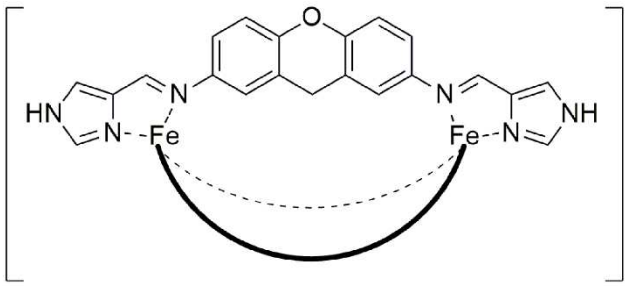

Meso-helicate X•Fe•4ImCHO:

2,7-diaminoxanthene (**X)** (30.0 mg, 0.14 mmol), 4-formylimidazole (27.2 mg, 0.28 mmol), and $Fe(NTf_2)_2$ (65.0 mg, 0.093 mmol) were combined in MeCN (10 mL) in a 25 mL round-bottom flask. The solution was then heated at 77°C for 18 h with stirring. The reaction mixture was cooled, and the acetonitrile removed in vacuo. The red solid was sonicated with 20 mL of 3:1 Et_2O:MeOH solution and filtered. After drying, the product was isolated as a red powder (81.8 mg, 75% yield). ^{1}H NMR (400 MHz; CD_3CN) δ 158.22 (s), 39.86 (s), 12.84 (s), 9.80 (s), 7.84 (s), 7.78 (s), 3.60 (s), -6.69 (s), -10.23 (s).

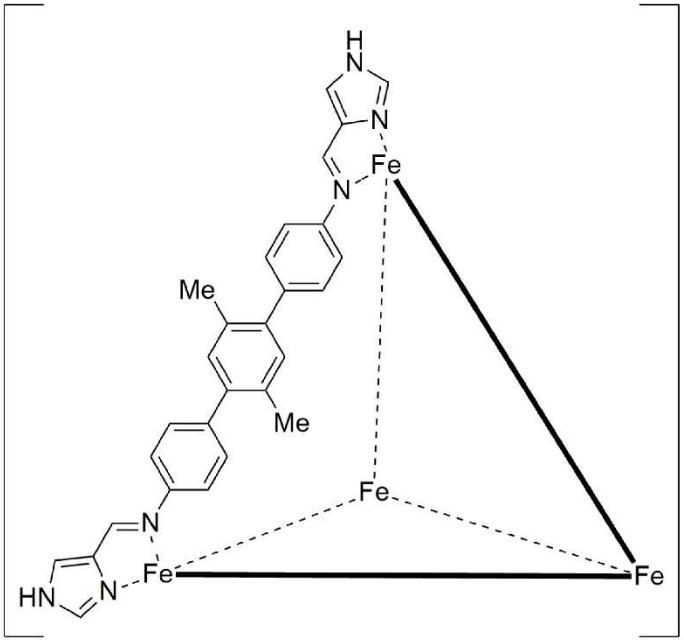

Cage Ph_2Xy•Fe•4ImCHO:

2,7-bis(4-aminophenyl) xylenes (**Ph_2Xy**) (26.0 mg, 0.090 mmol). 4-formylimidazole (17.3 mg, 0.18 mmol), and $Fe(NTf_2)_2$ (20.0 mg, 0.060 mmol) were combined in MeCN (10 mL) in a 25 mL round-bottom flask. The solution was then heated at 77°C for 24 h with stirring. The reaction mixture was cooled, and the acetonitrile removed in vacuo. The red solid was sonicated with 20 mL of 3:1 Et_2O:MeOH solution and filtered. After drying, the product was isolated as a red powder (76.9 mg, 49% yield). ^{1}H NMR (400 MHz; CD_3CN) δ 161.68 (d, J=414.64), 158.46 (d, J=888.05 Hz), 155.69 (m), 154.82 (s), 93.16 (d, J=219.52 Hz), 92.61 (s), 90.88 (t, J=168.12), 41.49 (d, J=849.29 Hz, br), 39.05 (m), 35.70 (d, J=724.24 Hz, br), 20.16 (s, br), 16.97 (s, br), 14.92 (d, 78.52), 14.35 (d, J=116.59 Hz), 13.63 (t, 116.72), 1.98 (s), 1.41 (d, J=83.43), 0.88 (s).

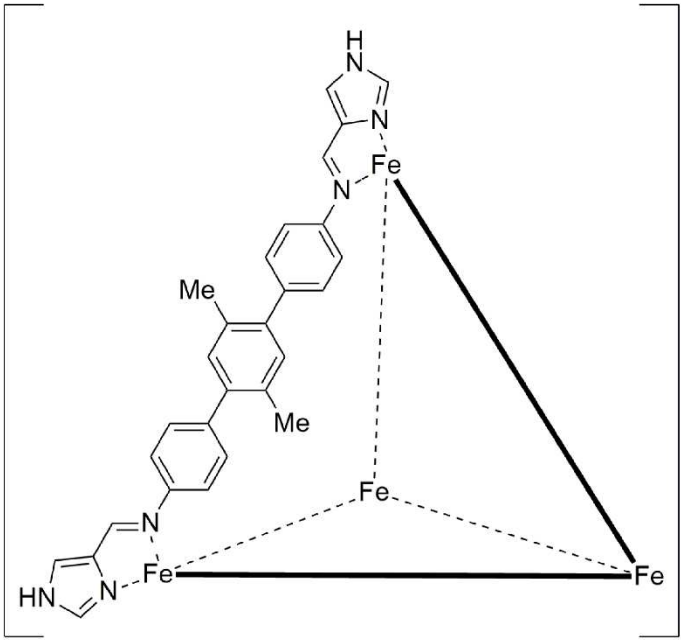

Cage Ph_2F•Fe•4ImCHO:

2,7-bis(4-aminophenyl) fluorene (**Ph_2F**) (20.0 mg, 0.057 mmol). 4-formylimidazole (11.0 mg, 0.12 mmol), and $Fe(NTf_2)_2$ (13.2 mg, 0.019 mmol) were combined in MeCN (10 mL) in a 25 mL round-bottom flask. The solution was then heated at 77°C for 24 h with stirring. The reaction mixture was cooled, and the acetonitrile removed in vacuo. The red solid was sonicated with 20 mL of 3:1 Et_2O:MeOH solution and filtered. After drying, the product was isolated as a red powder (80.0 mg, 52% yield). ^{1}H NMR (400 MHz; CD_3CN) δ 96.61(s), 93.00 (m), 90.26 (s), 87.90 (s), 74.20 (d, J=765.6 Hz), 39.77 (m), 20.25 (s), 14.66 (m), 13.00 (s), 7.73 (m), -6.36 (m).

6.4 Chapter 4 Experimental

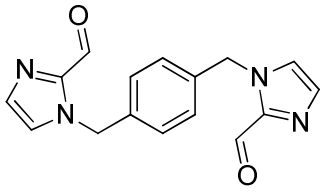

Synthesis of $XyIm_2$

In a 50 mL two neck flask α,α-dibromo-p-xylene (400 mg, 1.50 mmol) with 2-imdazolecarboxaldehyde (393 mg, 4.09 mmol) and K_2CO_3 (394 mg, 2.85 mmol) were combined. The flask was purged with N_2. Dry DMF (2 mL) was injected into the flask via syringe. The reaction stirred for 12 h at room temperature. The reaction was then triturated with hexanes, the solid was filtered and then dissolved in 30 mL DCM. The solution was extracted three times with 20 mL concentrated $NaHCO_3$ solution followed by 15 mL brine. The organic solution was then dried with $MgSO_4$ and filtered, remaining solvent was removed in vacuo leaving a white powder (210 mg, 47% yield). HRMS (ESI) m/z calcd for $C_{16}H_{14}N_4O_2$ 294.1075, found 295.1149 $(M-H)^+$. ^1H NMR (400 MHz, $CDCl_3$) δ 9.99 (s, 2H), δ 7.31 (d, J=16 Hz, 2H), δ 7.18 (d, 4H, J=3.8 Hz), 7.15 (s, 2H), δ 5.615 (s, 4H). ^{13}C NMR (400 MHz, $CDCl_3$) δ 201.55 (s), 176.79 (s), 137.88 (s), 130.71 (s), 126.64 (s), 122.85 (s), 121.00 (s), 45.04 (s), 25.67 (s). HRMS (ESI) m/z calcd for $C_{16}H_{14}N_4O_2$ 294.1117, found 295.1190 $(M-H)^+$.

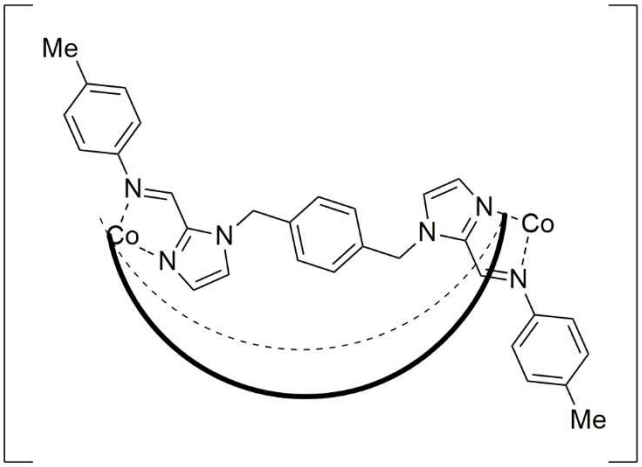

Synthesis of XyIm$_2$•Co•Toluidine

XyIm$_2$ (30.0 mg, 0.10 mmol), Co(NTf$_2$)$_2$ (63.2 mg, 0.066 mmol), and p-toluidine (21.8 mg, 0.20 mmol) were combined in a round bottom flask with MeCN (5 mL). The mixture reacted at 50 ˚C for 2 days. Solvent was removed in vacuo, then triturated with ether and filtered. Solid was washed with 1:3 methanol: ether (10 mL) resulting in a reddish brown solid (36 mg, 40% yield).

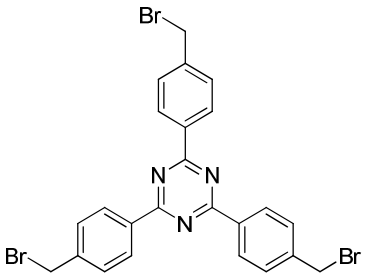

Synthesis of 2,4,6-tris(4-(bromomethyl)phenyl)-1,3,5-triazine (Tz)

4-Cyanobenzyl bromide (1.00 g, 5.1 mmol) was added to a 100 mL Schlenk flask. The flask was purged with N_2 and brought to 0 ˚C. Trifluoromethane Sulfuric Acid (1.35 mL, 5.1 mmol) was then added slowly via syringe, and purged again. Once the addition was

complete the flask was moved from the ice bath, allowed to warm to room temperature, and stirred for 12 hours. The mixture was then poured over cold water precipitate was then filtered and washed with acetone to yield a white solid (2.8 g, 95% yield). ^{1}H NMR (400 MHz, $CDCl_3$) δ 9.89 (d, 6H, J=8.4 Hz), δ 7.62 (d, 6H, J=8.4 Hz), δ 4.61 (s, 6H). ^{13}C NMR (MHz, $CDCl_3$) δ 171.13 (s), 142.30 (s), 136.07 (s), 129.41 (s), 32.73 (s). HRMS (ESI) m/z calcd for $C_{24}H_{18}Br_3N$ 584.9051, found 587.9103 $(M-H)^+$.

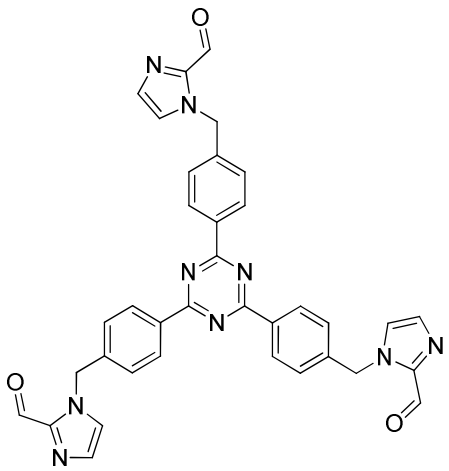

Synthesis of TzIm$_3$

To a 50 mL two neck flask **Tz** (300 mg, 0.51 mmol), 2-imidazolecarboxaldehyde (198.6 mg, 2.07 mmol), and K_2CO_3 (201 mg, 1.5 mmol) were combined. The flask was purged with N_2. Dry DMF (2 mL) was injected into the flask via syringe. The reaction stirred for 12 h at room temperature. The reaction was then triturated with hexanes, the solid was filtered and then dissolved in 30 mL DCM. The solution was extracted three times with 20 mL concentrated $NaHCO_3$ solution followed by 15 mL brine. The organic solution was then dried with $MgSO_4$ and filtered, remaining solvent was removed in vacuo leaving a

white powder (162 mg, 50% yield). ^{1}H NMR (400 MHz, $CDCl_3$) δ9.89 (s, 3H, J=0.8 Hz), δ 8.70 (d, 6H, J=8.4 Hz), δ 7.38 (d, 6H, J=8.4 Hz), δ 7.38 (d, 3H, J=0.8 Hz), δ 7.24 (s, 3H), δ 5.75 (s, 6H). ^{13}C NMR (400 MHz, $CDCl_3$) δ 182.24 (s), δ 171.5 (s), δ 143.36 (s), δ 140.37 (s), δ136.05 (s), δ132.12 (s), δ 129.60 (s), δ 127.80 (s), δ126.35 (s), δ 50.74 (s).

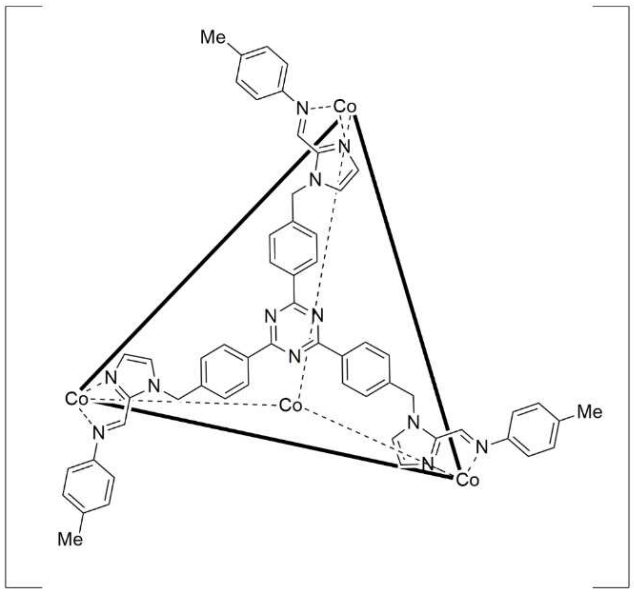

Synthesis of tripodal cage (TzIm$_3$•Co•PhMe•NTf$_2$)

TzIm$_3$ (50 mg, 0.079 mmol), $Co(NTf_2)_2$ (49 mg, 0.079 mmol), and p-toluidine (25 mg, 0.237 mmol) were combined in a round bottom flask with MeCN (5 mL). The mixture reacted at 50 ˚C for 2 days. Solvent was removed in vacuo, then triturated with ether and filtered. Solid was washed with 1:1 methanol: ether (10 mL) resulting in a reddish brown solid (93.8 mg, 78% yield). ^{1}H NMR (400 MHz, $CDCl_3$) δ 131.79 (s, br), 113.17 (s, br), 103.77 (s), 99.86 (s), 98.30 (s), 92.46 (s), 84.13 (s), 83.68 (s), 83.34 (dd, J=90.0, 54.6 Hz), 82.13 (s), 81.96 (s), 81.80 (s), 81.51 (s), 81.39 (s), 80.47 (s), 79.15 (s), 77.70 (s), 70.00 (s,

br), 68.50 (s), 61.28 (s, br), 57.44 (s, br), 55.10 (s), 49.09 (s), 45.54 (s,br), 43.93 (s, br), 42.72 (s, br), 39.54 (s br), 30.90 (s, br), 23.69 (s), 22.51 (s), 21.69 (s), 19.71 (s), 18.99 (s), 18.17 (s), 17.66 (s), 17.28 (s), 16.99 (s), 16.85 (s), 16.41 (s), 16.28 (s), 15.89 (s), 15.69 (s), 15.21 (s), 14.78 (s), 14.62 (s), 14.40 (s), 13.53 (s), 13.17 (s), 12.59 (s), 12.31 (s), 12.14 (s), 12.00 (s), 11.40 (s), 11.31 (s), 10.95 (s), 10.82 (s), 10.49 (s), 10.14 (s), 9.82 (s), 9.73 (s), 9.25 (s), 8.85 (s), 8.48 (s), 8.26 (s), 8.01 (s), 7.77 (s), 7.59 (s), 7.52 (s), 7.39 (s), 7.11 (s), 6.94 (s), 6.65 (s), 6.31 (s), 5.61 (s), 5.13 (s), 4.93 (s), 4.10 (s), 3.70 (s), 3.59 (s), 3.39 (s), 3.12 (s), 1.80 (s), 1.28 (s), 0.78 (s), 0.38 (s), 0.28 (s), -0.36 (s), -0.48 (s), -1.10 (s), -1.29 (s), -1.97 (s), -2.61 (s), -2.89 (s), -4.00 (s), -4.15 (s), -4.48 (s), -4.81 (s), -4.94 (s), -5.58 (s), -5.92 (s), -6.54 (s), -7.21 (s), -8.15 (s), -9.16 (s), -9.78 (s), -10.94 (s, br), -18.72 (s), -28.40 (s), -33.05 (s), -34.54 (s), -38.77 (s), -41.28 (s), -44.77 (s), -46.65 (s), -54.88 (s), -58.02 (s), -63.22 (s), -66.30 (s).

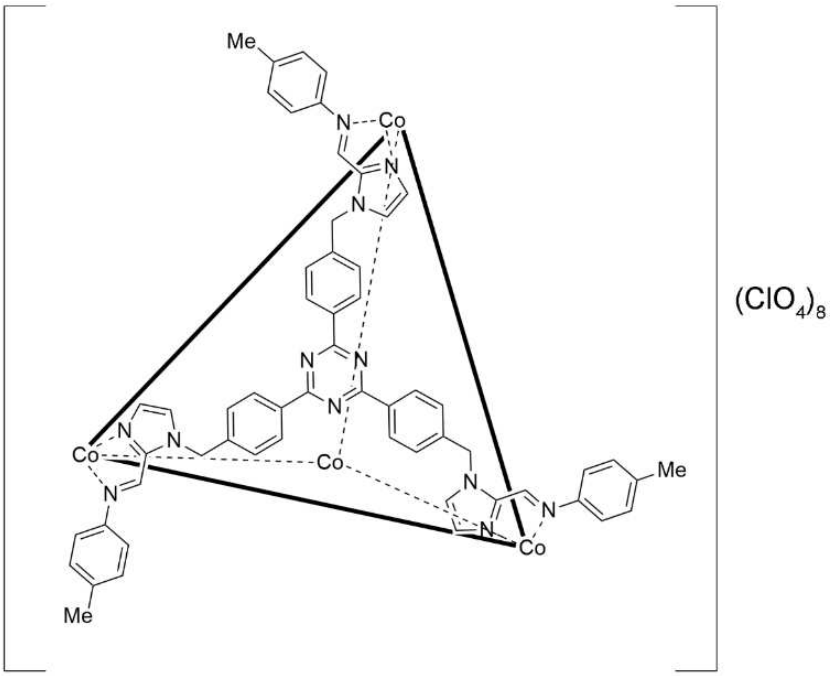

Synthesis of tripodal cage (TzIm$_3$•Co•PhMe•ClO$_4$)

TzIm$_3$ (50 mg, 0.079 mmol), $Co(ClO_4)_2$ (34.1 mg, 0.079 mmol), and p-toluidine (25 mg, 0.237 mmol) were combined in a round bottom flask with MeCN (5 mL). The mixture reacted at 50 ˚C for 2 days. Solvent was removed in vacuo, then triturated with ether and filtered. Solid was washed with 1:1 methanol: ether (10 mL) resulting in a reddish brown solid (33 mg, 36% yield). ^{1}H NMR (400 MHz, $CDCl_3$) δ 104.69 (s), 101.71 (s), 82.37 (s), 81.34 (s), 78.65 (s), 25.10 (s), 21.99 (s), 21.65 (s), 19.25 (s), 17.50 (s), 15.40 (s), 14.71 (s), 13.44 (s), 12.64 (s), 12.17 (s), 10.61 (d, J=55 Hz), 9.35 (s), 8.88 (d, J=74 Hz), 6.80 (m), 4.50 (s), 3.71 (s), 3.48 (s), 1.15 (s), 0.89 (s), 0.43 (s), 0.03 (s), -0.55 (s), -3.91 (s), -6.61 (s), -12.46 (s), -13.57 (s), -15.25 (s), -15.95 (s), -20.08 (s), -30.33 (s), -31.65 (s), -48.05 (s), -60.45 (s), -61.47 (s).

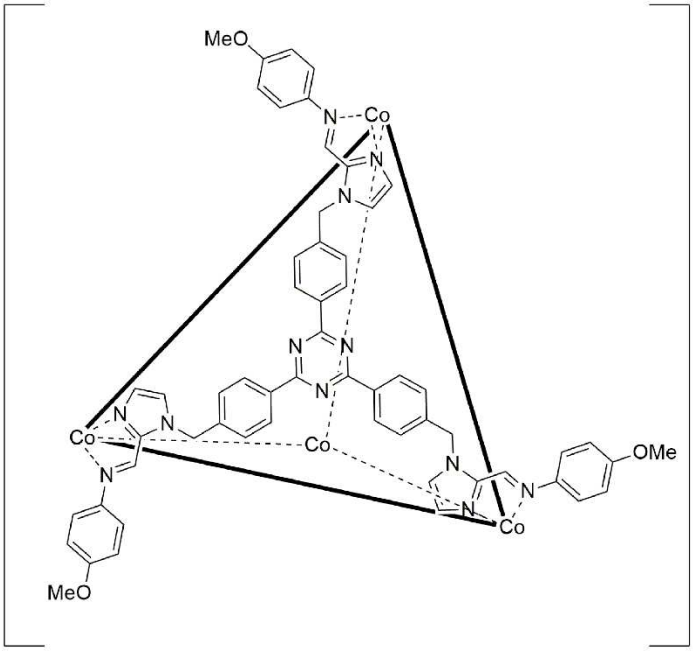

Synthesis of tripodal cage ($TzIm_3$•Co•PhOMe)

$TzIm_3$ (20 mg, 0.034 mmol), $Co(NTf_2)_2$ (19.5 mg, 0.034 mmol), and p-anisidine (4 mg, 0.102 mmol) were combined in a round bottom flask with MeCN (5 mL). The mixture reacted at 50 ˚C for 2 days. Solvent was removed in vacuo, then triturated with ether and filtered. Solid was washed with 1:1 methanol: ether (10 mL) resulting in a reddish brown solid (21.6 mg, 54% yield). ^{1}H NMR (400 MHz, $CDCl_3$) δ 82.03 (s), 44.98 (s), 16.78 (s), 11.91 (s), 11.34 (s), 6.93 (s), 6.68 (d, J=60.7), 3.70 (s), 2.19 (s), 1.96 (s), 1.30 (s), 0.88 (s), -.0.07 (s), -0.68 (s).

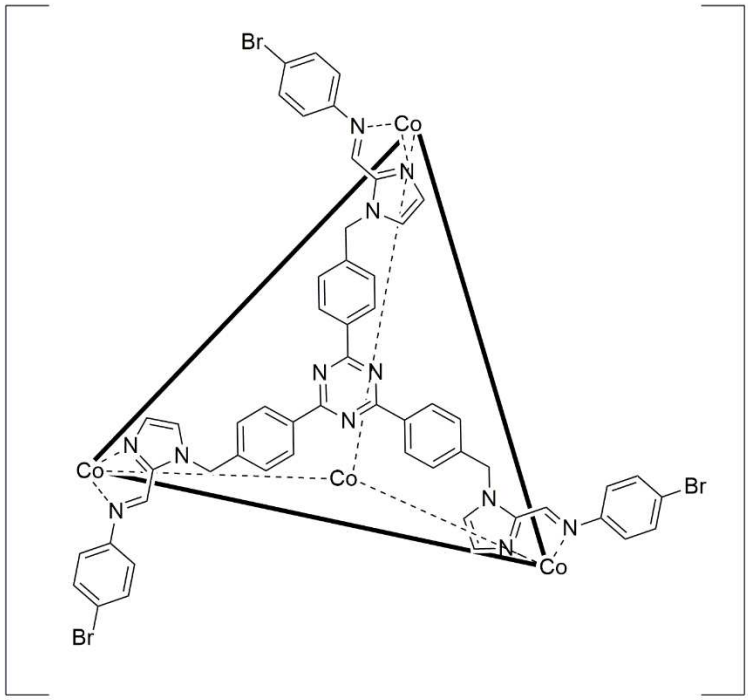

Synthesis of tripodal cage (TzIm$_3$•Co•PhBr)

TzIm$_3$ (30 mg, 0.047 mmol), $Co(ClO_4)_2$ (18.15 mg, 0.0.47 mmol), and 4-bromoaniline (25 mg, 0.142 mmol) were combined in a round bottom flask with MeCN (5 mL). The mixture reacted at 50 ˚C for 2 days. Solvent was removed in vacuo, then triturated with ether and filtered. Solid was washed with 1:1 methanol: ether (10 mL) resulting in a reddish brown solid (31.7 mg, 51% yield). ^{1}H NMR (400 MHz, $CDCl_3$) δ 114.40 (s),99.59 (s, br), 81.70 (s), 44.07 (s), 29.72 (s), 16.86 (m), 14.70 (m), 13.21 (m), 11.79 (s), 11.43 (s), 9.96 (d, J=72 Hz), 8.71 (d, J=72 Hz), 6.58 (m), -33.37 (s), -67.65 (s).

6.5 Chapter 5 Experimental

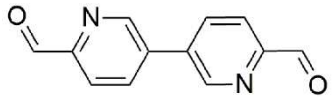

Synthesis of DimerPyCHO

In a two-neck flask, 5-bromo-2-pyridinecarboxaldehyde (100.0 mg, 0.538 mmol), bis(pinacolato)diboron (273.0 mg, 1.075 mmol), K_3PO_4, and $Pd(dppf)_2Cl_2$ (342.4 mg, 1.613 mmol) was purged with N_2 and combined with Dioxane. The mixture was reacted at 80° C for 16 h. To the reaction mixture 10 mL of DCM was added. The solution was extracted with 3 x 10 mL of brine and the organic layer was dried with $MgSO_4$ and filtered, remaining solvent was removed in vacuo leaving a white powder (24.5 mg, 43% yield). ^1H NMR (400 MHz, $CDCl_3$) δ 10.07 (s, 2H), 8.81 (d, J=2.35 Hz, 2H), 8.00 (dd, J=2.4, 8.2 Hz, 2H), 7.66 (d, J=8.1 Hz, 2H).

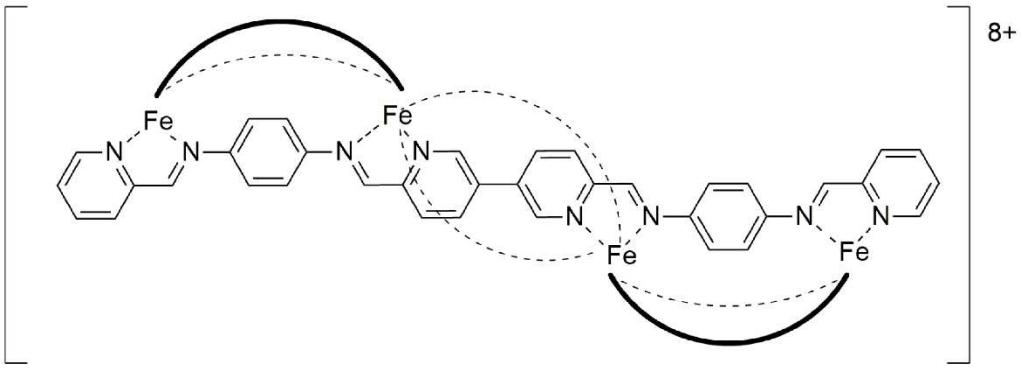

Synthesis of helicate DimerPyCHO(PhN)$_2$•Fe•PyCHO

DimerPyCHO (10 mg, 0.047 mmol), PyCHO (8.97 μL, 0.094 mmol), *p*-phenylene diamine (10.2 mg, 0.094 mmol), and $Fe(ClO_4)_2$ (20.5 mg, 0.063 mmol) were combined in an NMR tube in 400 μL CD_3CN and reacted at 80°C for 18 h.

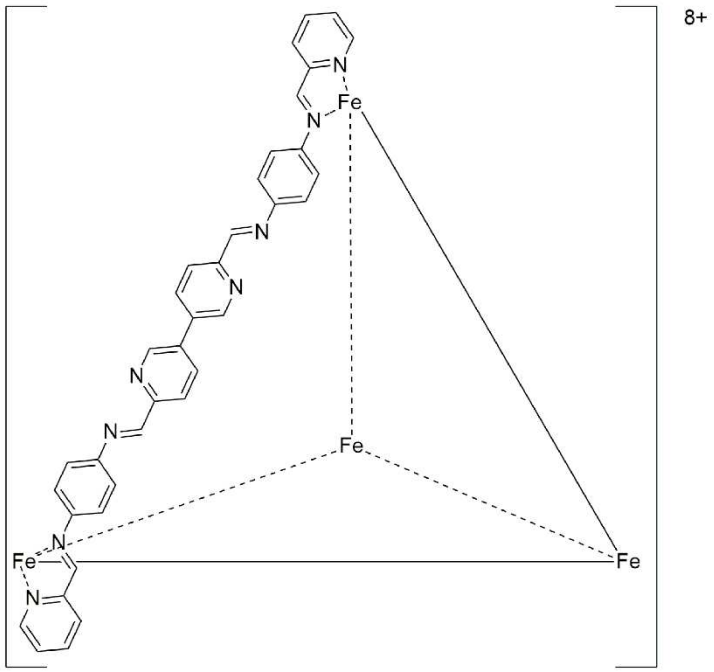

Synthesis of tetrahedal DimerPyCHO $(PhN)_2$•Fe•PyCHO

DimerPyCHO (10 mg, 0.047 mmol), PyCHO (8.97 μL, 0.094 mmol), *p*-phenylene diamine (10.2 mg, 0.094 mmol), and $Fe(ClO_4)_2$ (10.3 mg, 0.031 mmol) were combined in an NMR tube in 400 μL CD_3CN and reacted at 80°C for 18 h.

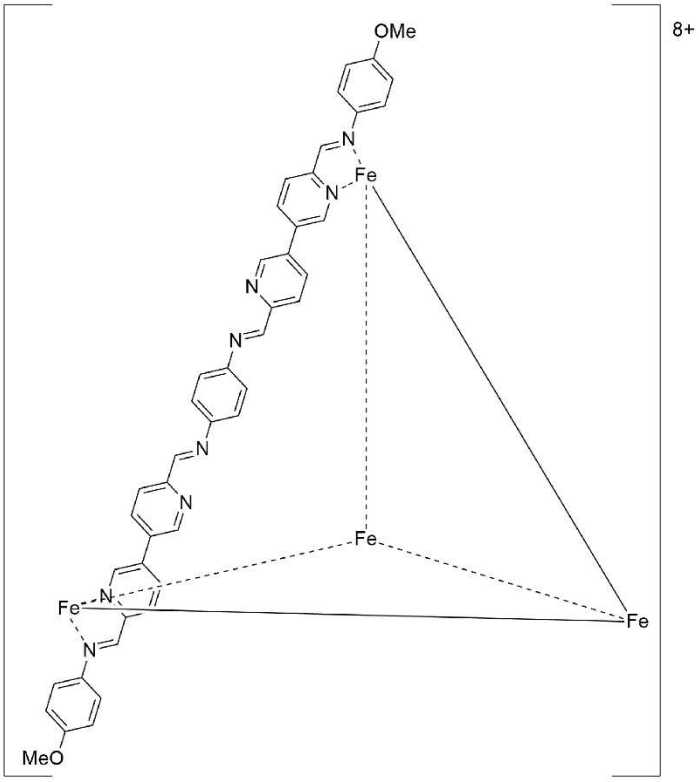

Synthesis of PhN(DimerPyCHO)$_2$•Fe•PhOMe

p-Phenylene Diamine (2.55 mg, 0.024 mmol), DimerPyCHO (10 mg, 0.047 mmol), p-anisidine (5.8 mg, 0.047 mmol), and $Fe(ClO_4)_2$ (5.1 mg, 0.16 mmol) were combined in an NMR tube in 400 μL CD_3CN and reacted at 80°C for 18 h.

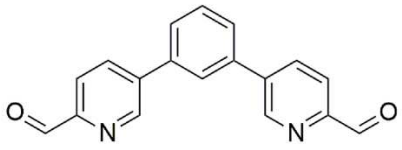

Synthesis of 1,3-Ph(PyCHO)$_2$

In a two-neck flask combine 1,3-boronic acid (50 mg, 0.603 mmol), 5-bromo-2-pyridinecarboxaldehyde (123.5 mg, 1.327 mmol), K_2CO_3 (125.1 mg, 1.81 mmol), and

$Pd(OAc)_2$ (5.35 mg, 0.060 mmol) in 3 mL 3:1 EtOH:H_2O. React at 75°C for 4 h. Precipitate product with H_2O and filter the precipitate. (109.4 mg, 63% yield). ^1H NMR (400 MHz, DMSO) δ 10.1 (s, 2H), 9.20 (s, 2H), 8.34 (s, 1H) 8.13 (d, J=3.1, 4H), 7.90 (s, 1H), 7.76 (s, 2H).

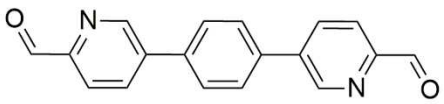

Synthesis of 1,4-Ph(PyCHO)$_2$

In a two-neck flask combine 1,3-boronic acid (50 mg, 0.603 mmol), 5-bromo-2-pyridinecarboxaldehyde (123.5 mg, 1.327 mmol), K_2CO_3 (125.1 mg, 1.81 mmol), and $Pd(OAc)_2$ (5.35 mg, 0.060 mmol) in 3 mL 3:1 EtOH:H_2O. React at 75°C for 4 h. Precipitate product with H_2O and filter the precipitate. (132 mg, 76% yield). ^1H NMR (400 MHz, DMSO) δ 10.1 (s, 2H), 9.17 (s, 2H), 8.36 (s, 4H), 8.33 (dd, J=2.1, 8.2 Hz, 2H), 8.29 (d, J=8.3 Hz, 2H).

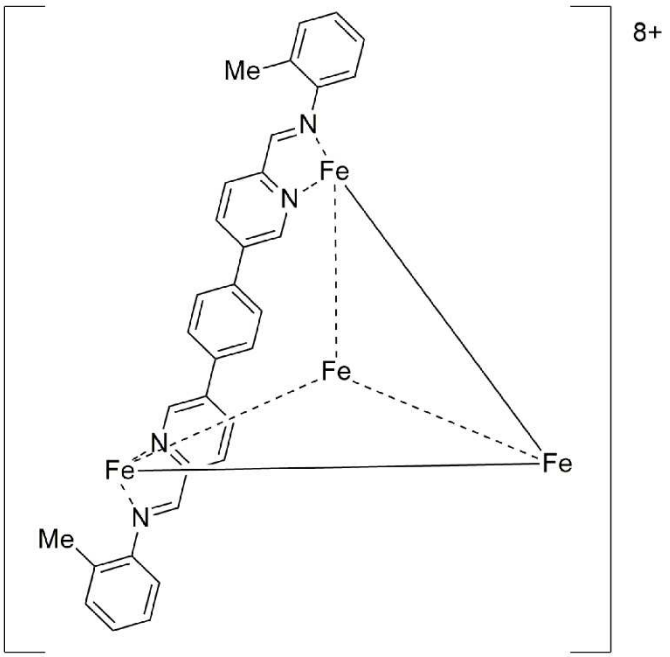

Synthesis of 1,4-Ph(PyCHO)$_2$•Fe•*o*PhMe

In a round bottom flask **1,4-Ph(PyCHO)$_2$** (20 mg, 0.069 mmol), *o*-toluidine (30 mg, 0.139 mmol), and $Fe(BF_4)$ (15.6 mg, 0.046 mmol) were combined with 3 mL MeCN and heated to 80°C for 16 h. The reaction mixture is combined with Et_2O and the precipitate is filtered out.

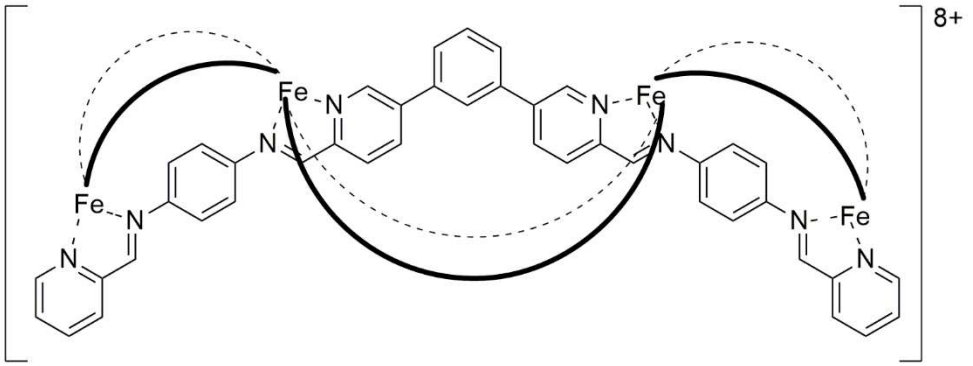

Synthesis of 1,3- Ph(PyCHO)$_2$•Fe•PhN•PyCHO

In a round bottom flask, **1,3-Ph(PyCHO)$_2$** (10 mg, 0.035 mmol), *p*-phenylene diamine (15 mg, 0.070 mmol), PyCHO (7.5 μL, 0.070 mmol), and Fe(BF_4) (15.6 mg, 0.046 mmol) were combined and purged with N_2 followed by the addition of 3 mL dry MeCN and heated to 80°C for 16 h.

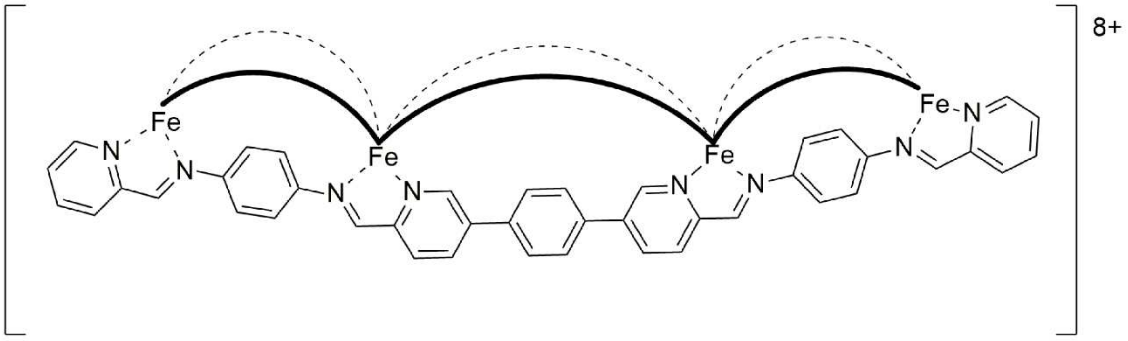

Synthesis of 1,4- Ph(PyCHO)$_2$•Fe•PhN•PyCHO

In an NMR tube, **1,4-Ph(PyCHO)$_2$** (10 mg, 0.035 mmol), *p*-phenylene diamine (15 mg, 0.070 mmol), PyCHO (7.5 μL, 0.070 mmol), and Fe(BF_4) (15.6 mg, 0.046 mmol) were combined and purged with N_2 followed by the addition of 3 mL dry MeCN and heated to 80°C for 16 h.

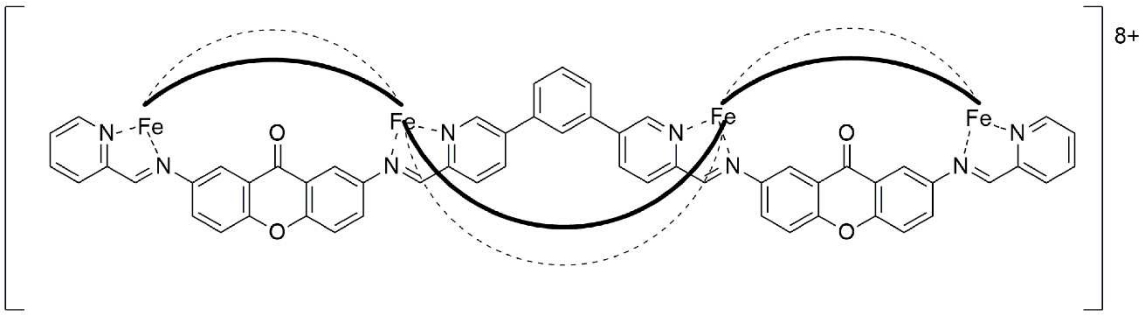

Synthesis of 1,3- Ph(PyCHO)$_2$•Fe•XO•PyCHO

In a NMR tube, **1,3-Ph(PyCHO)$_2$** (10 mg, 0.0069 mmol), 2,7-diaminoxanthone (3.14 mg, 0.014 mmol), PyCHO (1.32 μL, 0.0014 mmol), and $Fe(BF_4)$ (13.13mg, 0.0093 mmol) were combined and purged with N_2 followed by the addition of 3 mL dry MeCN and heated to 80°C for 16 h.

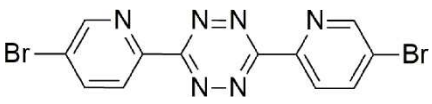

Synthesis of BrPy•Tet•BrPy

In a two-neck flask 5-bromo-2-carbonitrile (366.0 mg, 2 mmol) and mercaptopropionic acid (87 μL, 1 mmol) were combined and purged with N_2. Dry EtOH (100 μL) was added and the reaction vessel was cooled to 0°C then H_2NNH_2•H_2O (777 μL, 16 mmol) was added slowly via syringe. Dry DCM was added to aid in solvation and reaction was heated to 38°C and allowed to react for 16 h. Reaction solution was then added to 150 mL ice water followed by $NaNO_2$ (1.03 g, 15 mmol). 1M HCl was added to solution until gas evolution ceased (pH 3-4). The solution was then extracted with 3x20 mL DCM and the organic layers were combined and washed with 50mL brine. The organic layer was dried with

$MgSO_4$. (154.3 mg, 20% yield). ^1H NMR (400 MHz, $CDCl_3$) δ 8.66 (d, J=1.74 Hz, 2H), 8.13 (dd, J=0.6, 8.38 Hz, 2H), 8.03 (tt, J=2.2 Hz, 9.3 Hz, 17.7 Hz, 2H)

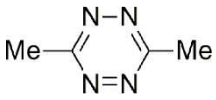

Synthesis of Me•Tet•Me

In a two-neck flask acetonitrile (104.45 µL, 2 mmol), and mercaptopropionic acid (87 µL, 1 mmol) were combined and purged with N_2. Dry EtOH (200 µL) was added and the reaction vessel was cooled to 0°C then $H_2NNH_2•H_2O$ (156 µL, 16 mmol) was added slowly via syringe. Dry DCM was added to aid in solvation and reaction was heated to 38°C and allowed to react for 16 h. Reaction solution was then added to 150 mL ice water followed by $NaNO_2$ (1.03 g, 15 mmol). 1M HCl was added to solution until gas evolution ceased (pH 3-4). The solution was then extracted with 3x20 mL DCM and the organic layers were combined and washed with 50mL brine. The organic layer was dried with $MgSO_4$. (28.6 mg, 13% yield).

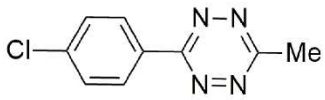

Synthesis of ClBn•Tet•Me

In a two-neck flask acetonitrile (835.6 µL, 16 mmol), *p*-chlorobenzonitrile (275.14 mg, 2 mmol), and mercaptopropionic acid (348 µL, 2 mmol) were combined and purged with N_2. Dry EtOH (2 mL) was added and the reaction vessel was cooled to 0°C then $H_2NNH_2•H_2O$

(3.1 mL, 64 mmol) was added slowly via syringe. Dry DCM was added to aid in solvation and reaction was heated to 38°C and allowed to react for 16 h. Reaction solution was then added to 150 mL ice water followed by $NaNO_2$ (4 g, 60 mmol). 1M HCl was added to solution until gas evolution ceased (pH 3-4). The solution was then extracted with 3x20 mL DCM and the organic layers were combined and washed with 50mL brine. The organic layer was dried with $MgSO_4$. (132.2 mg, 32% yield). ^{1}H NMR (400 MHz, $CDCl_3$) δ 8.57 (d, 8.7 Hz, 2H), 8.13 (d, J=7.2, 2H), 3.13 (s, 3H).

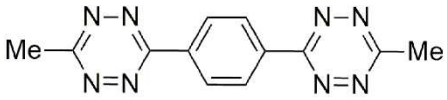

Synthesis of Me•Tet•TP•Tet•Me

In a two-neck flask acetonitrile (417.8 μL, 16 mmol), terephthalonitrile (128.13 mg, 1mmol), and mercaptopropionic acid (174 μL, 2 mmol) were combined and purged with N_2. Dry EtOH (200 μL) was added and the reaction vessel was cooled to 0°C then $H_2NNH_2•H_2O$ (1554 μL, 32 mmol) was added slowly via syringe. Dry DCM was added to aid in solvation and reaction was heated to 38°C and allowed to react for 16 h. Reaction solution was then added to 150 mL ice water followed by $NaNO_2$ (4 g, 60 mmol). 1M HCl was added to solution until gas evolution ceased (pH 3-4). The solution was then extracted with 3x20 mL DCM and the organic layers were combined and washed with 50mL brine. The organic layer was dried with $MgSO_4$. (90.5 mg, 34% yield). ^{1}H NMR (400 MHz, $CDCl_3$) δ 8.86 (s, 4H), 3.17 (s, 6H)

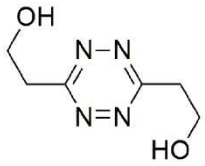

Synthesis of V•Tet•V

In a two-neck flask acrylonitrile (131.66 µL, 2 mmol), and mercaptopropionic acid (87 µL, 1 mmol) were combined and purged with N_2. Dry EtOH (200 µL) was added and the reaction vessel was cooled to 0°C then $H_2NNH_2•H_2O$ (156 µL, 16 mmol) was added slowly via syringe. Dry DCM was added to aid in solvation and reaction was heated to 38°C and allowed to react for 16 h. Reaction solution was then added to 150 mL ice water followed by $NaNO_2$ (1.03 g, 15 mmol). 1M HCl was added to solution until gas evolution ceased (pH 3-4). The solution was then extracted with 3x20 mL DCM and the organic layers were combined and washed with 50mL brine. The organic layer was dried with $MgSO_4$. (25.5 mg, 15% yield). ^{1}H NMR (400 MHz, $CDCl_3$) δ 4.99 (m, H), 4.13 (t, J=8.4, 2H), 2.89 (t, J=8.8, 2H).

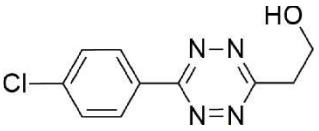

Synthesis of BnCl•Tet•$(CH_2)_2$OH

In a two-neck flask acrylonitrile (526.6 µL, 8 mmol), *p*-chlorobenzonitrile (137.57 mg, 1 mmol), and mercaptopropionic acid (87 µL, 1 mmol) were combined and purged with N_2. Dry EtOH (200 µL) was added and the reaction vessel was cooled to 0°C then $H_2NNH_2•H_2O$ (777 µL, 16 mmol) was added slowly via syringe. Dry DCM was added to

aid in solvation and reaction was heated to 38°C and allowed to react for 16 h. Reaction solution was then added to 150 mL ice water followed by $NaNO_2$ (1.03 g, 15 mmol). 1M HCl was added to solution until gas evolution ceased (pH 3-4). The solution was then extracted with 3x20 mL DCM and the organic layers were combined and washed with 50mL brine. The organic layer was dried with $MgSO_4$. (33.1 mg, 14% yield). ^{1}H NMR (400 MHz, $CDCl_3$) δ 8.61 (d, J=8.8 Hz, 2H), 7.61 (d, J=8.8 Hz, 2H), 4.23 (t, J=8.8 Hz, 2H), 2.97 (t, J=9.07 Hz, 3H).

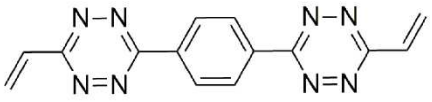

Synthesis of V•Tet•TP•Tet•V

In a two-neck flask acrylonitrile (1053.3 μL, 16 mmol), terephthalonitrile (128.13 mg, 1 mmol), and mercaptopropionic acid (174 μL, 2 mmol) were combined and purged with N_2. Dry EtOH (200 μL) was added and the reaction vessel was cooled to 0°C then $H_2NNH_2•H_2O$ (1554 μL, 32 mmol) was added slowly via syringe. Dry DCM was added to aid in solvation and reaction was heated to 38°C and allowed to react for 16 h. Reaction solution was then added to 150 mL ice water followed by $NaNO_2$ (4 g, 60 mmol). 1M HCl was added to solution until gas evolution ceased (pH 3-4). The solution was then extracted with 3x20 mL DCM and the organic layers were combined and washed with 50mL brine. The organic layer was dried with $MgSO_4$. (78 mg, 27% yield). ^{1}H NMR (400 MHz, $CDCl_3$) δ 7.81 (s, 4H), 4.21 (t, J=8.8, 4H), 2.97 (t, J=8.8, 6H)

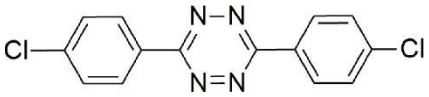

Synthesis of BnCl•Tet•BnCl

In a two-neck flask *p*-chlorobenzonitrile (275.14 mg, 1 mmol), and mercaptopropionic acid (87 μL, 1 mmol) were combined and purged with N_2. Dry EtOH (100 μL) was added and the reaction vessel was cooled to 0°C then $H_2NNH_2•H_2O$ (156 μL, 16 mmol) was added slowly via syringe. Dry DCM was added to aid in solvation and reaction was heated to 38°C and allowed to react for 16 h. Reaction solution was then added to 150 mL ice water followed by $NaNO_2$ (1.03 g, 15 mmol). 1M HCl was added to solution until gas evolution ceased (pH 3-4). The solution was then extracted with 3x20 mL DCM and the organic layers were combined and washed with 50mL brine. The organic layer was dried with $MgSO_4$. (52.9 mg, 35% yield). ^{1}H NMR (400 MHz, $CDCl_3$) δ 8.11 (s, 8H).

Bromination Attempt 1 of BnCl•Tet•Me

In a two-neck flask **BnCl•Tet•Me** (50.0 mg, 0.245 mmol), benzoyl peroxide (11.75 mg, 0.049 mmol), and NBS (51.8 mg, 0.291 mmol) were purged with N_2 and 10 mL dry benzene was added via syringe. Mixture was reacted at 80°C for 18 h. Mixture was filtered to remove precipitate and remaining solvent was removed *in vacuo*.

Bromination Attempt 2 of BnCl•Tet•Me

In a two-neck flask **BnCl•Tet•Me** (50.0 mg, 0.245 mmol), AIBN (51.8 mg, 0.318 mmol), and NBS (51.8 mg, 0.245 mmol) were purged with N_2 and 10 mL Benzene was added via

syringe. Mixture was reacted at 80°C for 18 h. Reaction mixture was cooled to room temperature and diluted with 20 ml of Et_2O. Product was extracted with brine (10 mL), sat. sodium bicarbonate solution (10 mL), and DI H_2O (10 mL). Organic layer was dried with $MgSO_4$ and remaining solvent was removed *in vacuo*.

Bromination Attempt 3 of BnCl•Tet•Me

In a two-neck flask **BnCl•Tet•Me** (50.0 mg, 0.245 mmol), benzoyl peroxide (23.51 mg, 0.097), and NBS (51.8 mg, 0.291 mmol) were purged with N_2 and 3 mL dry benzene was added via syringe. Mixture was reacted at 80°C for 18 h. Mixture was filtered to remove precipitate and remaining solvent was removed *in vacuo*.

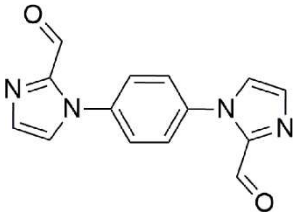

Synthesis of $BnIm_2$

In a two neck round bottom flask *p*-dibromobenzene (236 mg, 1 mmol), phenanthroline (27.03 mg, 0.15 mmol), 2-formylimidazole (230.6 mg, 2.4 mmol), $CsCO_3$ (0.9 g, 2.8 mmol), and CuO_2 (7.2 mg, 0.05 mmol) were combined and purged with N_2. N-methyl-2-pyrrolidone (0.5 mL) was added via syringe. The mixture reacted for 3 days at 110°C. The reaction mixture was then cooled to room temperature. The solution was diluted with DCM and ran through a celite plug. The remaining solvent was removed *in vacuo*. ^{1}H NMR (600 MHz, $CDCl_3$) δ 9.23 (s, 2H), 8.29 (d, J=7.3, 2H), 7.83 (s, 4H), 7.68 (d, J=8.1, 2H).

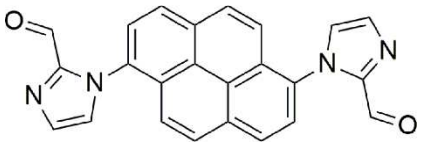

Synthesis of PyrIm$_2$

In a two neck round bottom flask -dibromopryene (360.05 mg, 1 mmol), phenanthroline (27.03 mg, 0.15 mmol), 2-formylimidazole (230.6 mg, 2.4 mmol), $CsCO_3$ (0.9 g, 2.8 mmol), and CuO_2 (7.2 mg, 0.05 mmol) were combined and purged with N_2. N-methyl-2-pyrrolidone (0.5 mL) was added via syringe. The mixture reacted for 3 days at 110°C. The reaction mixture was then cooled to room temperature. The solution was diluted with DCM and ran through a celite plug. The remaining solvent was removed *in vacuo*.

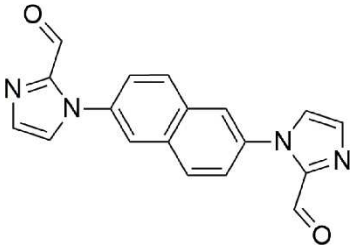

Synthesis of NaphIm$_2$

In a two neck round bottom flask 2,6-dibromonaphthalene (285.96 mg, 1 mmol), phenanthroline (27.03 mg, 0.15 mmol), 2-formylimidazole (230.6 mg, 2.4 mmol), $CsCO_3$ (0.9 g, 2.8 mmol), and CuO_2 (7.2 mg, 0.05 mmol) were combined and purged with N_2. N-methyl-2-pyrrolidone (0.5 mL) was added via syringe. The mixture reacted for 3 days at 110°C. The reaction mixture was then cooled to room temperature. The solution was

diluted with DCM and ran through a celite plug. The remaining solvent was removed *in vacuo*.

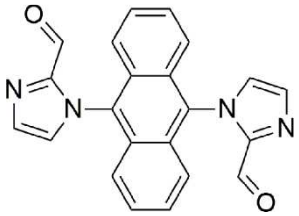

Synthesis of AntIm$_2$

In a two neck round bottom flask 9,10-dibromobenzene (336.02 mg, 1 mmol), phenanthroline (27.03 mg, 0.15 mmol), 2-formylimidazole (230.6 mg, 2.4 mmol), $CsCO_3$ (0.9 g, 2.8 mmol), and CuO_2 (7.2 mg, 0.05 mmol) were combined and purged with N_2. N-methyl-2-pyrrolidone (0.5 mL) was added via syringe. The mixture reacted for 3 days at 110°C. The reaction mixture was then cooled to room temperature. The solution was diluted with DCM and ran through a celite plug. The remaining solvent was removed *in vacuo*. ^{1}H NMR (400 MHz, $CDCl_3$) δ 10.15 (s, 2H), 7.76 (d, J=1.6 Hz, 2H), 7.54 (d, J=4.7 Hz, 4H), 7.36 (d, J=8.7, 6H)

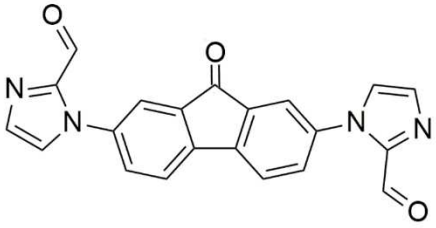

Synthesis of FOIm$_2$

In a two neck round bottom flask 2,7-dibromofluorene (352.0 mg, 1 mmol), phenanthroline (27.03 mg, 0.15 mmol), 2-formylimidazole (230.6 mg, 2.4 mmol), $CsCO_3$ (0.9 g, 2.8 mmol), and CuO_2 (7.2 mg, 0.05 mmol) were combined and purged with N_2. N-methyl-2-pyrrolidone (0.5 mL) was added via syringe. The mixture reacted for 3 days at 110°C. The reaction mixture was then cooled to room temperature. The solution was diluted with DCM and ran through a celite plug. The remaining solvent was removed *in vacuo*.

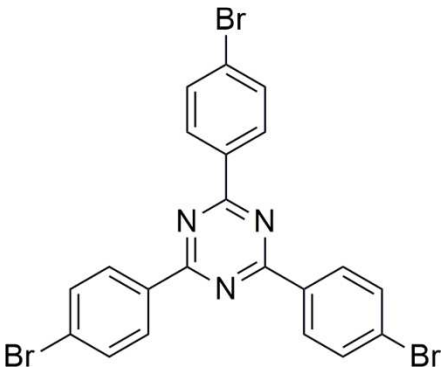

Synthesis of RTz

4-bromobenzonitrile (1.00 g, 5.49 mmol) was added to a 100 mL Schlenk flask. The flask was purged with N_2 and brought to 0 ˚C. Trifluoromethane Sulfuric Acid (1.35 mL, 5.67 mmol) was then added slowly via syringe, and purged again. Once the addition was

complete the flask was moved from the ice bath, allowed to warm to room temperature, and stirred for 12 hours. The mixture was then poured over cold water precipitate was then filtered and washed with acetone to yield a white solid (2.8 g, 94% yield). ^{1}H NMR (400 MHz, $CDCl_3$) δ 8.62 (d, J=8.6 Hz, 6H), 7.76 (d, J=8.8 Hz, 6H).

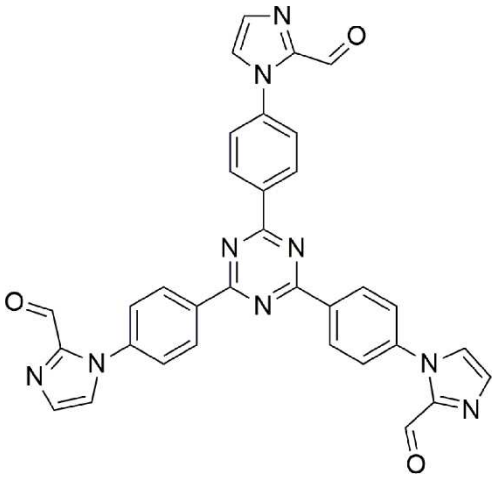

Synthesis of RTzIm$_3$

To a 50 mL two neck flask **RTz** (546.02 mg, 1 mmol), 2-imidazolecarboxaldehyde (230.6 mg, 2.4 mmol), phenanthroline (23.03 mg, 0.15 mmol), Cs_2CO_3 (0.9 g, 2.8 mmol), and Cu_2O (7.2 mg, 0.05 mmol) were combined. The flask was purged with N_2. Dry NMP (1.5 mL) was injected into the flask via syringe. The reaction stirred for 2 d at 110°C. The reaction was then cooled to room temperature. The solution was diluted with DCM and ran through a celite plug. The remaining solvent was removed *in vacuo*. (273.5 mg, 46% yield). ^{1}H NMR (400 MHz, $CDCl_3$) δ 10.19 (s, 3H), 8.73 (d, J=7.75, 6H), 8.64 (d, J=7.75 Hz, 6H), 7.75 (d, J=5.44, 6H), 7.70 (d, J=5.54 Hz, 6H).

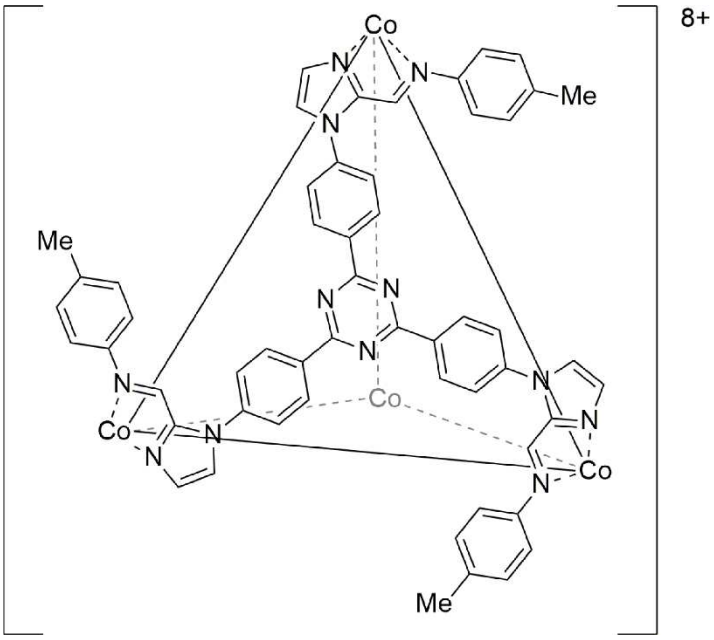

Synthesis of tripodal cage (RTzIm$_3$•Co•PhMe•NTf$_2$)

RTzIm$_3$ (30 mg, 0.055 mmol), Co(NTf$_2$)$_2$ (34 mg, 0.055 mmol), and p-toluidine (11.77 mg, 0.110 mmol) were combined in a round bottom flask with MeCN (5 mL). The mixture reacted at 50 ˚C for 2 days. Solvent was removed in vacuo, then triturated with ether and filtered. Solid was washed with 1:1 methanol: ether (10 mL) resulting in a reddish brown solid (38.9 mg, 65% yield). ^{1}H NMR (400 MHz, CD$_3$CN) δ 104.32 (s), 100.28 (s), 83.80 (m), 82.83 (s), 81.85 (s), 81.63 (s), 80.77 (s), 23.84 (s), 21.81 (s), 19.68 (s), 19.25 (s), 17.88 (s), 17.45 (s), 16.96 (s), 16.45 (s), 15.88 (s), 14.75 (s), 14.46 (s), 13.58 (s), 13.26 (s), 12.70 (s), 12.44 (s), 12.28 (s), 12.05 (s), 11.92 (s), 11.66 (s), 11.45 (s), 11.34 (s), 10.92 (s), 10.81 (s), 10.57 (s), 9.80 (s), 9.67 (s), 9.28 (s), 8.89 (s), 8.77 (s), 8.61 (s), 8.46 (s), 7.72 (s), 7.48 (s), 7.31 (s), 7.27 (s), 6.93 (d, J=7.8 Hz), 6.61 (s), 6.57 (d, J=7.6 Hz), 6.39 (s), 6.02 (s), 5.91 (s), 5.79 (s), 5.67 (s), 5.18 (s), 4.04 (s), 3.63 (s), 1.30 (s), 0.89 (s), 0.39 (s), 0.10 (s), -0.64 (s), -1.14 (s), -2.72 (s), -3.05 (s), -4.12 (s), -4.26 (s), -4.65 (s), -4.77 (s), -4.82 (s), -5.58 (s),

-5.89 (s), -6.00 (s), -7.18 (s), -8.81 (s), -19.15 (s), -29.51 (s), -33.10 (s), -35.15 (s), -38.43 (s), -47.24 (s), -54.72 (s), -63.24 (s).

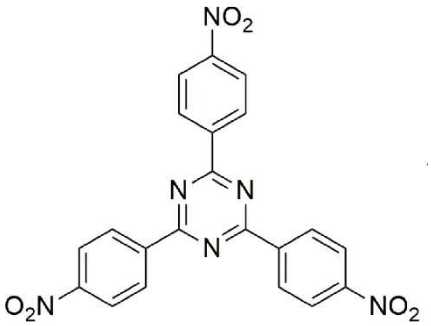

Synthesis of NO_2Tz

In round bottom flask combine 18-crown-6 (1 g, 3.8 mmol) and KOH (0.225 g, 4 mmol) with 5 mL of MeOH for 10 min. at room temperature. Remove MeOH *in vacuo*, the product should be an oil. Add the oil and 4-nitrobenzonitrile (10 g, 6.8 mmol) to a sealed tube and heat to 200°C for 7 h. Let the tube cool to room temperature and wash the solid with DI H_2O. Recrystallized with toluene and add hexanes dropwise as necessary (2.87 g, 95% yield). ^{1}H NMR (400 MHz, DMSO) δ 8.39 (d, J=8.29 Hz, 6H), 8.19 (d, J=8.42, 6H).

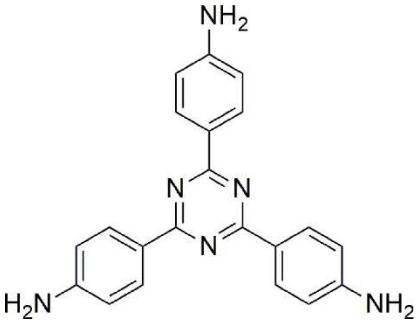

Synthesis of AmTz

In a two-neck flask **NO_2Tz** (100 mg, 0.450 mmol), Raney nickel (3 mL), and ammonium formate (400 mg, 13.5 mmol) were combined and purged with N_2. The mixture was heated at 75°C for 1h. The reaction was allowed to cool to room temperature and filtered through celite. The remaining solvent was removed *in vacuo*. (140 mg, 88% yield). ^{1}H NMR (400 MHz, DMSO) 7.05 (s, 6H), 6.55 (s, 6H), and 3.54 (s, 6H).

6.6 Chapter 2 Selected Spectra

NMR and ESI-MS Characterization of New Cage Compounds

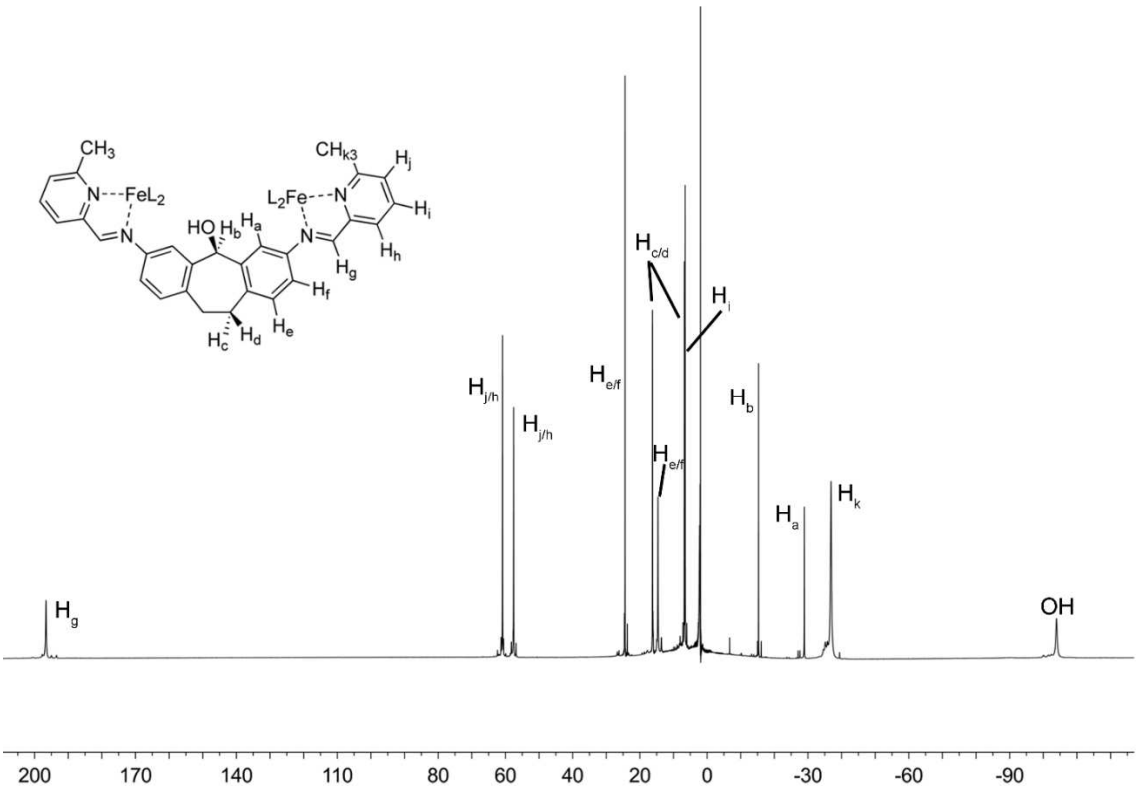

Figure 6.6: ^{1}H NMR spectrum of paramagnetic cage **SOH•Fe•MePyCHO•(NTf$_2$)$_4$** (CD_3CN, 400 MHz, 298 K).

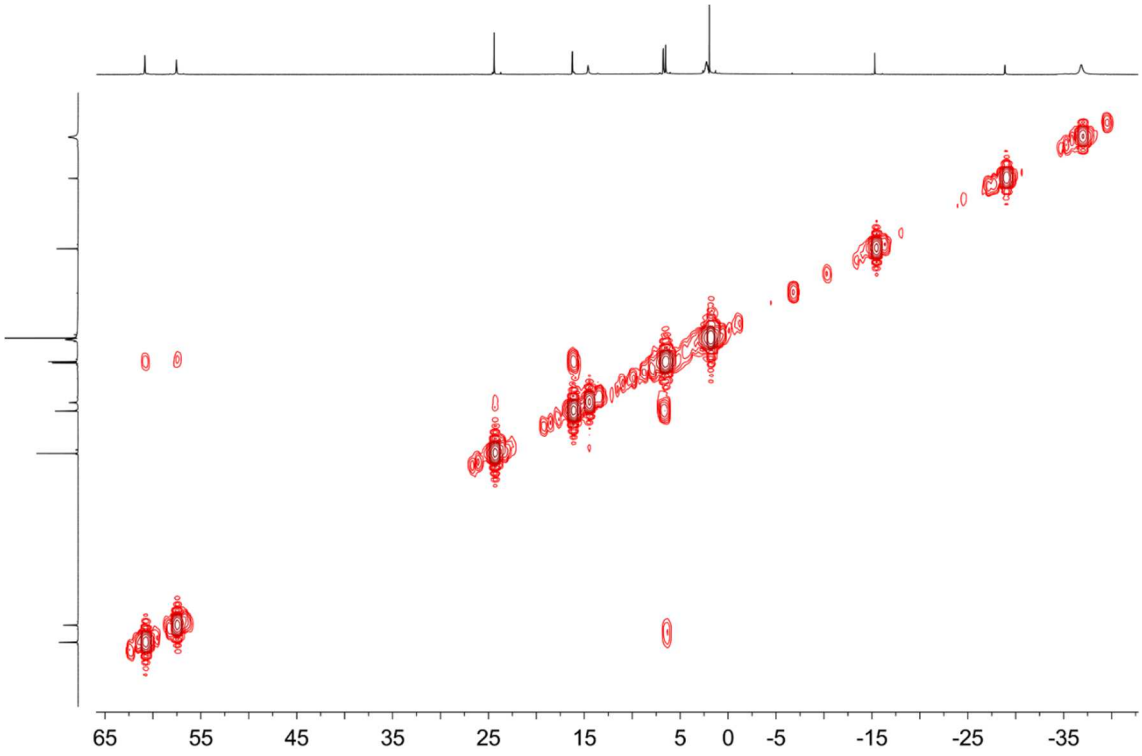

Figure 6.7: Full gCOSY spectrum of paramagnetic cage **SOH•Fe•MePyCHO•$(NTf_2)_4$** (CD_3CN, 400 MHz, 298 K).

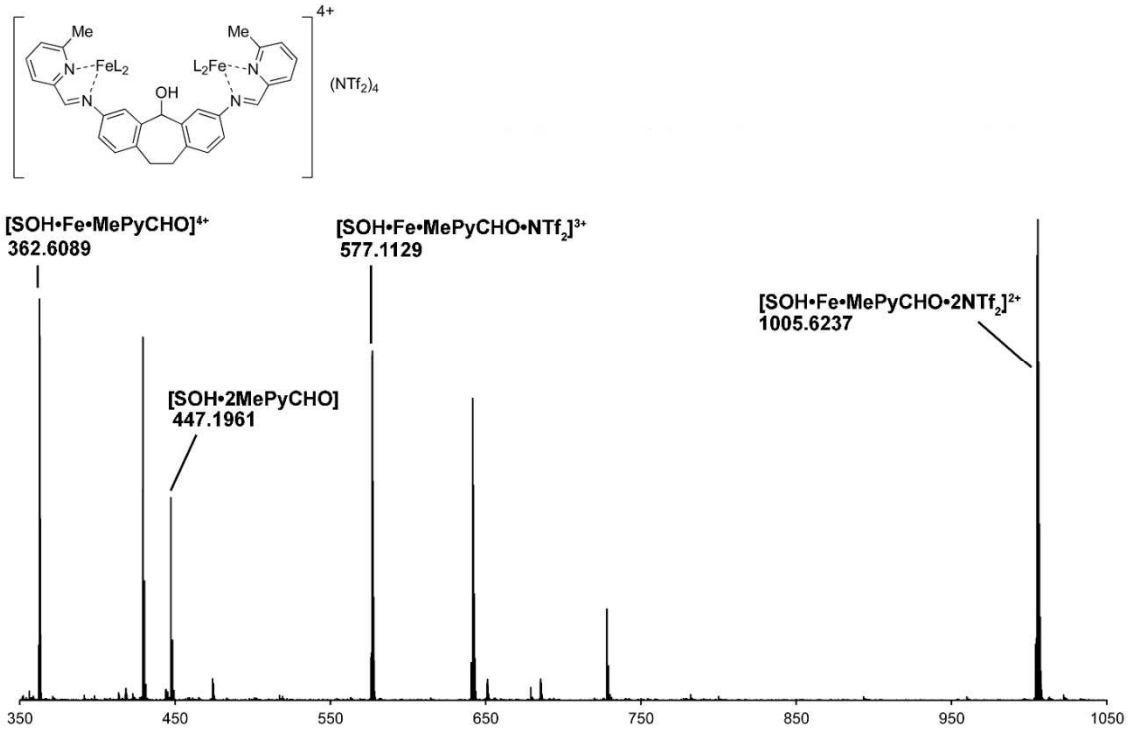

Figure 6.8: Full ESI-MS of cage **SOH•Fe•MePyCHO•(NTf$_2$)$_4$** (CH_3CN).

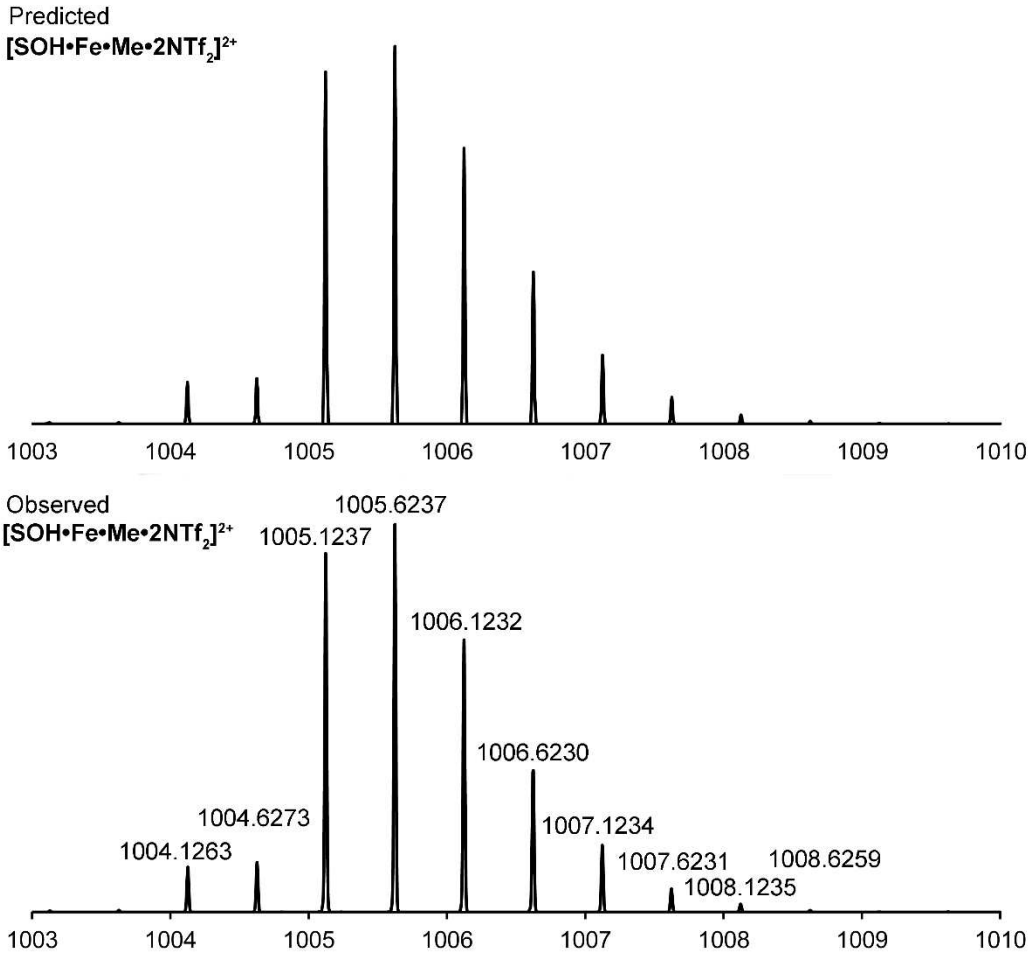

Figure 6.9: Expansion of the [**SOH•Fe•MePyCHO•**$(ClO_4)_2$]$^{2+}$ region vs the predicted values for cage **SOH•Fe•MePyCHO•$(ClO_4)_4$** (CH_3CN).

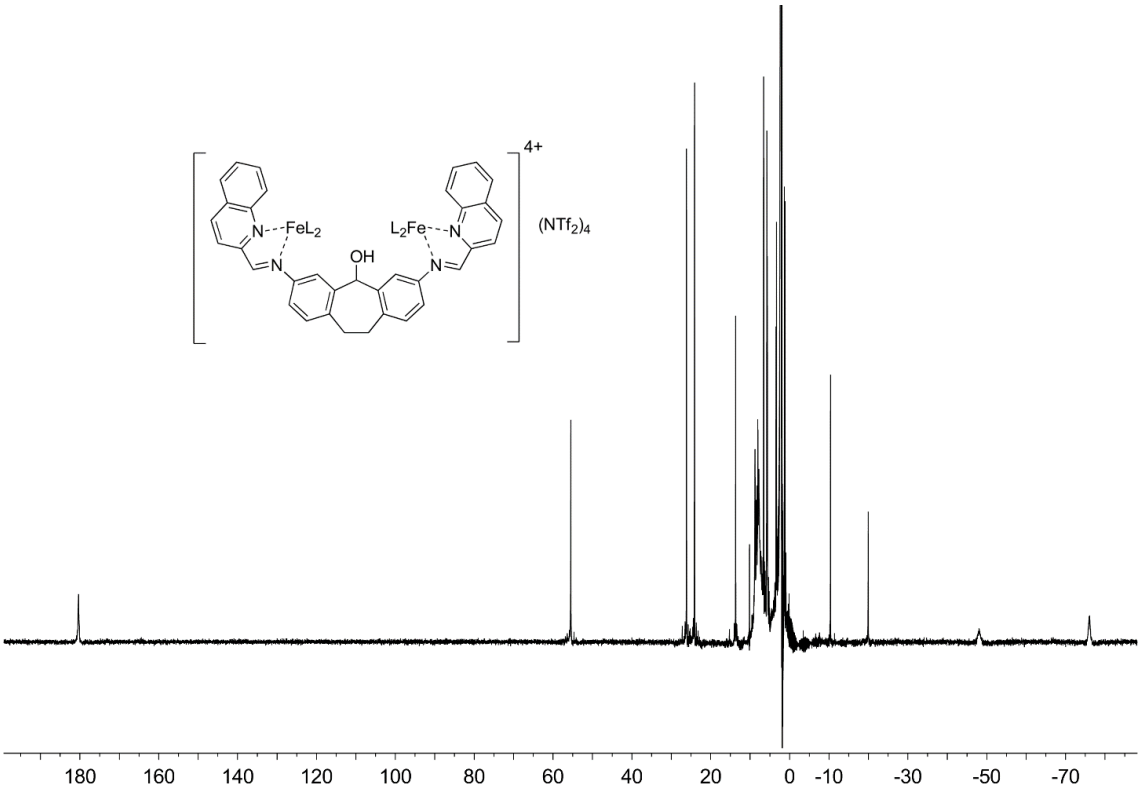

Figure 6.10: ^{1}H NMR spectrum of **SOH•Fe•QnCHO•$(NTf_2)_4$** (CD_3CN, 400 MHz, 298 K).

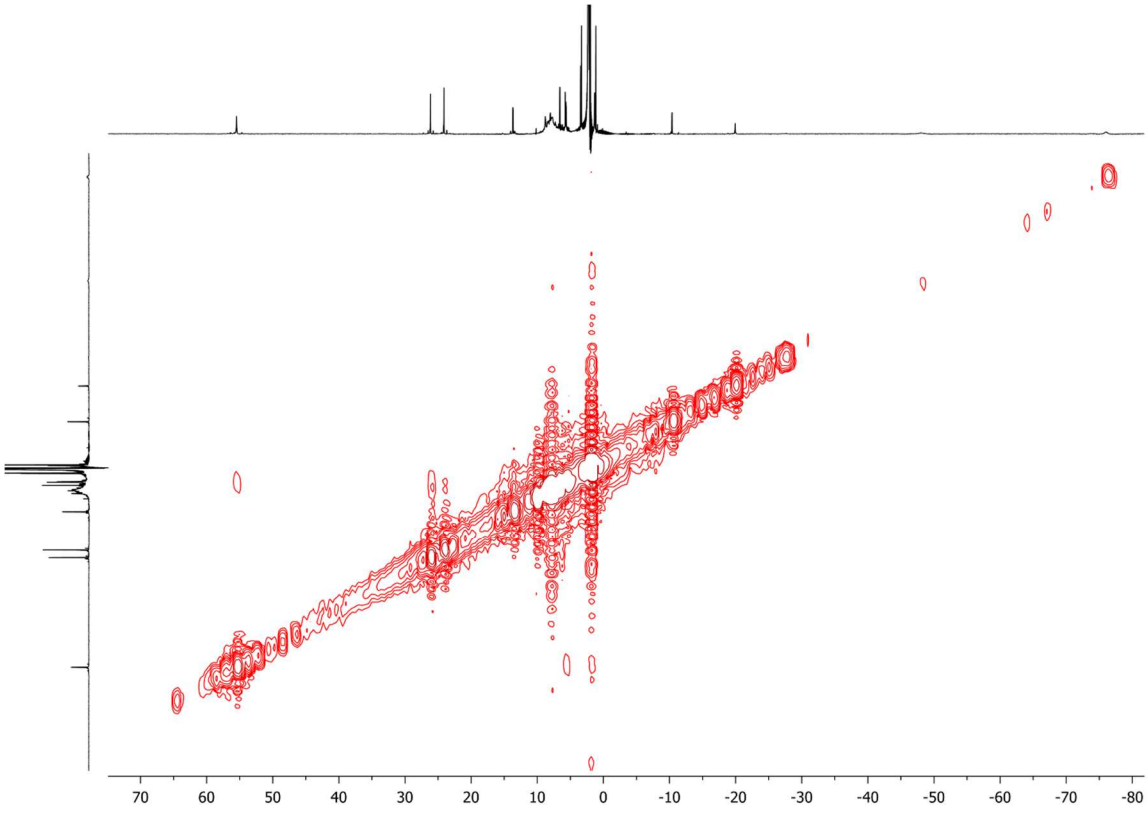

Figure 6.11: Full gCOSY spectrum of **SOH•Fe•QnCHO•(NTf$_2$)$_4$** (CD_3CN, 400 MHz, 298 K).

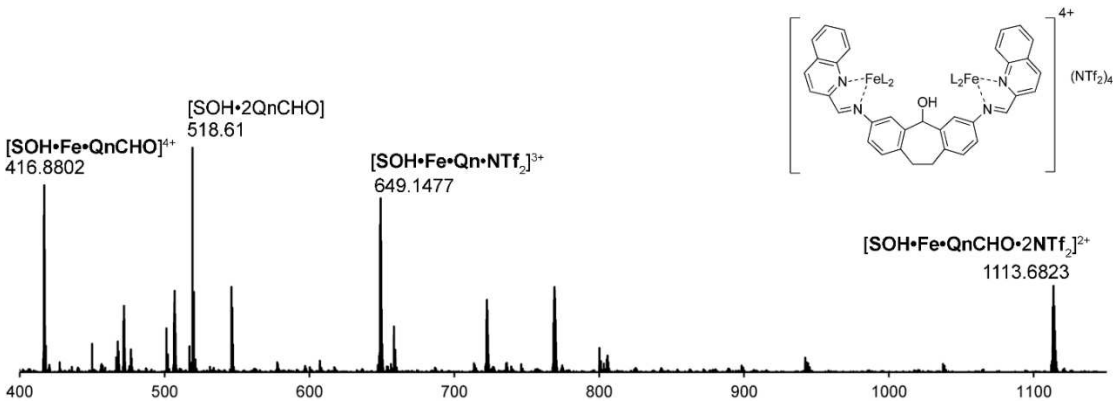

Figure 6.12: Full ESI-MS of cage **SOH•Fe•QnCHO•(NTf$_2$)$_4$** (CH_3CN).

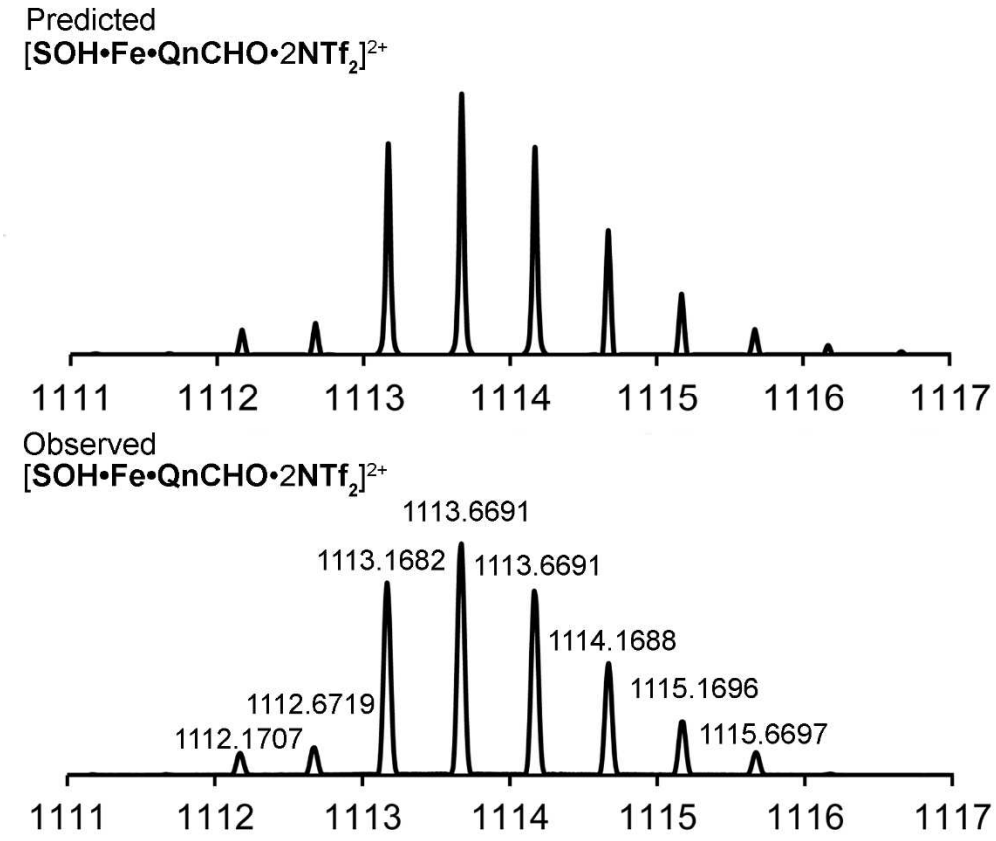

Figure 6.13: Expansion of the [**SOH•FeQnCHO•(NTf$_2$)$_4$** (CH_3CN).

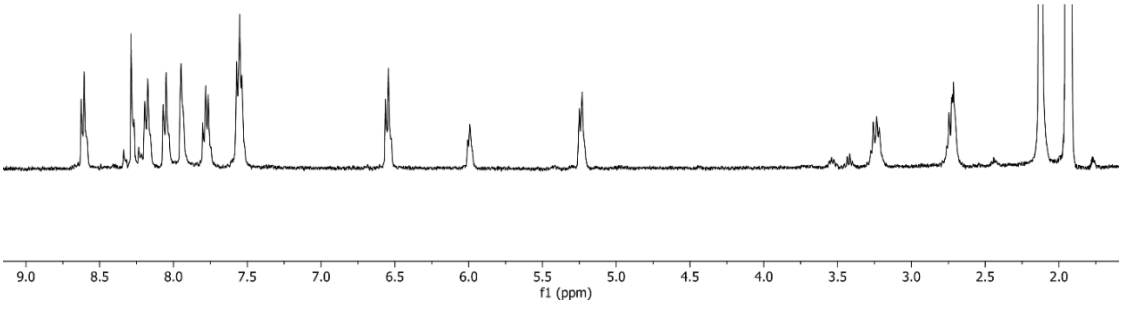

Figure 6.14: ^{1}H NMR spectrum of **SOH•Cd•QnCHO** (CD_3CN, 400 MHz, 298 K).

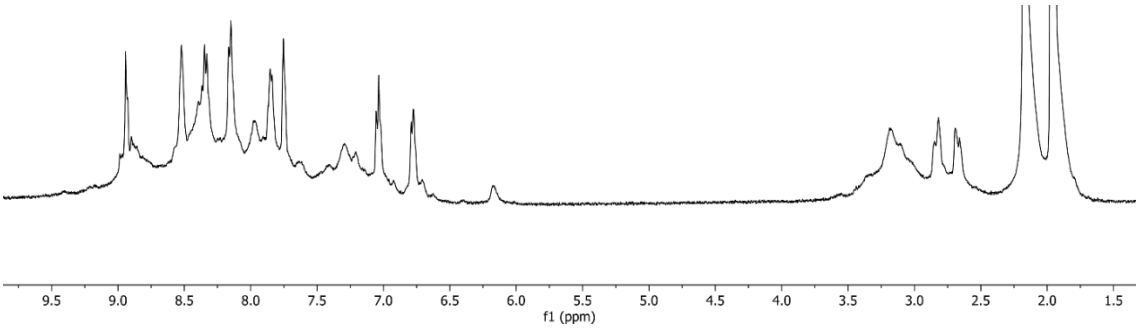

Figure 6.15: ^{1}H NMR spectrum of **SO•Cd•PyCHO** (CD_3CN, 400 MHz, 298 K).

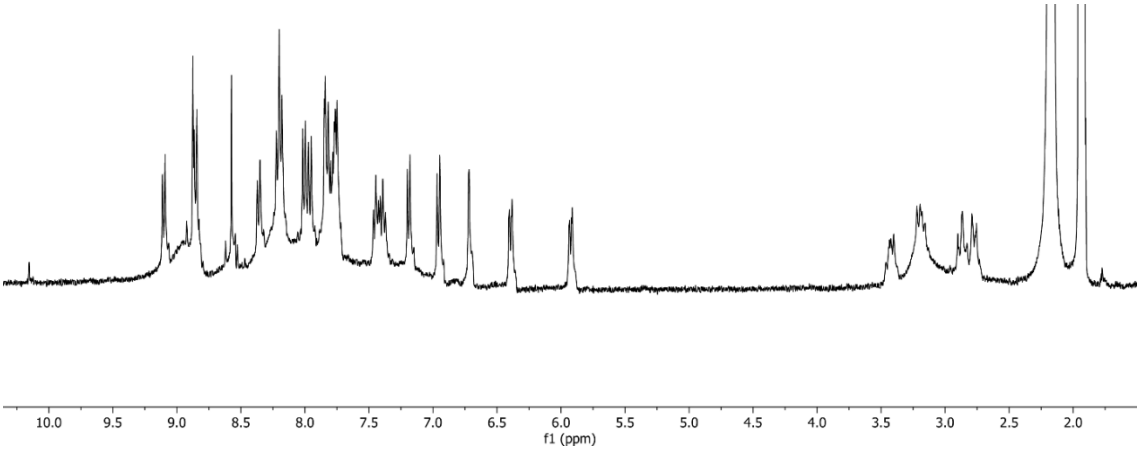

Figure 6.16: ^{1}H NMR spectrum of **SO•Cd•QnCHO** (CD_3CN, 400 MHz, 298 K).

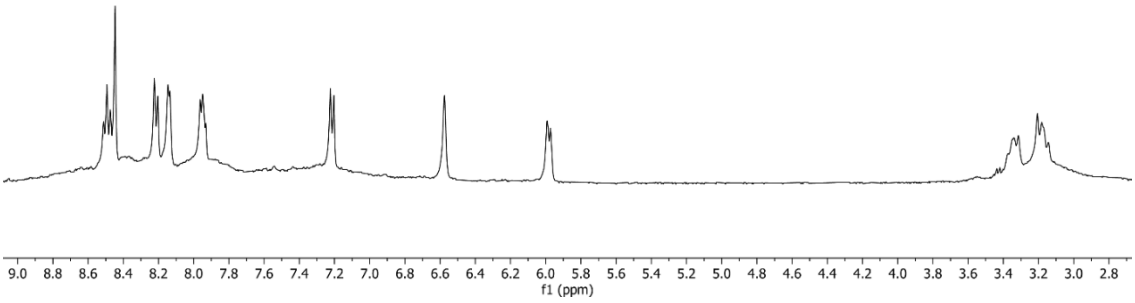

Figure 6.17: ^{1}H NMR spectrum of **SO•Zn•PyCHO** (CD_3CN, 400 MHz, 298 K).

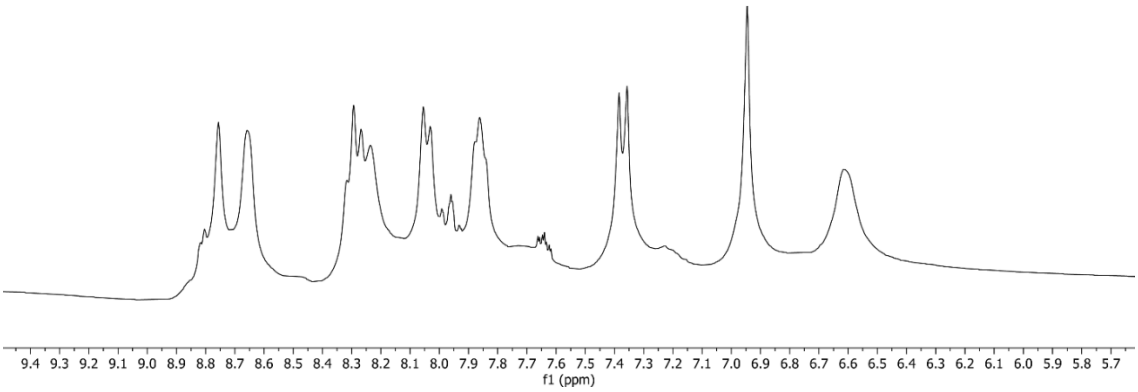

Figure 6.18: ^{1}H NMR spectrum of **SE•Cd•PyCHO** (CD_3CN, 400 MHz, 298 K).

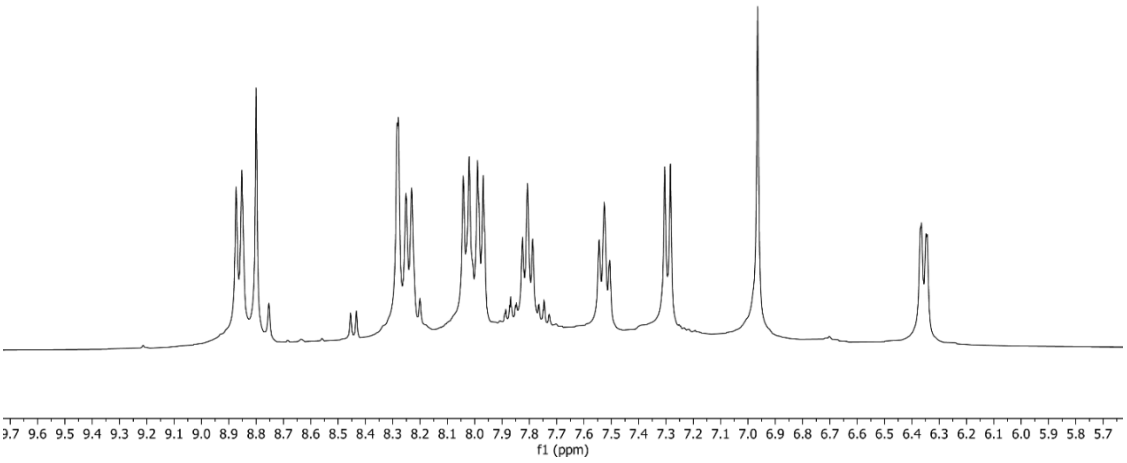

Figure 6.19: ^{1}H NMR spectrum of **SE•Cd•QnCHO** (CD_3CN, 400 MHz, 298 K).

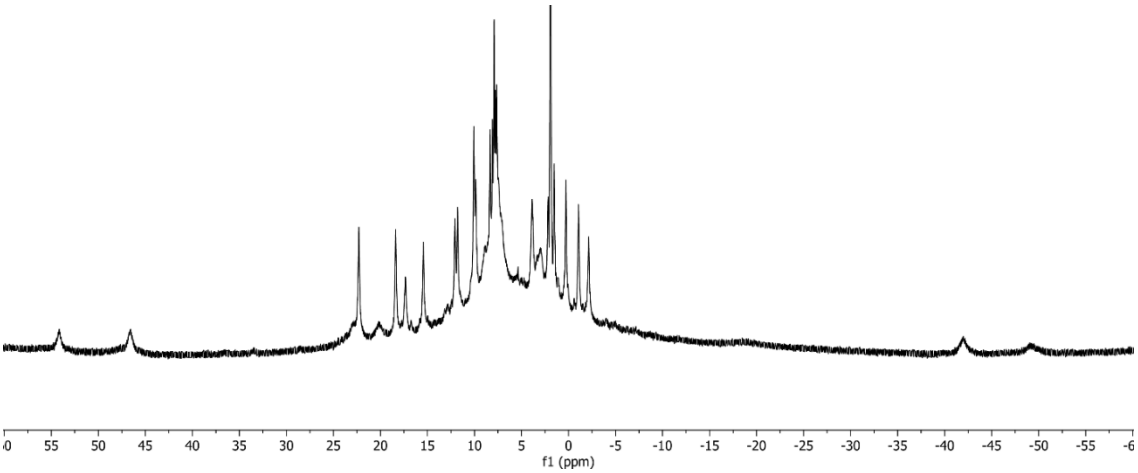

Figure 6.20: ^{1}H NMR spectrum of **SOCF$_3$•Fe•QnCHO** (CD_3CN, 400 MHz, 298 K).

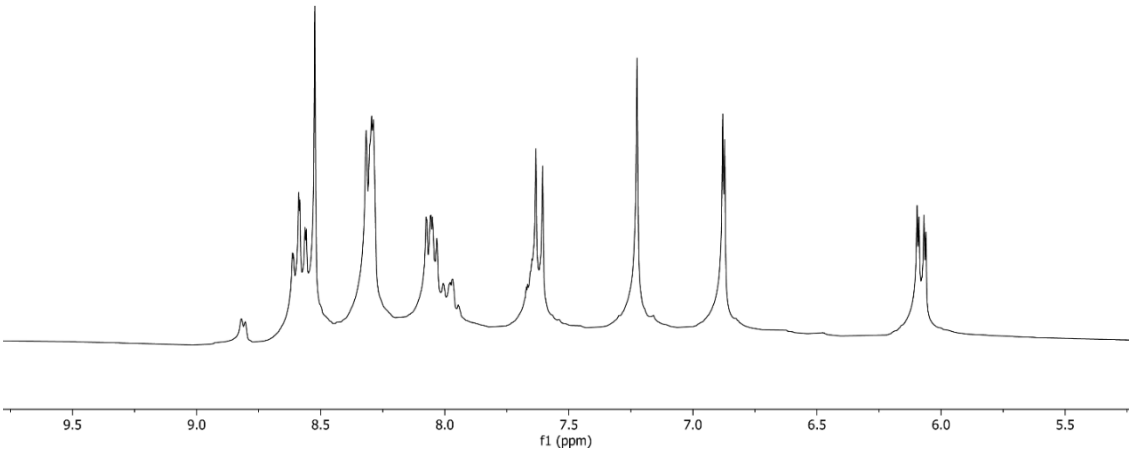

Figure 6.21: ^{1}H NMR spectrum of **SE•Zn•PyCHO** (CD_3CN, 400 MHz, 298 K).

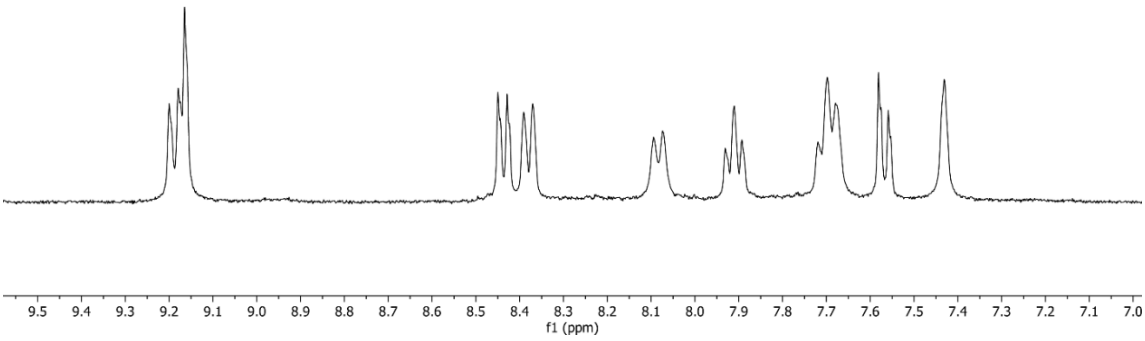

Figure 6.22: ^{1}H NMR spectrum of **XO•Zn•QnCHO** (CD_3CN, 400 MHz, 298 K).

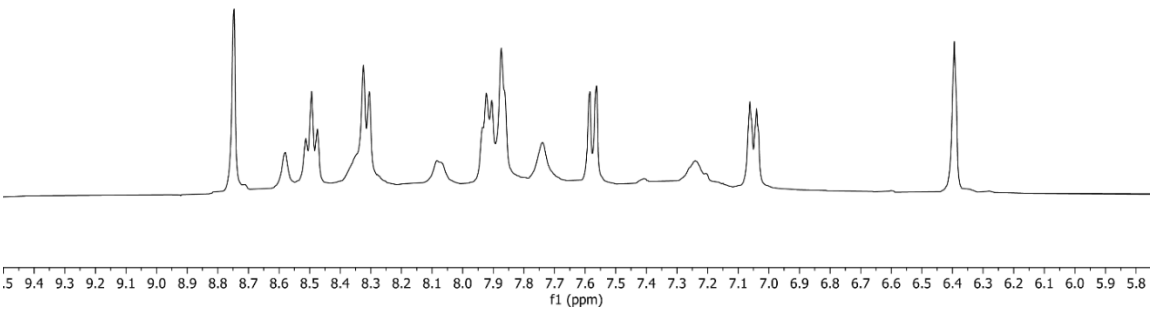

Figure 6.23: ^{1}H NMR spectrum of **XO•Zn•PyCHO** (CD_3CN, 400 MHz, 298 K).

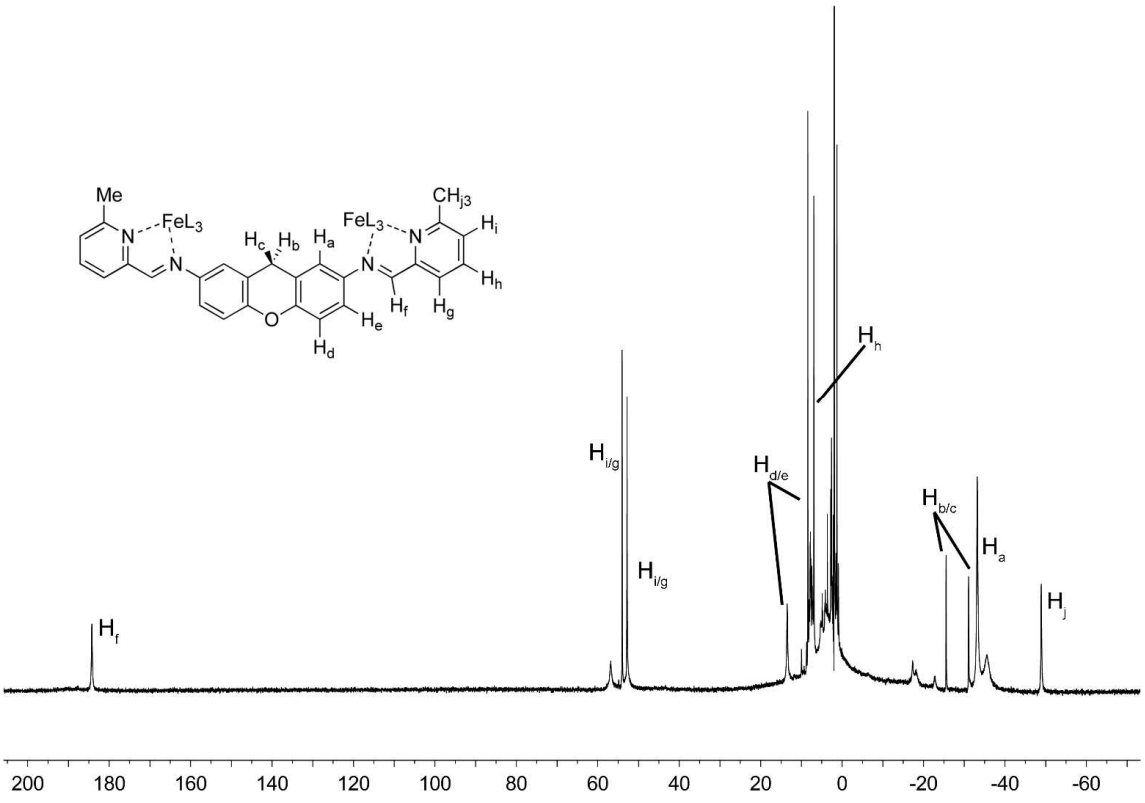

Figure 6.24: ^{1}H NMR spectrum of **X•Fe•MePyCHO** (CD_3CN, 400 MHz, 298 K).

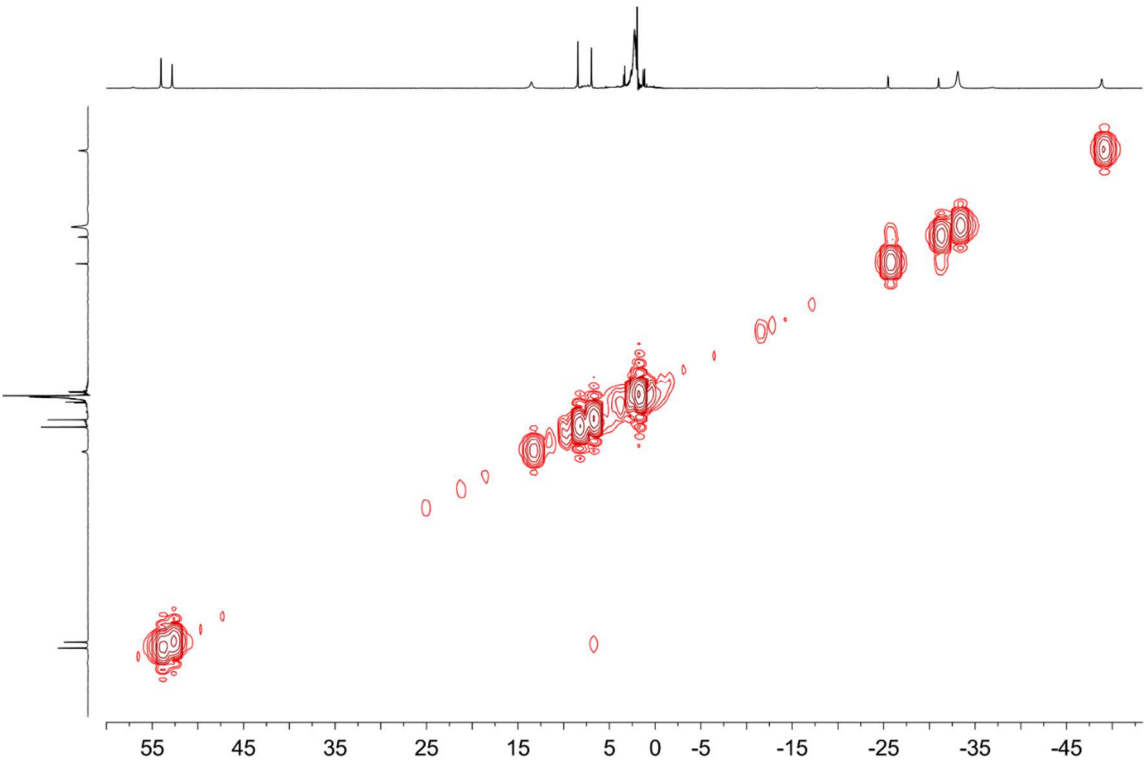

Figure 6.25: Full gCOSY spectrum of **X•Fe•MePyCHO** (CD_3CN, 400 MHz, 298 K).

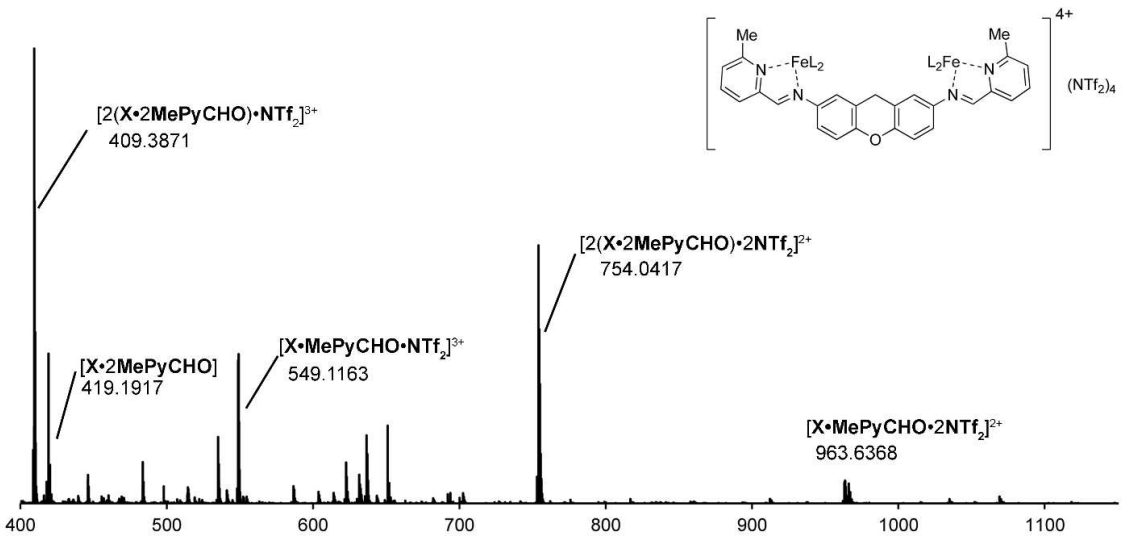

Figure 6.26: Full ESI-MS of cage **X•Fe•MePyCHO•$(NTf_2)_4$** (CH_3CN).

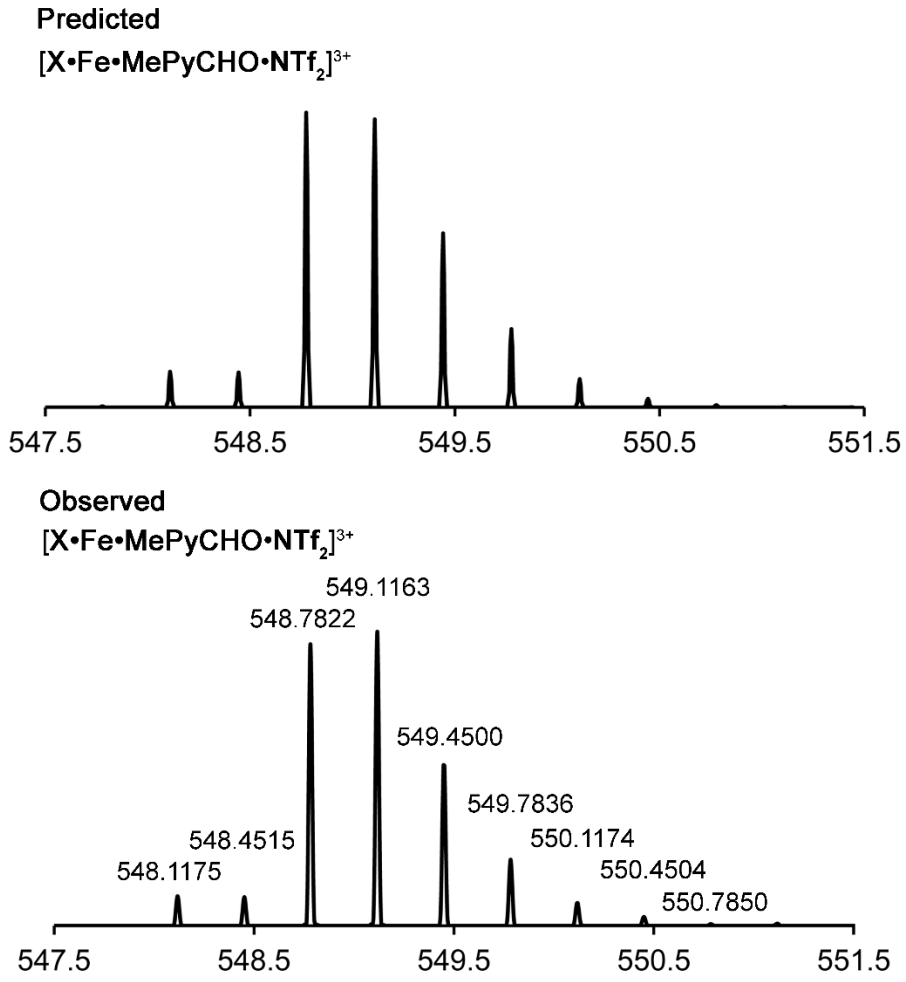

Figure 6.27: Expansion of the [**X•Fe•MePyCHO** (NTf_2)]$^{3+}$ region vs the predicted values for cage **X•Fe•MePyCHO•(NTf$_2$)$_4$** (CH_3CN).

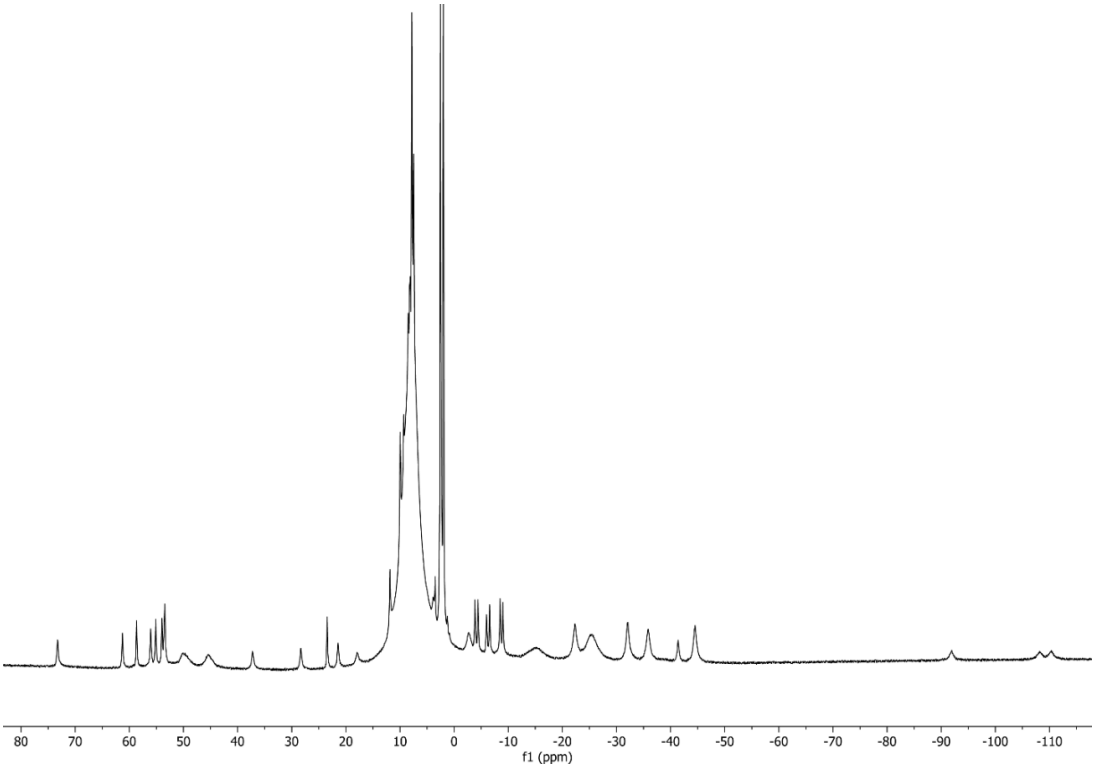

Figure 6.28: ^{1}H NMR spectrum of **FOH•Fe•QnCHO** (CD_3CN, 400 MHz, 298 K).

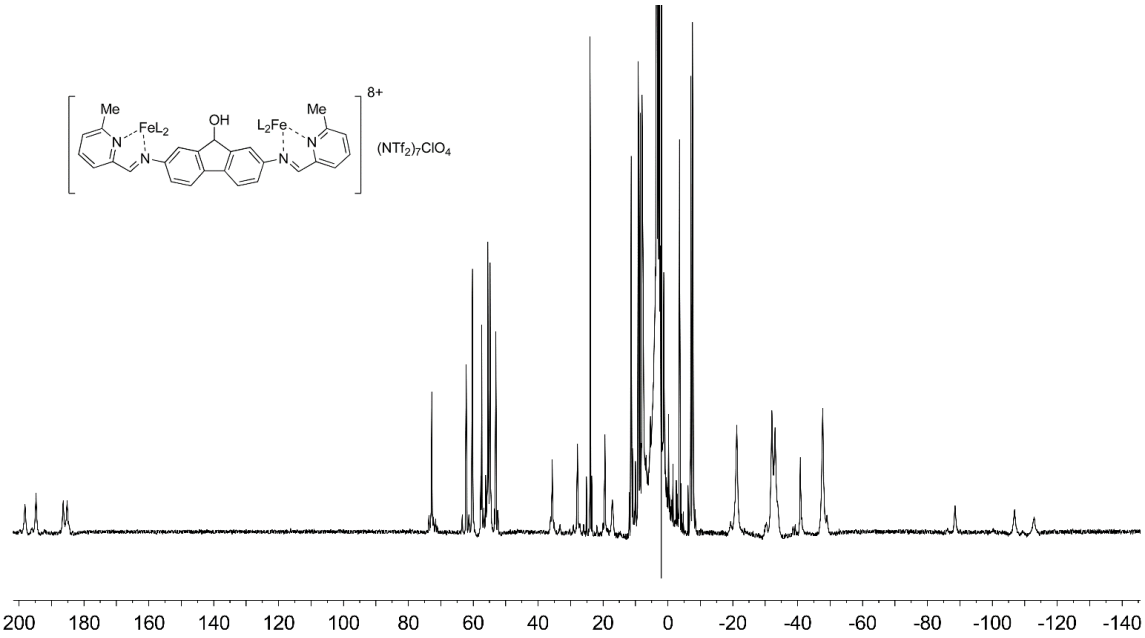

Figure 6.29: ^{1}H NMR spectrum of **FOH•Fe•MePyCHO•$(NTf_2)_7(ClO_4)$** (CD_3CN, 400 MHz, 298 K).

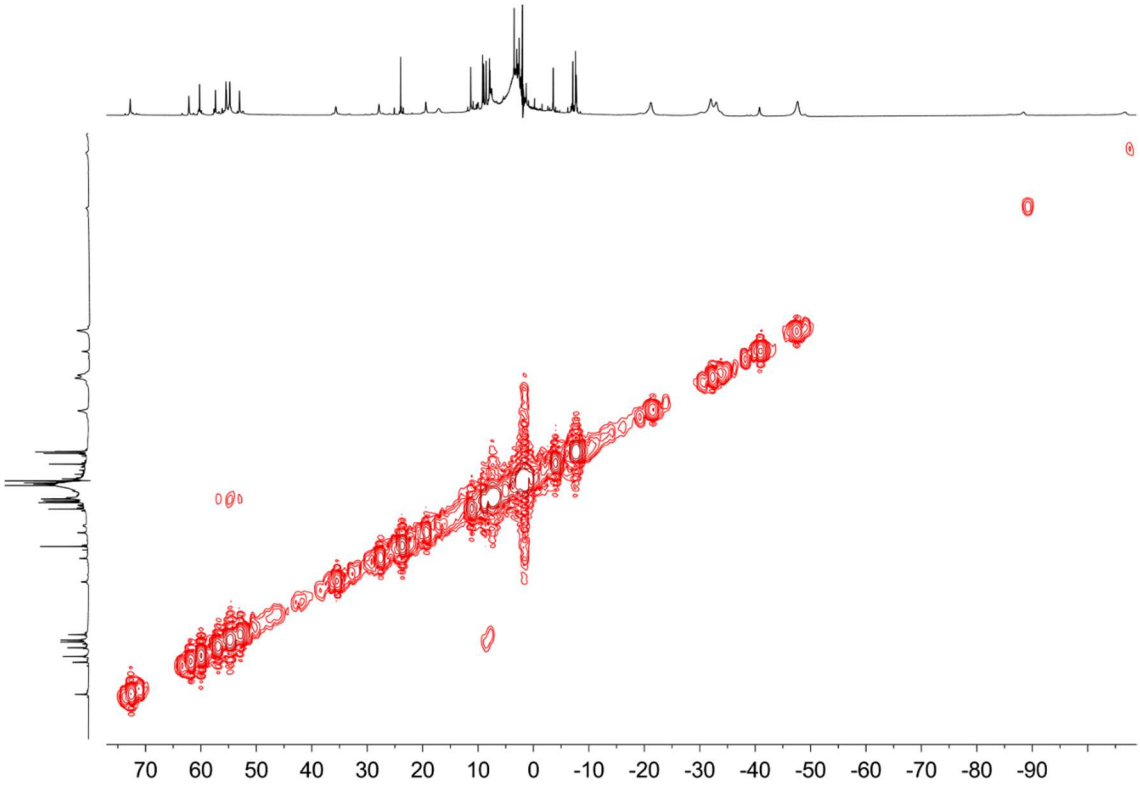

Figure 6.30: Full gCOSY spectrum of paramagnetic cage **FOH•Fe•MePyCHO•(NTf$_2$)$_7$(ClO$_4$)** (CD_3CN, 400 MHz, 298 K).

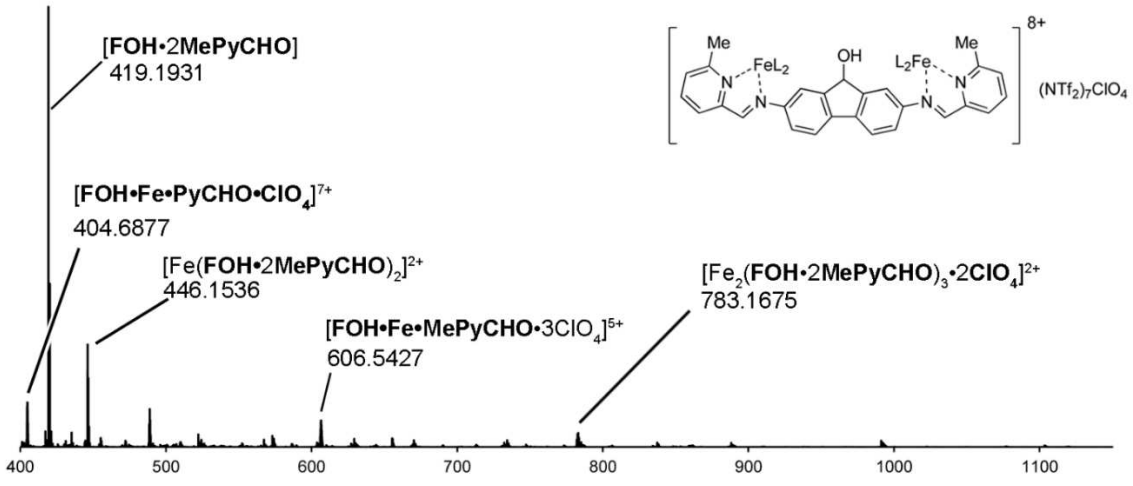

Figure 6.31: Full ESI-MS of Cage **FOH•Fe•MePyCHO•(ClO$_4$)$_8$** (CH_3CN).

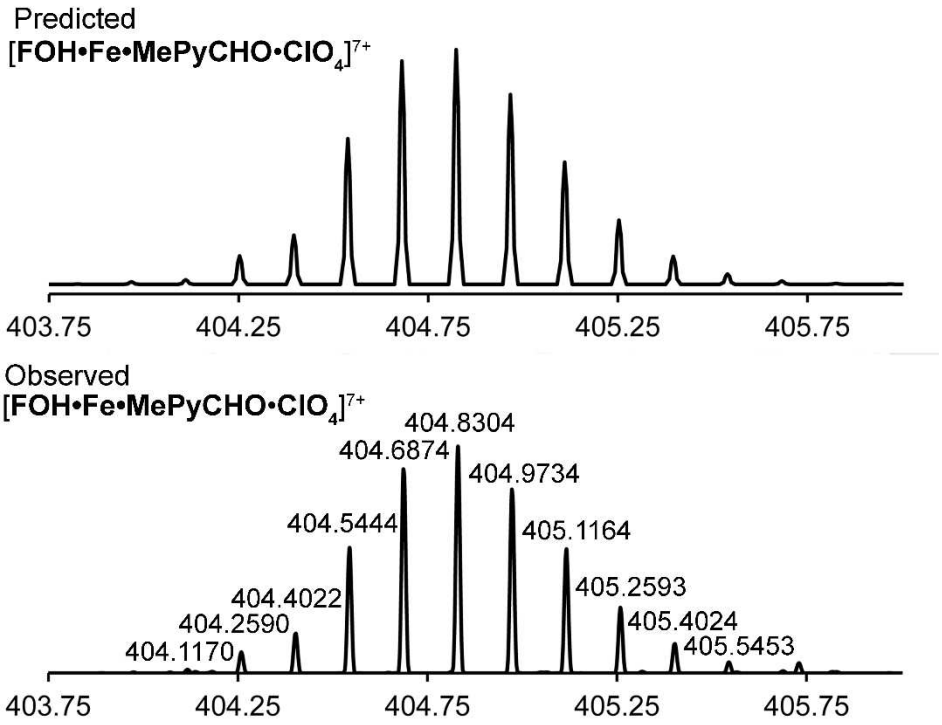

Figure 6.32: Expansion of the [**FOH•Fe•MePyCHO•**(ClO_4)]$^{7+}$ region vs the predicted values for Cage **FOH•Fe•MePyCHO•(ClO_4)**$^{7+}$ (CH_3CN).

Magnetic Susceptibility Measurements.

Experiments were performed using a previously established method. A solution was made using 7.5 mg of cage in a 99:1 CD_3CN:DCE solvent system. An initial ^1H NMR was taken at room temperature on a Bruker Avance 600 MHz NMR. A flame-sealed melting point tube containing a solution of 99:1 CD_3CN:DCE was inserted into the NMR tube and used as reference. The NMR was then cooled to -40°C and the temperature was raised at 10°C increments up to 50°C. Mass susceptibility was determined by equation 1, where Δf is peak separation (Hz), f is the NMR frequency (Hz), m is mass per cm^3, and χ_o is -0.534 x $10^{-6}cm^3g^{-1}$, the mass susceptibility of CD_3CN.

$$\chi_g = \frac{3\Delta f}{4\pi f m} + \chi_0$$

Molar susceptibility, χ_M, is determined by equation 2, where M is the molar mass of the complex.

$\chi_M = \chi_g * M$

Molar susceptibility χ_M contains the diamagnetic correction (χ_M^{dia}) which, due to the large M_W of these species cannot be ignored. The corrected molar susceptibility ($\chi_{M'}$) was calculated using values determined from Pascal's constants to correct for the diamagnetic contributions from the ligands and Fe(II) core electrons and counterions. χ_M^{dia} for cages are **1•Me**, **1•Qn**, **3•Me**, and **4•Me** are -0.001210 $cm^3\ mol^{-1}$, -0.001369 $cm^3\ mol^{-1}$, -0.001141 $cm^3\ mol^{-1}$, and -0.002210 $cm^3\ mol^{-1}$ respectively.

$\chi_{M'} = \chi_M + \chi_M^{dia}$

The magnetic moment was calculated from the equation $\mu_{eff} = \sqrt{8\chi_p T} \approx \sqrt{n(n+2)}$, where χ_p is the paramagnetic susceptibility. χ_p calculated from $\chi_p = \chi_M - \chi_M^{sol}$, where Δf is peak separation (Hz), f is the NMR frequency (Hz), and m is mass per cm^3.

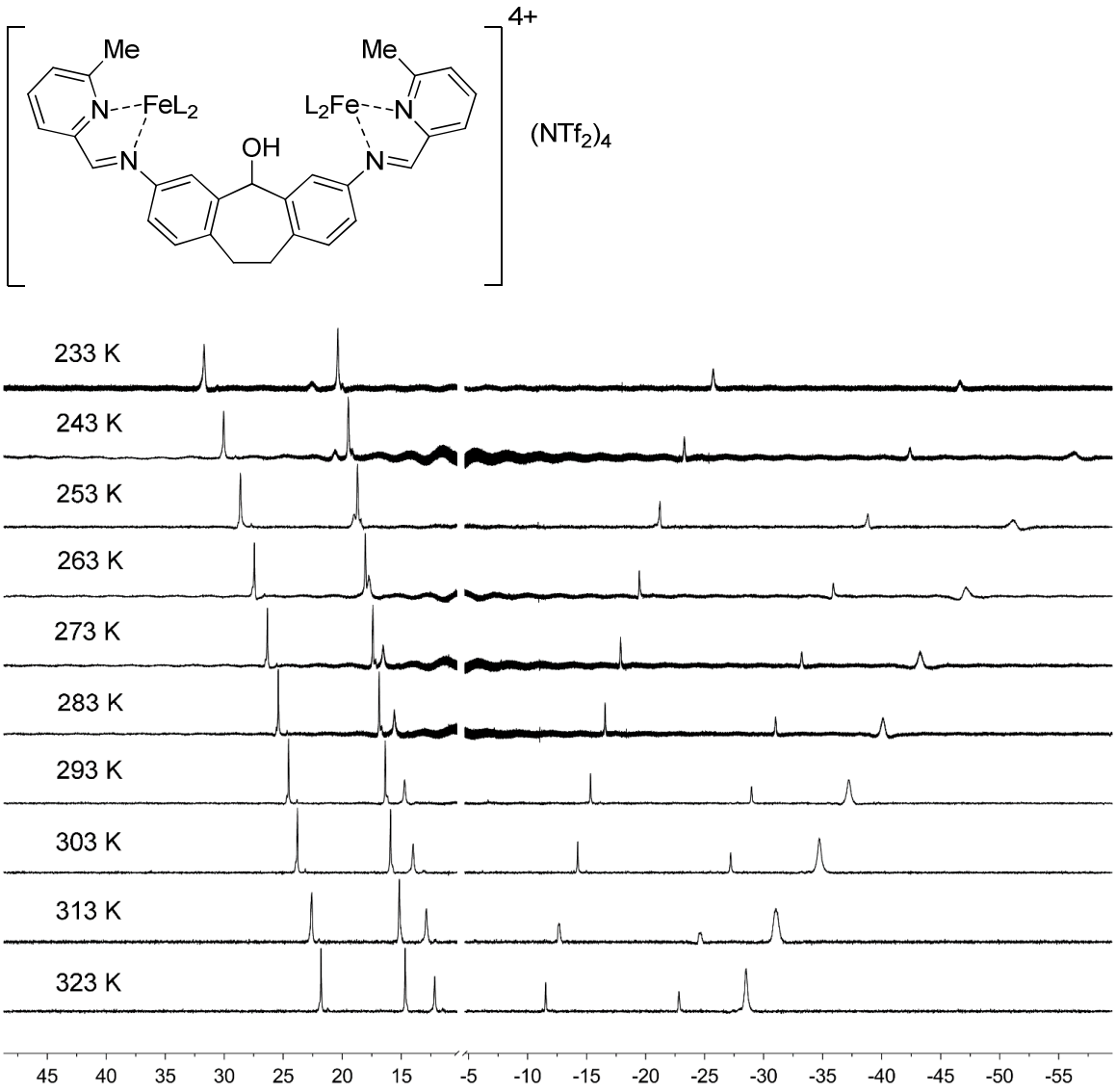

Figure 6.33: Variable temperature ^{1}H NMR spectra of 3.03 mM **SOH•Fe•MePyCHO** $[NTf_2]_4$ in 99:1 CD_3CN: Dichloroethane

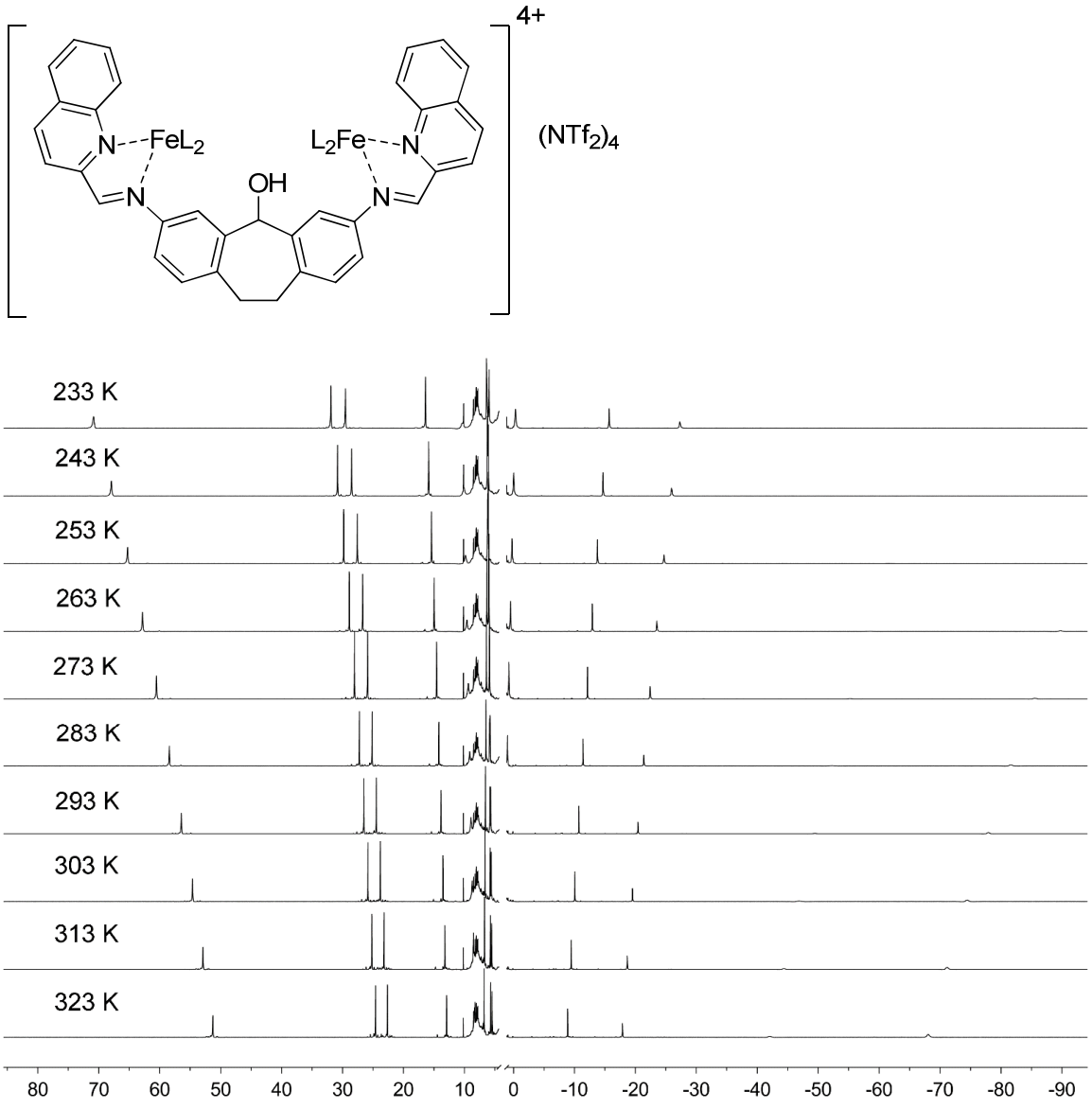

Figure 6.34: Variable temperature ^{1}H NMR spectra of 2.69 mM **SOH•Fe•QnCHO** $[NTf_2]_4$ in 99:1 CD_3CN: Dichloroethane

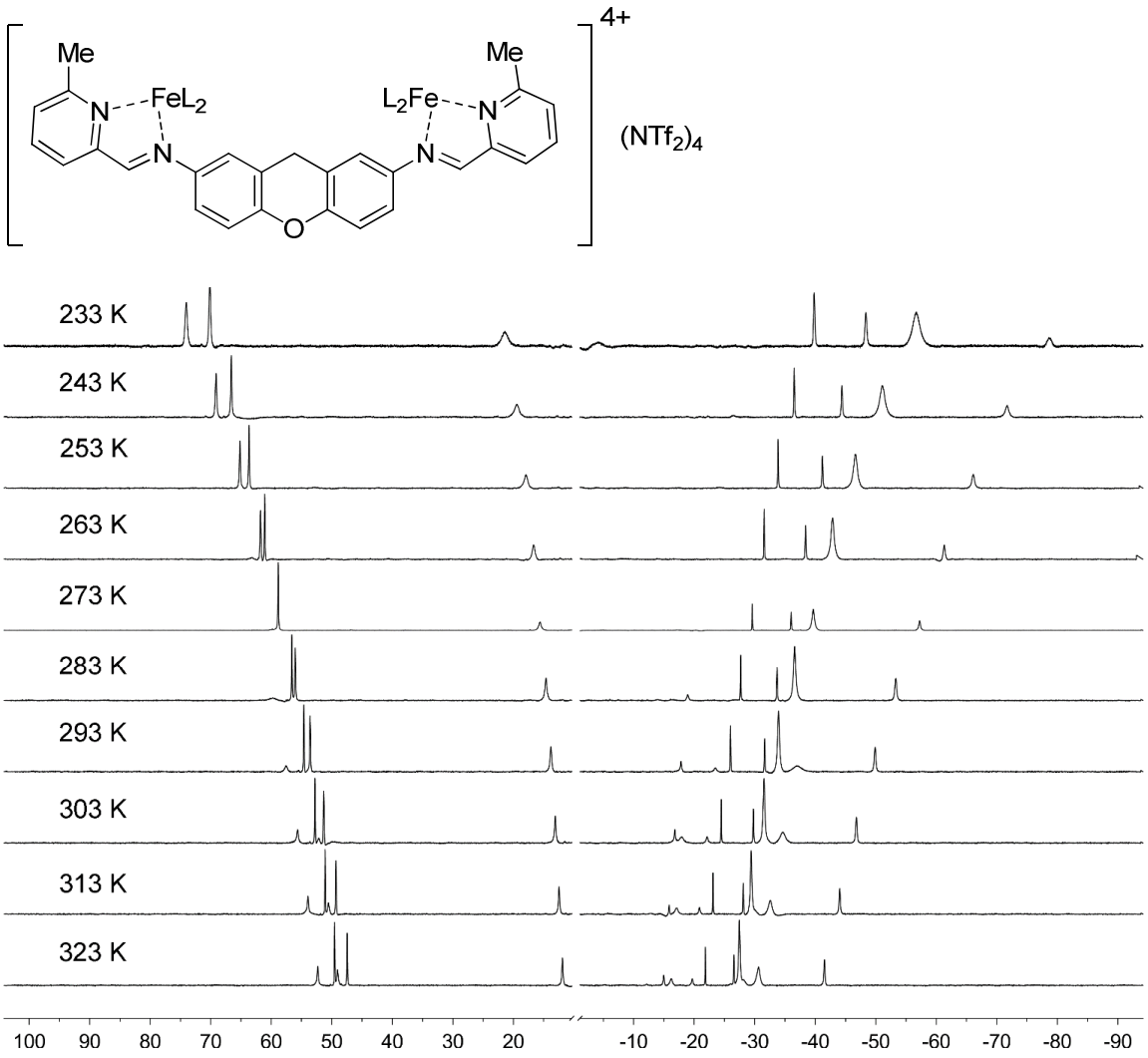

Figure 6.35: Variable temperature ^{1}H NMR spectra of 3.12 mM **X•Fe•MePyCHO** $[NTf_2]_4$ in 99:1 CD_3CN: Dichloroethane.

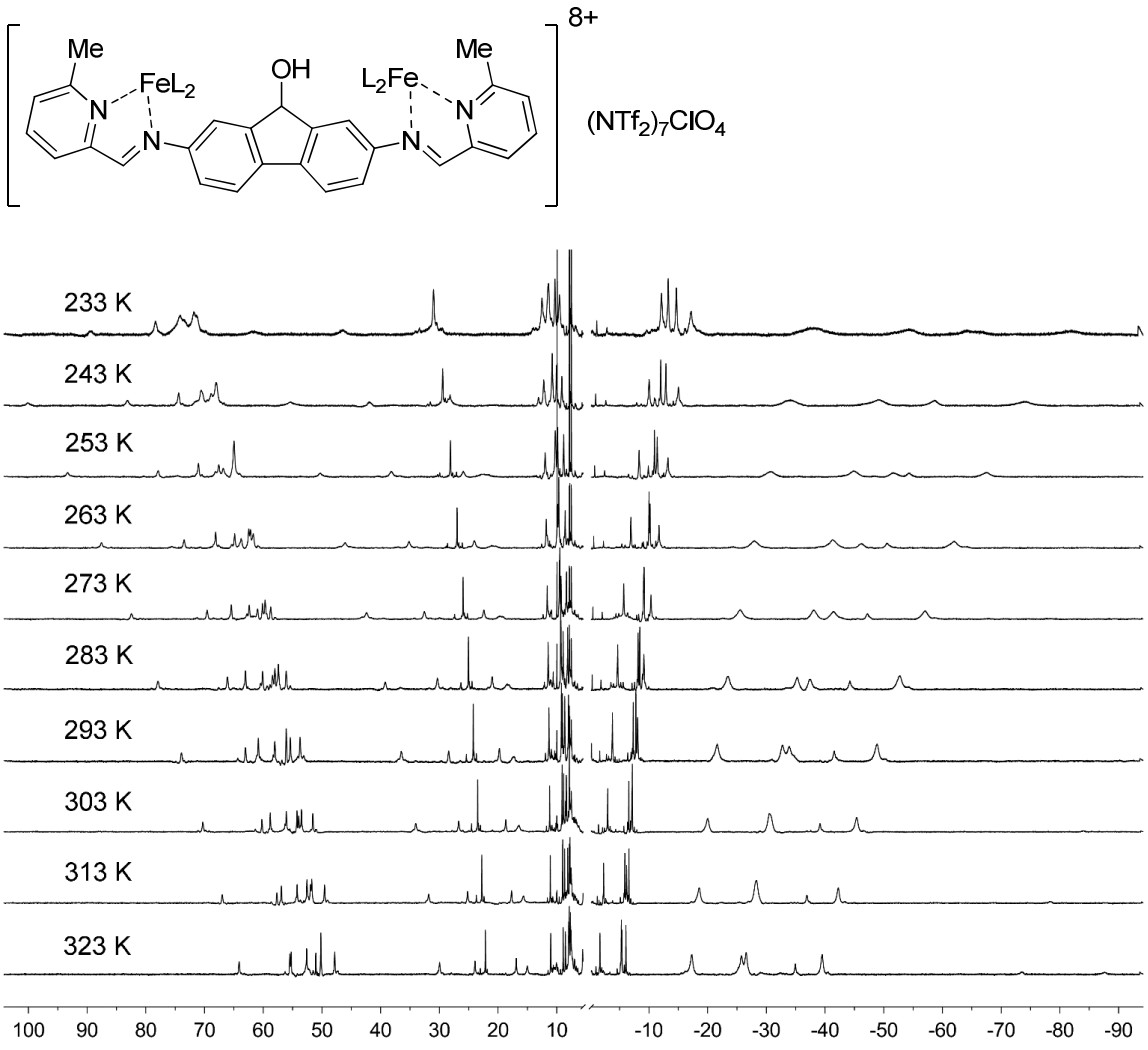

Figure 6.36: Variable temperature ^{1}H NMR spectra of 3.39 mM **FOH•Fe•MePyCHO** $[NTf_2]_7(ClO_4)$ in 99:1 CD_3CN: Dichloroethane.

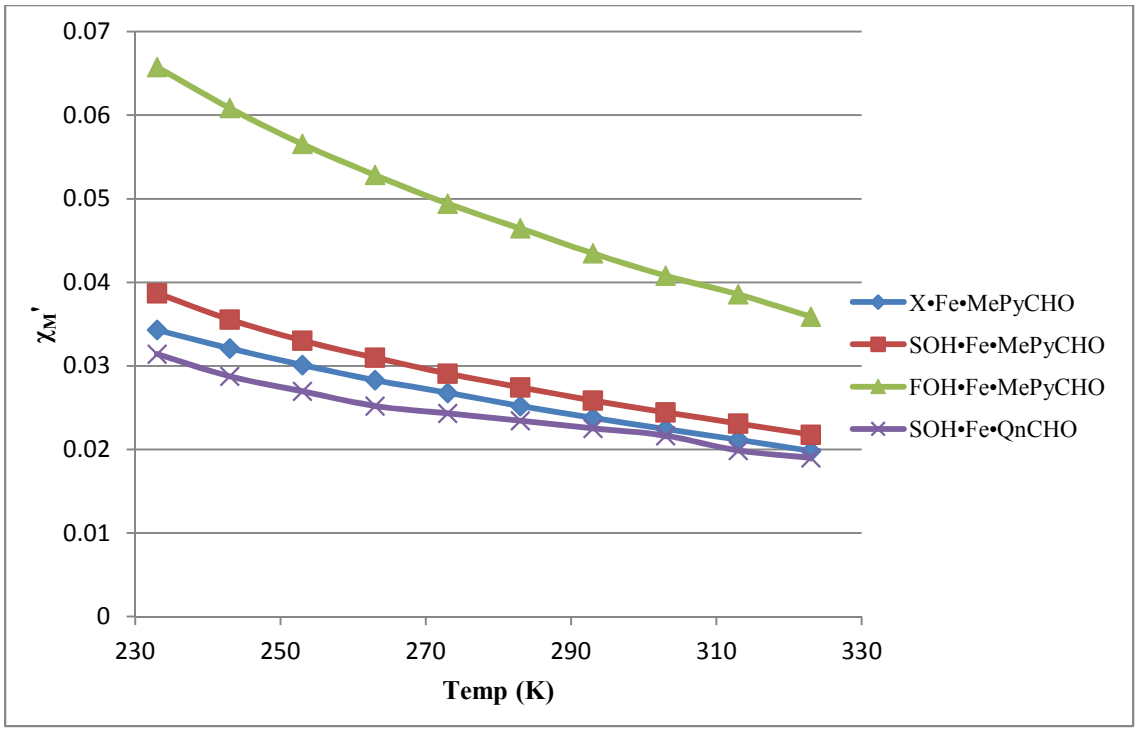

Figure 6.37: Graph of corrected molar susceptibility ($\chi_{M'}$) for cages **SOH•Fe•MePyCHO**, **SOH•Fe•QnCHO**, **X•Fe•MePyCHO**, and **FOH•Fe•MePyCHO** versus temperature (K).

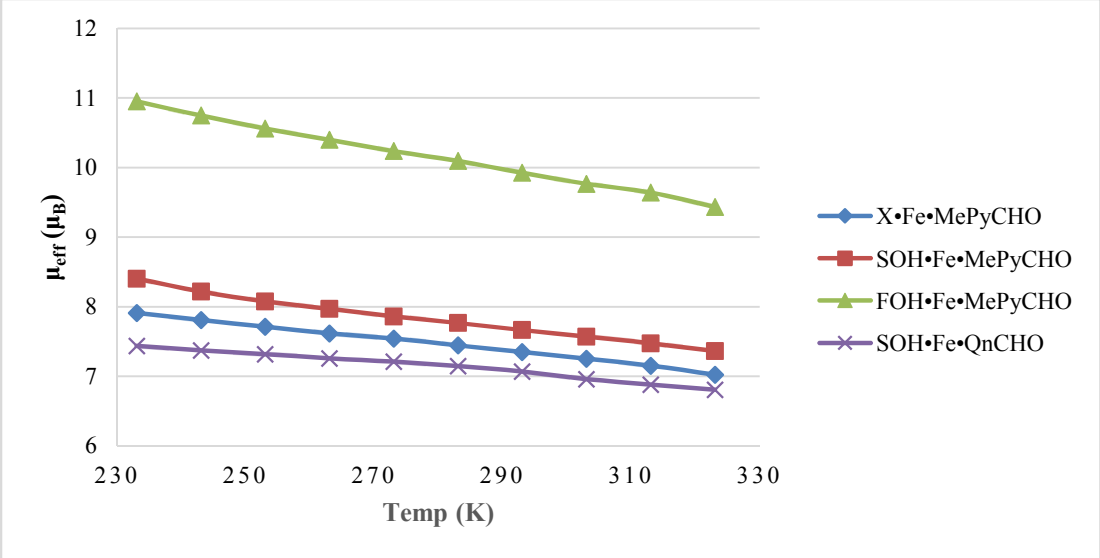

Figure 6.38: Graph of Effective magnetic moment, μ_{eff} (μ_B), for cages **SOH•Fe•MePyCHO**, **SOH•Fe•QnCHO**, **X•Fe•MePyCHO**, and **FOH•Fe•MePyCHO** versus temperature (K).

Ligand Selectivity Experiments (Dianiline Cores)

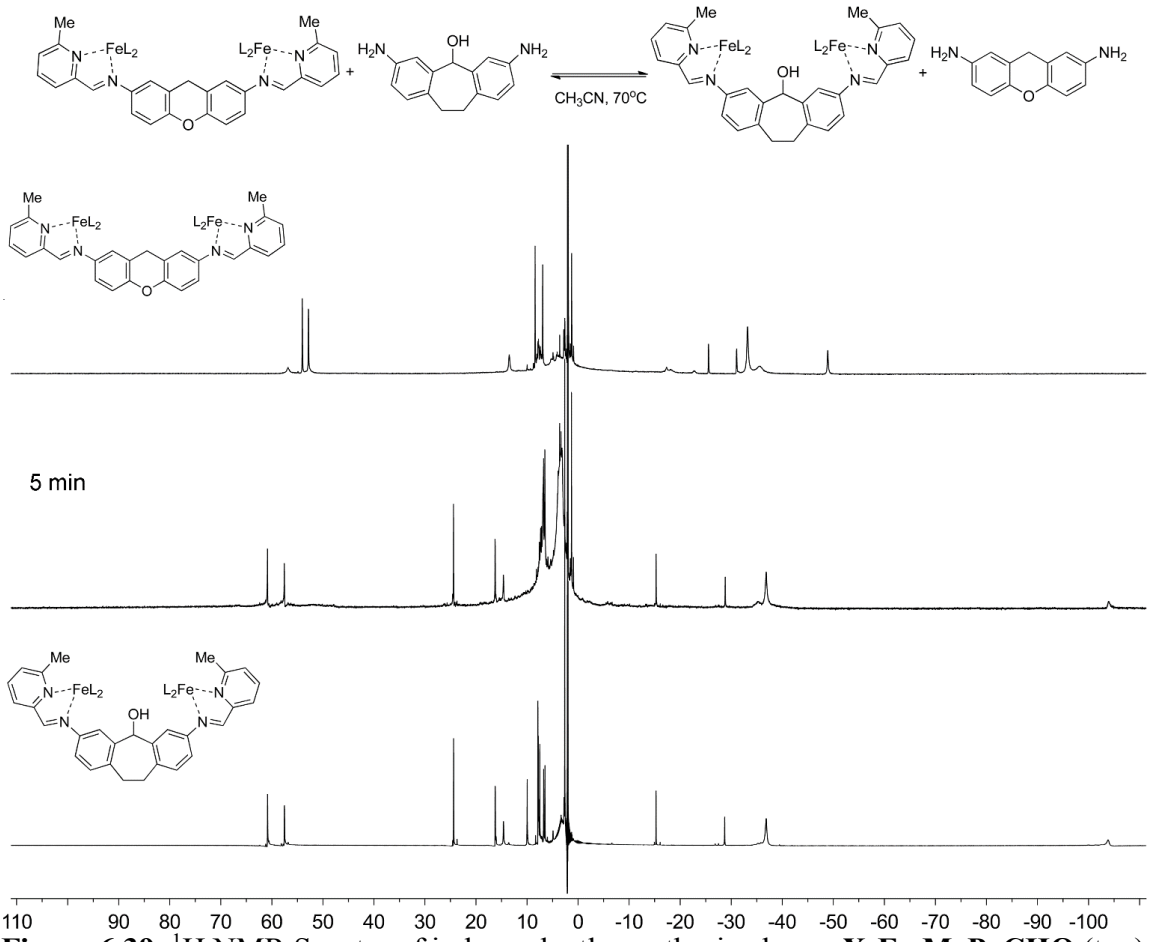

Figure 6.39: ^{1}H NMR Spectra of independently synthesized cage **X•Fe•MePyCHO** (top), product obtained after mixing **X•Fe•MePyCHO** (10 mg, 0.004 mmol) with **SOH** (4.3 mg, 0.012 mmol, 3 eq.) for 24 hours at 25°C (middle), and independently synthesized cage **SOH•Fe•MePyCHO** (bottom) (CD_3CN, 400MHz, 298 K).

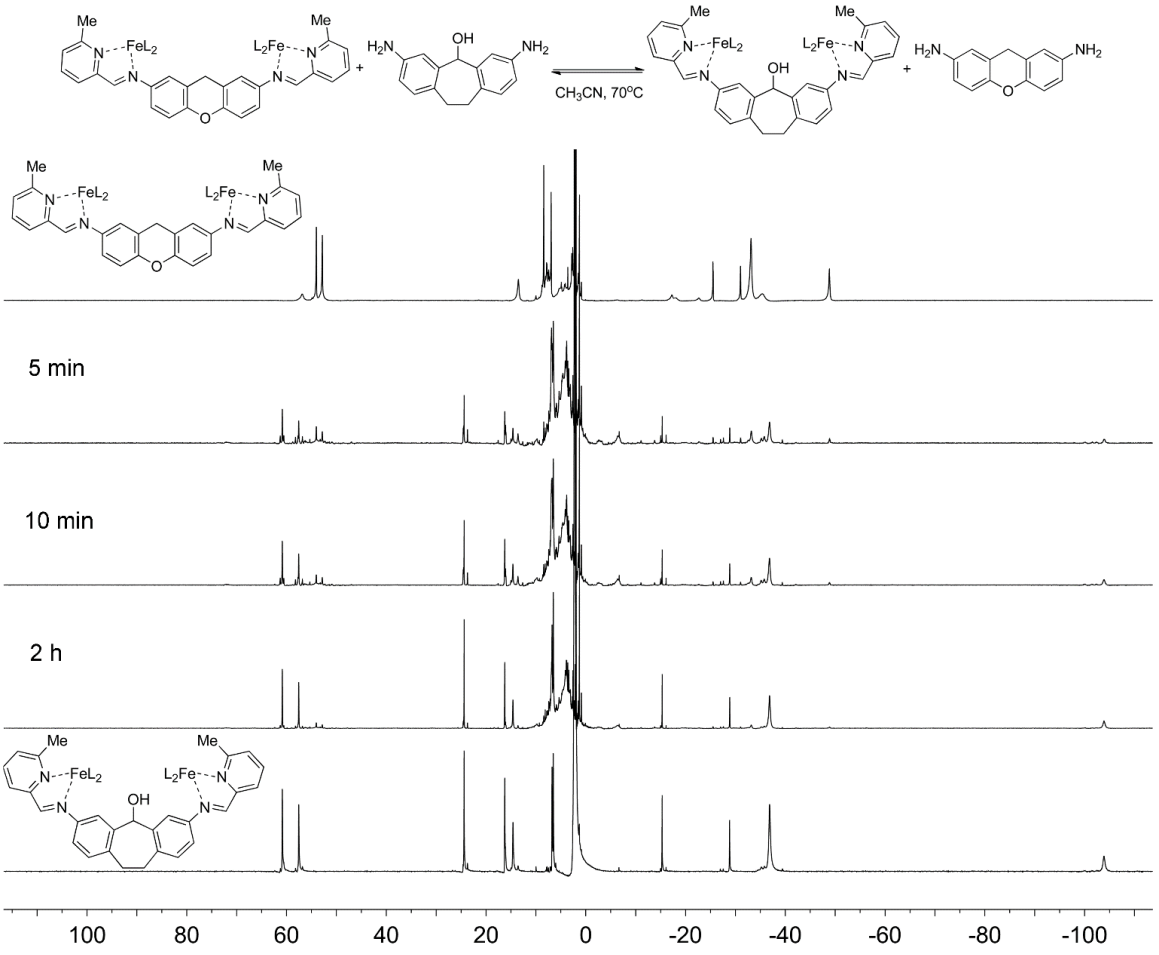

Figure 6.40: ^{1}H NMR Spectra of independently synthesized cage **X•Fe•MePyCHO** (top), products obtained after mixing **X•Fe•MePyCHO** (10 mg, 0.004 mmol) with **SOH** (4.3 mg, 0.012 mmol, 3 eq.) over time at 25°C, and independently synthesized cage **SOH•Fe•MePyCHO** (bottom) (CD_3CN, 400MHz, 298 K).

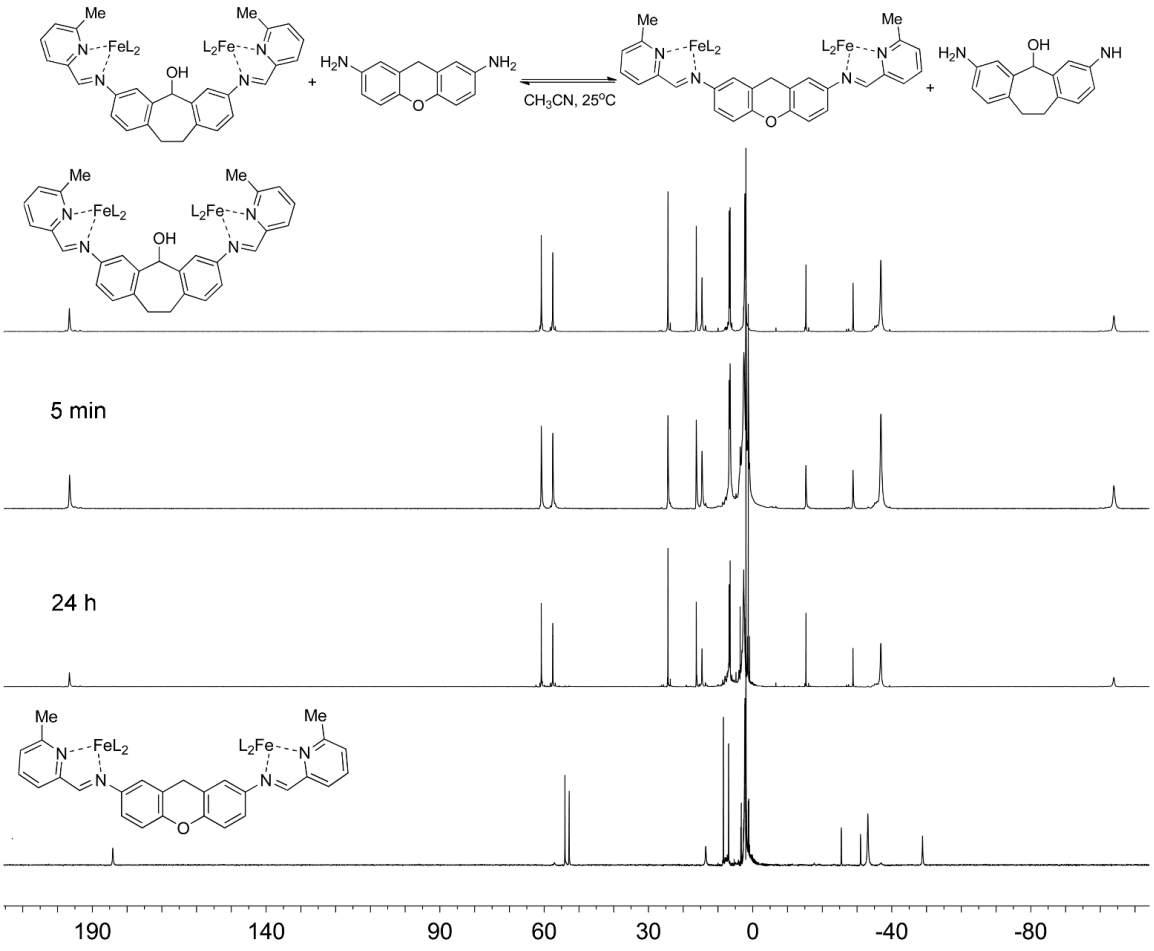

Figure 6.41: ^{1}H NMR Spectra of independently synthesized cage **SOH•Fe•MePyCHO** (top), products obtained after mixing **SOH•Fe•MePyCHO** (10 mg, 0.004 mmol) with **X** (4.3 mg, 0.012 mmol, 3 eq.) over time at 25°C, and independently synthesized cage **X•Fe•MePyCHO** (bottom) (CD_3CN, 400MHz, 298 K).

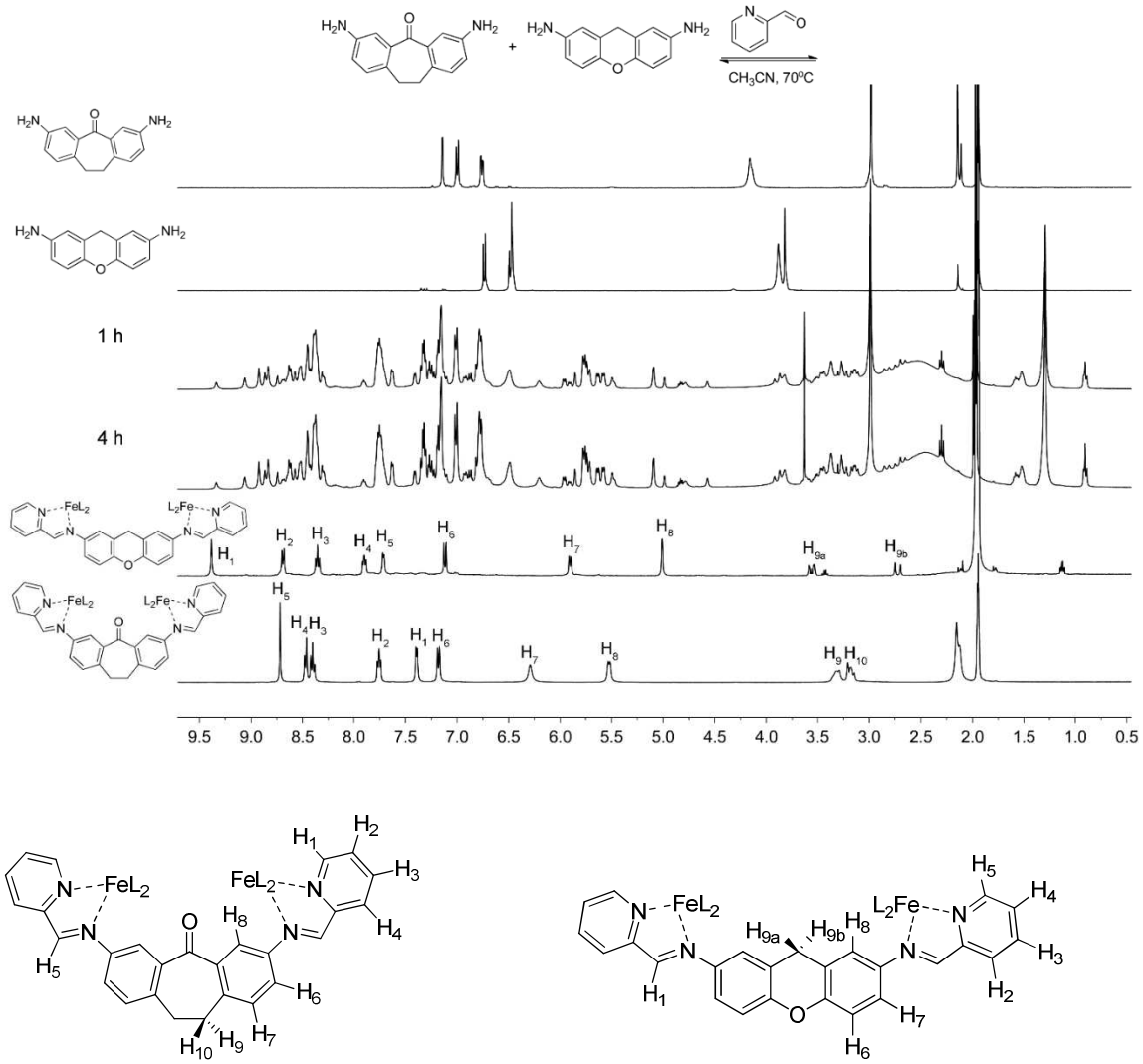

Figure 6.42: ^{1}H NMR Spectrum of products observed over time when equal amounts of ligands **X** (0.02 mmol) and **SO** (0.02 mmol) are reacted with PyCHO (0.04 mmol) and $Fe(NTf_2)_2$ (0.013 mmol) at 77 °C over 4 hours (CD_3CN, 400 MHz, 298 K). The energy difference between the homocomplexes is not great enough to allow for narcissistic self-sorting in this case. The ^{1}H NMR peak assignment for **SO•Fe•PyCHO** and **X•Fe•PyCHO** is shown at the base of the figure.

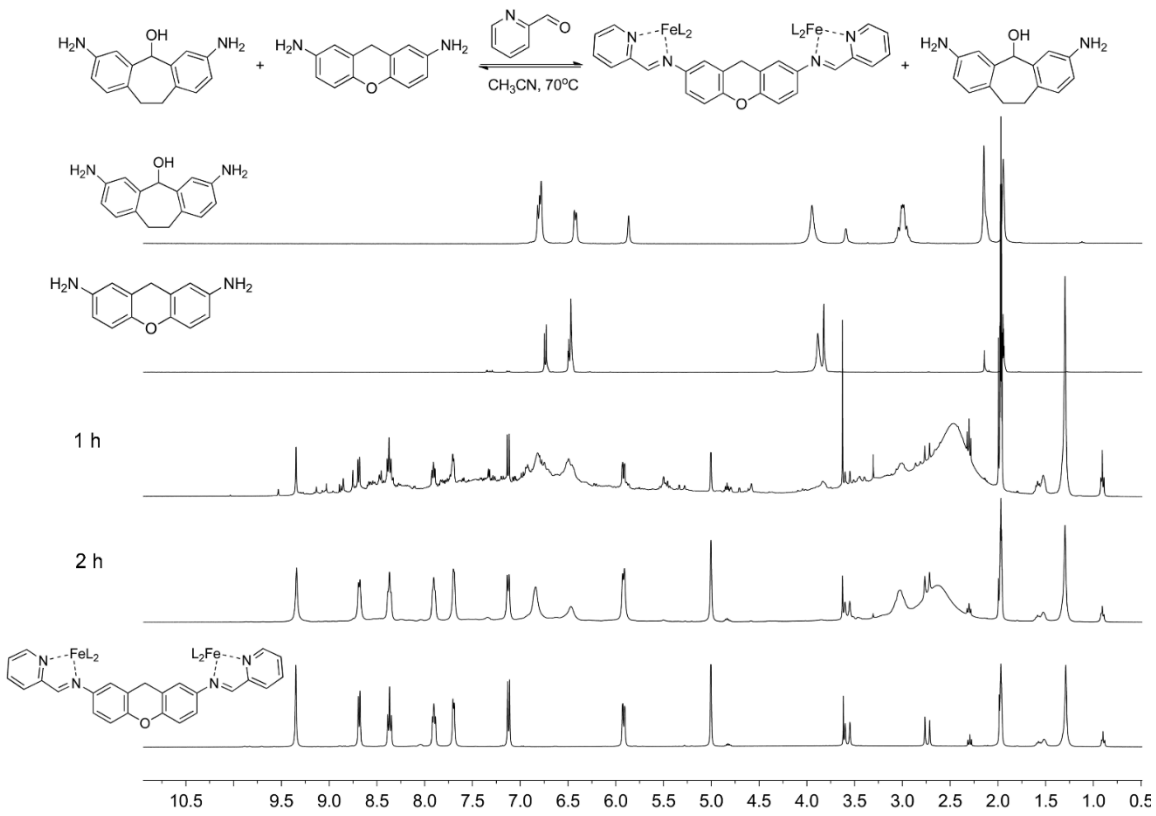

Figure 6.43: ^{1}H NMR Spectrum of products observed over time when equal amounts of ligands **X** (0.02 mmol) and **SOH** (0.02 mmol) are reacted with PyCHO (0.04 mmol) and $Fe(NTf_2)_2$ (0.013 mmol) at 77 °C over 2 hours (CD_3CN, 400 MHz, 298 K). The homocomplex **X•Fe•PyCHO** is preferred over **SOH•Fe•MePyCHO** or heterocomplexes. See Fig S-26 for assignment of **X•Fe•PyCHO**, Figure 6.6 for assignment of **SOH•Fe•MePyCHO**.

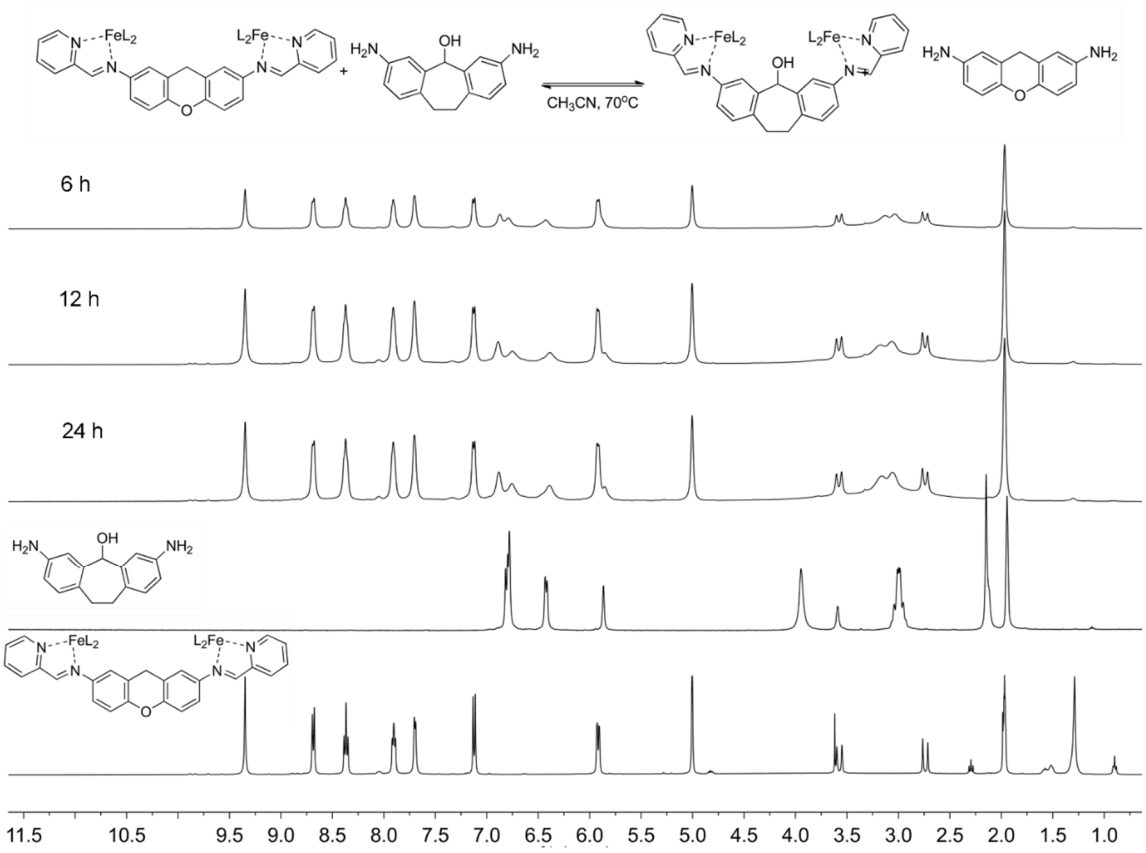

Figure 6.43: ^{1}H NMR Spectrum of products observed over time when cage **X•Fe•PyCHO** (0.007 mmol) was heated with **SOH** (0.02 mmol) at 77 °C over 2 hours (CD_3CN, 400 MHz, 298 K). No displacement of ligand **X** was observed. See Figure 6.24 for assignment of **X•Fe•PyCHO**, Figure 6.6 for assignment of **SOH•Fe•PyCHO**.

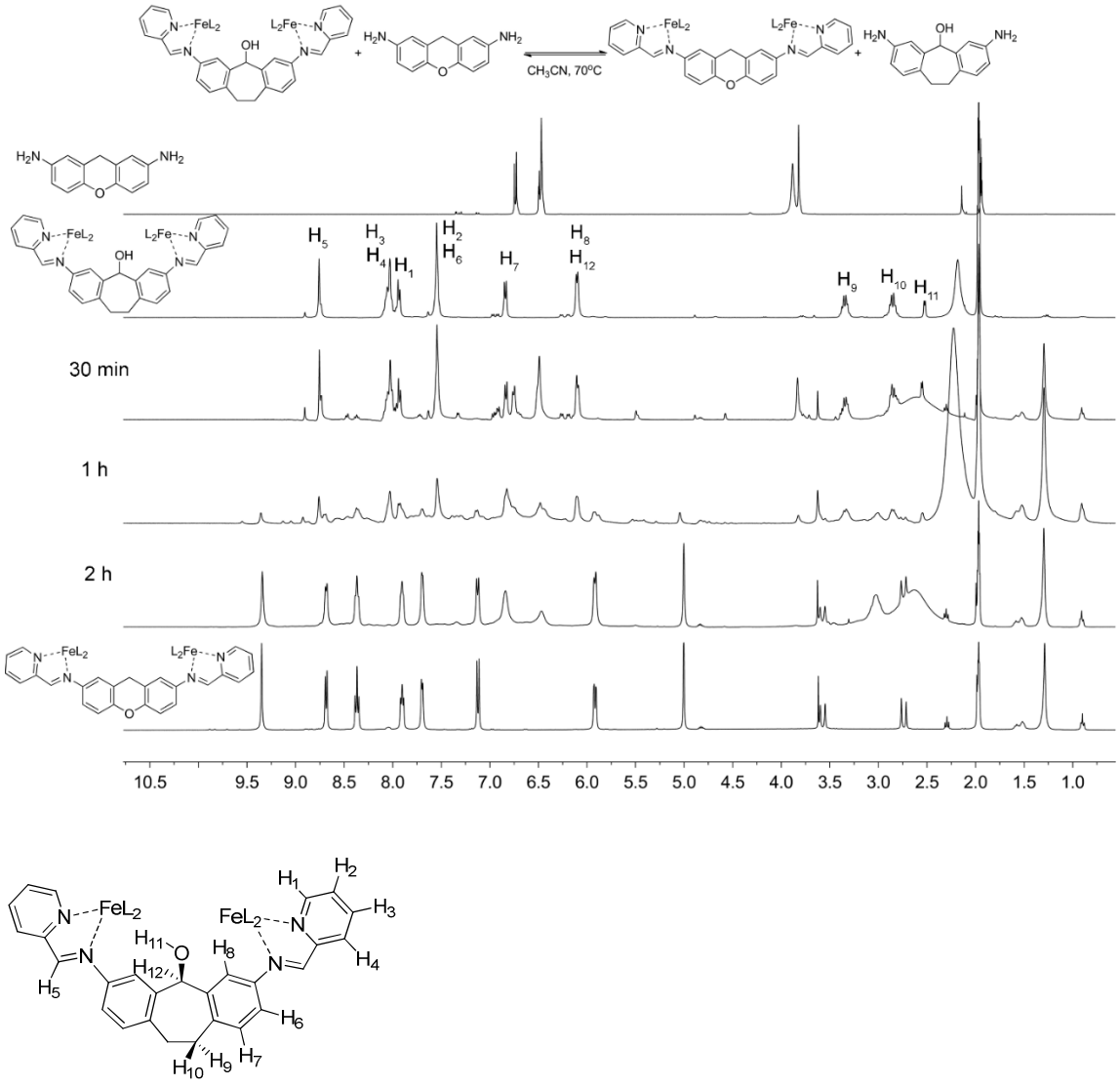

Figure 6.44: ^{1}H NMR Spectrum of products observed over time when cage **SOH•Fe•PyCHO** (0.007 mmol) was heated with **X** (0.02 mmol) at 77 °C over 2 hours (CD_3CN, 400 MHz, 298 K). Displacement of ligand **SOH** from **SOH•Fe•PyCHO** was observed within 30 minutes and was complete after 2 hours. The ^{1}H NMR peak assignment for **SOH•Fe•PyCHO** is shown at the base of the figure.

Turn-Off Spin State Switching via Aldehyde Exchange

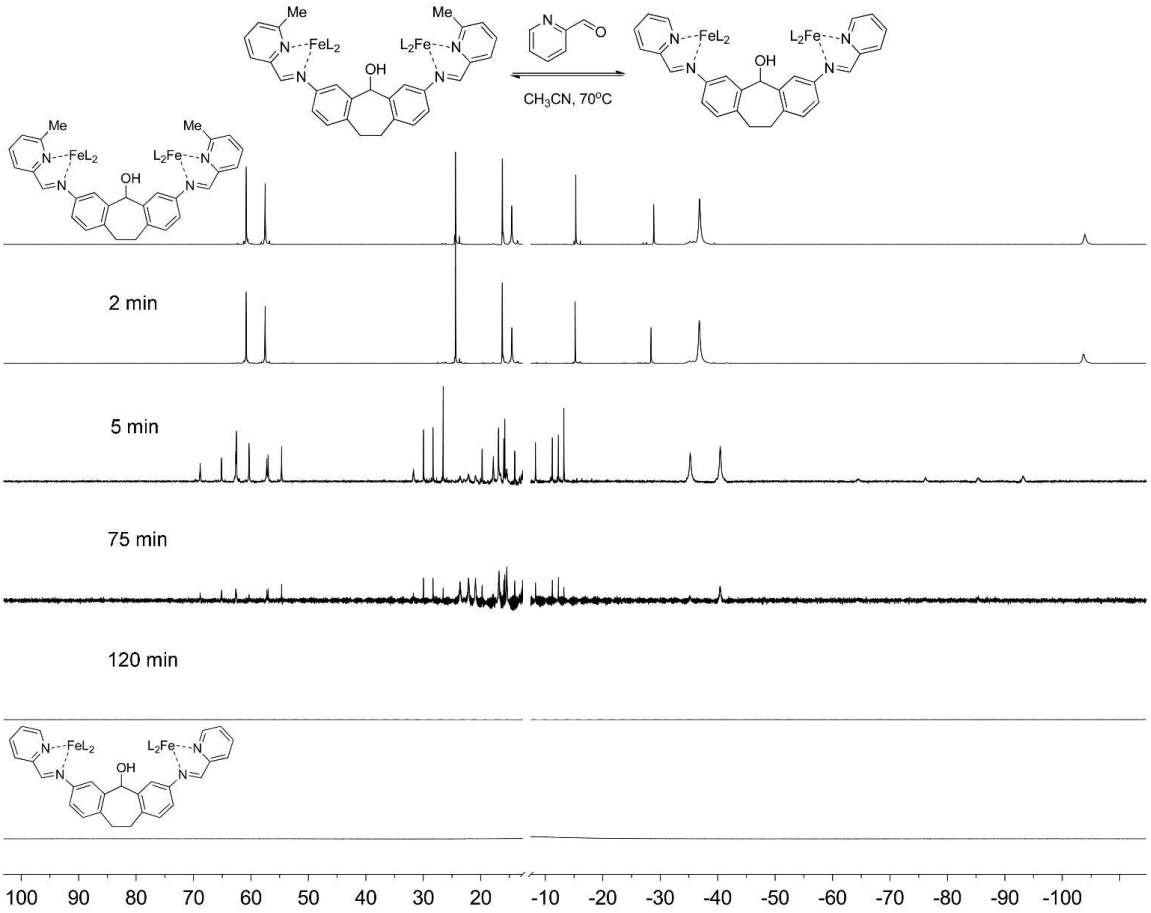

Figure 6.45: Broad range, 100 to -110 ppm, ^{1}H NMR spectrum to observe intermediates of a partially reacted aldehyde displacement of **SOH•Fe•MePyCHO** (10 mg, 0.0004 mmol) with 2-pyridinecarboxaldehyde (2.22 μL, 0.023 mmol, 6 eq.) heated at 25°C and monitored over 2 hours (CD_3CN, 400 MHz, 298 K).

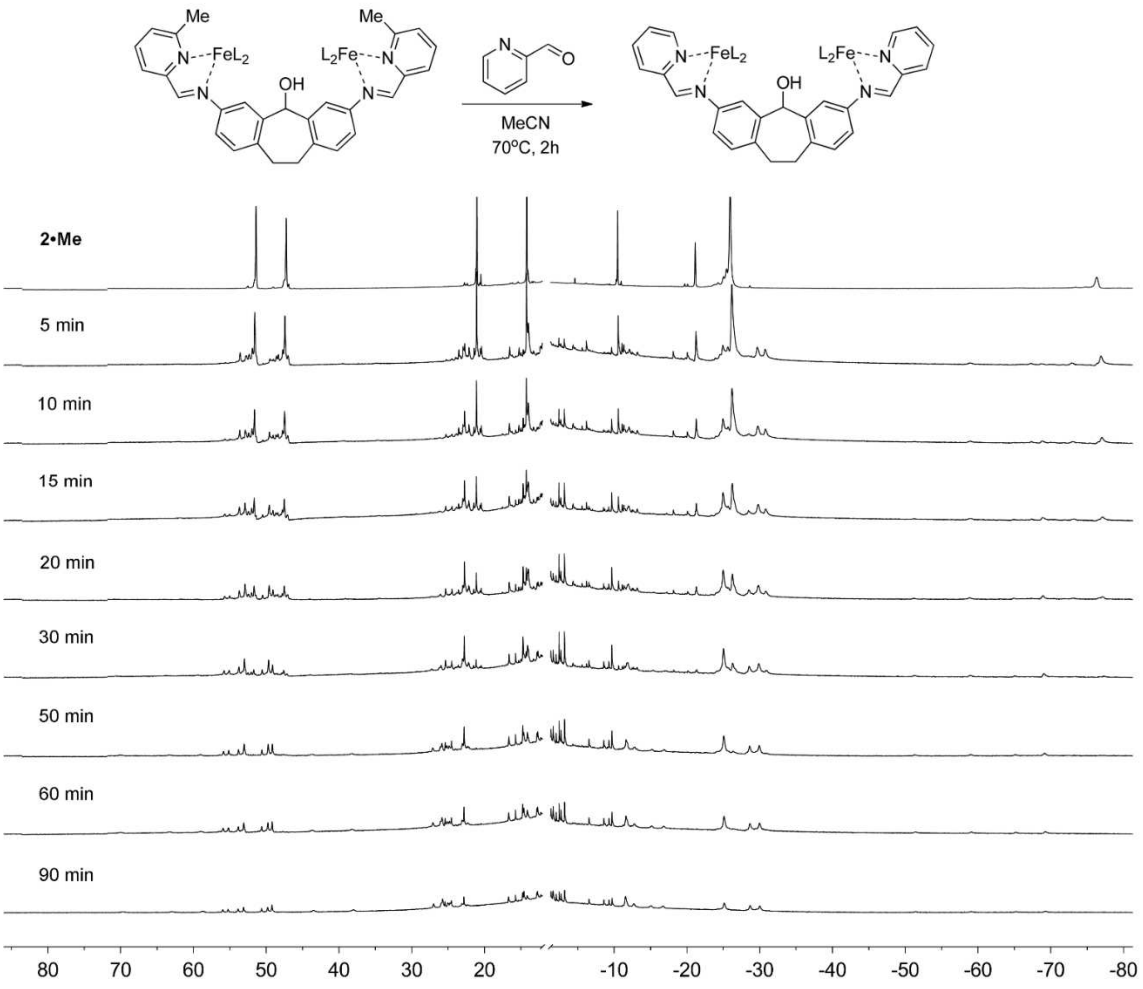

Figure 6.46: Broad range, 80 to -80 ppm, ^{1}H NMR spectrum to observe intermediates of a partially reacted aldehyde displacement of **SOH•Fe•MePyCHO** (10 mg, 0.0004 mmol) with 2-pyridinecarboxaldehyde (2.22 μL, 0.023 mmol, 6 eq.) heated at 70°C and monitored over 2 hours (CD_3CN, 400 MHz, 368 K).

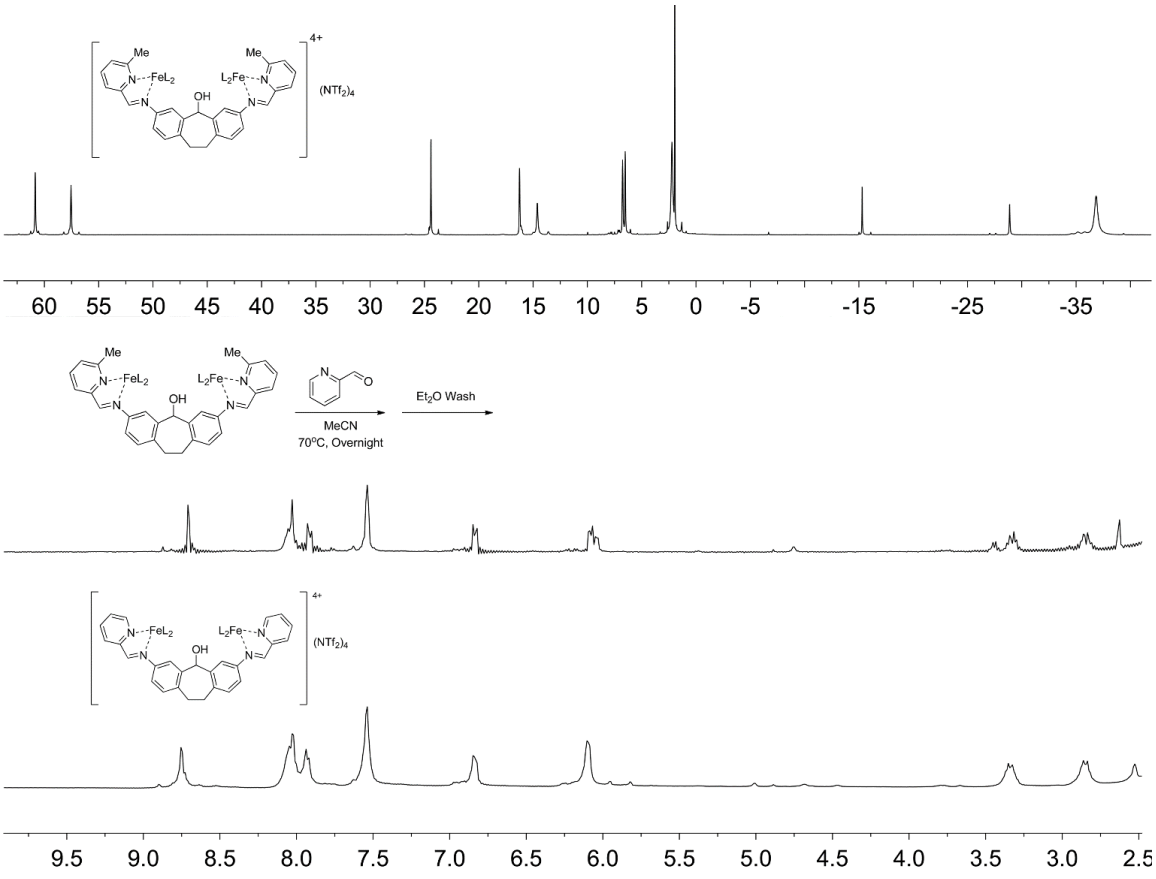

Figure 6.47: ^{1}H NMR spectrum of (top) cage **SOH•Fe•MePyCHO**, (middle) Aldehyde Displacement of **SOH•Fe•MePyCHO** (10 mg, 0.0004 mmol) with 2-pyridinecarboxaldehyde (2.40 μL, 0.025 mmol, 6.3 eq.) heated at 70°C overnight and washed with Et_2O, and (bottom) cage **SOH•Fe•PyCHO** (CD_3CN, 400 MHz, 298 K).

6.7 Chapter 3 Selected Spectra

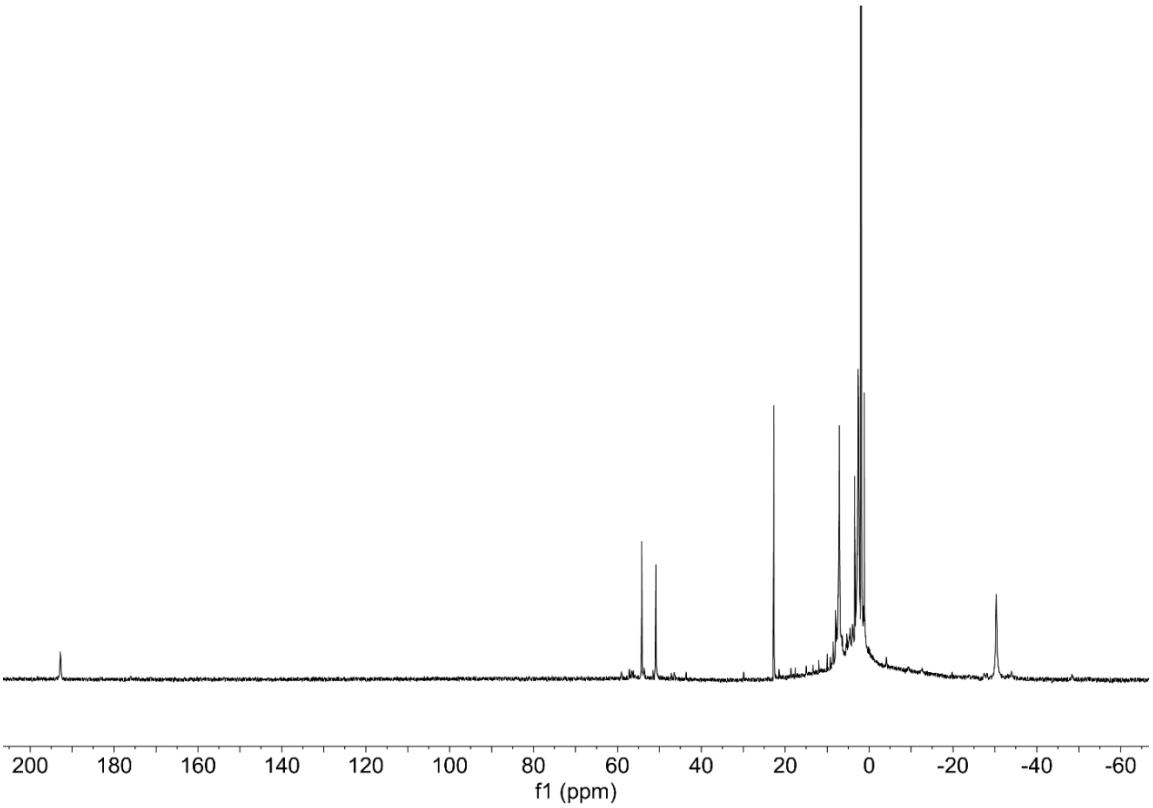

Figure 6.48: ^{1}H NMR spectrum of **DPM•Fe•MePyCHO** (CD_3CN, 400 MHz, 298 K).

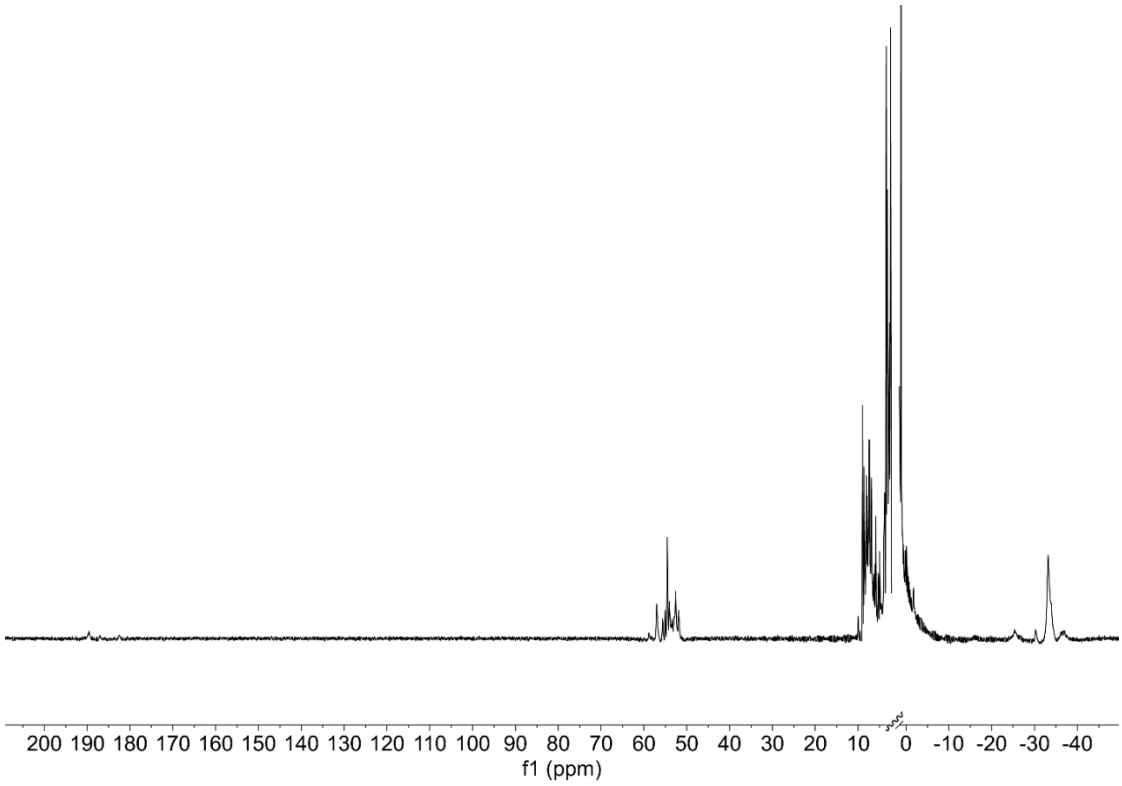

Figure 6.49: ^{1}H NMR spectrum of **APA•Fe•MePyCHO** (CD_3CN, 400 MHz, 298 K).

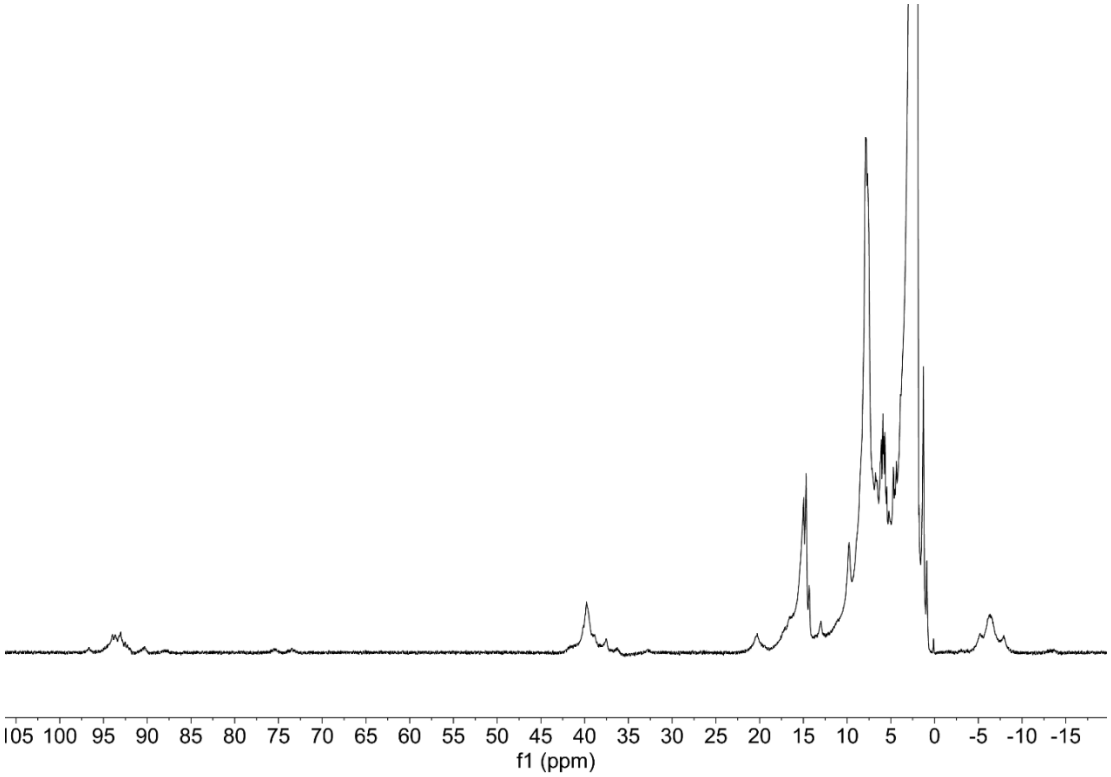

Figure 6.50: ^{1}H NMR spectrum of **Ph_2F•Fe•4ImCHO** (CD_3CN, 400 MHz, 298 K).

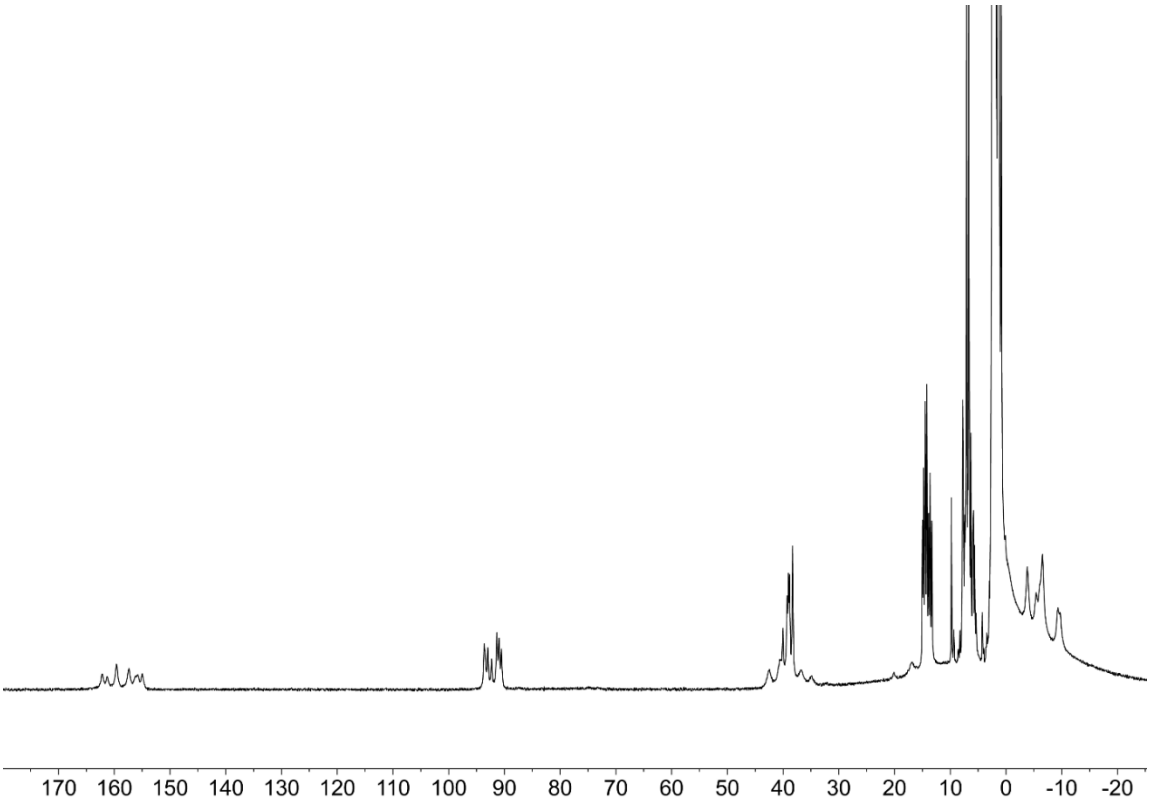

Figure 6.51: ^{1}H NMR spectrum of **Ph_2Xy•Fe•4ImCHO** (CD_3CN, 400 MHz, 298 K).

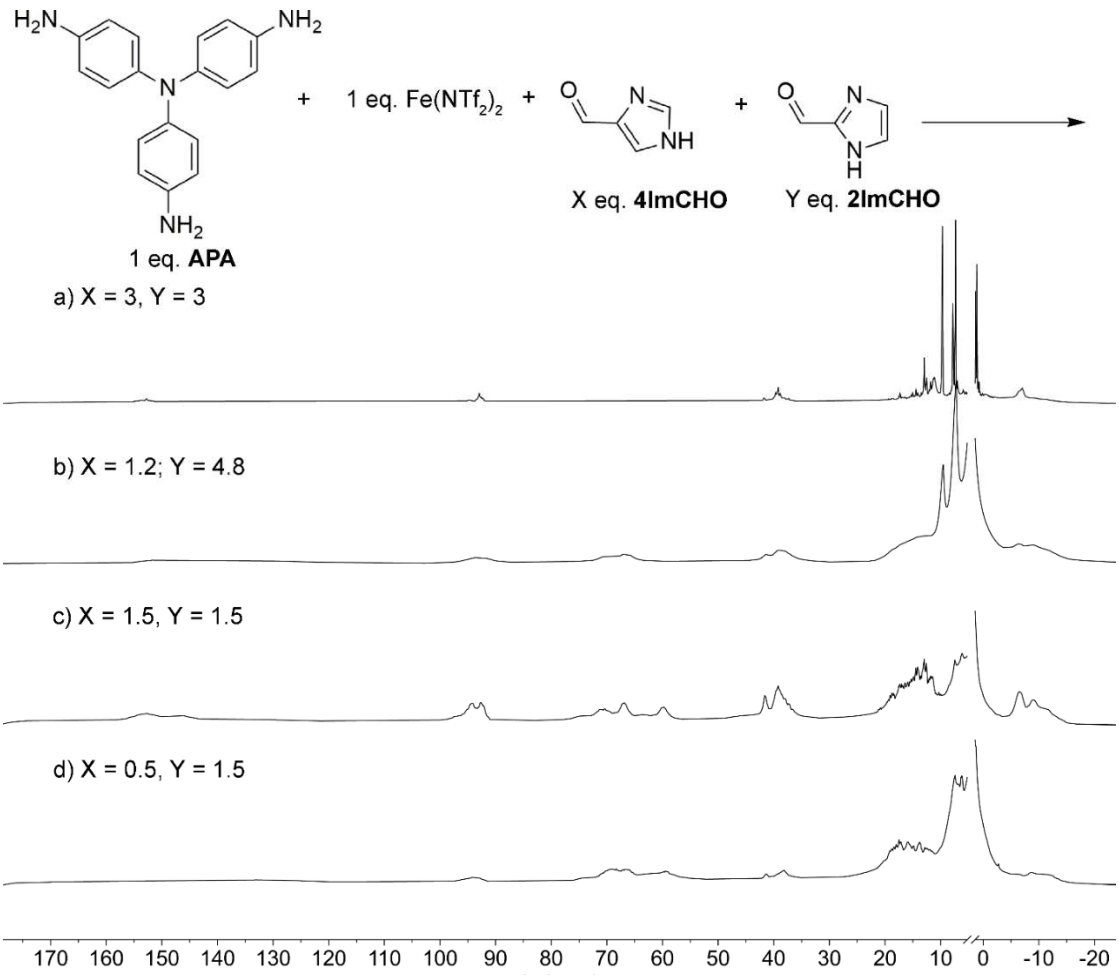

Figure 6.52: Full ^{1}H NMR spectra of varying ratios of **4ImCHO**:**2ImCHO** a) 3:3, b) 1.2:4.8, c) 1.5:1.5, and d) 0.5:1.5 (400 MHz, 298 K, CD_3CN).

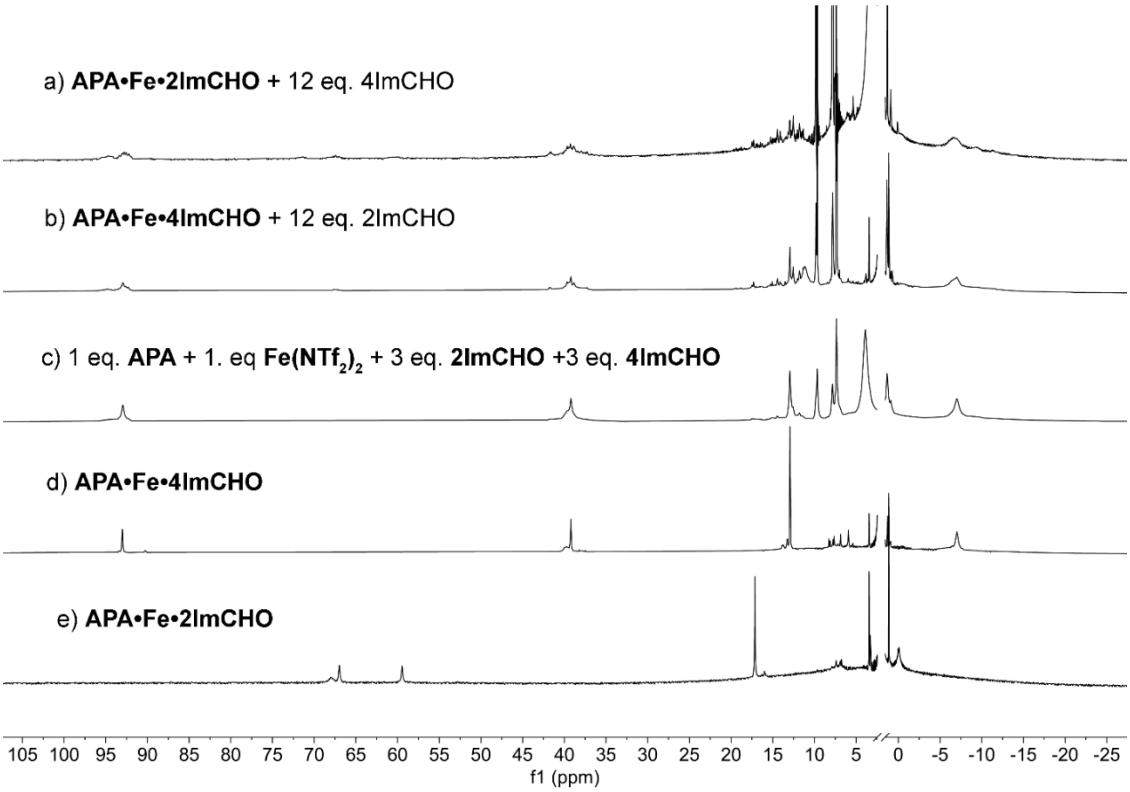

Figure 6.53: Displacement and competition reactions of **2ImCHO** and **4ImCHO** with **APA** ligand: a) 1 eq. **APA•Fe•4ImCHO** cage and 12 eq. **2ImCHO**, b) 1 eq. **APA•Fe•2ImCHO** cage and 12 eq. **4ImCHO**, c) Combination of 1 eq. APA, 1 eq. $Fe(NTf_2)_2$, 3 eq. **2ImCHO**, and 3 eq. **4ImCHO**, d) **APA•Fe•4ImCHO**, e) **APA•Fe•2ImCHO** (400 MHz, 298 K, CD_3CN).

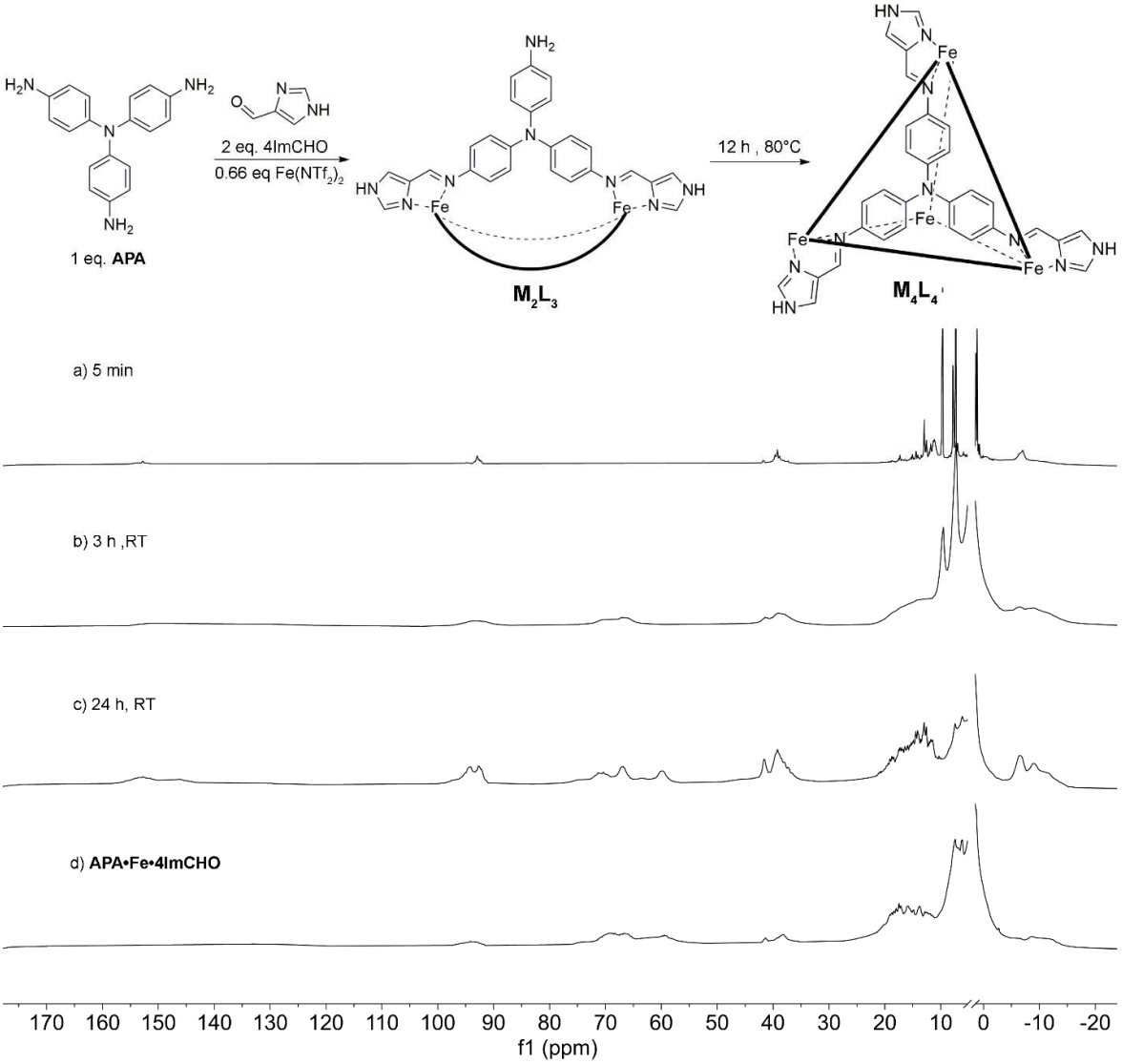

Figure 6.54: Full [1]The combination of 1 eq. **APA**, 2 eq. **4ImCHO**, 0.66 eq $Fe(NTf_2)_2$ heated at reflux at time a) 5 minutes, b) 1 h, c) 3h, d) 6 days. and e) preformed cage **APA•Fe•4ImCHO** (400 MHz, 298 K, CD_3CN).

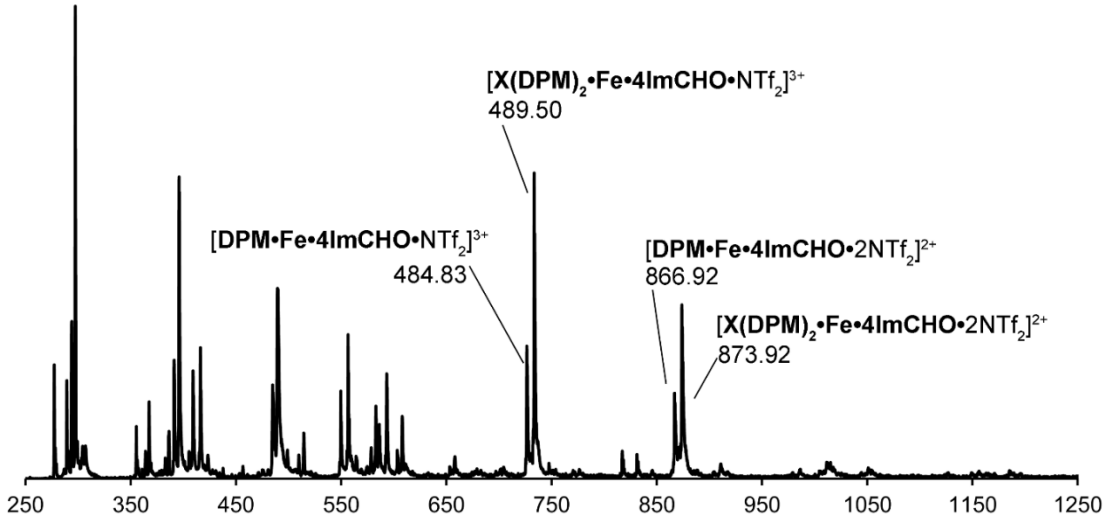

Figure 6.55: ESI MS of 1 eq **DPM**, 1 eq. **X**, 0.66 eq $Fe(NTf_2)_2$, and 2 eq. **4ImCHO** (CH_3CN).

6.8 Chapter 4 Selected Spectra

NMR and ESI-MS Characterization of New Cage Compounds

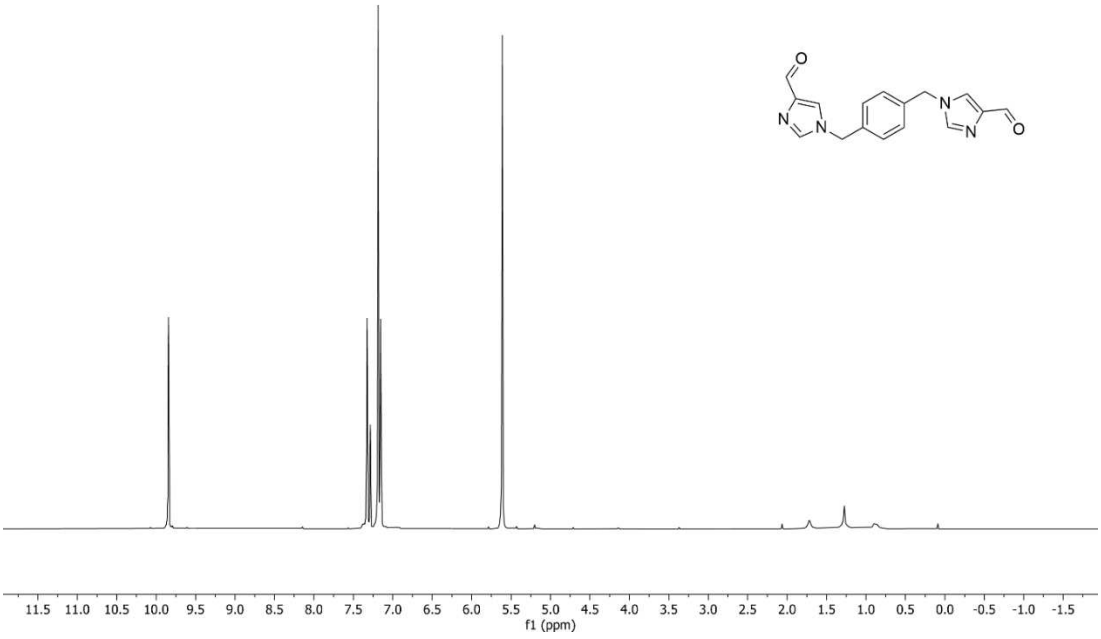

Figure 6.56: ^{1}H NMR spectrum of diimidazole **4.1** (CD_3CN, 400 MHz, 298 K).

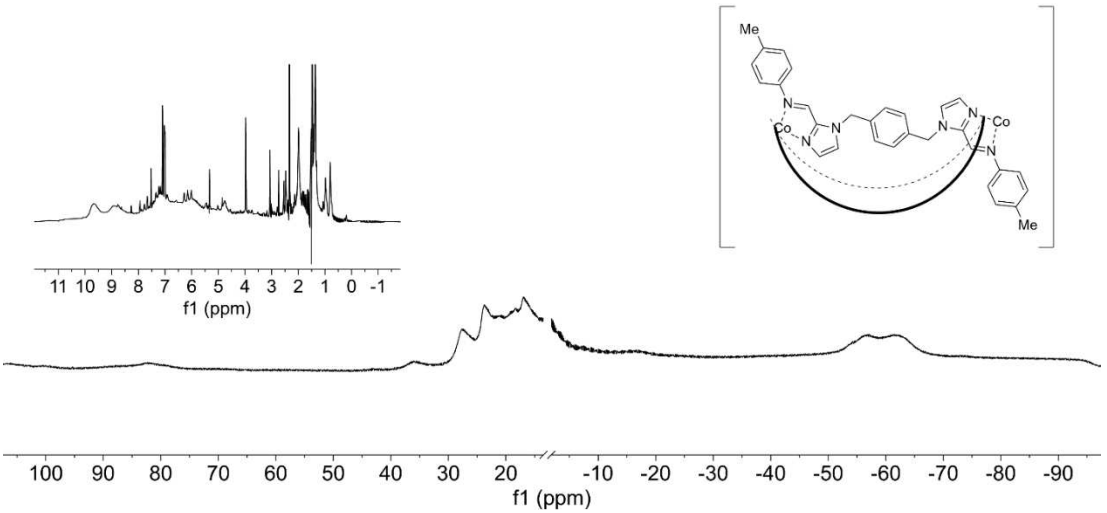

Figure 6.57: ^{1}H NMR spectrum of diimidazole cage **XylIm$_2$•Co•PhMe** (CD_3CN, 400 MHz, 298 K).

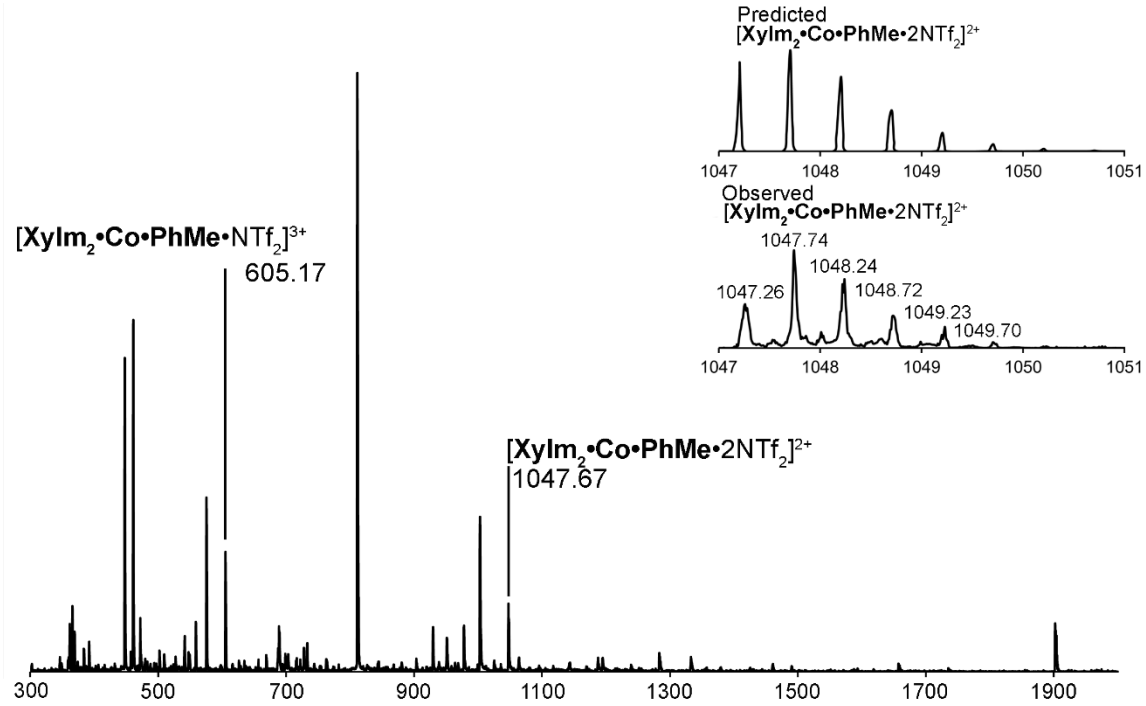

Figure 6.58: ESI-MS of cage **XylIm$_2$•Co•PhMe** (CH_3CN).

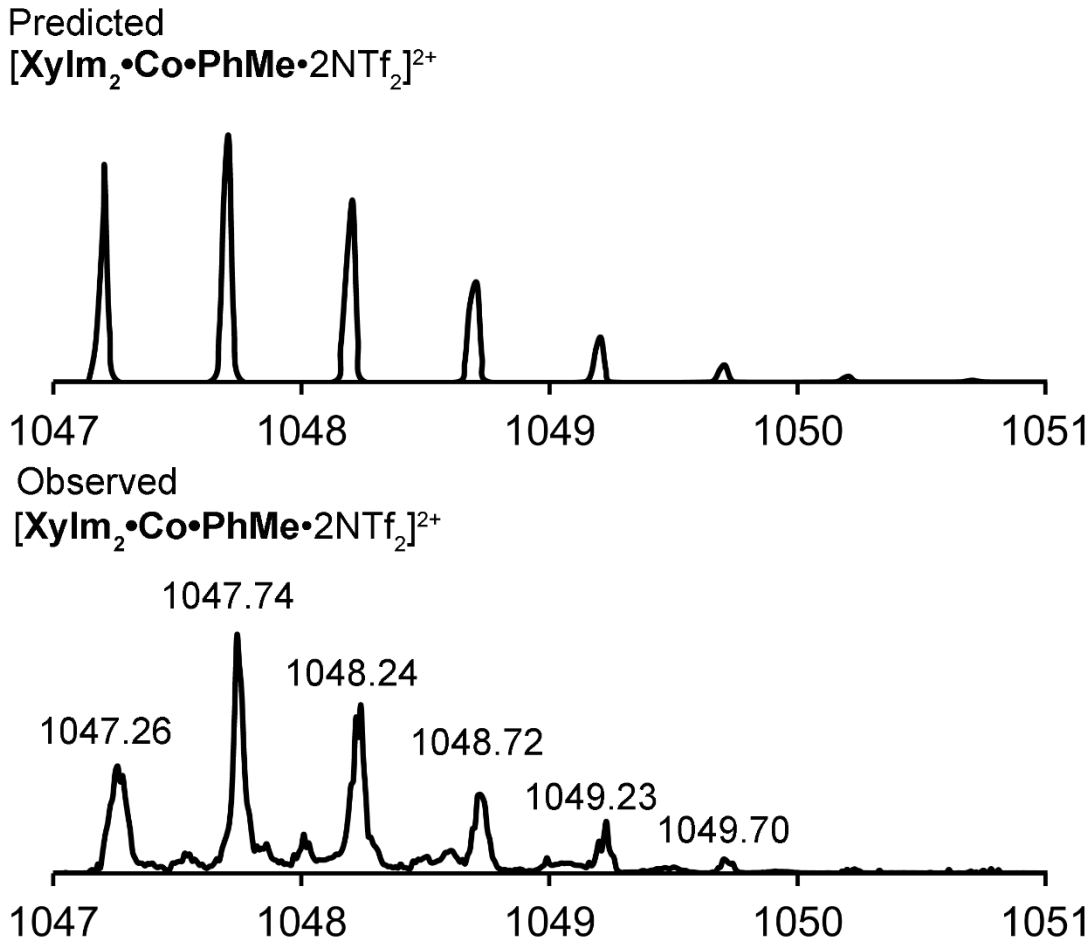

Figure 6.59: Expansion of the [**TzIm$_3$•Co•PhMe** •2NTf$_2$)]$^{2+}$ region vs the predicted values for Cage [**TzIm$_3$•Co•PhMe** •2NTf$_2$)]$^{2+}$ (CH_3CN).

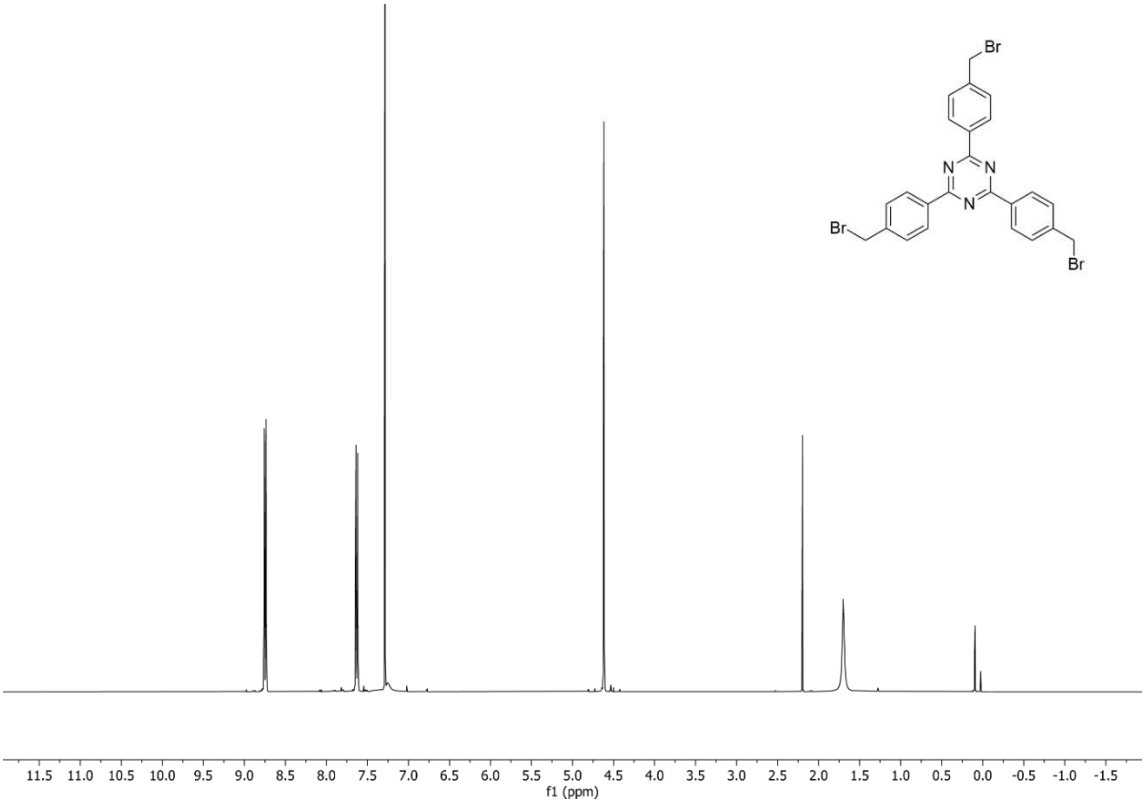

Figure 6.60: ^{1}H NMR spectrum of tribromo **Tz** (CD_3CN, 400 MHz, 298 K).

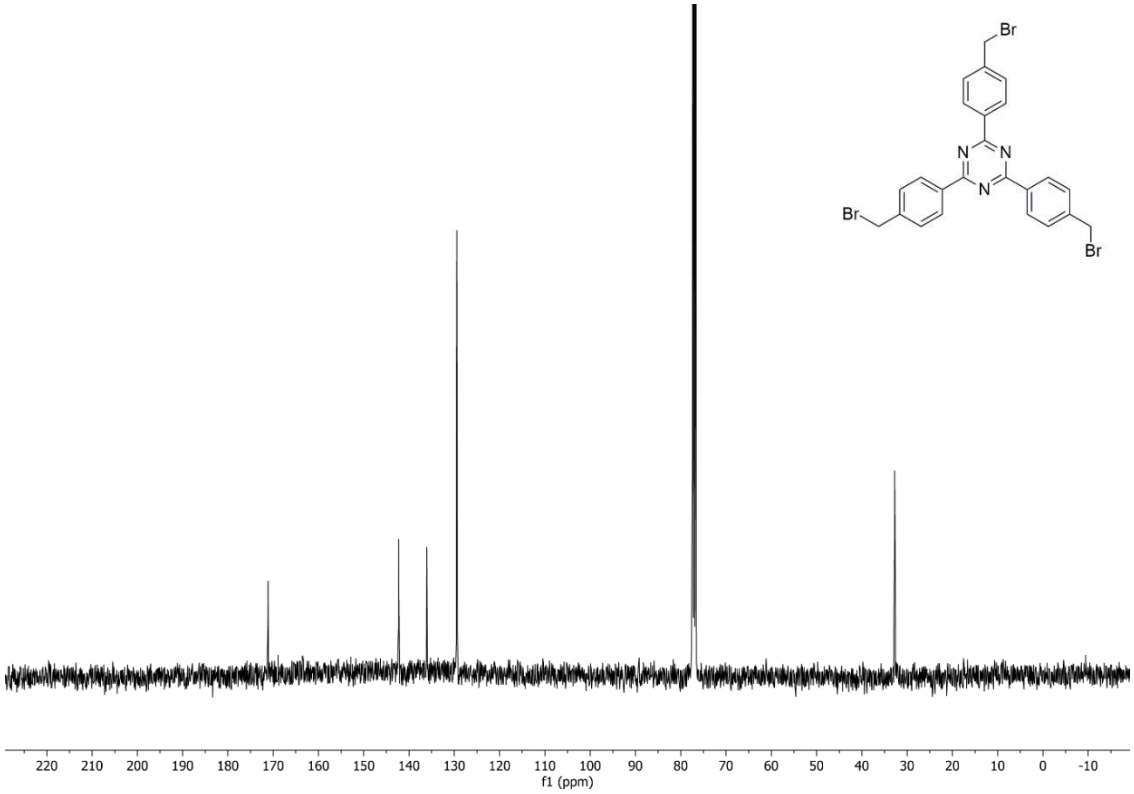

Figure 6.61: ^{13}C NMR spectrum of tribromo **Tz** (CD_3CN, 400 MHz, 298 K).

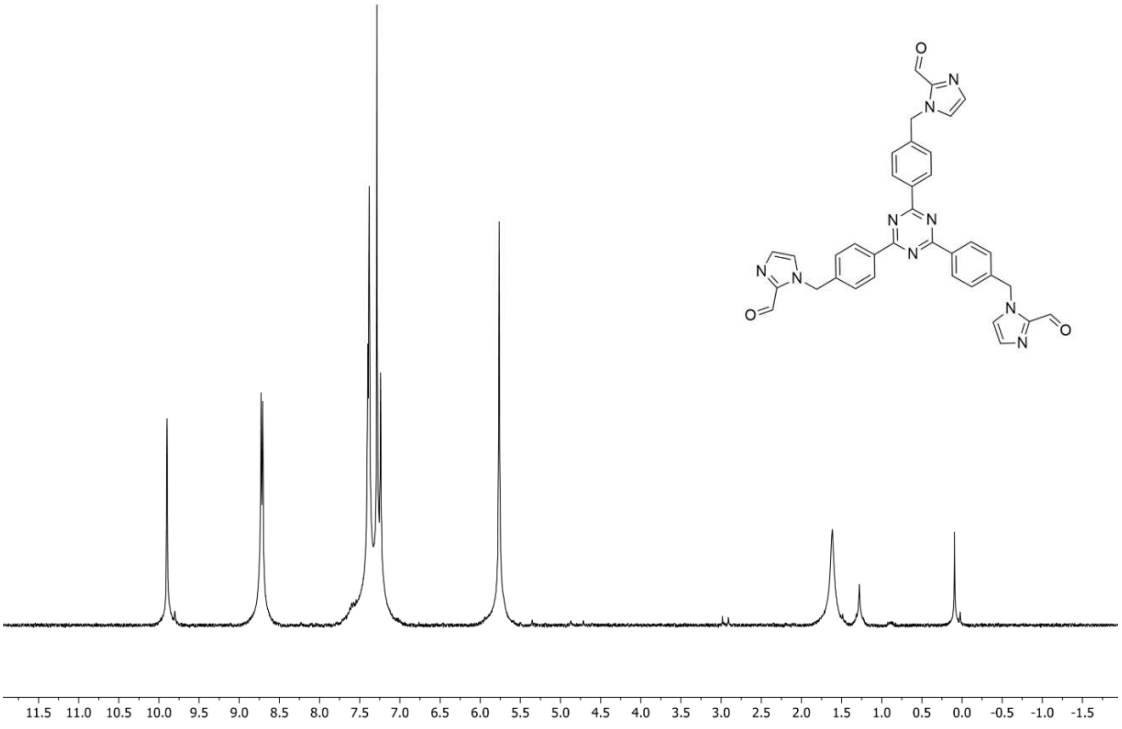

Figure 6.62: ^{1}H NMR spectrum of triimidazole **TzIm$_3$** (CD_3CN, 400 MHz, 298 K).

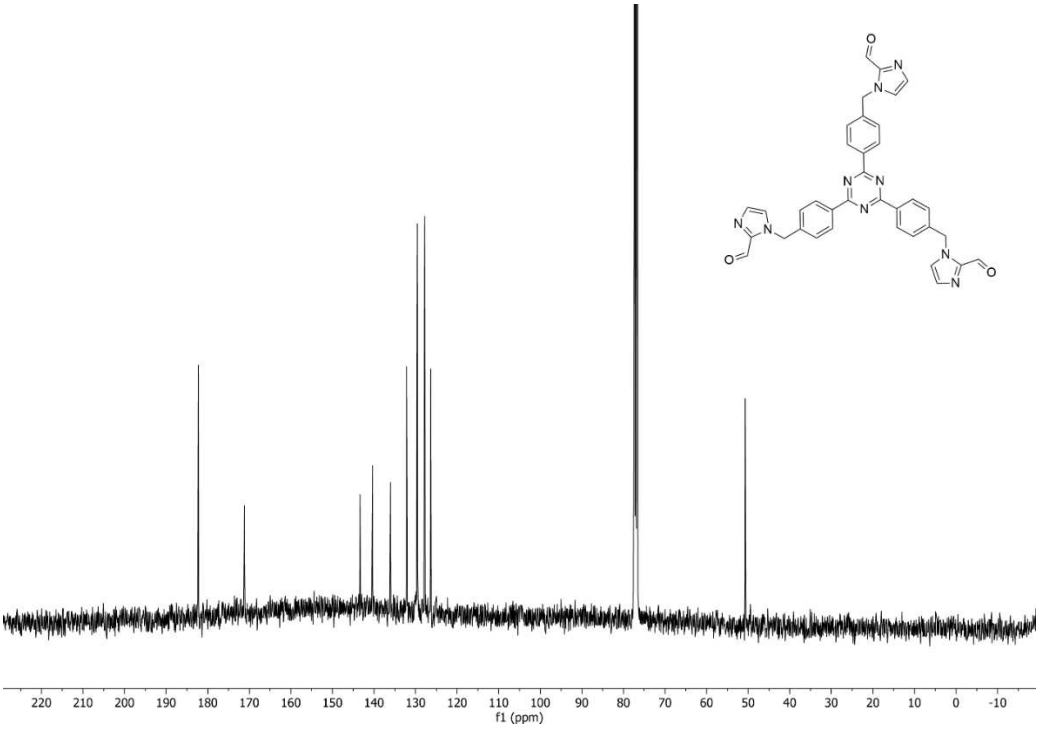

Figure 6.63: ^{13}C NMR spectrum of triimidazole **TzIm$_3$** (CD_3CN, 400 MHz, 298 K).

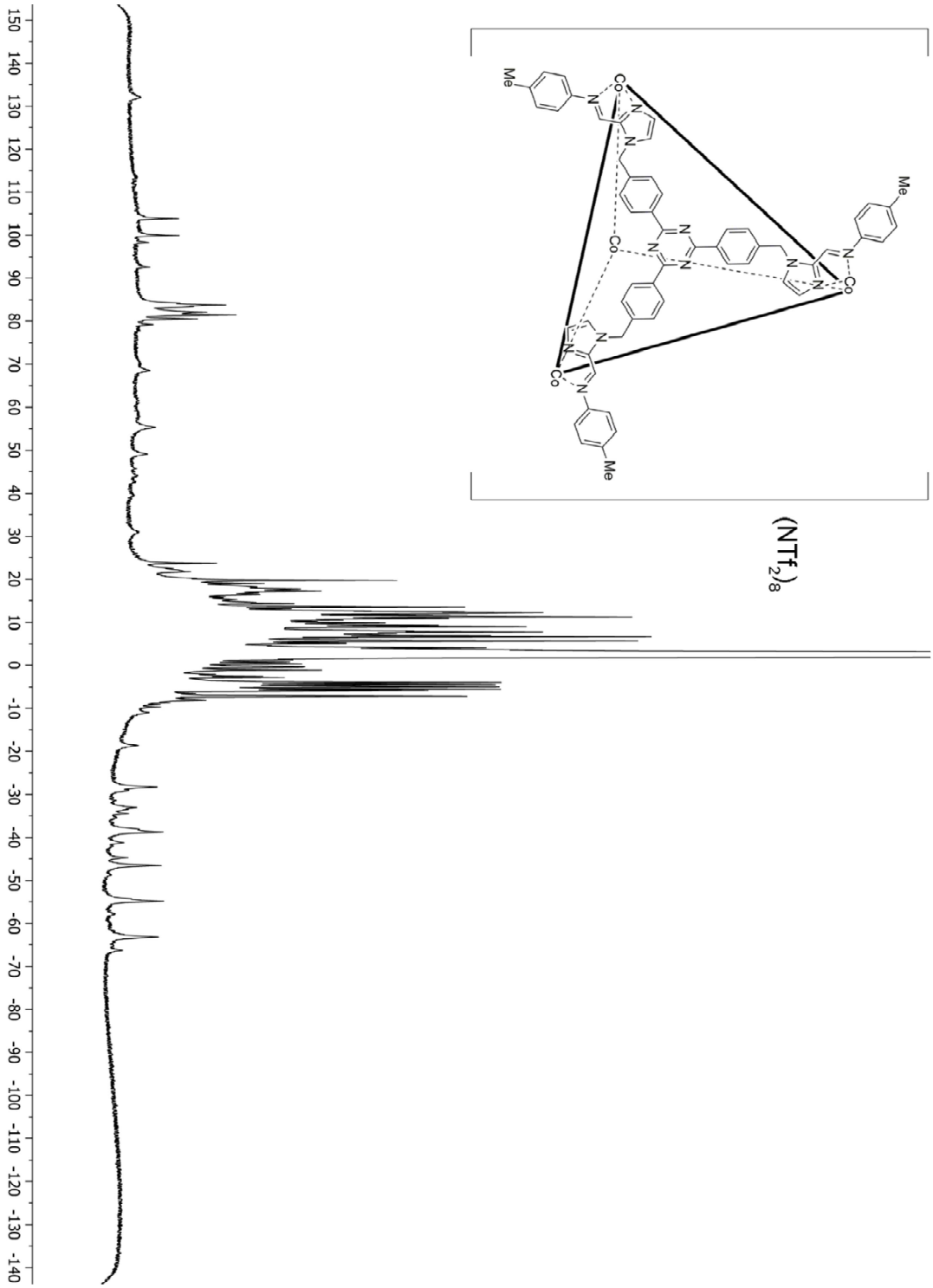

Figure 6.64: ^{1}H NMR spectrum of cage **TzIm$_3$•Co•PhMe•NTf$_2$** (CD_3CN, 400 MHz, 298 K).

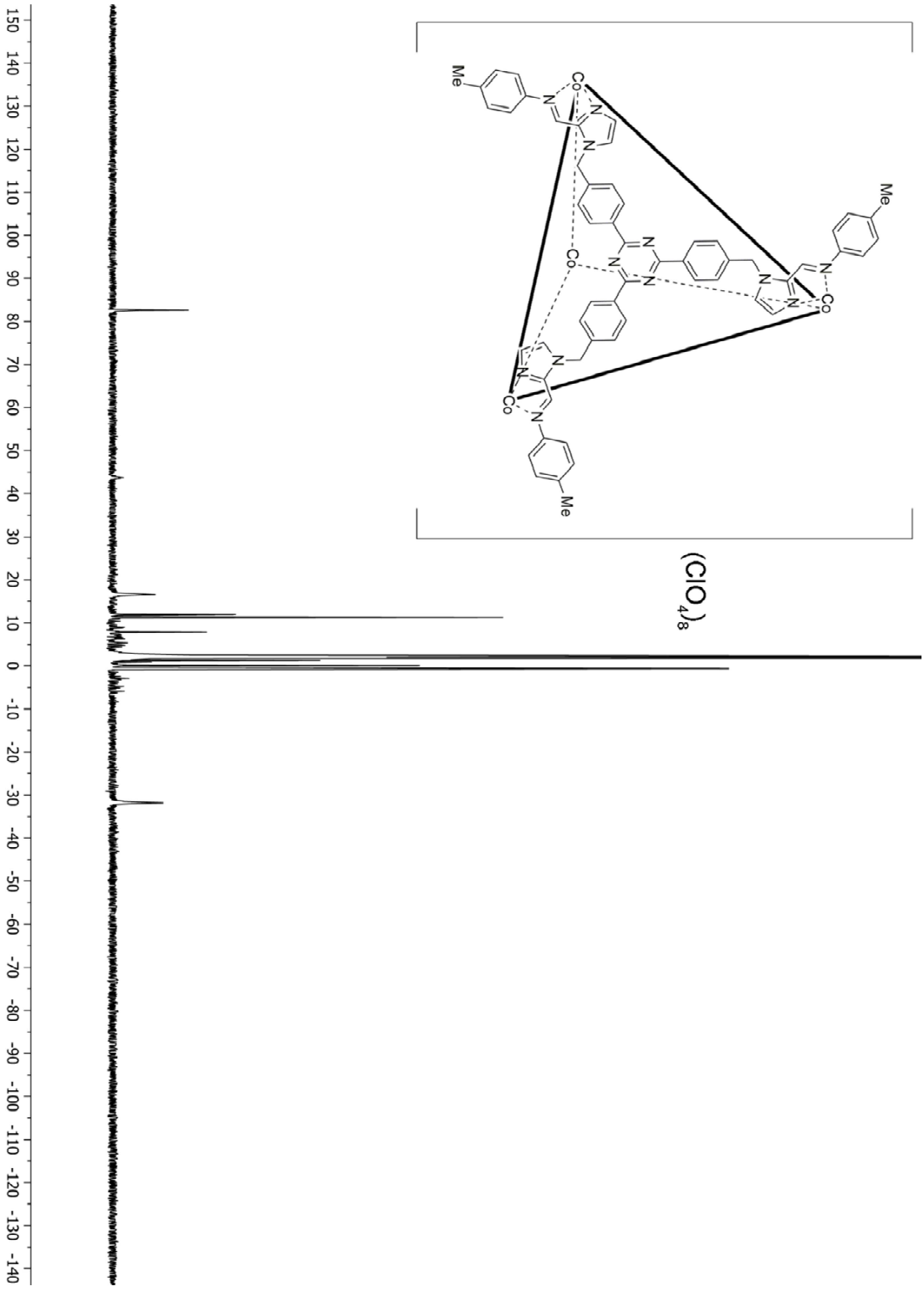

Figure 6.65: ^{1}H NMR spectrum of cage **TzIm$_3$•Co•PhMe•ClO$_4$** (CD_3CN, 400 MHz, 298

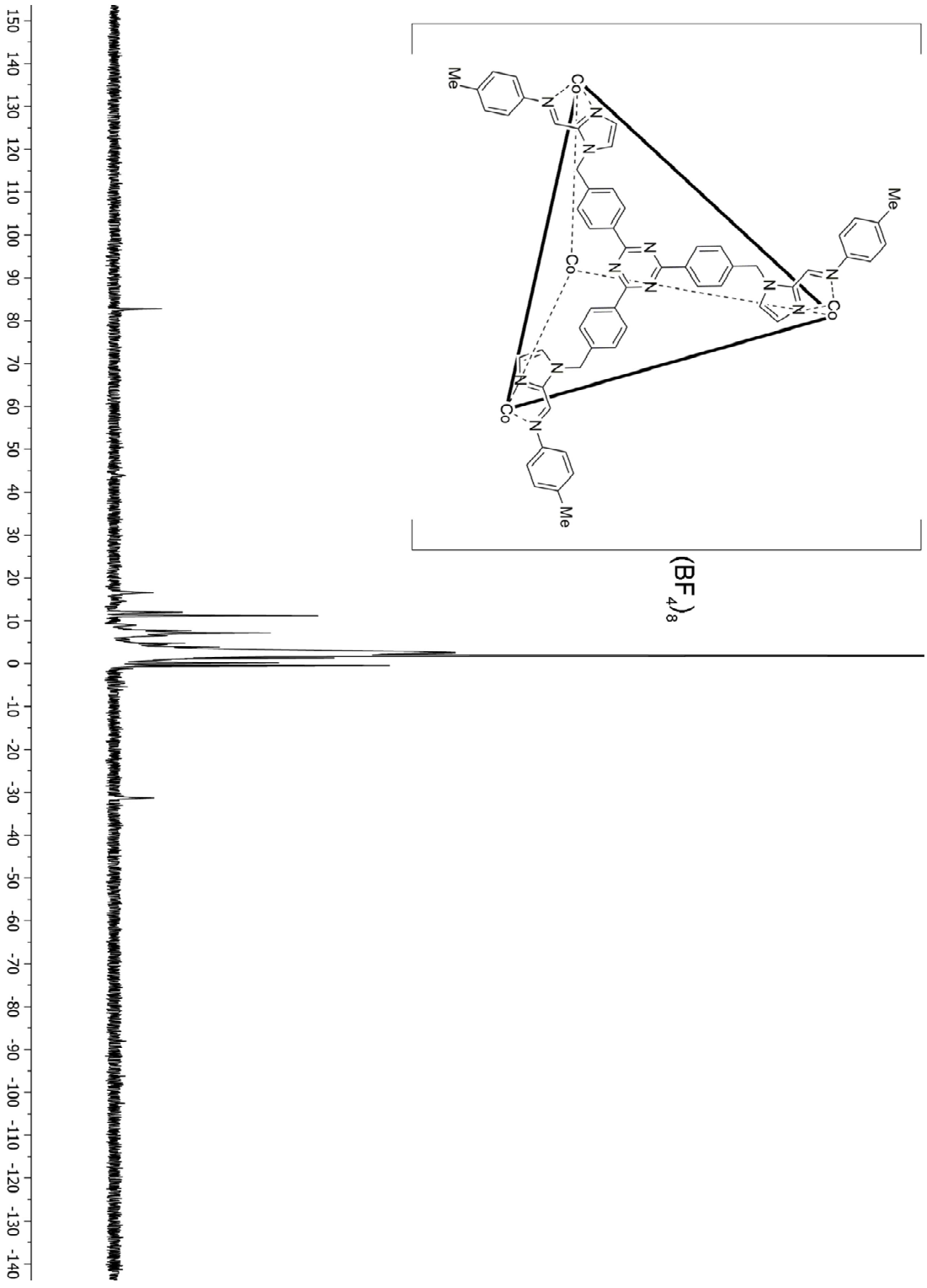

Figure 6.66: ^{1}H NMR spectrum of cage **TzIm$_3$•Co•PhMe•BF$_4$** (CD_3CN, 400 MHz, 298 K).

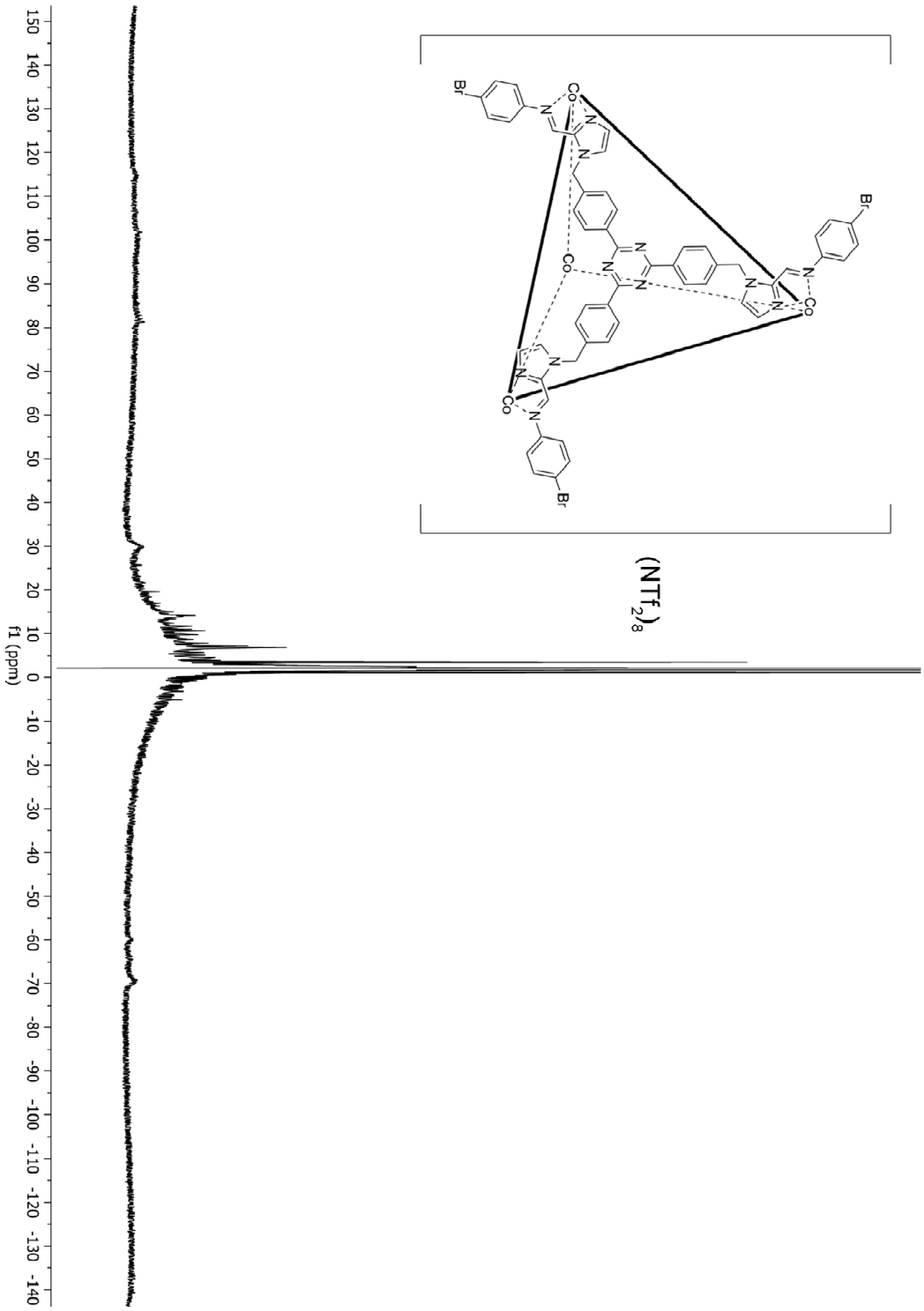

Figure 6.67: ^{1}H NMR spectrum of cage **TzIm$_3$•Co•PhMe•NTf$_2$** (CD_3CN, 400 MHz, 298 K).

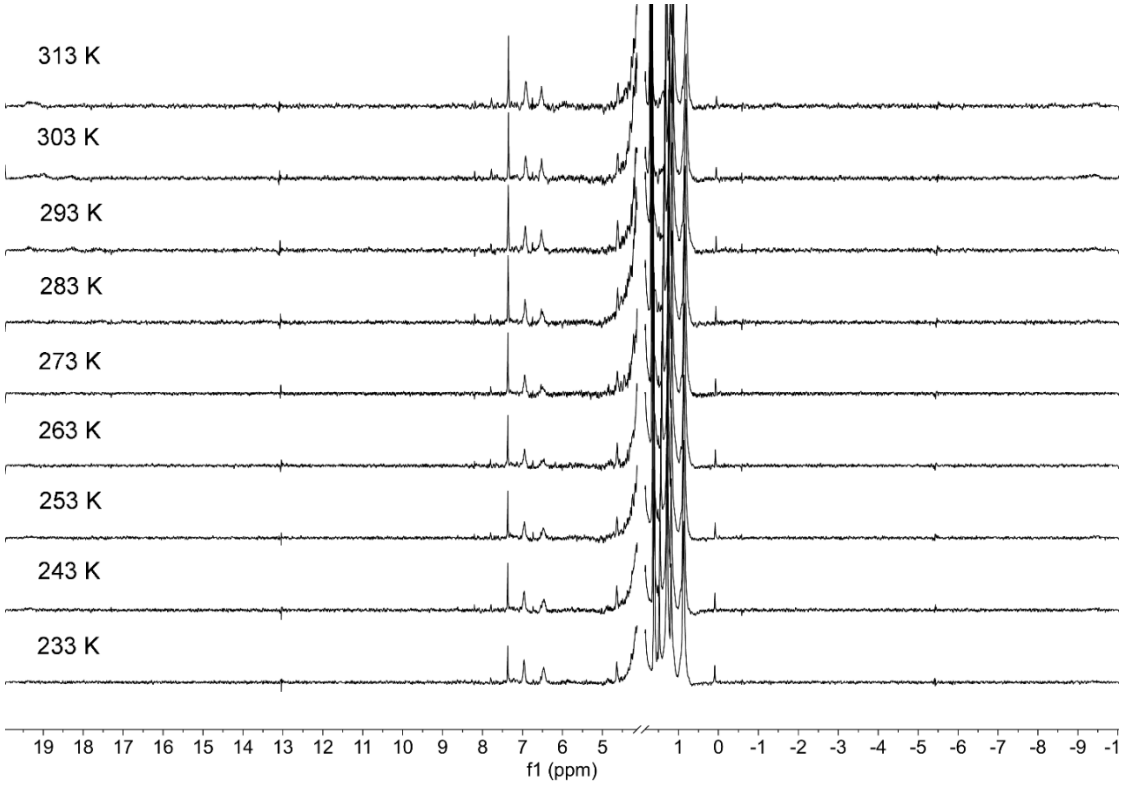

Figure 6.68: ^{1}H NMR spectra taken from 313-233 K in 10 degree increments with a dichloroethane standard for magnetic moment data of cage **XyIm$_2$•Co•PhMe•NTf$_2$** (600 MHz, CD_3CN).

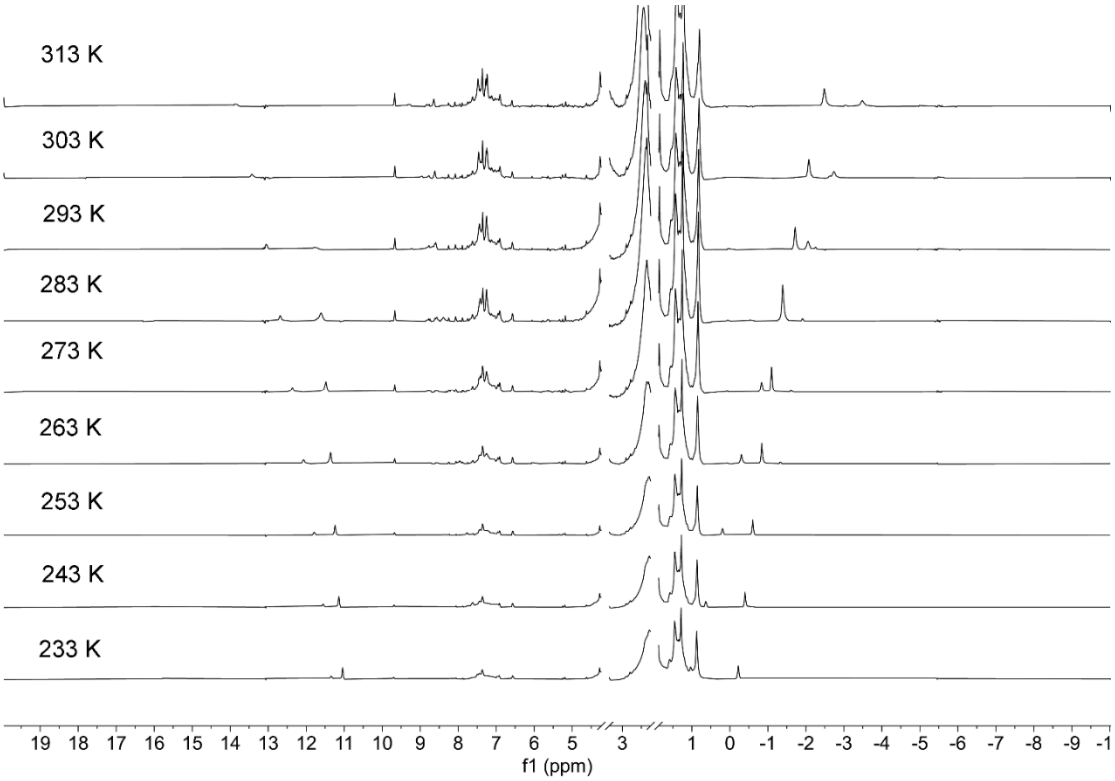

Figure 6.69: ^{1}H NMR spectra taken from 313-233 K in 10 degree increments with a dichloroethane standard for magnetic moment data of cage **TzIm$_3$•Co•PhMe•ClO$_4$** (600 MHz, CD_3CN).

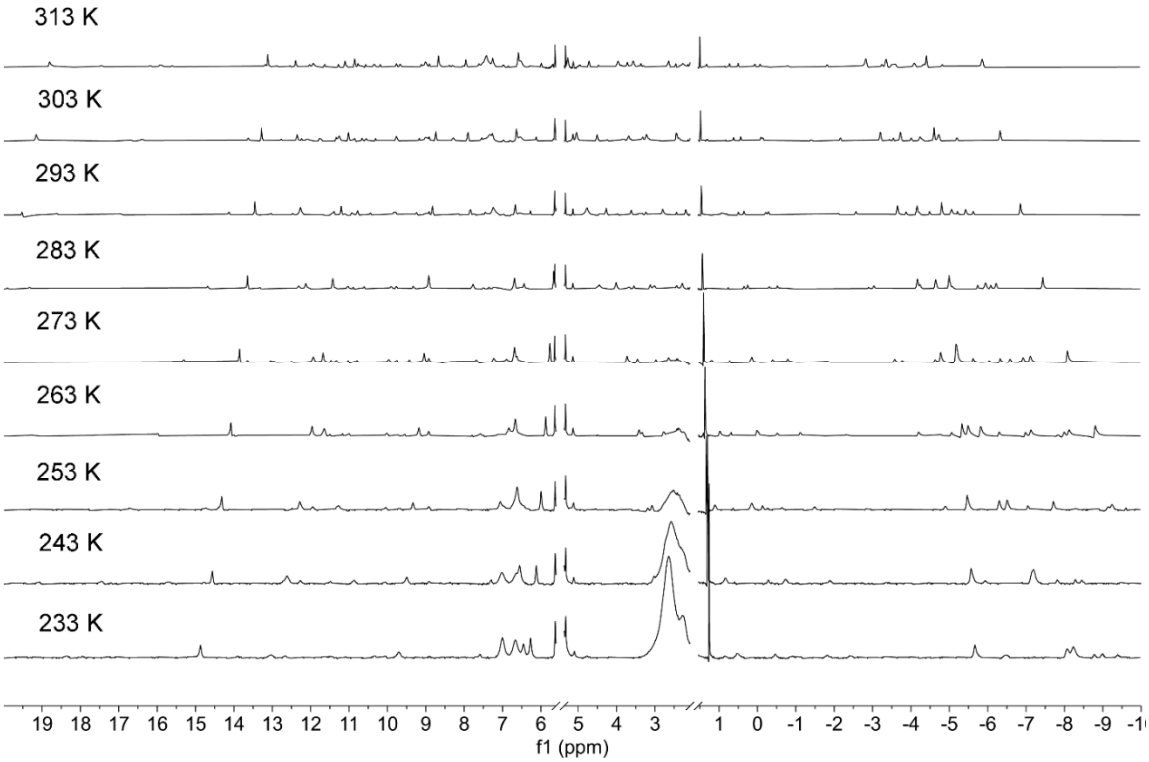

Figure 6.70: ^{1}H NMR spectra taken from 313-233 K in 10 degree increments with a dichloroethane standard for magnetic moment data of cage **TzIm$_3$•Co•PhMe•NTf$_2$** (600 MHz, CD_3CN).

Magnetic Susceptibility Experiments

Table 6.3: Molar Susceptibility (χ_M), corrected molar susceptibility ($\chi_{M'}$), and effective magnetic moment (μ_{eff}) for cages **XyIm$_2$•Co•PhMe**, **TzIm$_3$•Co•PhMe•ClO$_4$**, and **TzIm$_3$•Co•PhMe•NTf$_2$** at 293 K.

Cage	Δf (Hz)	χ_M ($cm^3\ mol^{-1}$)	$\chi_{M'}$ ($cm^3\ mol^{-1}$)	μ_{eff}
XyIm$_2$•Co•PhMe	312.72	0.0273	0.0282	8.01
TzIm$_3$•Co•PhMe•ClO$_4$	107.40	0.00187	0.00190	6.67
TzIm$_3$•Co•PhMe•NTf$_2$	326.22	0.0283	0.0292	8.15

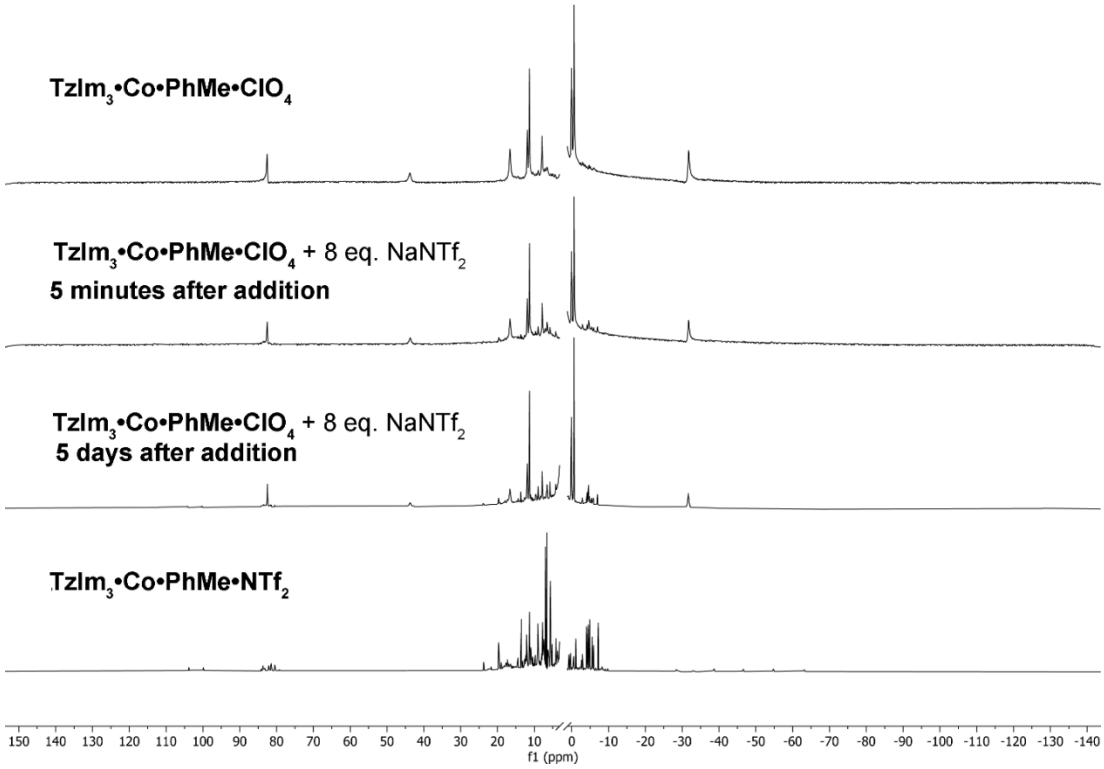

Figure 6.71: **TzIm3•Co•PhMe•ClO4** combined with 8 eq. $NaNTf_2$, reaction monitored via ^1H NMR at 5 min after addition and 5 days after addition (CD_3CN, 400 MHz, 298 K).

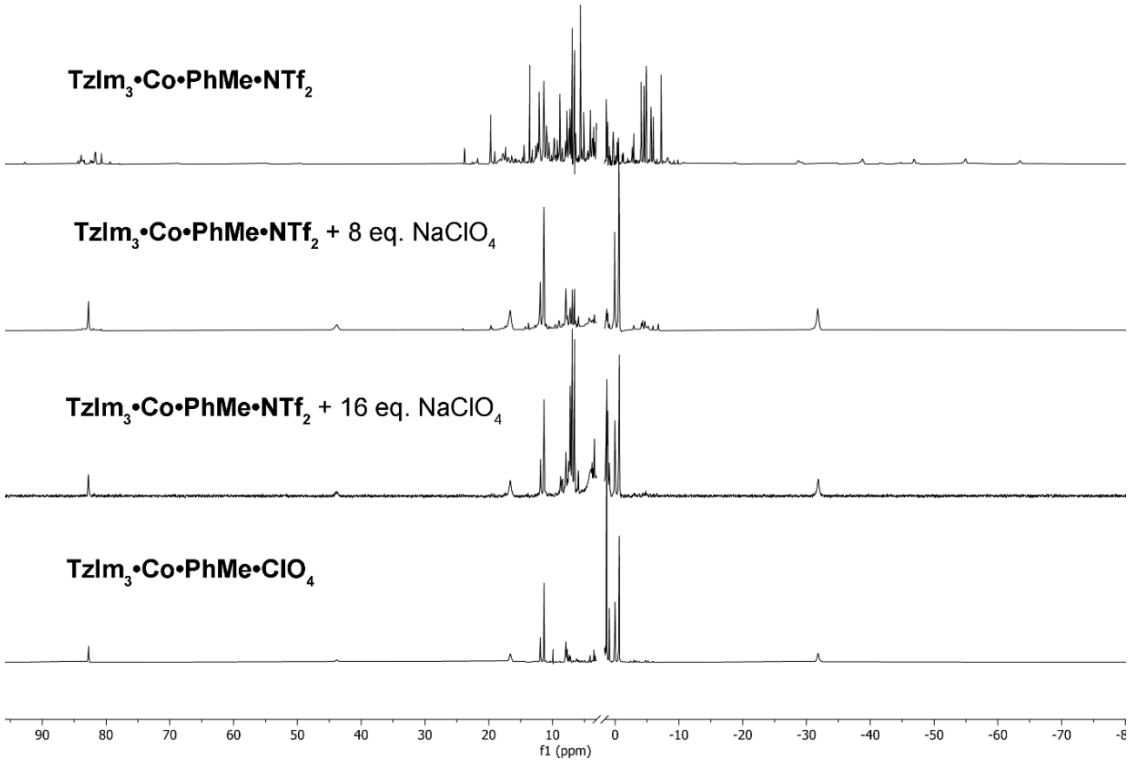

Figure 6.72: **$TzIm_3$•Co•PhMe•NTf_2** combined $NaNTf_2$ ^1H NMR spectra taken at 8 eq. $NaNTf_2$ and 16 eq. $NaNTf_2$ (CD_3CN, 400 MHz, 298 K).

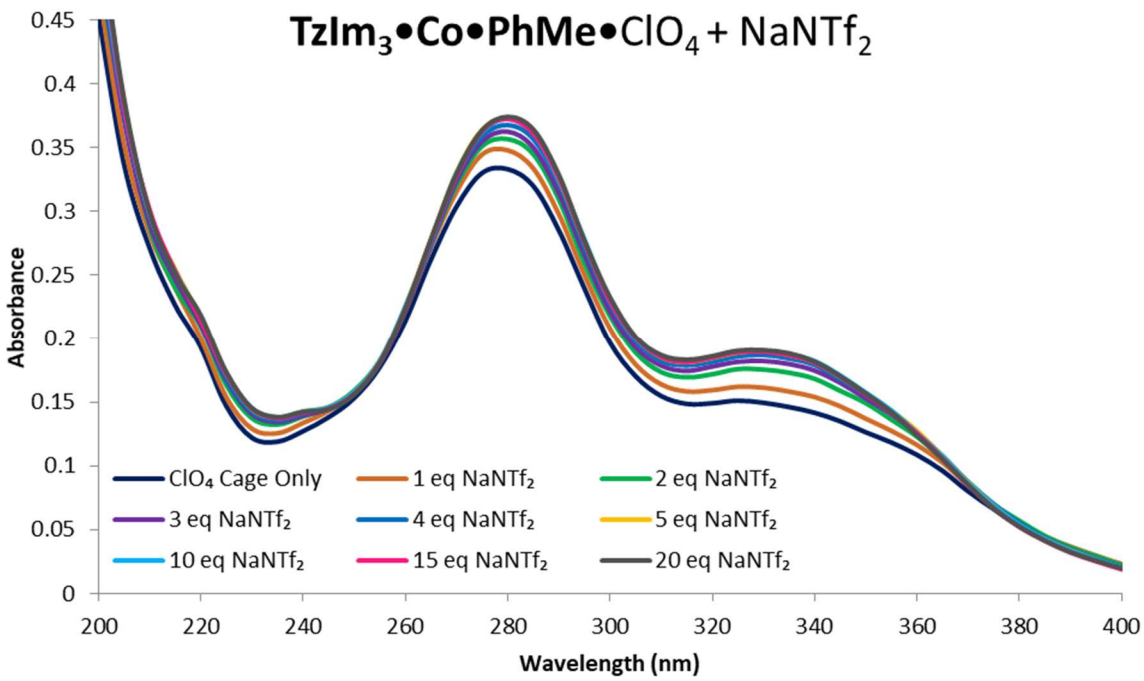

Figure 6.73: UV-Vis absorption spectrum of the titration of $NaNTf_2$ into a 5 μM solution of cage **TzIm3•Co•PhMe** in CH_3CN. $NaNTf_2$ was added in 1 μL aliquots from a 5 mM stock solution in CH_3CN.

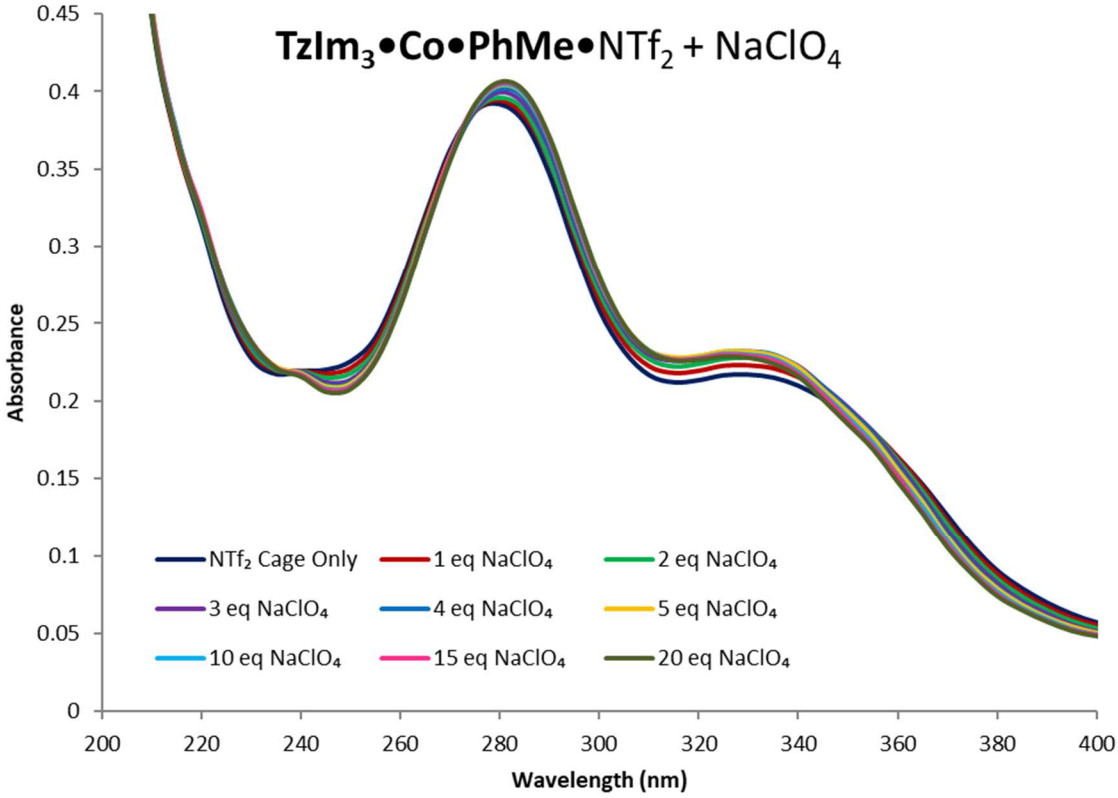

Figure 6.74: UV-Vis absorption spectrum of the titration of $NaNTf_2$ into a 5 μM solution of cage **TzIm3•Co•PhMe** in CH_3CN. $NaNTf_2$ was added in 1 μL aliquots from a 5 mM stock solution in CH_3CN.

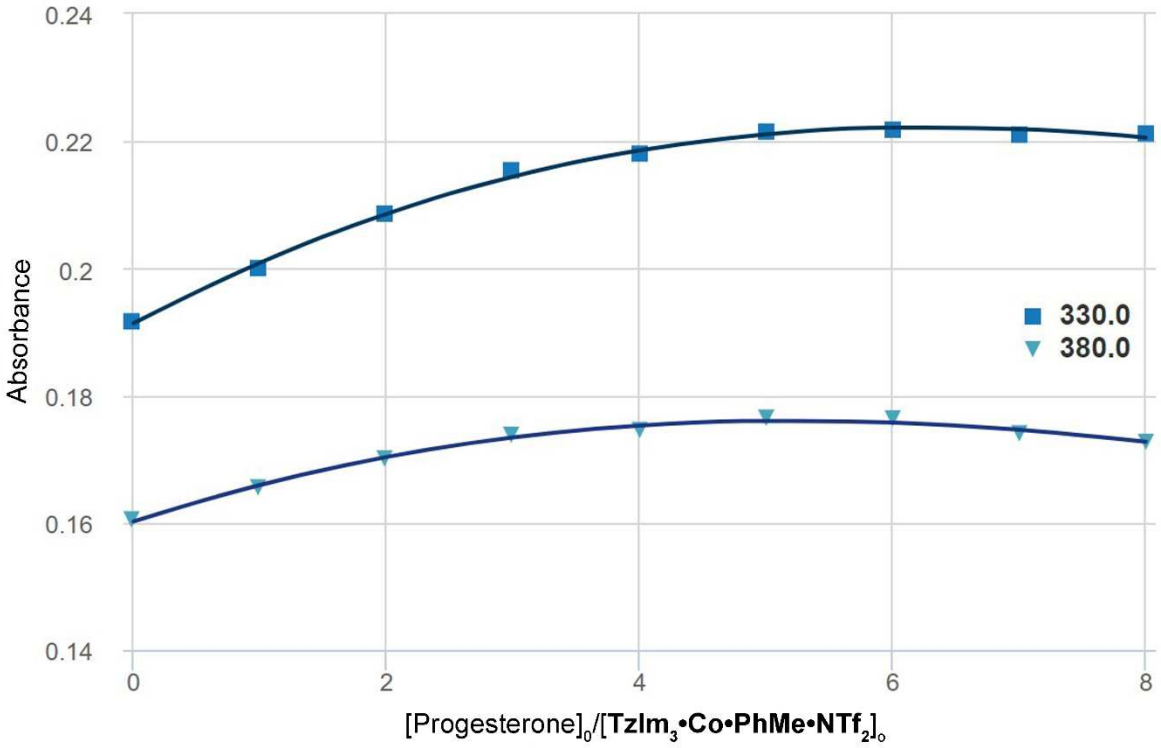

Figure 6.75: Fitting curves and plots of residual magnitude obtained when fitting the UV binding data for progesterone with cage **$TzIm_3$•Co•PhMe•NTf_2** to the 1:2 Host:Guest binding model.

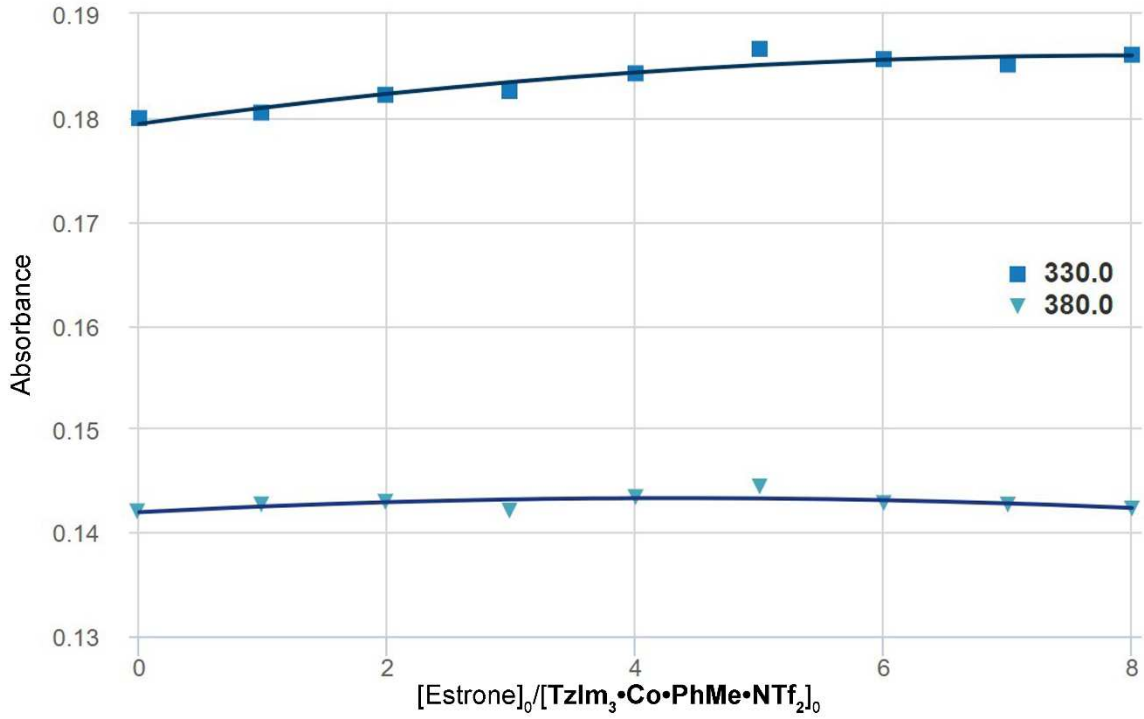

Figure 6.76: Fitting curves and plots of residual magnitude obtained when fitting the UV binding data for estrone with cage **$TzIm_3$•Co•PhMe•NTf_2** to the 1:2 Host:Guest binding model.

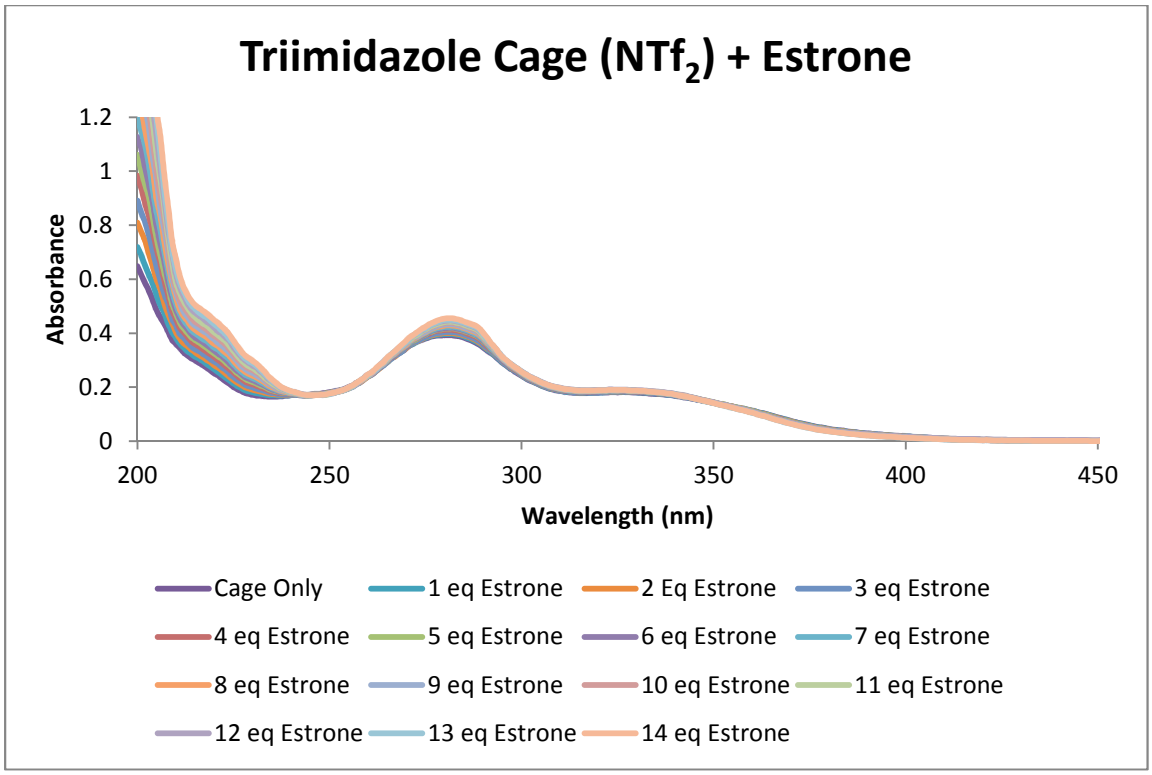

Figure 6.77: UV-Vis absorption spectrum of the titration of progesterone into a 5 μM solution of cage **TzIm$_3$•Co•PhMe•NTf$_2$** in CH_3CN. estrone was added in 1 μL aliquots from a 5 mM stock solution in CH_3CN. An energy minimized spartan model of two progesterone molecules inside cage **TzIm$_3$•Co•PhMe**.

6.9 Chapter 5 Selected Spectra

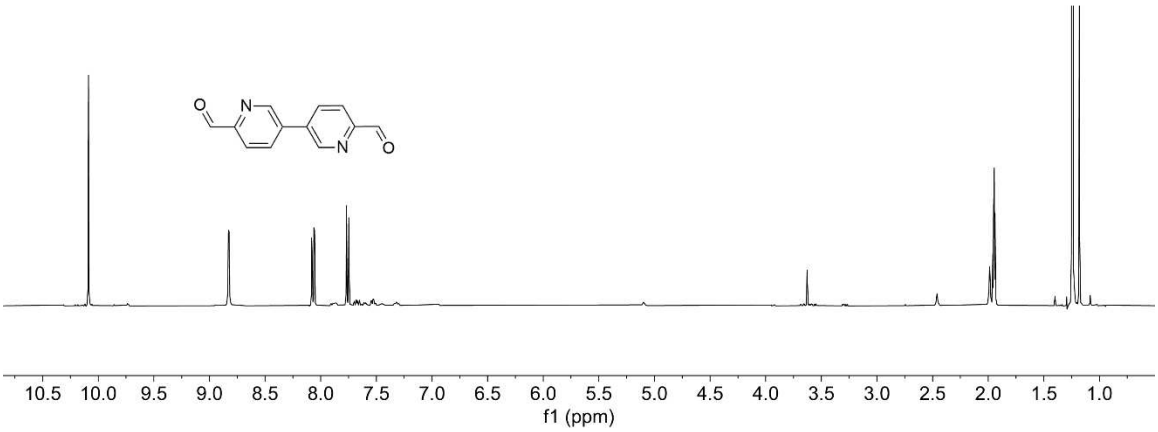

Figure 6.78: ^{1}H NMR spectrum of **DimerPyCHO** (CD_3CN, 400 MHz, 298 K).

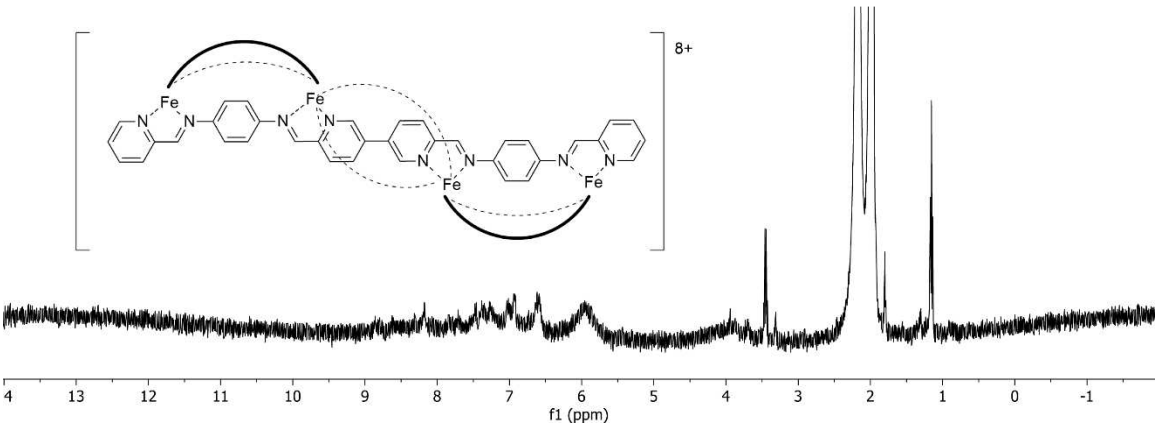

Figure 6.79: ^{1}H NMR spectrum of cage **PhN(DimerPyCHO)$_2$•Fe•PyCHO** (CD_3CN, 400 MHz, 298 K).

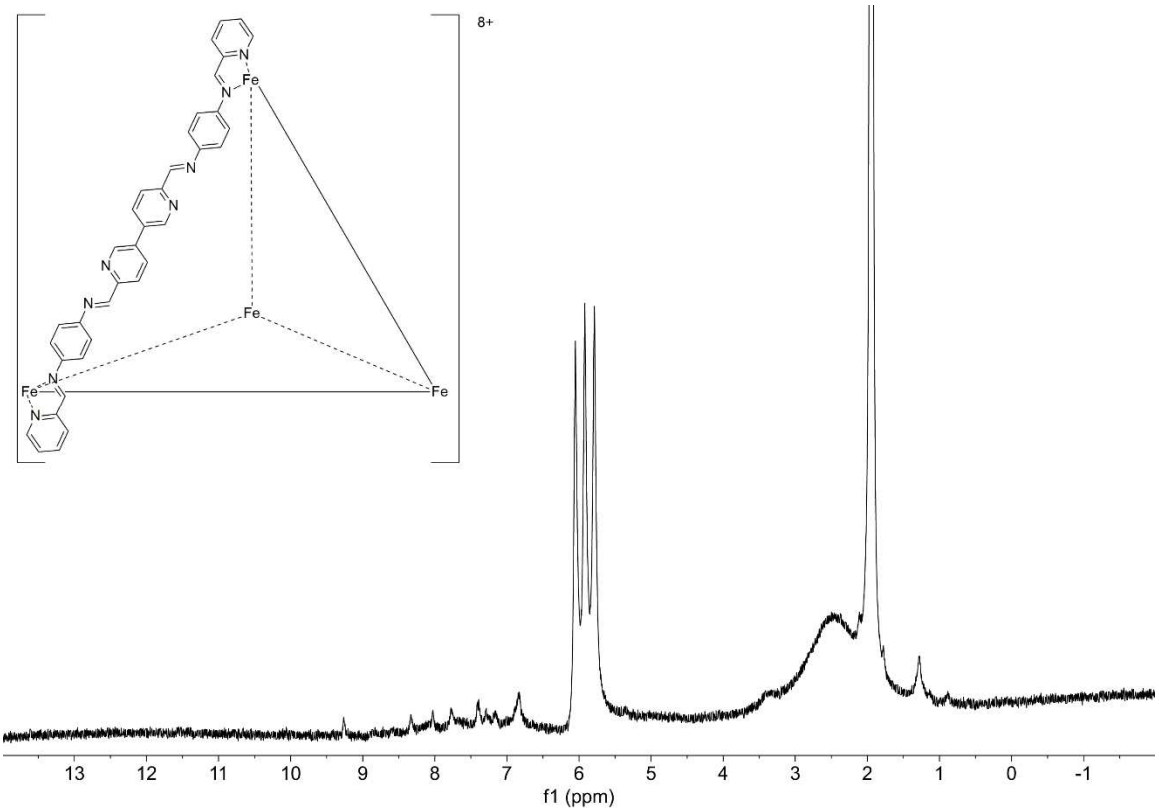

Figure 6.80: ^{1}H NMR spectrum of tetrahedral cage **PhN(DimerPyCHO)$_2$•Fe•PyCHO** (CD_3CN, 400 MHz, 298 K).

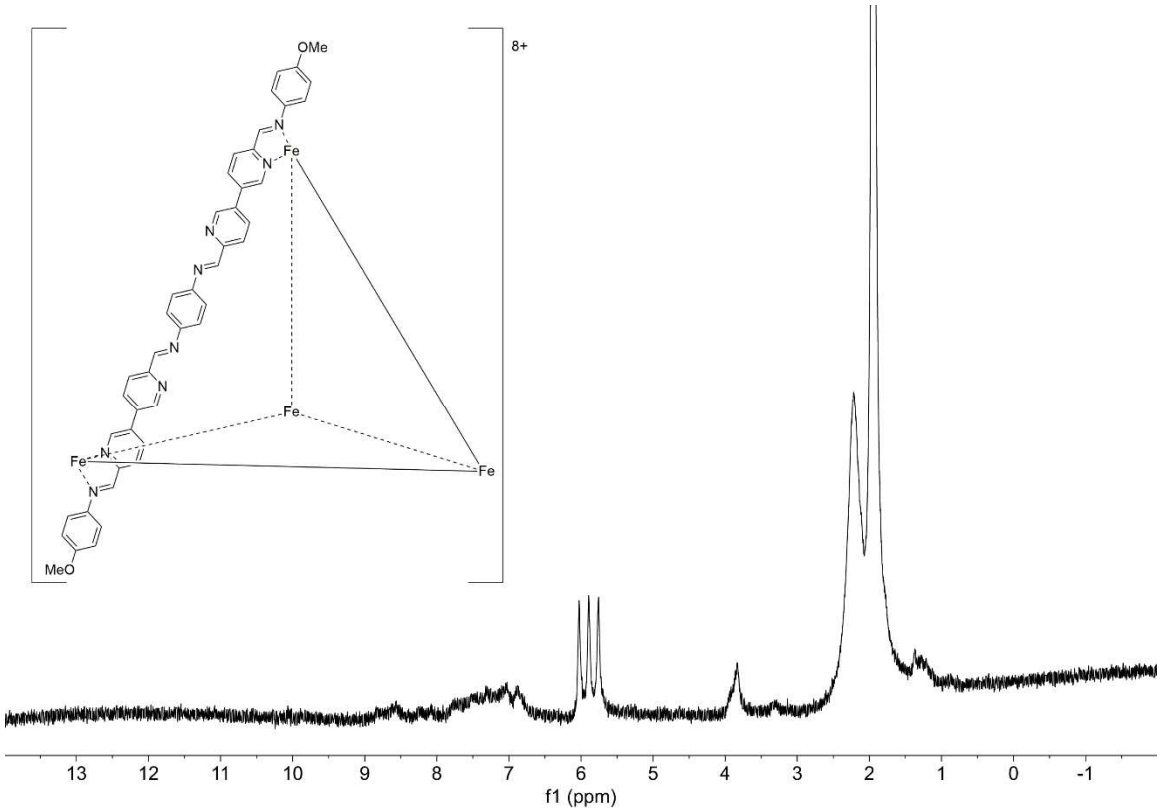

Figure 6.81: ^{1}H NMR spectrum of tetrahedral cage **DimerPyCHO(PhN)$_2$•Fe•PhOMe** (CD_3CN, 400 MHz, 298 K).

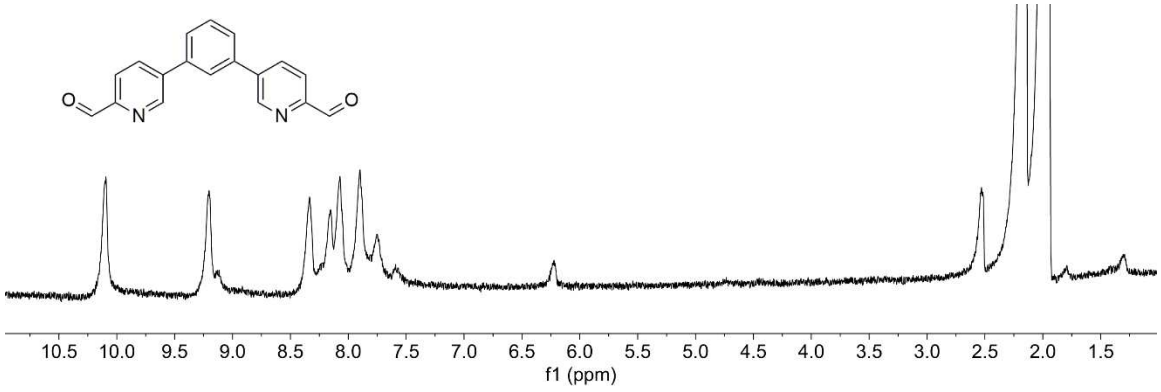

Figure 6.82: ^{1}H NMR spectrum of tetrahedral cage **1,3-Ph(PyCHO)$_2$** (CD_3CN, 400 MHz, 298 K).

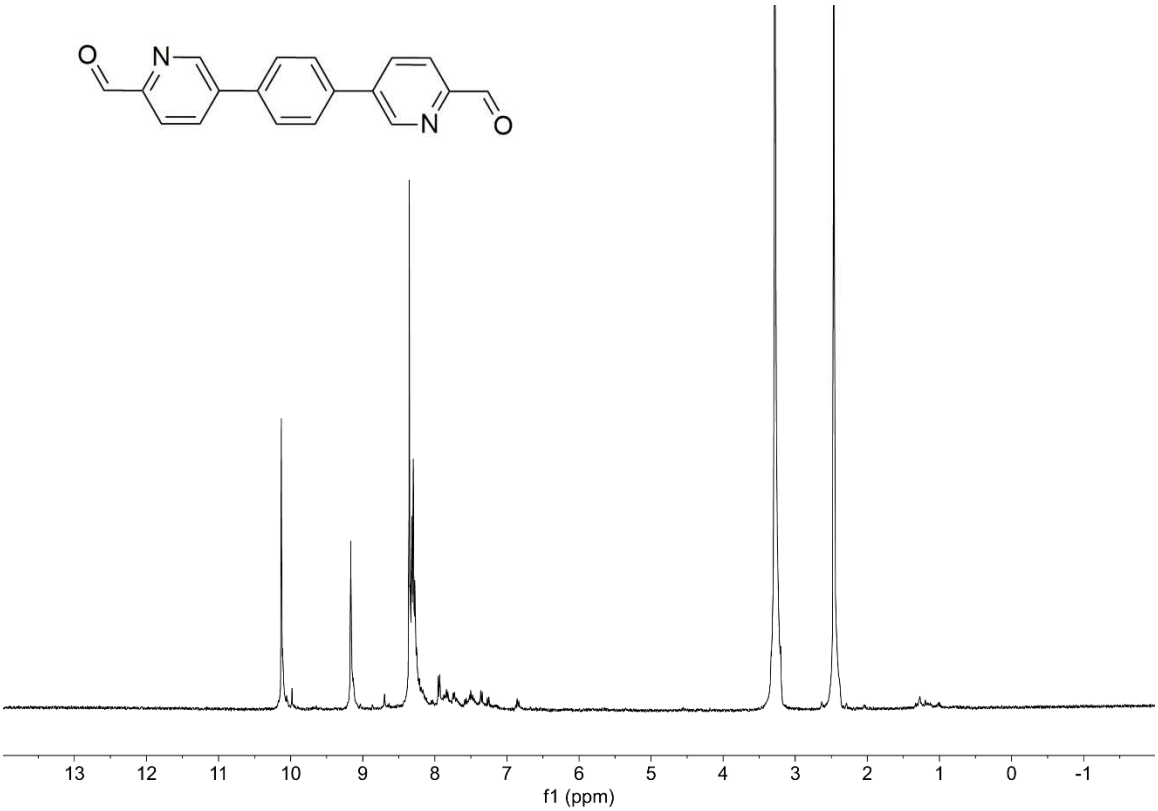

Figure 6.83: ^{1}H NMR spectrum of tetrahedral cage **1,4-Ph(PyCHO)$_2$** (CD_3CN, 400 MHz, 298 K).

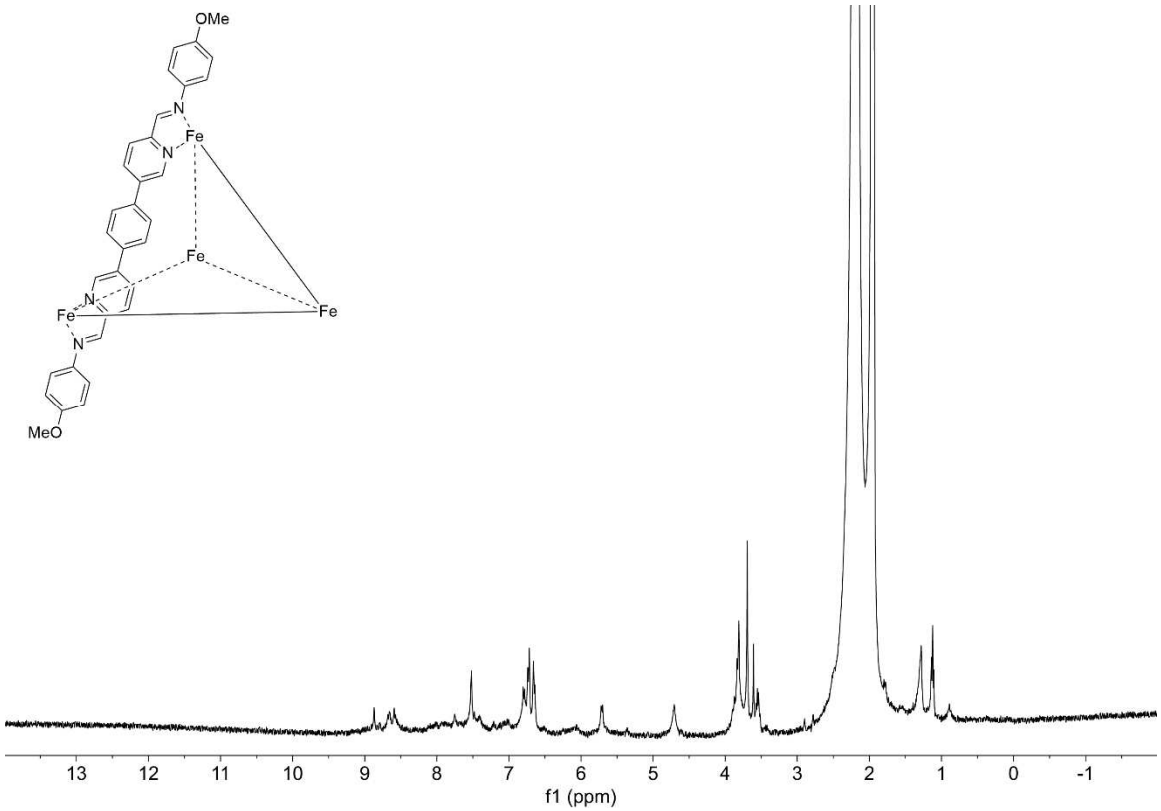

Figure 6.84: ^{1}H NMR spectrum of tetrahedral cage **1,4-Ph(PyCHO)$_2$•Fe•PhOMe** (CD_3CN, 400 MHz, 298 K).

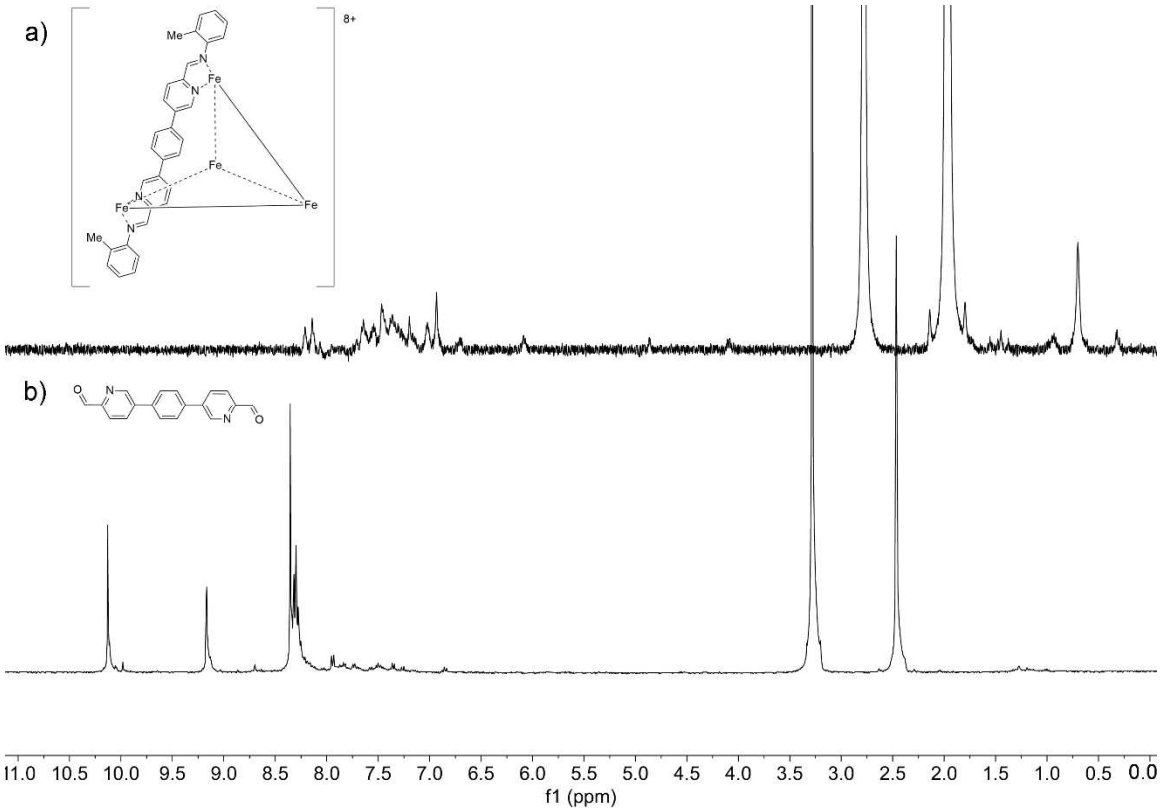

Figure 6.85: ^{1}H NMR spectra of a) tetrahedral cage **1,4-Ph(PyCHO)$_2$•Fe•*o*PhMe** and b) **1,4-Ph(PyCHO)$_2$** (CD_3CN, 400 MHz, 298 K).

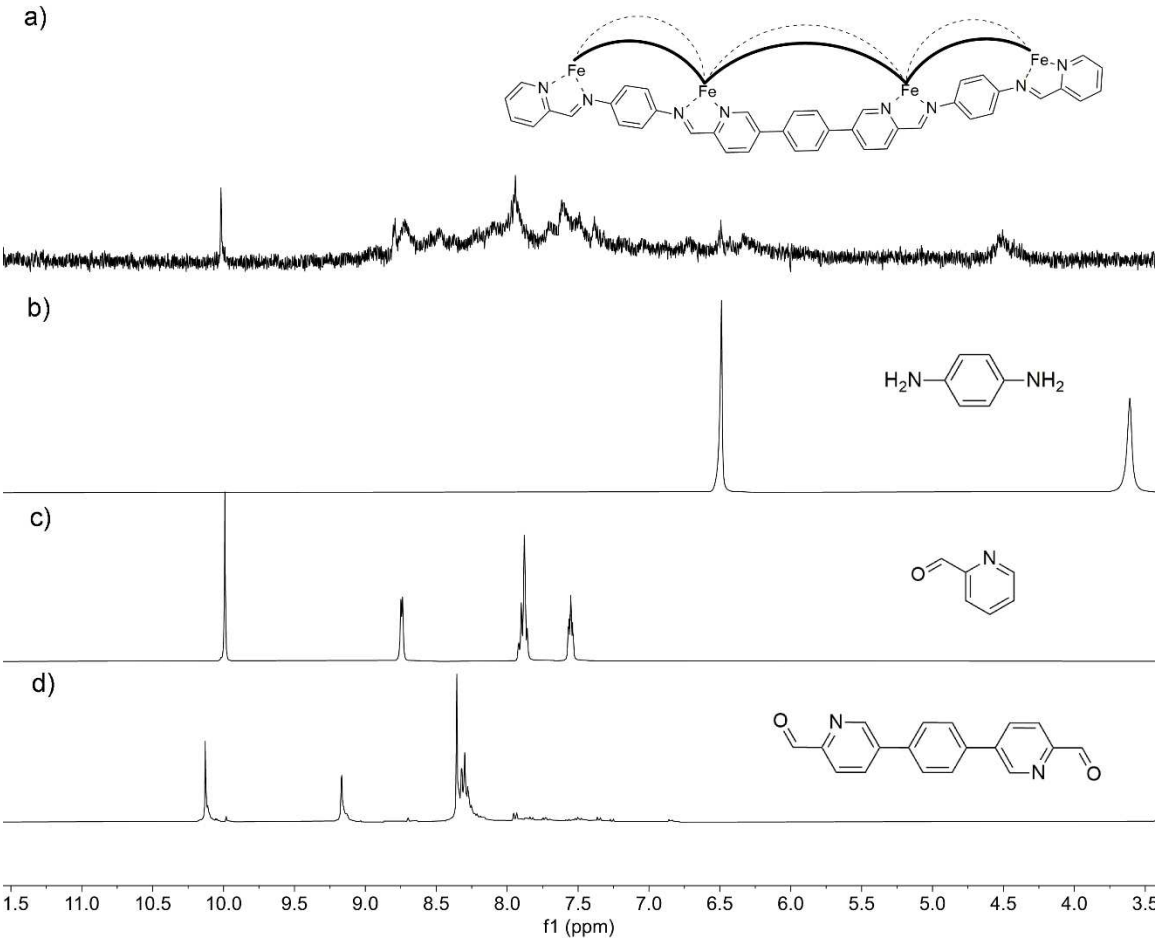

Figure 6.86: ^{1}H NMR spectra of a) cage **PhN(1,4-Ph(PyCHO)$_2$)$_2$•Fe•PyCHO**, b) phenylene diamine, c) **PyCHO**, and d) **1,4-Ph(PyCHO)$_2$** (CD_3CN, 400 MHz, 298 K).

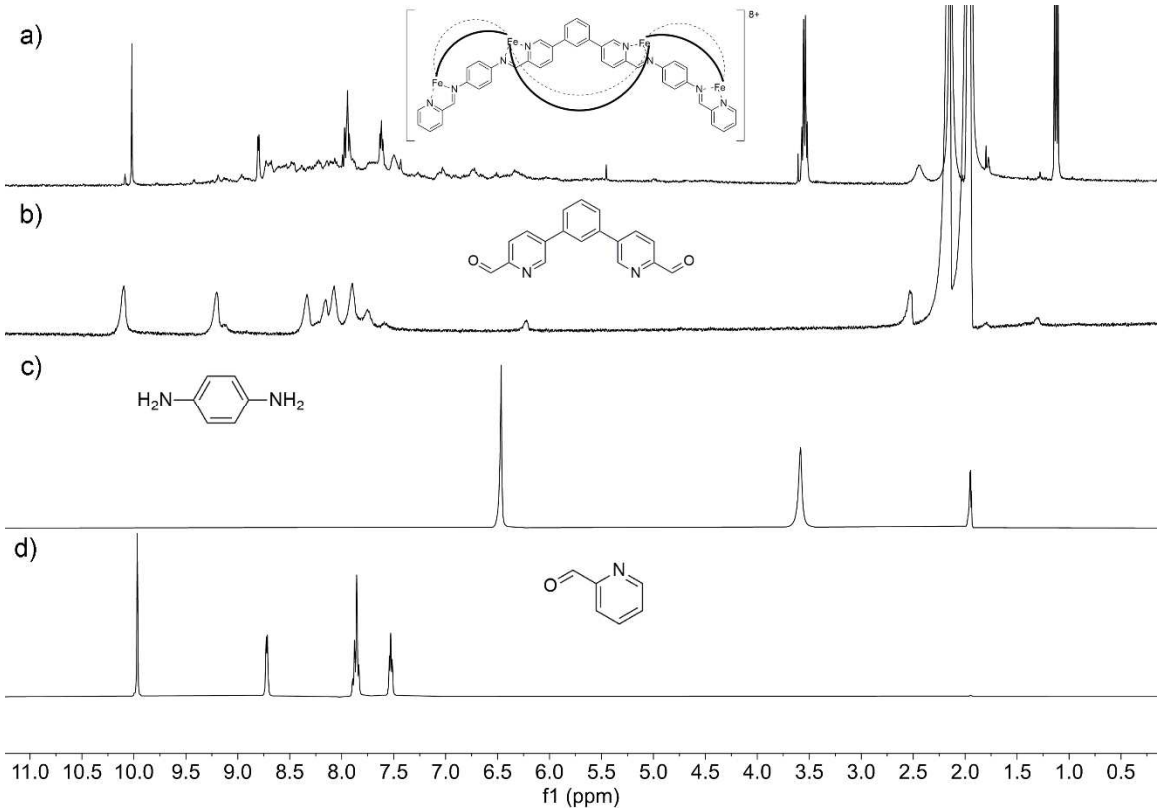

Figure 6.87: ^{1}H NMR spectra of a) cage **PhN(1,3-Ph(PyCHO)$_2$)$_2$•Fe•PyCHO**, b) **1,3-Ph(PyCHO)$_2$**, c) phenylene diamine, and d) **PyCHO**, (CD_3CN, 400 MHz, 298 K).

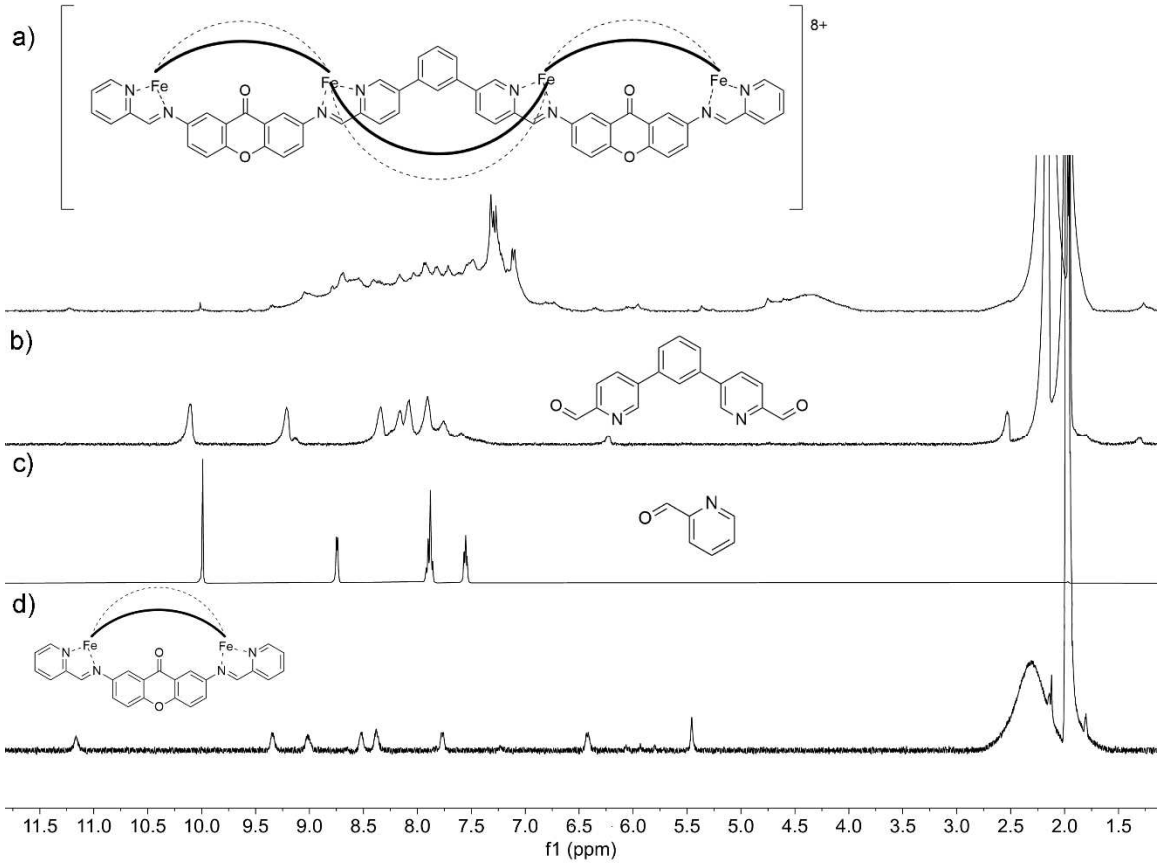

Figure 6.88: ^{1}H NMR spectra of a) cage **XO(1,3-Ph(PyCHO)$_2$)$_2$•Fe•PyCHO**, b) **1,3-Ph(PyCHO)$_2$**, c) phenylene diamine, and d) **PyCHO**, (CD_3CN, 400 MHz, 298 K).

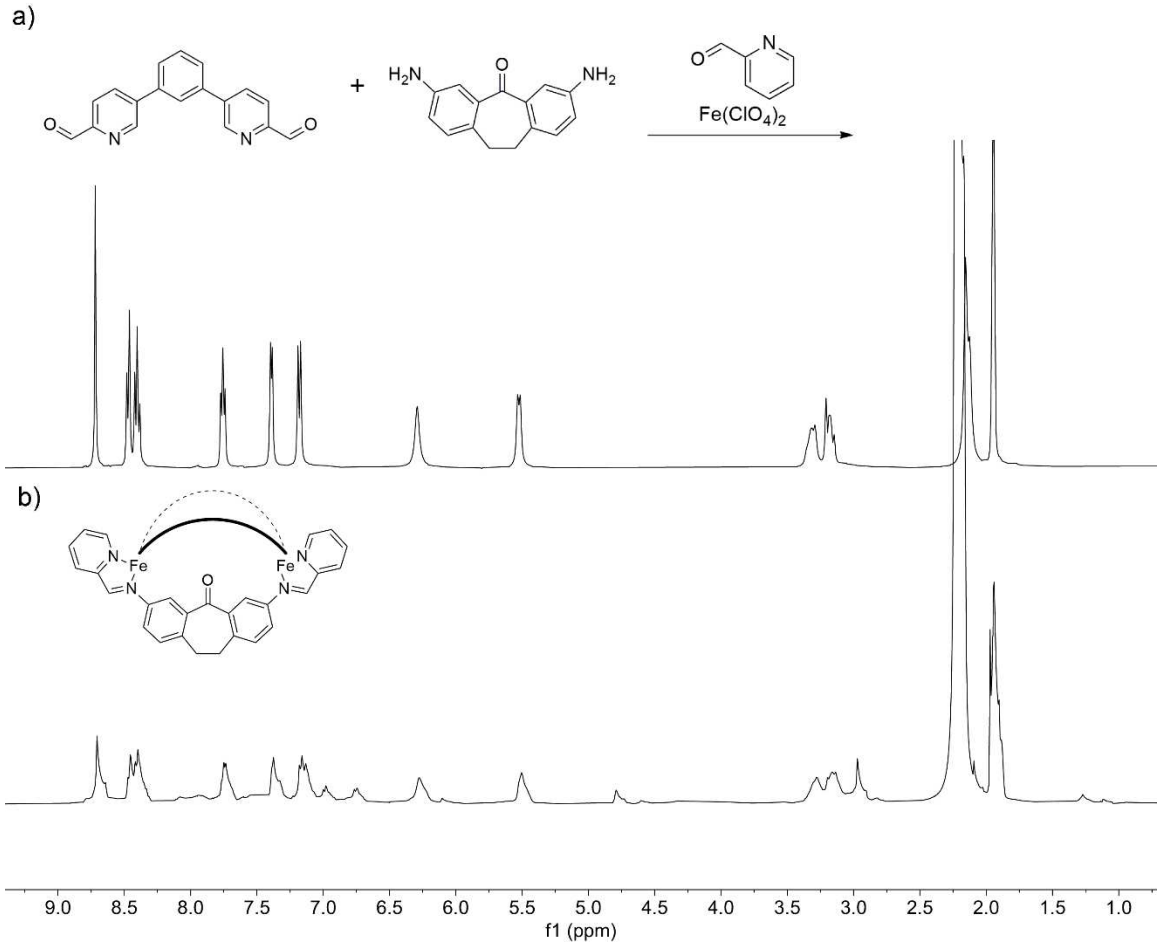

Figure 6.89: ^{1}H NMR spectra of a) attempted cage **SO(1,3-Ph(PyCHO)$_2$)$_2$•Fe•PyCHO** and b) **SO Fe•PyCHO** (CD_3CN, 400 MHz, 298 K).

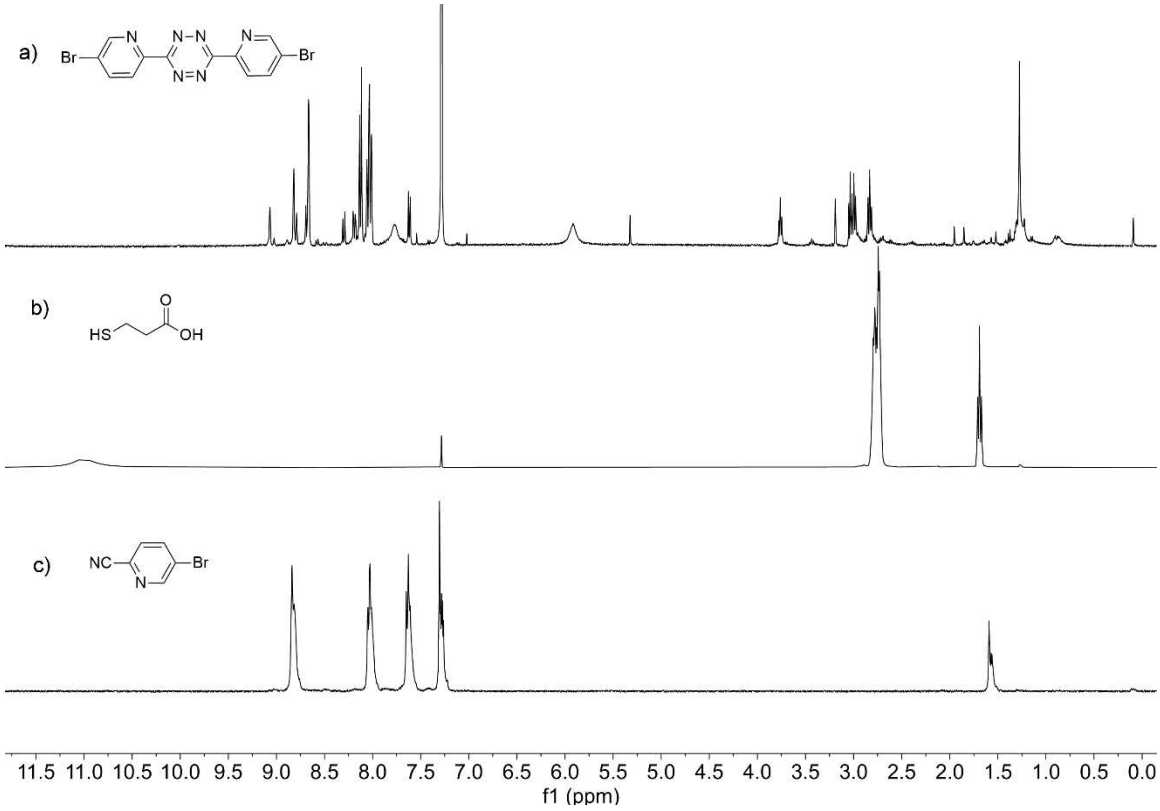

Figure 6.90: ^{1}H NMR spectra of a) tetrazine **BrPy•Tet•BrPy** and b) mercaptopropionic acid **BrPyCN** ($CDCl_3$, 400 MHz, 298 K).

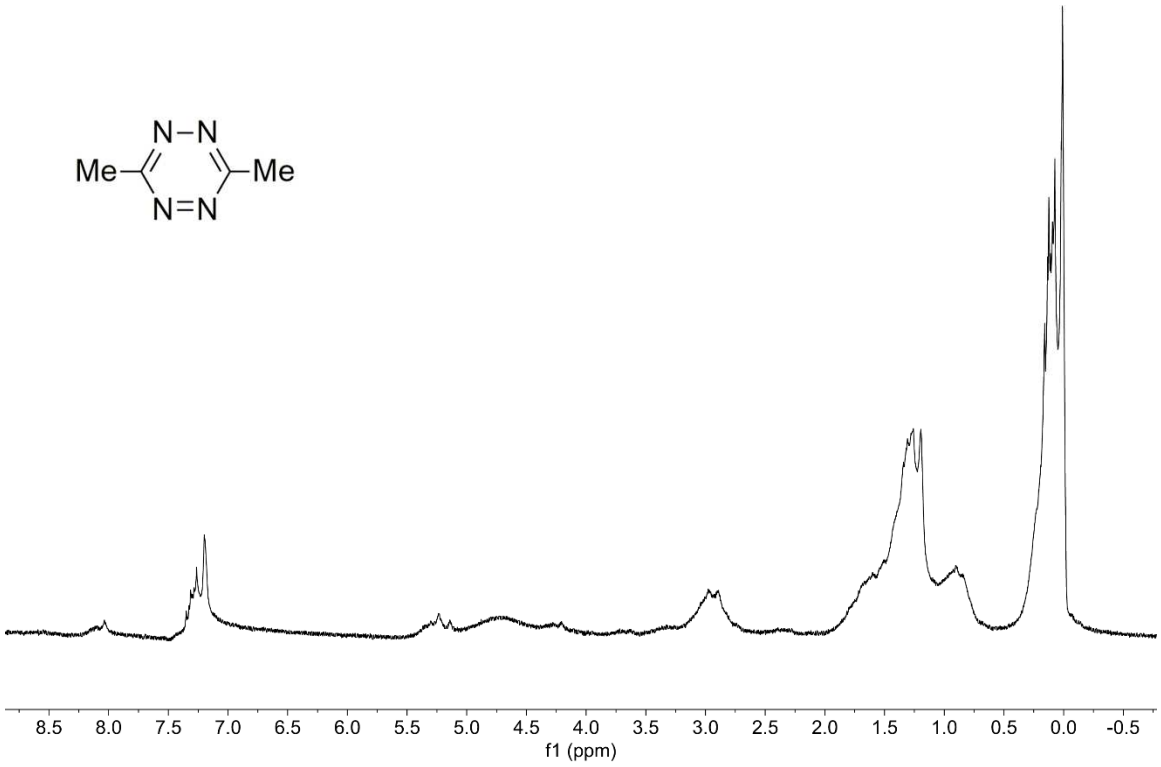

Figure 6.91: ^{1}H NMR spectra of tetrazine **Me•Tet•Me** ($CDCl_3$, 400 MHz, 298 K).

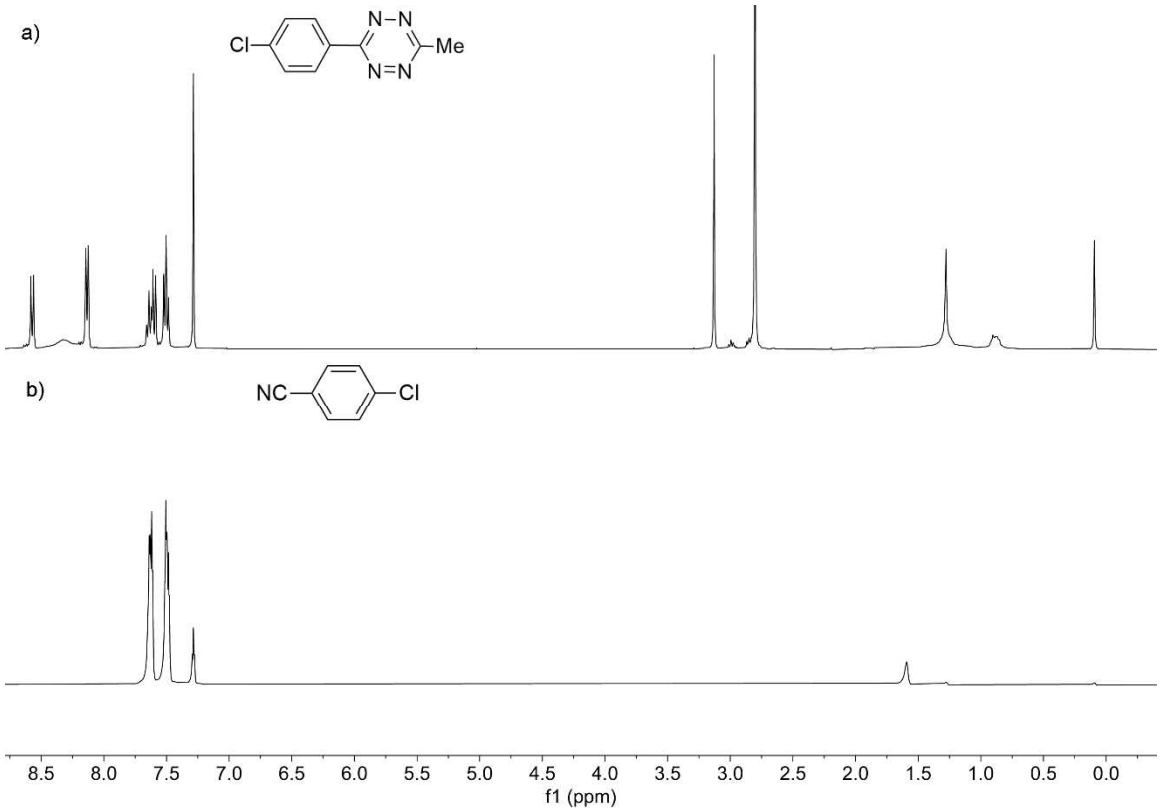

Figure 6.92: ^{1}H NMR spectra of a) tetrazine **BnCl•Tet•Me** and b) **BnCl** ($CDCl_3$, 400 MHz, 298 K).

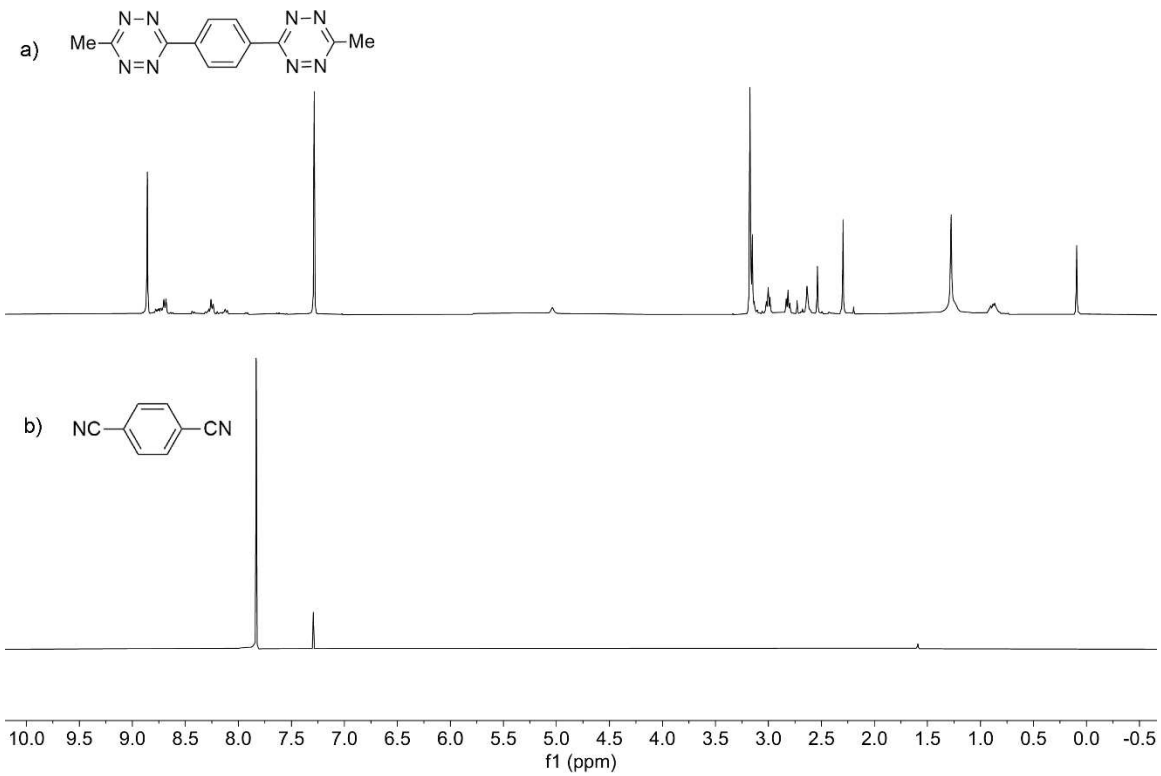

Figure 6.93: ^{1}H NMR spectra of a) tetrazine **Me•Tet•TP•Tet•Me** and b) **TPCN** ($CDCl_3$, 400 MHz, 298 K).

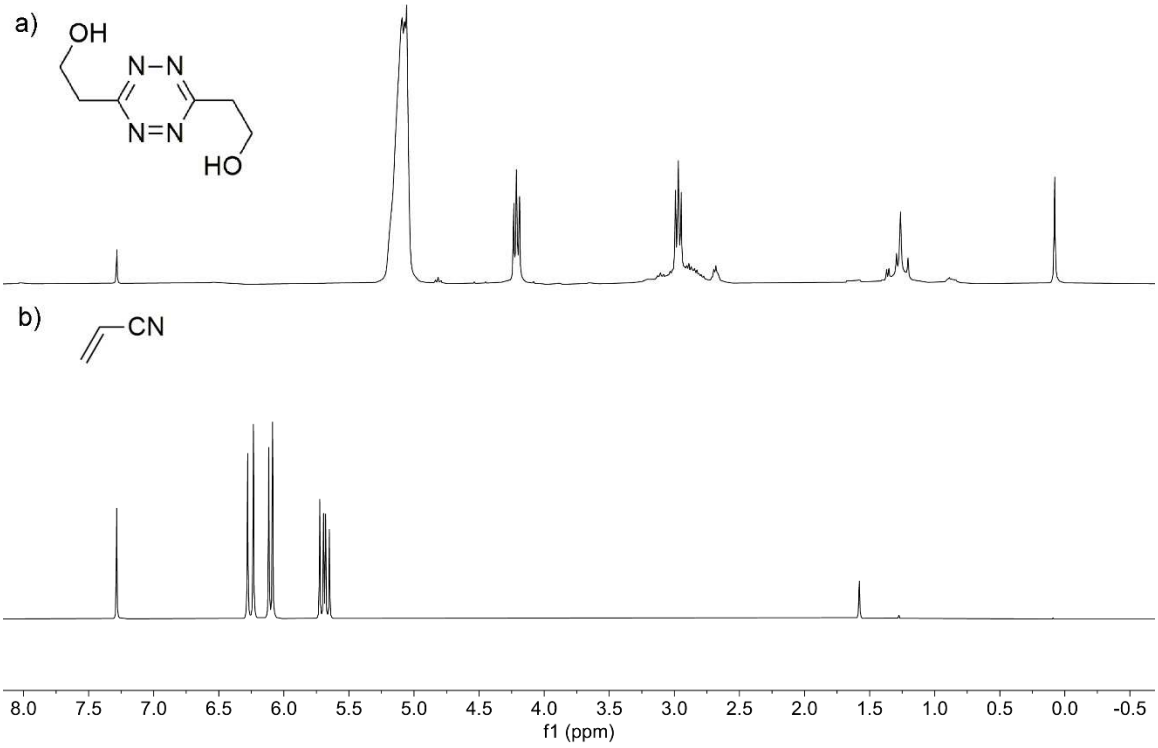

Figure 6.94: ^{1}H NMR spectra of a) tetrazine **V•Tet•V** which had reacted with the mercaptopropionic acid to form **CH_2OH•Tet•CH_2OH** and b) **VCN** ($CDCl_3$, 400 MHz, 298 K).

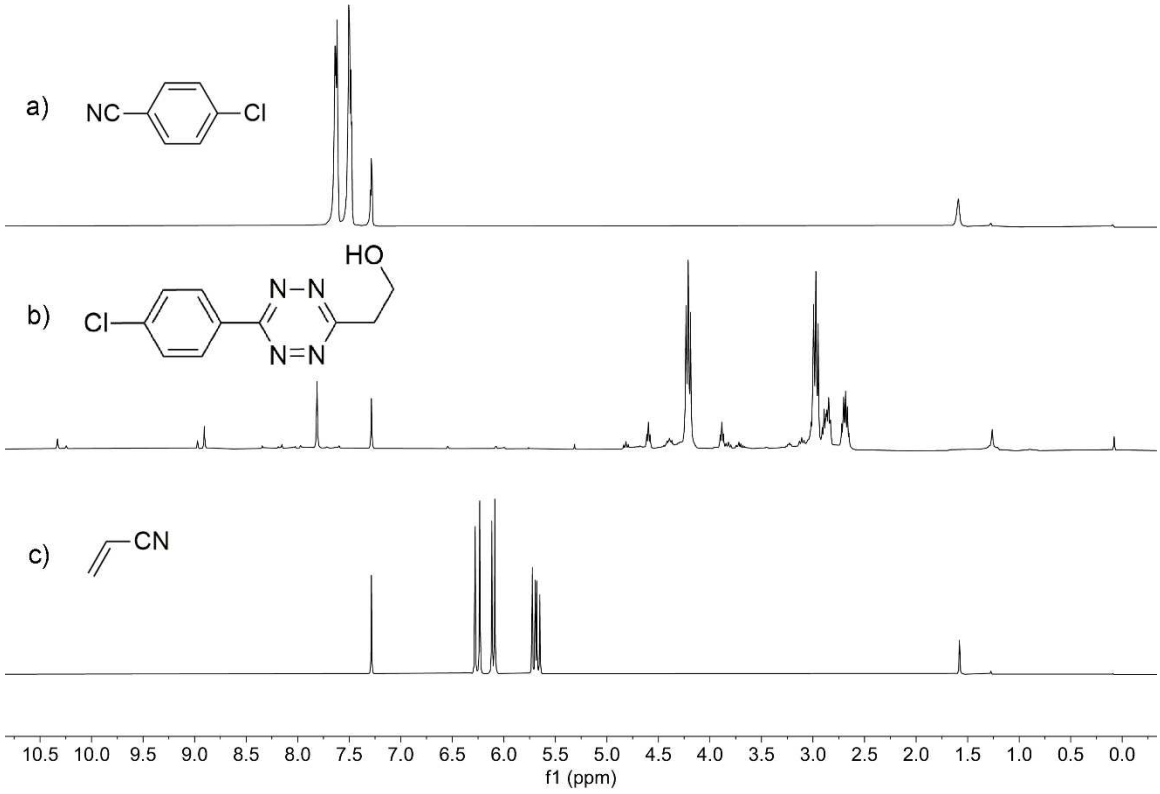

Figure 6.95: ^{1}H NMR spectra of a) **BnClCN**, b) tetrazine **BnCl•Tet•V** which reacted with mercaptopropionic acid to form **BnCl•Tet•Ch$_2$OH**, and c) **VCN** ($CDCl_3$, 400 MHz, 298 K).

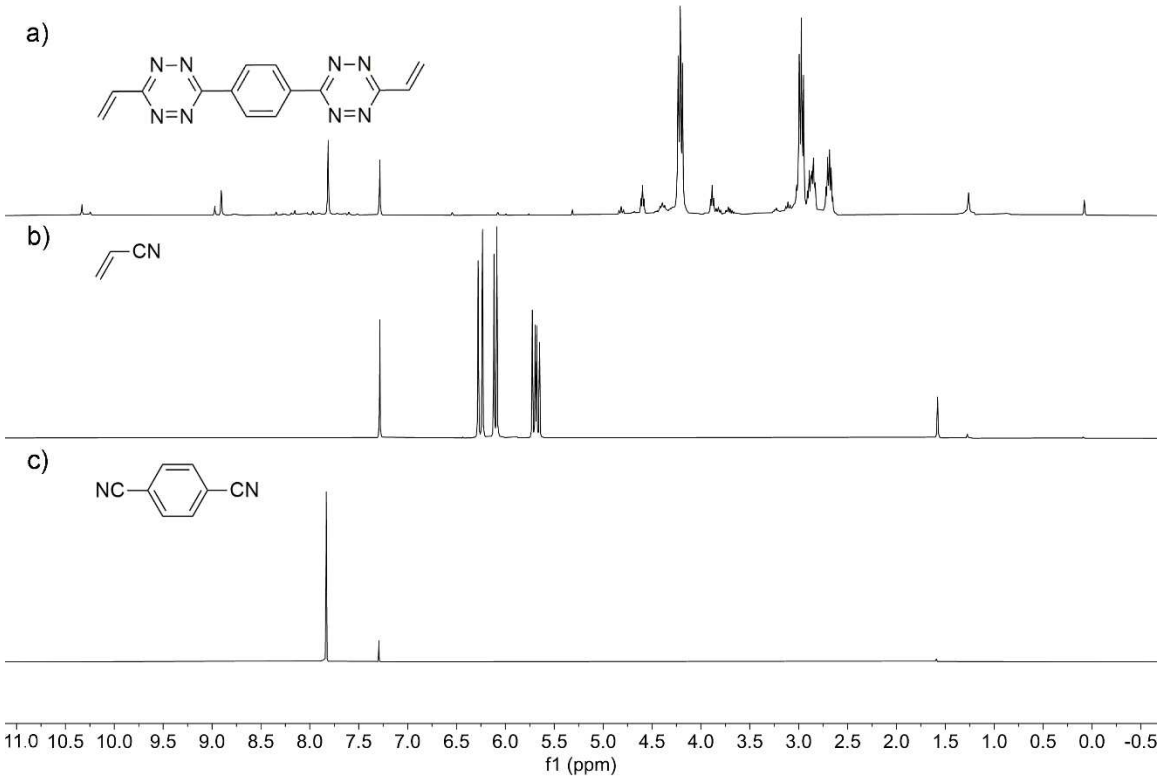

Figure 6.96: ^{1}H NMR spectra of a) tetrazine **V•Tet•TP•Tet•V**, b) **VCN** and c) **TPCN** ($CDCl_3$, 400 MHz, 298 K).

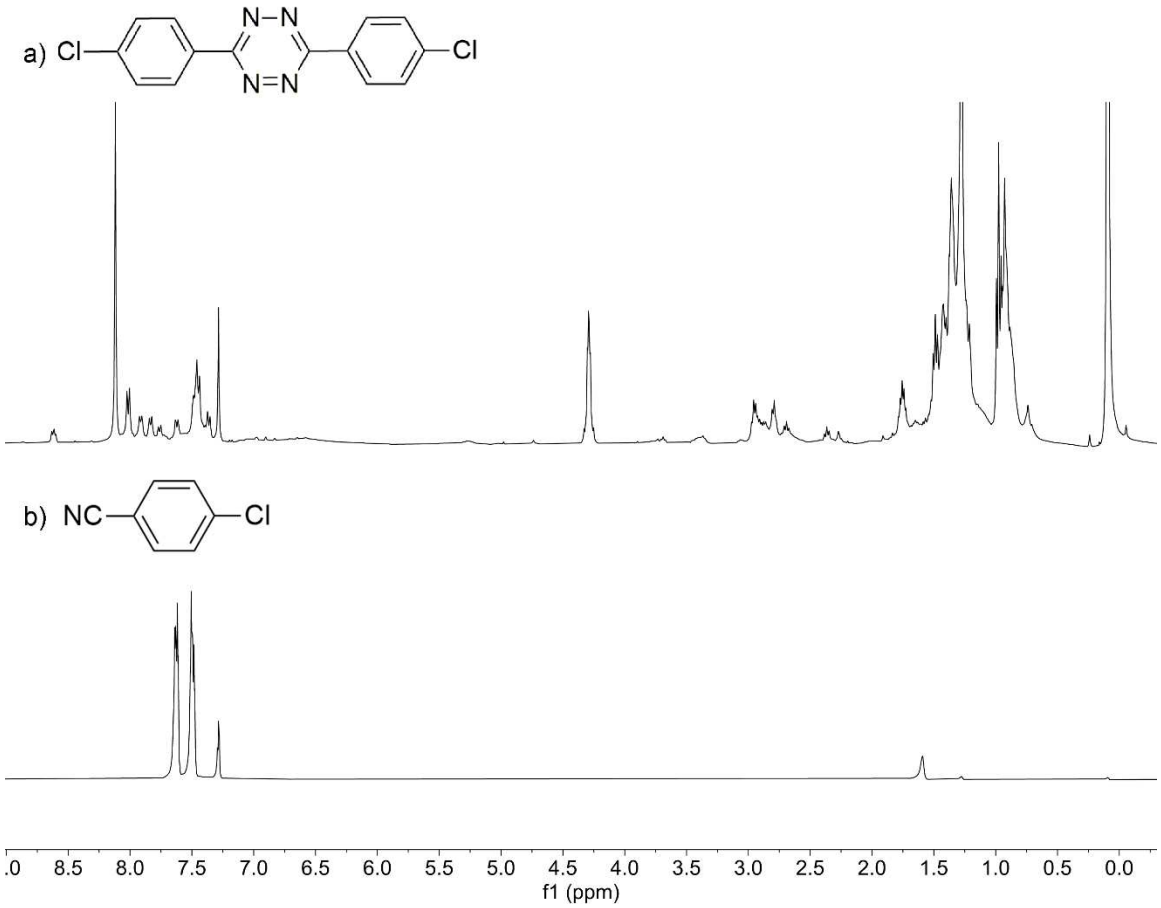

Figure 6.97: ^{1}H NMR spectra of a) tetrazine **BnCl•Tet•BnCl** and b) **BnClCN** ($CDCl_3$, 400 MHz, 298 K).

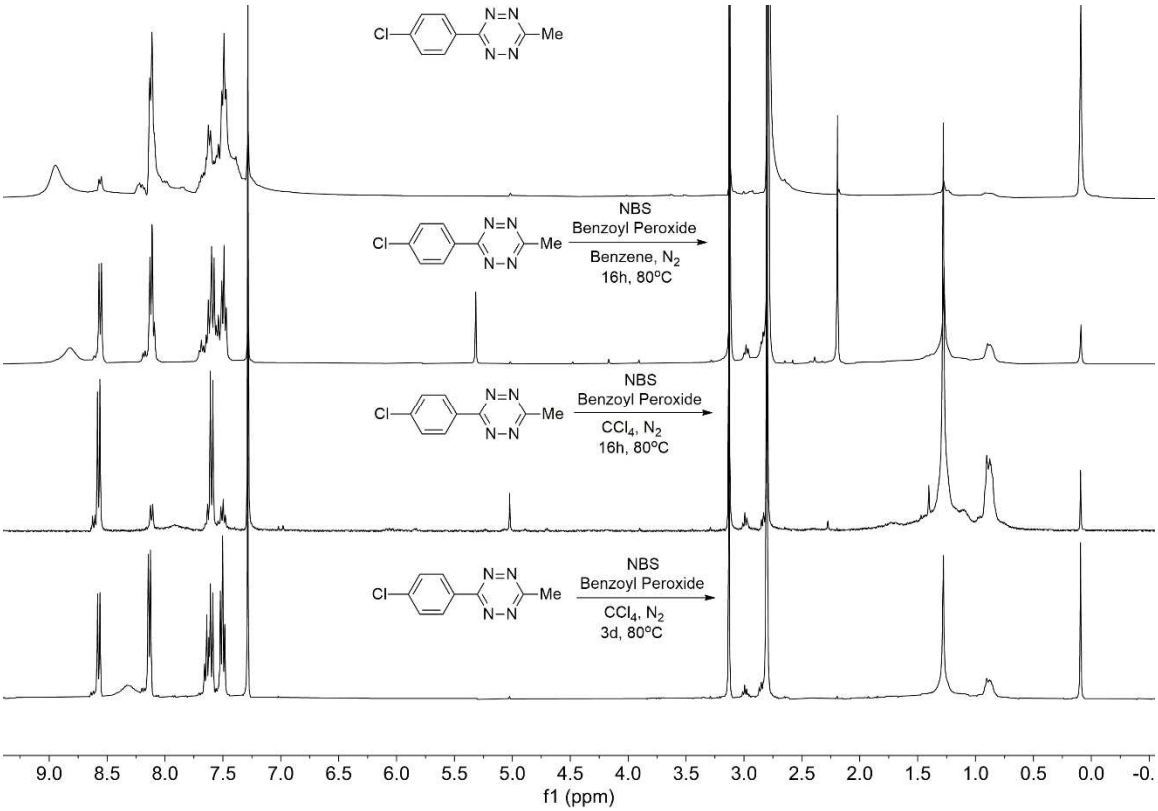

Figure 6.98: ^{1}H NMR spectra of a) tetrazine **BnCl•Tet•Me** and b-d) attempted bromination reactions of **BnClCN**. ($CDCl_3$, 400 MHz, 298 K).

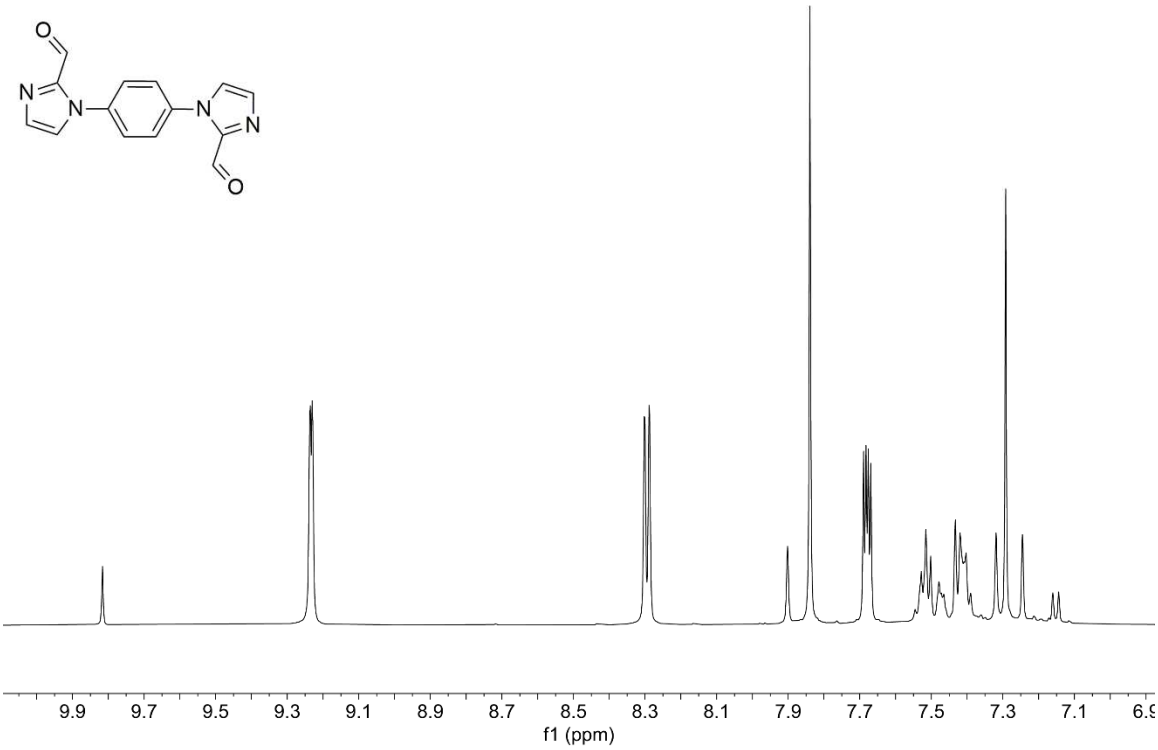

Figure 6.99: ^{1}H NMR spectra of **BnIm$_2$** ($CDCl_3$, 400 MHz, 298 K).

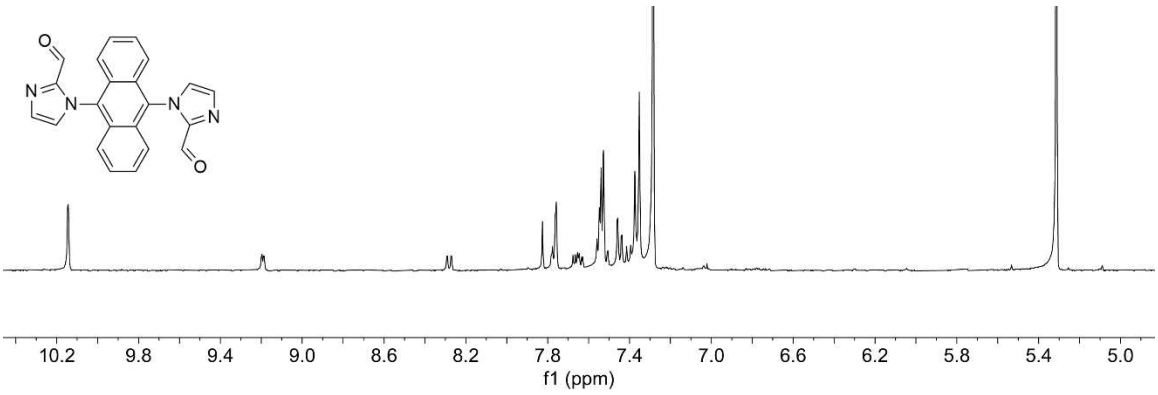

Figure 6.100: ^{1}H NMR spectra of **AntIm$_2$** ($CDCl_3$, 400 MHz, 298 K).

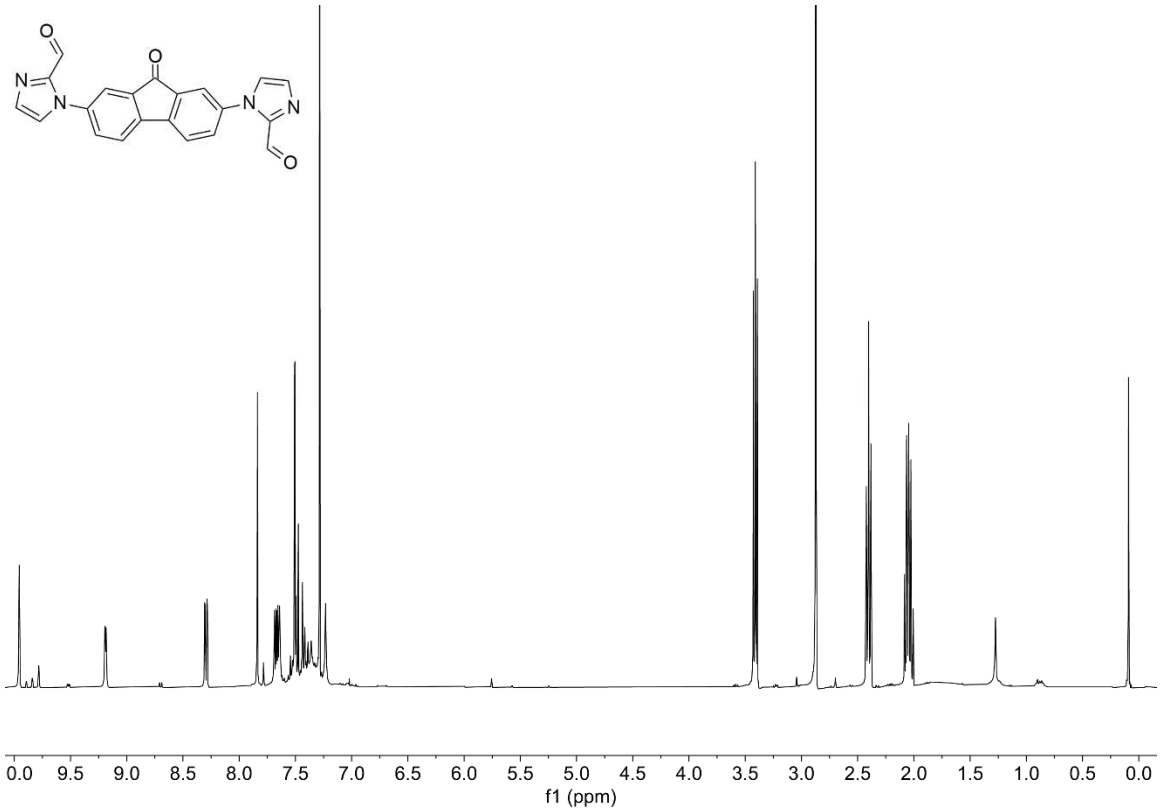

Figure 6.101: Synthesized from 2.7-dibromofluorene and oxidized during the reaction, ^{1}H NMR spectra of **FOIm$_2$** ($CDCl_3$, 400 MHz, 298 K).

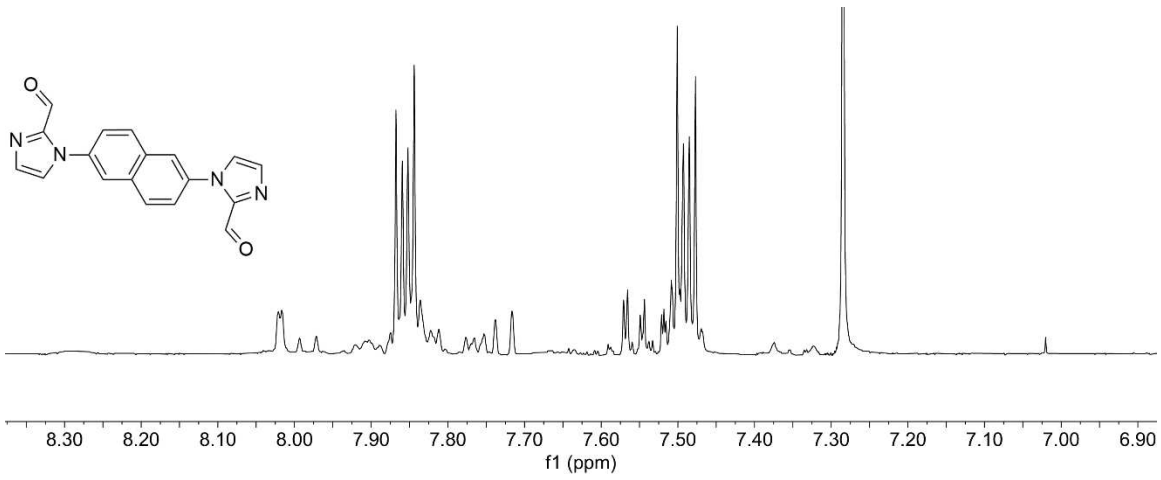

Figure 6.102: ^{1}H NMR spectra of **NaphIm$_2$** ($CDCl_3$, 400 MHz, 298 K).

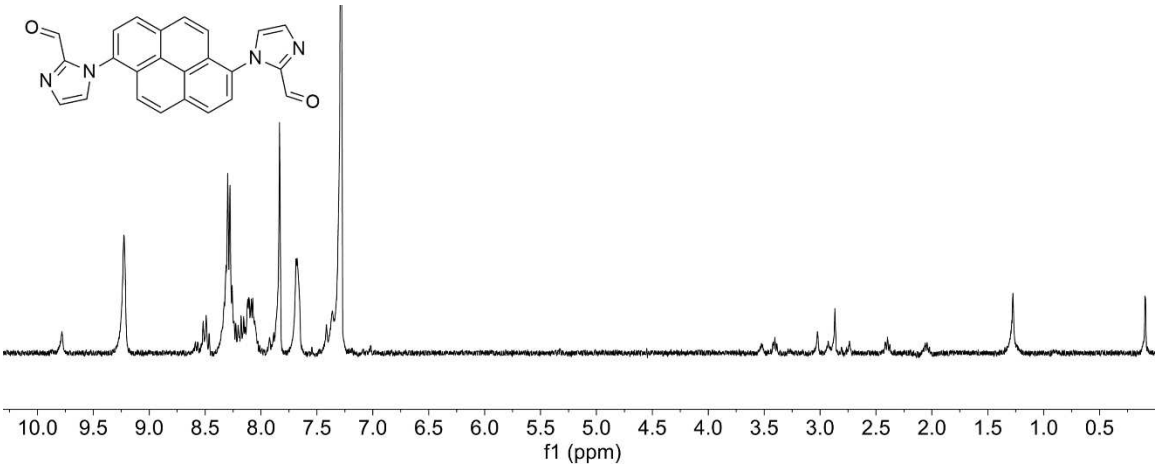

Figure 6.103: ^{1}H NMR spectra of **PyrIm$_2$** ($CDCl_3$, 400 MHz, 298 K).

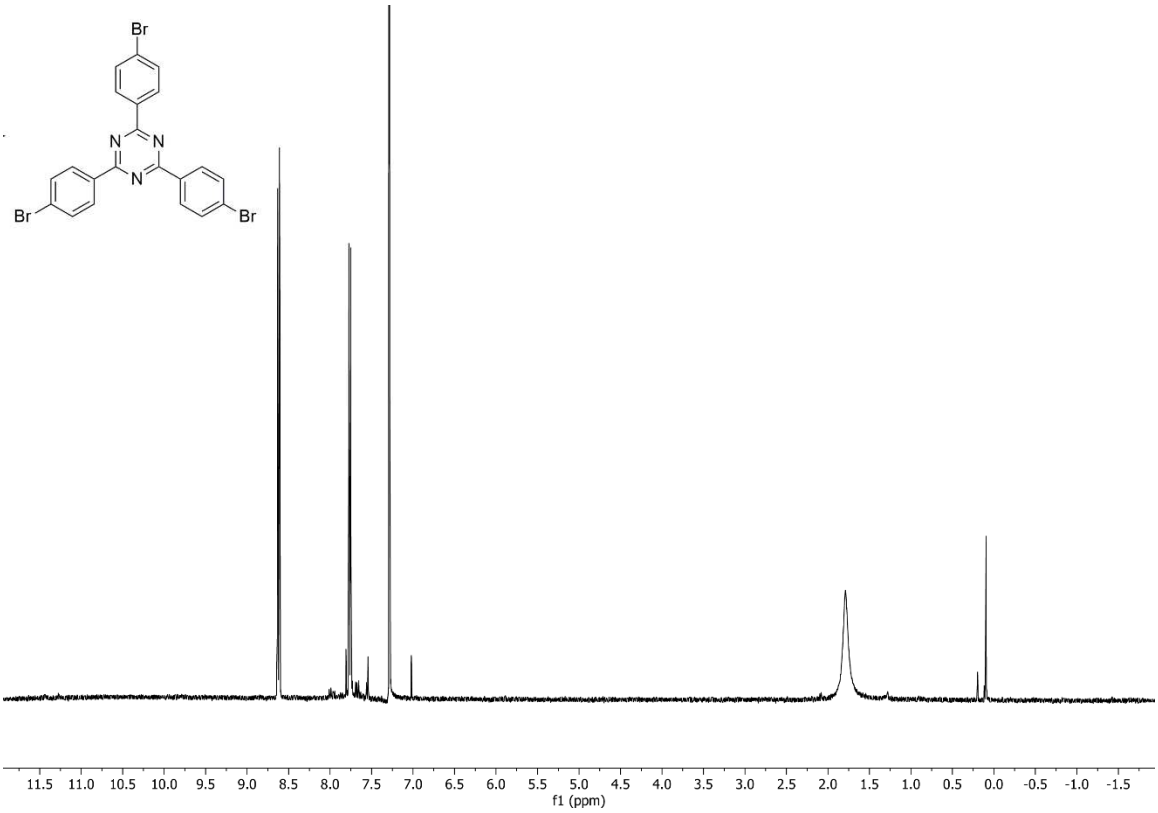

Figure 6.104: ^{1}H NMR spectra of **RTz** ($CDCl_3$, 400 MHz, 298 K).

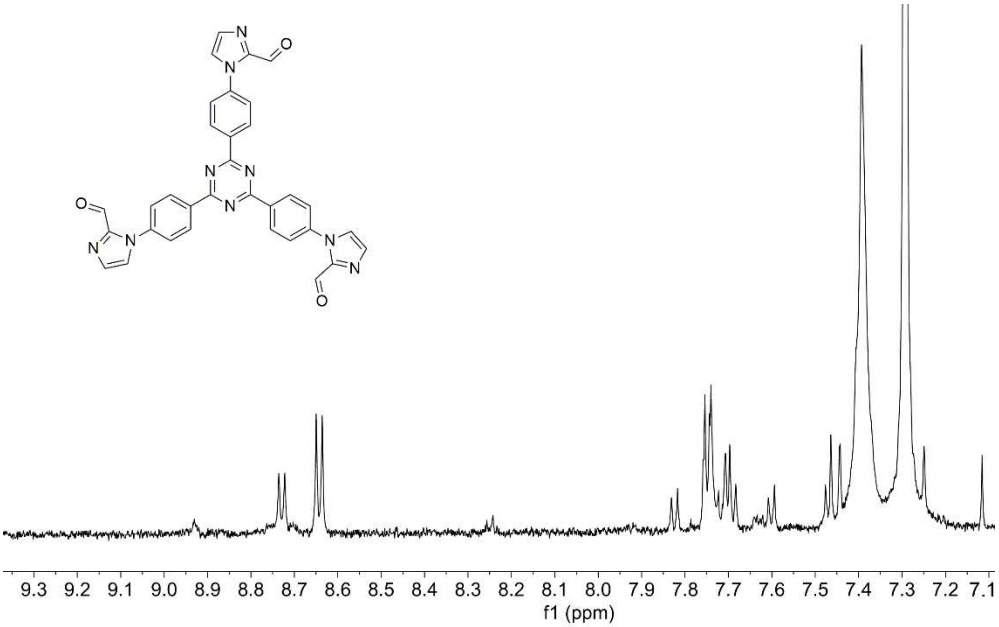

Figure 6.105: ^{1}H NMR spectra of **RTzIm$_3$** ($CDCl_3$, 400 MHz, 298 K).

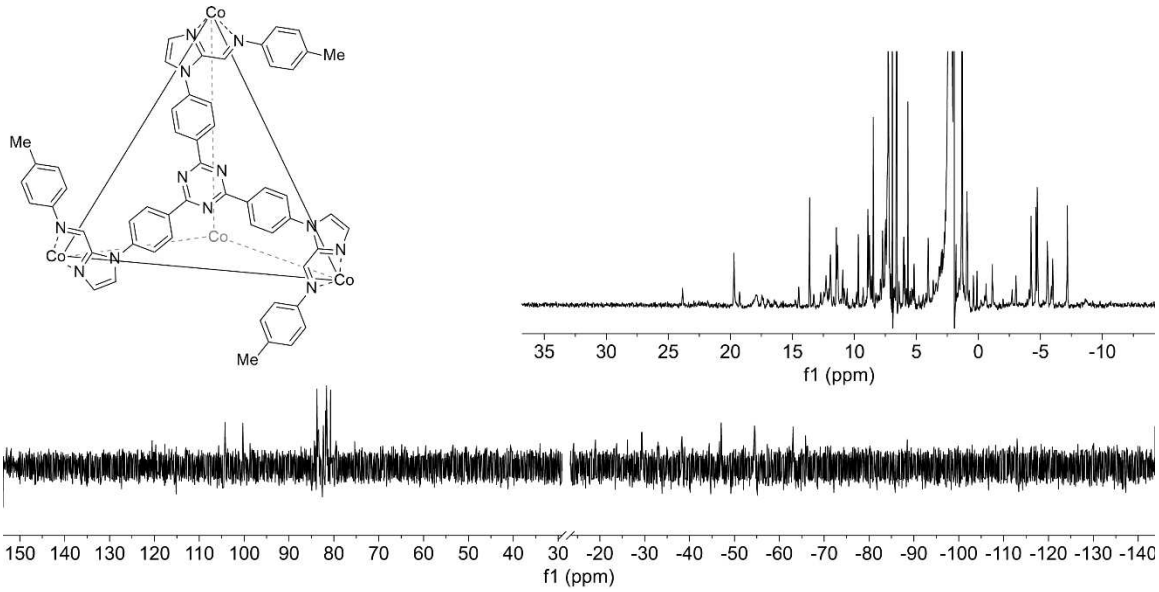

Figure 6.106: ^{1}H NMR spectrum of cage **RTzIm$_3$•Co•PhMe** ($CDCl_3$, 400 MHz, 298 K).

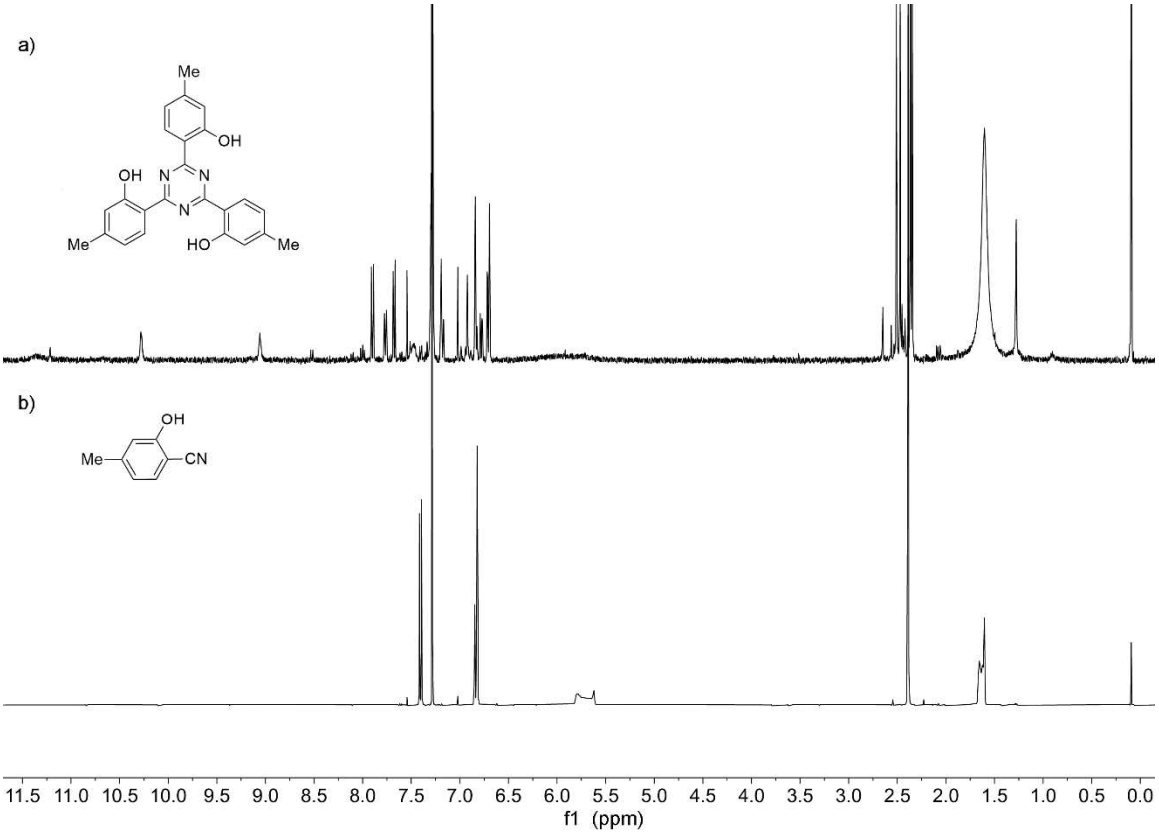

Figure 6.107: ^{1}H NMR spectra of a) triazine **Tz(OHMe)$_3$** and b) precursor 2-hydroxy-4-methylbenzonitrile ($CDCl_3$, 400 MHz, 298 K).

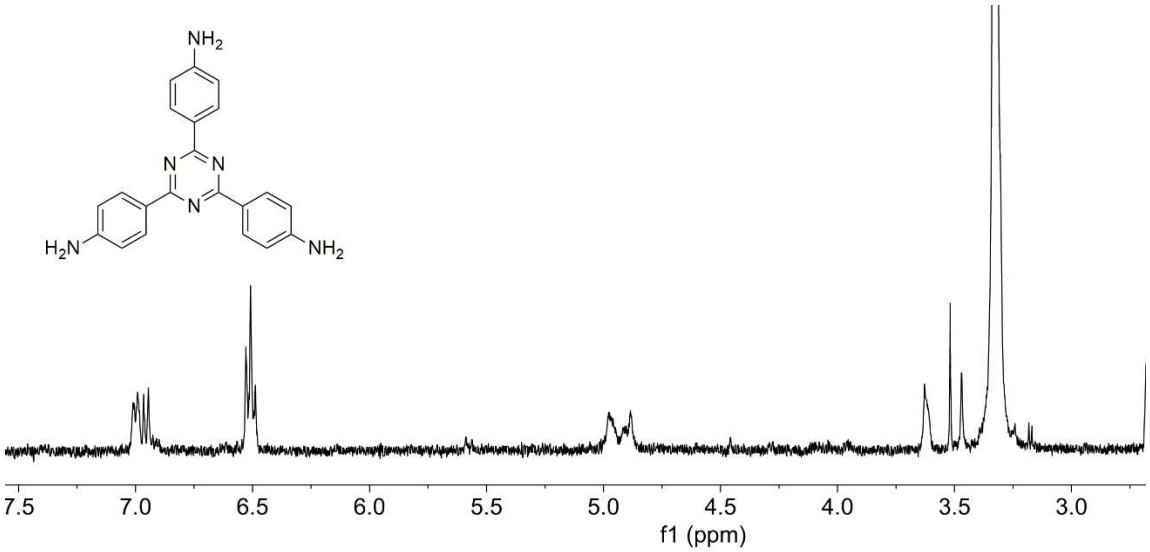

Figure 6.108: ^{1}H NMR spectrum of triazine **AmTz** ($CDCl_3$, 400 MHz, 298 K).

6.6 References

1. *APEX 2,* version 2014.1-1, Bruker (2014), Bruker AXS Inc., Madison, Wisconsin, USA.
2. *SAINT,* version V8.34A, Bruker (2012), Bruker AXS Inc., Madison, Wisconsin, USA.
3. *SADABS,* version 2012/1, Bruker (2012), Bruker AXS Inc., Madison, Wisconsin, USA.
4. *SHELXTL,* version 2013/4, Bruker (2013), Bruker AXS Inc., Madison, Wisconsin, USA.